UNIVERSITY OF BIRMINGHAM

PREPARATION OF NANOSTRUCTURED METAL OXIDES FOR GREEN ENERGY APPLICATIONS VIA CATHODIC CORROSION

by

MATTHEW JOHN LAWRENCE

A thesis submitted to the University of Birmingham for the degree of

DOCTOR OF PHILOSOPHY

School of Chemistry

College of Engineering and Physical Sciences

University of Birmingham

September 2020

Abstract

An increase in global population and advances in the development and implementation of technology during the 20th and 21st centuries has resulted in many societies across the globe being heavily reliant on technology for industrial, professional, social and personal use, particularly in developed and developing countries, causing an ever-increasing demand for sustainable and reliable energy. Traditionally, much of the energy produced across the world is sourced from carbon-based fuels, coal, oil and natural gas, which induce detrimental environmental consequences such as the increase in anthropogenic carbon dioxide (CO_2) upon consumption, which is associated with the observed global warming. There is social and political pressure to counteract current trends in energy production and CO_2 emissions, requiring the large-scale realisation of green energy technologies. However, the intermittent nature of solar, wind and wave power is not suitable to provide reliable energy on-demand. Thus, storing the electrical energy generated by green energy in chemical bonds is advantageous.

Hydrogen production via water splitting is a promising approach for energy storage due to the large natural abundance of water. However, this technology is not fully developed due to the limitations of existing materials to effectively catalyse the oxygen evolution reaction (OER). Electrochemically, the most active catalysts (IrO_2 and RuO_2) are not earth-abundant and therefore have high associated costs. Photoelectrochemically, the intrinsic properties of binary oxides are not suitable to take advantage of the majority of the solar spectrum. One of the routes towards the optimisation of metal oxide (photo)catalysts for the OER and involves doping the metal oxide semiconductor resulting in changes of the width and position of the semiconductor band gap, in addition to improvement in conductivity and long-term stability. However, the synthetic routes employed for the synthesis of active metal oxide photocatalysts are inefficient, often involving high temperatures and pressures over long timescales.

The electrochemical conversion of CO_2 (CO_2RR) to useful, value-added chemicals is the subject of significant research effort because this avenue affords an opportunity to take advantage of electrical energy generated by renewable sources such as wind, water and solar. The specific chemical and physical properties of the CO_2 reduction reaction (CO_2RR) catalyst plays a significant role in the catalytic process. Cu catalysts alone are capable of reducing CO_2 to multi-carbon products. Elemental composition, surface geometry, oxidation state, particle size and morphology impact the selectivity and efficiency of CO_2RR

Herein the production of mixed metal oxide nanostructures via cathodic corrosion is presented for the first time. Cathodic corrosion is a single-pot electrochemical etching technique performed at ambient temperatures and pressures, atomising bulk metals into nanoparticles.

The as-prepared oxides were extensively characterised by physical, optical and electrochemical methods, revealing the homogeneity in particle size and elemental composition for binary and mixed metal oxide nanostructures. The optical absorption properties of titanate nanowires was tuned by doping with 3 wt.% Cu^{2+}, leading to enhanced PEC activity. *In situ* XAS of Cu-titanates during CO_2RR revealed that chemical confinement is an effective route to stabilise oxidised Cu species, which have been reported to enhance the selectivity of oxide-derived Cu species towards C_{2+} products.

Dedication

First, giving honour to God, the Giver and Sustainer of life:

“The fear of the Lord is the beginning of wisdom, and the knowledge of the Holy One is insight.”

Proverbs 9:10 *English Standard Version*

To my love, my wife, Sidumisile. Thank you for your love and support and the joy and laughter that you and Ezekiel always bring into my life, amidst the stresses and challenges of postgraduate research. When I look back I realise how fortunate I was to have had you working so close by during the early years of my PhD research, the many fond memories of our commutes to and from the University. Thank you for your patience and continued support during my research visits around the world and, more recently, for soldiering on with much of the planning for our wedding while I was writing up this thesis. I can’t express how grateful I am.

Last, but certainly by no means least, I wish to dedicate this thesis to Mom and Dad. Your consistent prayers, words of encouragement, home-cooked meals and sacrifices over the years have afforded me with so many opportunities that I never could have imagined. I’m so thankful for all that you’ve done.

I am because you are. This is for you.

Acknowledgements

I would like to acknowledge my PhD supervisor, Dr Paramaconi Rodriguez (Boss). Unlike some PhD students I can honestly say that I will always look back on this time with fond memories. Thank you for always being willing to offer guidance, support and advice, both academically and personally, and for providing me with opportunities to experience the world as part of my research degree. I have learned a lot about electrochemistry, materials, the world and myself as a result of the time spent in your research group. I wish you nothing but success for the future.

To the members of the AMPERE group past and present, thank you for creating such a fun, friendly and productive research environment and group experience. Special mentions to Javi Monzo and Adam Kolodziej who initially encouraged me to apply for the PhD studentship and who helped me find my feet in the first year of my PhD, I'm grateful.

Much of the work presented in this thesis was conducted in collaboration with other research groups. Thanks to Veronica Celorrio (Diamond Light Source UK) and Nicholas Adkins (School of Metalurgy Materials, University of Birmingham) for your contributions over the years by way of XAS analyses and alloy preparation, respectively. I would also like to thank Joaquin and the members of the Rodriguez-Lopez group at the University of Illinois at Urbana-Champaign for hosting me in your group for 6 months where the photoelectrochemical measurements presented in this thesis were recorded. Likewise to Gu Meng at Southern University of Science and Technology (SUSTec) for hosting me and providing hands on training and experience of HRTEM imaging.

Contents

1. INTRODUCTION

In this general thesis introduction, the motivating factors behind the experimental work undertaken is explored, providing important context and relevance for this work.

1.1. Energy Consumption: Demand and Consequences

The global demand and consumption of energy has increased drastically in recent decades due to concurrent increases in the global population. Coupled with the rapid and numerous advances in the development and implementation of technology during the 20th and 21st centuries, societies across the globe have developed technological dependencies for industrial, professional, social and personal use, particularly in developed and developing countries. At the start of the 21st century the average global energy consumption rate was 13.5 TW, which was predicted to rise to 43 TW by 2100.[1]

Greater than 80% of global energy production is sourced from carbon-based fuels, namely coal, oil and natural gas. These fuels, commonly referred to as fossil fuels, first came to prominence during the industrial revolution of the late 1700s. In the UK in particular, the advent of the coal-powered steam engine provided a means of continuous energy generation that had a significant impact on economic output by relieving dependence on wind, water (H_2O) and muscle power, significantly improving productivity of individual labourers.[2] Transportation industries and infrastructure were also revolutionised by steam engines by the 19th century, with the time taken to produce and transport goods from mainland Britain to the capital, ports and across the world greatly reduced. This stimulated a boom in the development of industrial towns and cities like Birmingham and the Black Country in the West

Midlands, a collection of industrial towns aptly named after the infamous thick black smog that bellowed out of factory chimneys and persistently lingered over the region during the period.

Fast forward to the present day and, although the vast majority of these industrial towns and cities have ceased to operate as before, the 21st century lifestyle is heavily dependent on having consistent and reliable energy available on-demand and increased industrialisation is an indicator of economic advancement for developing countries. Coal still plays a crucial role in energy production. Coal-powered energy plants are responsible for 38% of global electricity.[3] Fossil fuels possess high energy densities due to the energy stored within chemical bonds. This means that there is negligible to minimal energy losses associated with the storage and transportation of coal/oil and natural gas, respectively, which continues to make the use of these fuels attractive, particularly for developing countries.

The existing reliance on fossil fuels isn't sustainable from resource and environmental perspectives. Fossil fuels are produced by nature at a significantly slower rate than the rate of their consumption in energy generation, *i.e.* depleting resources. Early estimates purported that fossil fuel reserves would be critically depleted by the end of the current century, but more recent estimates suggest that there are sufficient fossil fuel resources for centuries to come (**Figure 1**).[1, 4] The unequal distribution of these resources globally is thought to be a stimulater of political tensions and unrest.

Detrimental environmental consequences are associated with the use of these fuels. The combustion of fossil fuels increases the concentration of atmospheric greenhouse gases (GHGs), carbon dioxide (CO_2), methane (CH_4) and nitrous oxide (N_2O), which inhibit the reflection and radiation of heat from the earth's surface to space, contributing to the greenhouse effect and global warming. CO_2 is the most prominent GHG, accountable for 75% of total global GHG emissions, with more than 50% generated by developing countries, and

90% of total emissions arising from combustion of fossil fuels, discounting wood fuels and forest fires.[5]

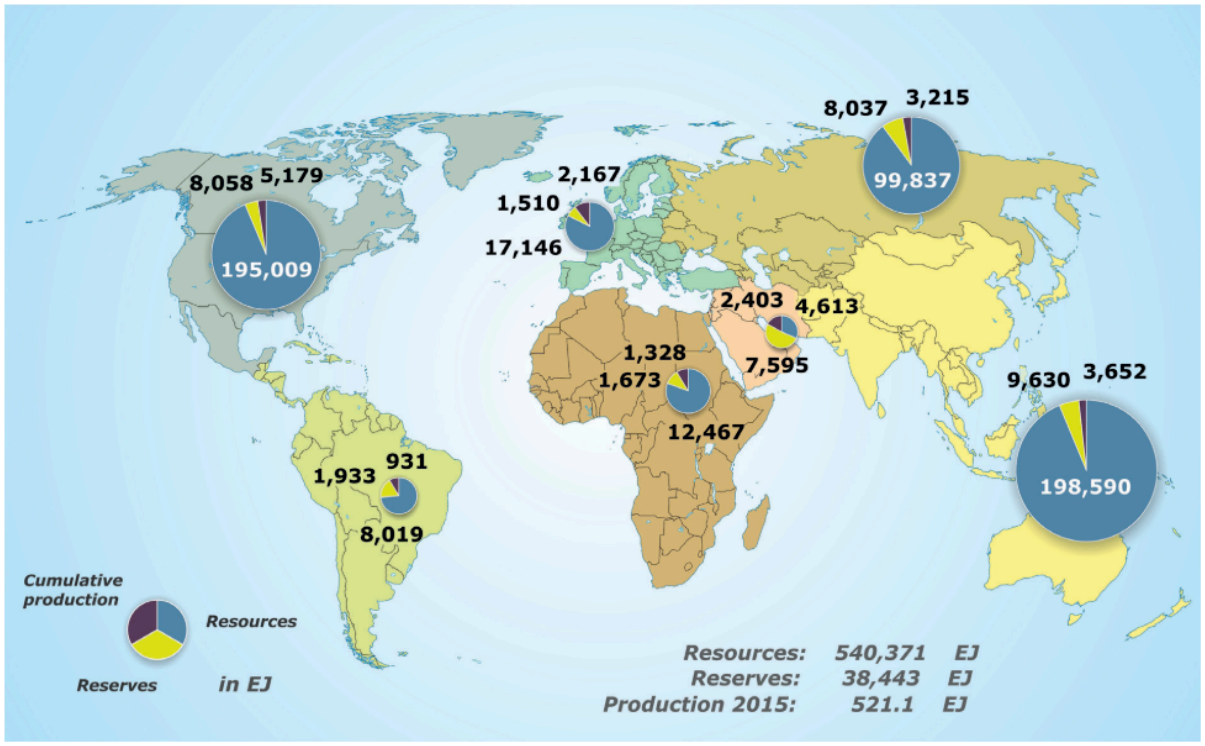

Figure 1. Total potential of fossil energy resources including uranium in 2015: regional distribution excluding coal resources in the Antarctic, and excluding resources of oil shale, aquifer gas, natural gas from gas hydrates, and thorium, because these cannot be classified regionally (estimated accumulative production of coal since 1950). Reprinted from BGR (2016): Energy Study 2016. reserves, resources and availability of energy resources (20). – 180 p., Hannover.[4]

No atmospheric CO_2 degradation mechanism exists other than convection, which occurs over a period of a few hundred and a few thousand years.[1] The convection mechanism presents environmental issues due to the acidification of oceans and other bodies of water (**Equation 1**) which is harmful to marine species and their historic ecosystems. Increased sea temperatures, resulting from the greenhouse effect and global warming, shift the equilibrium to the left and hinder the CO_2 dissolution process. Consequently, the high concentration of atmospheric CO_2 worsens and further contributes to the increase of global surface temperatures.[6, 7]

$$H_2O + CO_2 \rightleftharpoons CO_3^{2-} + 2\,H^+ \qquad (1)$$

The global concern surrounding the effect of increasing GHG emissions and climate change as a consequence of global warming has prompted both national and international political action. The UK government legislated the Climate Change Act 2008 which set a target to reduce net UK CO_2 emissions to lower than 80% of the 1990 baseline by 2050 and established an independent Committee on Climate Change.[8] The United Nations Paris Agreement, signed by the majority of countries across the world in 2016, aimed to provide a global response to the climate change problem by seeking to limit global temperature rises to 1.5 °C above pre-industrial revolution levels in the context of sustainable development and economic advancement.[9] **Figure 2a** presents the evolution of global mean temperature change observed in 2017 relative to 1850-1900 and estimates of the likely range in future global warming under 3 modelled pathways: *(i)* anthropogenic CO_2 emissions decrease from 2020 to net-zero in 2040, *(ii)* CO_2 emissions decrease from 2020 to net-zero in 2055, *(iii)* no reduction in non-CO_2 radiative forcing, the shift in equilibrium caused by other GHGs affecting the energy radiated back to space. The results suggest that without significant changes to the levels of CO_2 emissions that the 1.5 °C global warming limit could be exceeded a decade before 2050 and that even with the highly optimistic model of a linear decrease in CO_2 emissions from 2020 to net-zero in 2040 (**Figure 2b**) the 1.5 °C limit could still be breached.

Therefore, to combat the current reliance on fossil fuels for energy production, reduce GHG emissions achieve the net zero CO_2 emissions target and have a better probability of maintaining the 1.5 °C temperature rise target, sustainable and efficient alternative carbon-neutral methods of energy production, storage and transportation are desired. The ideal energy production scenario should involve the use naturally abundant resources that avoid the adverse environmental effects associated with fossil fuel combustion.

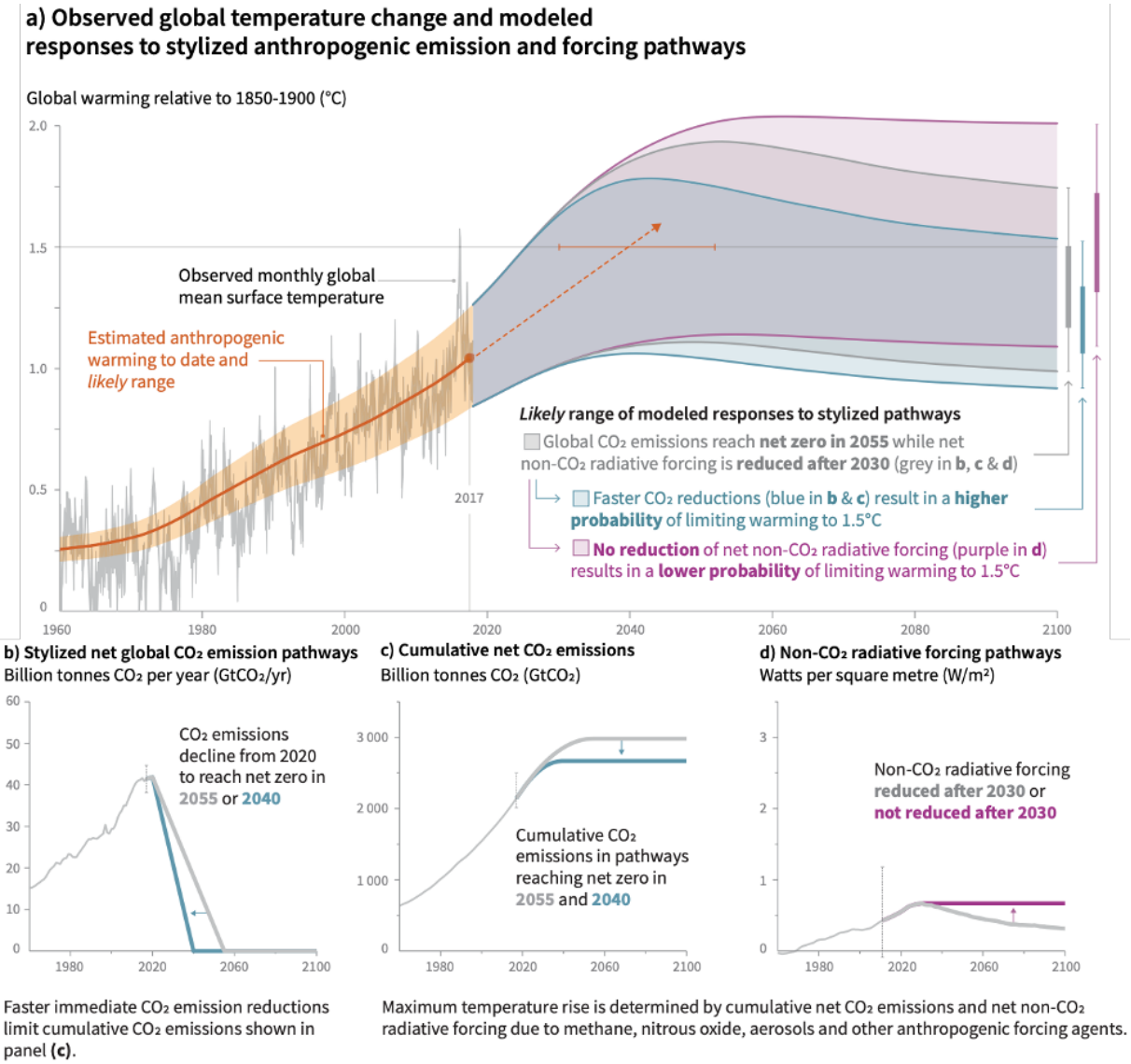

Figure 2. (a) Monthly global mean surface temperature change [grey line], estimated anthropogenic global warming [solid orange line] and likely range [orange shaded area] up to 2017. The central estimate and likely range of the time at which global warming of 1.5 °C is reached under the current rate of warming is represented by the dashed orange arrow and horizontal error bar, respectively. Grey shaded area [middle plume in (a)] indicates the likely range of warming responses, computed with a simple climate model, to a stylized hypothetical future in which net CO_2 emissions [grey line in panels (b) and (c)] decline in a linearly from 2020 to reach net zero in 2055 and net non-CO_2 radiative forcing [grey line in (d)] increases to 2030 and then declines. The blue shaded area [bottom plume in (a)] shows the response to faster reductions in CO_2 emissions [blue line in (b)], reaching net zero in 2040, reducing cumulative CO2 emissions (c). The purple shaded area [top plume in (a)] shows the response to net CO2 emissions declining to zero in 2055, with net non-CO2 forcing remaining constant after 2030. The vertical error bars (a) show the likely ranges of the estimated distribution of warming in 2100 under the three rendered pathways. Reprinted from Summary for Policymakers. In: Global warming of 1.5 °C. An IPCC Special Report on the impacts of global warming of 1.5 °C above pre-industrial levels and related global greenhouse gas emission pathways, in the context of strengthening the global response to the threat of climate change, sustainable development, and efforts to eradicate poverty. Copyright © 2018, International Panel on Climate Change.[10]

1.2. Green Energy

Solar, wind and water technologies, commonly referred to as renewables, are examples of electrical energy production methods that use naturally occurring primary energy sources and that enact negligible environmental damage once implemented, *i.e.* green energy.[11] Green energy technologies are advantageous because they are unlimited natural resources that are available in all corners of the globe that cannot be monopolised. This is particularly important for developing countries, many of which benefit from prolonged periods of sunlight. The supply of solar energy irradiating the Earth vastly outweighs current demand such that the total global solar energy supplied per hour is greater than the total annual energy consumed through human activity.[12]

Much of the early work targeting the utilisation of sunlight for green energy applications focused on the direct conversion of light into water heating systems.[13] Photovoltaic (PV) technology, aptly named, directly converts solar energy into electrical energy by absorption of infrared and visible light and provides a source of sustainable, usable energy with negligible environmental effects.[14] With the relatively low energy of infrared photons it is advantageous and often more efficient to convert the solar energy to heat but significant energy losses are inherent with the storage of both electricity and heat.[15] Unfortunately, solar energy is intermittent by nature, with varying energy intensities dependent on daily and seasonal weather conditions. Coupled with the inefficiencies of electrical energy storage and the costly materials used in batteries, conversion of solar energy to electricity is not the perfect alternative to fossil fuels in the pursuit of stable and consistent energy to meet the demands of a growing population. Furthermore, electricity consumed in both industrial and domestic settings corresponds to ≅ 30% of the total global energy consumption and does not address transportation demands.[16] Rather, mimicking nature by converting and storing solar energy as chemical fuels presents a promising alternative, provided that there is negligible

environmental impact involved in the energy conversion process and that the products released through use of the fuels do not further contribute to the greenhouse effect and global warming. Biological photosynthesis is an example of a naturally occurring solar fuel production process, converting CO_2 and H_2O into glucose and O_2. However, biological photosynthesis is highly inefficient and significant land resources would need to be surrendered and cultivated in order to utilise this pathway to meet the growing energy demand solar energy-to-fuel conversion, particularly challenging in light of the expanding population.[17, 18]

1.3. A Sustainable Hydrogen Economy

Hydrogen (H_2) is the most abundant element above the earth, found predominantly chemically bound in H_2O. It has a high energy capacity, is non-hazardous to the environment as the product of H_2 combustion is H_2O and is a versatile fuel resource. It can be utilised in electrochemical fuel cells as another method of electricity generation, as a fuel in combustion engines, can be reacted with CO_2 to produce industrially significant chemicals and is much easier to store than energy in the form of heat or electricity.[16, 19-21] Hydrogen storage, although still a developing technology in terms of maximising the reversibility and efficiency of the storage process, is easier to store than energy in the form of heat or electricity.

At present H_2 is usually produced through the use of fossil fuels in energetically demanding processes. Steam reforming of CH_4 and other hydrocarbon gases at temperatures up to 900 °C and pressures of 1.3 – 3 MPa is the most common route.[22] Coal gasification, also performed at high temperatures and pressures is another production route employed at the industrial scale.[23] The by-products of these H_2 generation pathways are CO, CH_4 and CO_2, albeit the amount of CO_2 produced is no greater than would be released upon combustion of CH_4.[22] The political and environmental concern over the use of fossil fuels means that alternative H_2 producing pathways are more desirable.

That the majority of the earth's surface is covered in H_2O, H_2 sourced from this naturally abundant resource has potential to be the most sustainable alternative renewable fuel, also re-forming H_2O through its use. H_2O is a very stable molecule across a wide temperature range and significant incident energy is required to break the strong O-H bonds and alleviate the bound H_2. Conventionally this has been achieved at the large scale via water electrolysis, commonly referred to as water splitting, splitting H_2O into O_2 and H_2 gas, respectively, under applied electric potential and can be conducted in either acidic or basic aqueous media, also via a solid polymer electrolyte.[24] Such an electrochemical energy conversion process can take advantage of the electrical energy produced via the intermittent green energy technologies, converting and storing the energy in H_2 chemical bonds.

In acid, the oxidation of H_2O at the anode evolves O_2, releasing protons and electrons, the oxygen evolution reaction (OER). Subsequent migration of the protons through the electrolyte to the cathode and the flow of the electrons through the external circuit to the cathode results in the reduction of the protons to form H_2, the hydrogen evolution reaction (HER). Under basic conditions the OER proceeds via the oxidation of hydroxyl anions, forming H_2O, as a by-product, and electrons. The reduction of H_2O molecules at the cathode via basic HER generates H_2; **Scheme 1** summarises the half reactions for OER and HER in both acidic and basic media. Whether performed in acid or base, the thermodynamic potential difference required to split water electrochemically at standard temperatures and pressures is 1.23 V. However, the economic motivation for the widespread utilisation of this green energy application is presently hindered by the OER. It is kinetically limiting, a 4 electron transfer process comprising multiple adsorbed surface intermediate species for the evolution of 1 mole of O_2 gas and the release of protons.[24, 25] Thus, considerable overpotentials are required in reality, attributed to the kinetic constraints of individual reaction steps, in to order to drive the water splitting reaction at an appreciable rate. Moreover, catalysts that have

demonstrated exceptional OER catalytic performance are oxides of precious metals, IrO_2 and RuO_2, with low natural abundance and considerably high cost.[26-29] IrO_2 in particular has demonstrated notable OER activity and stability in both acidic and basic conditions.[24] The need for a more cost effective catalysts has stimulated research into the use of earth-abundant transition metal oxides for alkaline electrolysers, where such materials display significant stability over a wide anodic range with appreciable activity.[30]

Scheme 1. Water electrolysis half reactions (OER and HER) and standard electrode potentials in acidic and basic media.

Acidic media

Anode:	$H_2O_{(l)} \rightarrow 2\ H^+_{(aq)} + 2\ e^- + \frac{1}{2} O_{2(g)}$	E_0 = +1.23 V (SHE)
Cathode:	$2\ H^+_{(aq)} + 2e^- \rightarrow H_{2\ (g)}$	E_0 = 0.00 V (SHE)

Basic media

Anode:	$2\ OH^-_{(aq)} \rightarrow H_2O_{(l)} + 2\ e^- + \frac{1}{2} O_{2(g)}$	E_0 = +0.40 V (SHE)
Cathode:	$2\ H_2O_{(l)} + 2e^- \rightarrow H_{2(g)} + 2\ OH^-_{(aq)}$	E_0 = -0.83 V (SHE)

Overall

	$\mathbf{H_2O_{(l)} \rightarrow H_{2(g)} + \frac{1}{2} O_{2(g)}}$	$\boldsymbol{E_0}$ **= +1.23 V**

1.3.1. Solar H_2 production via Photoelectrochemistry

Whilst water electrolysis provides an indirect solar energy utilisation route for the production of H_2, photoelectrochemical (PEC) water splitting provides a direct green energy conversion and storage pathway. A solar fuel is one produced via a light-driven chemical reaction, storing chemical energy which can later be released upon reaction with oxygen (**Equation 2**). The criteria of a solar fuel include: *(i)* the fuel formation reaction must be endergonic, *i.e.* an energetically uphill process; *(ii)* the fuel production reaction must be reversible to regain all the stored energy; *(iii)* side-reactions must be completely eradicated to prevent the degradation of the starting materials; *(iv)* the reverse reaction should be highly unfavourable under normal conditions but proceed rapidly during energy release.[13] Additionally, to be suitable for widespread use the fuel should be non-toxic and easily stored and transported. The PEC water splitting reaction satisfies all of the above criteria, with H_2O on the left side of **Equation 2** and H_2 being the solar fuel (*F*).

$$A + B \rightleftharpoons F + O_2 \quad (2)$$

The field of photoelectrochemistry began to gain traction following the work of Brattain and Garrett in the 1950s who demonstrated that light irradiation onto germanium semiconductor electrodes increased the current measured at the electrode surface due to the formation of a semiconductor-electrolyte (SE) junction.[31] This work provided an explanation for the photovoltage and photocurrent observed by Becquerel in 1839 upon light illumination of a AgCl electrode in a 2-electrode electrochemical cell due to the presence of a semiconductor at the electrode-electrolyte interface.[32] was due to the formation of a semiconductor-electrolyte (SE) junction; a during Becquerel's experiment.

To better understand the SE junction, it is important to outline the properties of semiconductors that enable their use in green energy applications.

1.3.1.1. Semiconductor properties

Solids formed from large numbers of atoms form energy bands through the stacking and combination of the atomic orbitals into which electrons are distributed across the entire solid. The bands have differing energies and are separated, similar to individual electronic orbitals. Comparisons to molecular orbitals can be made. The valence band (VB) is the highest energy filled (occupied) band state (*cf*. HOMO), the conduction band (CB) is the lowest energy unoccupied band state (*cf.* LUMO) and the difference in energy between the VB and the CB is known as the band gap, E_g (**Figure 3A**). A semiconductor is a material with a band gap small enough to allow the excitation of electrons from the VB to the CB, leading to the formation of a positive hole (h^+) and electron (e^-) pair induced by an energetic stimulus. At temperatures > 0 K, electron promotion from the VB to the CB can occur through the absorption of thermal energy (**Figure 3B**).[33] Importantly, in the context of green energy applications, absorption of a photon with energy sufficient to overcome the band gap produces electron excitation to the CB. The photogenerated charge carriers are able to migrate through the solid semiconductor generating a photocurrent, *i.e.* the result of the photovoltaic effect, the process that affords the successful operation of PV cells.

The nature and electronic behaviour of semiconductors can be significantly altered by introducing low concentrations of dopant heteroatoms. Using Si as an example, an intrinsic semiconductor used in many commercial PV cells,[15] doping with atoms of elements directly adjacent to Si in the periodic table affects the occupancy of the VB such that the replacement of one Si atom with one P atom of the same charge provides an additional electron relative to the pure Si semiconductor. A narrow band is formed that can donate electrons to the CB, rendering the semiconductor as an electron donor, referred to as an n-type semiconductor (**Figure 3C**). Analogous replacement of Si with Al instead results in an electron deficient VB and the formation of an electron accepting band, rendering the semiconductor an electron

acceptor, a p-type semiconductor (**Figure 3D**). The Fermi level (E_F), described practically as the top of highest occupied levels in the case of n-type and p-type semiconductors above 0 K, is affected by the type of doping, as illustrated in **Figure 3**.

The formation of a junction is observed whenever there is a difference in Fermi levels between the semiconductor and the hetero-phase it contacts. A transfer of charge carriers from the semiconductor occurs in order to reach thermodynamic equilibrium and balance out the Fermi levels, generating a space-charge region (**Figure 4**); region widths have been reported to range from 50 to 2000 Å.[34] An interface potential barrier is created as a result of the equilibration of the Fermi levels causing band bending, and it is this potential barrier (the space charge region) that affords the separation of charge carriers and gives rise to photocurrent generation upon junction illumination.[16, 34, 35] Furthermore, the photogenerated charge carriers are reactive and can participate in electrochemical reactions at the catalyst surface.[18]

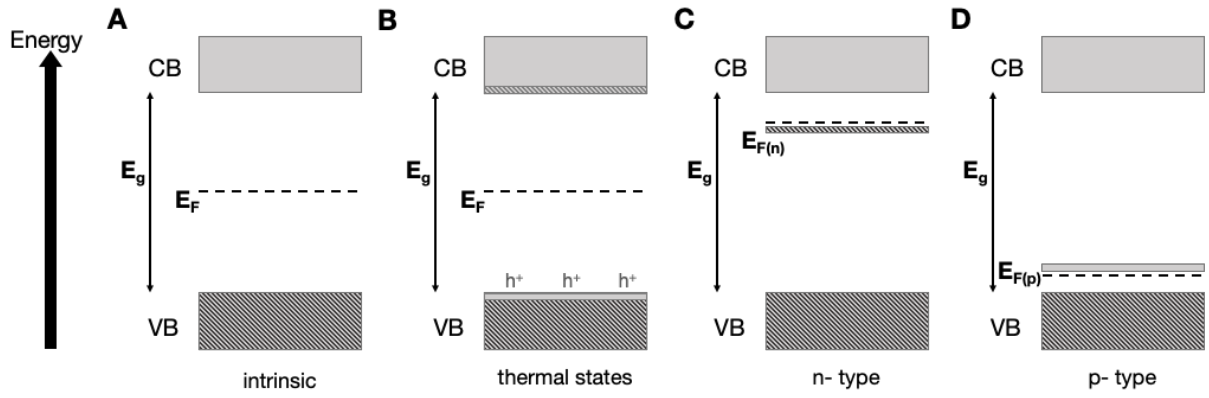

Figure 3. Schematic representation of (A) the intrinsic position and occupancy of the VB and CB in a semiconductor, (B) thermal states present at T > 0 K due to thermal excitation of electrons to the CB. (C) n-type and (D) p-type semiconductors formed through doping with heteroatoms. E_g denotes the band gap and E_F (dashed line) represents the Fermi level of the intrinsic semiconductor. $E_{F(n)}$ and $E_{F(p)}$ correspond to the Fermi level of a n-type and p-type semiconductor, respectively.

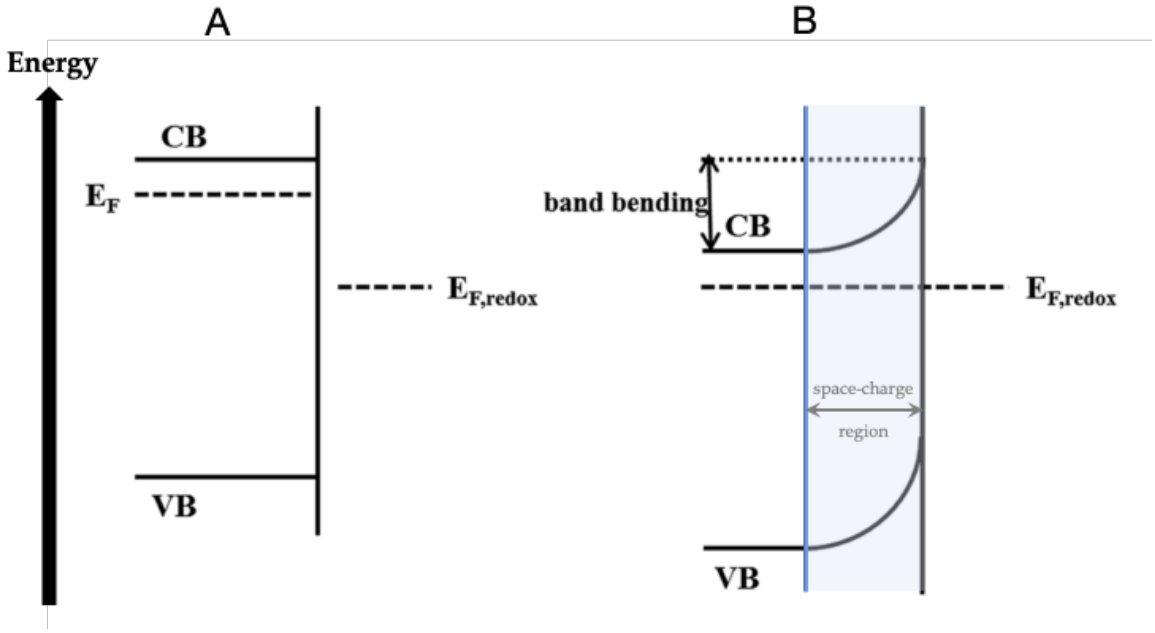

Figure 4. Fermi level (E_F) equilibration and space-charge region (band bending) formation resultant at a semiconductor-electrolyte junction, (A) before and (B) after contact with electrolyte. Adapted from reference[34]. Copyright © 2016, Royal Society of Chemistry.

SE junctions are more advantageous than the p-n junctions used in PV cells.[36] The transparency of the electrolyte and inherent generation of SE junctions upon contact with the electrolyte means that almost all of the irradiated light can directly interact with the generated space-charge region with the distance photogenerated charge carriers need to travel to the reactive sites being minimal, thus the need to factor in expensive junction engineering to more efficiently separate the charge carriers is removed.[18, 37]

1.4. Photoelectrochemical water splitting

The unassisted solar photon absorption of H_2O occurs at wavelengths <200 nm, *i.e.* high energy UV and/or low energy X-rays.[13] Therefore, semiconductors are utilised as photocatalysts to facilitate solar light absorption, which is predominantly visible light. Fujishima and Honda first constructed a functional H_2-producing PEC cell using a TiO_2 n-type semiconductor photoanode irradiated with UV light and a Pt-black cathode;[38, 39] **Scheme 2** outlines the half and overall PEC water splitting reactions.

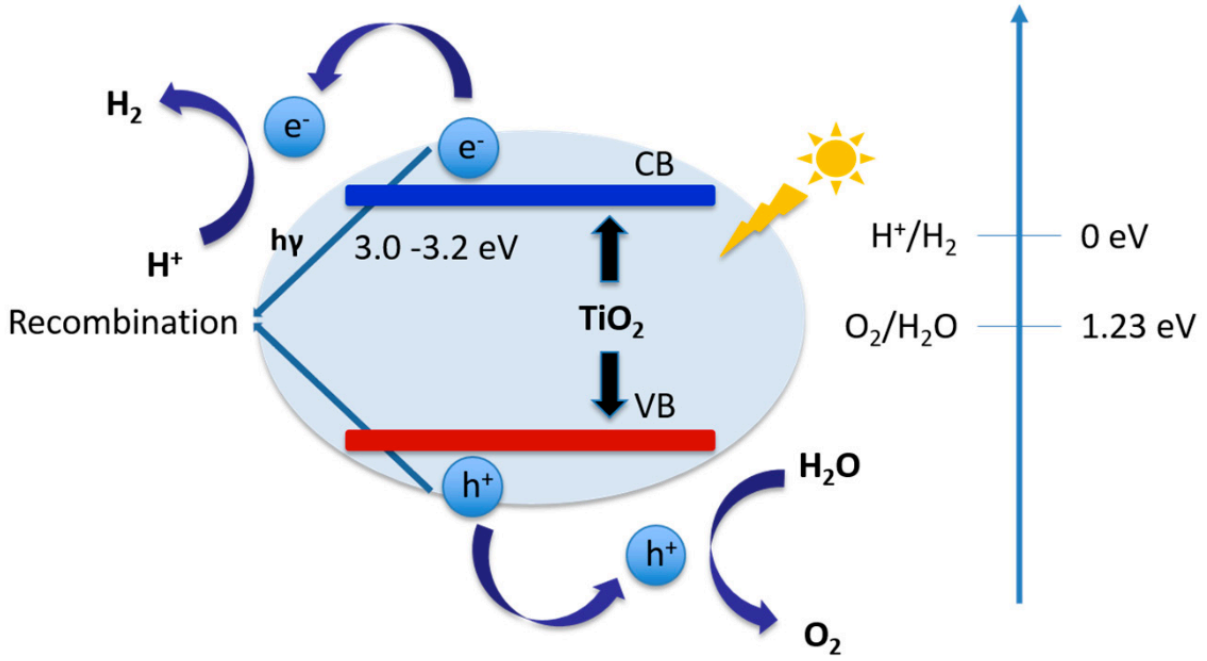

Figure 5. Schematic illustration of PEC water splitting via a TiO_2 semiconductor photoelectrocatalyst. Reprinted from reference [23].

Scheme 2. PEC water splitting OER and HER half reactions, as well as overall reaction equation.

Anode: $H_2O_{(l)}\ 2\ h^+ \rightarrow \frac{1}{2}\ O_{2(g)} + 2\ H^+_{(aq)}$

Cathode: $2\ H^+_{(aq)} + 2\ e^- \rightarrow H_{2\ (g)}$

Overall: $\mathbf{H_2O_{(l)} \rightarrow H_{2(g)} + \frac{1}{2}\ O_{2(g)}}$

For a semiconductor to successfully facilitate the overall PEC water splitting reaction, the band gap of the semiconductor must be ≥ 1.23 eV to provide sufficiently energetic photogenerated charge carriers, the VB upper limit ought to be more positive than the standard OER potential and the CB lower limit ought to be more negative than the standard HER potential, relative to the normal hydrogen electrode (NHE).[23] TiO_2 is one such material that satisfies the above requirements (**Figure 5**). However, the intrinsic physical properties of TiO_2 are not practicable for industrialised solar PEC water splitting applications. The size of the band gap (3.0 eV for rutile and 3.2 eV for anatase crystal structures, respectively) means

that only predominantly UV photons can be absorbed with very little visible light absorption possible. Furthermore, it suffers from high bulk charge carrier recombination.

Significant research effort has been given towards the improvement in (photo)electrocatalytic activity for promising electrode materials by tuning various physicochemical parameters that either (*i*) increase the number of active sites for a given amount of material or (*ii*) increase the intrinsic activity of the active sites present (**Figure 6**). The ideal semiconductor for solar PEC water splitting ought to possess a band gap in the range 1.6 to 2.2 eV to allow for absorption of the vast majority of the solar spectrum, have efficient e^-/h^+ pair generation and migration to the catalyst surface and have minimal energy losses through heat generation or exciton-lattice interactions.[31] Overall, transition metal oxides are advantageous as PEC catalysts due to their relatively low cost, low toxicity and excellent stability in aqueous media. The empty d orbitals of early transition metal oxides result in low lying VBs, that, combined with the strongly polarising O 2p orbitals, result in the formation of wide band gaps.[23, 40] Contrastingly, the occupied d orbitals of the later transition metal oxides (*e.g.* Fe) result in much narrower band gaps and the presence of strong d-d transitions that significantly impact on PEC reactions.[41]

Notable n-type transition metal oxide semiconductors include Fe_2O_3, $BiVO_4$ and WO_3 (**Figure 7**). Fe_2O_3 has a band gap that ranges between 1.9 and 2.2 eV, depending on the specific synthetic route, which enables it to absorb visible and near-infrared photons.[17] However, it suffers from short hole diffusion lengths, considerable charge recombination (due to the d-d transitions) and sluggish surface kinetics that limits the PEC catalytic performance.[42] $BiVO_4$ and WO_3 also have band gaps that allow for visible light absorption (2.4 and 2.8 eV, respectively) but the CB positions limit their use only to catalysing the anodic OER. Therefore, heterojunction architectures and tandem cells, using combinations of different semiconductor materials with varying band gaps and CB/VB positions, need to be implemented for scale-up of PEC water splitting with these metal oxides.[42]

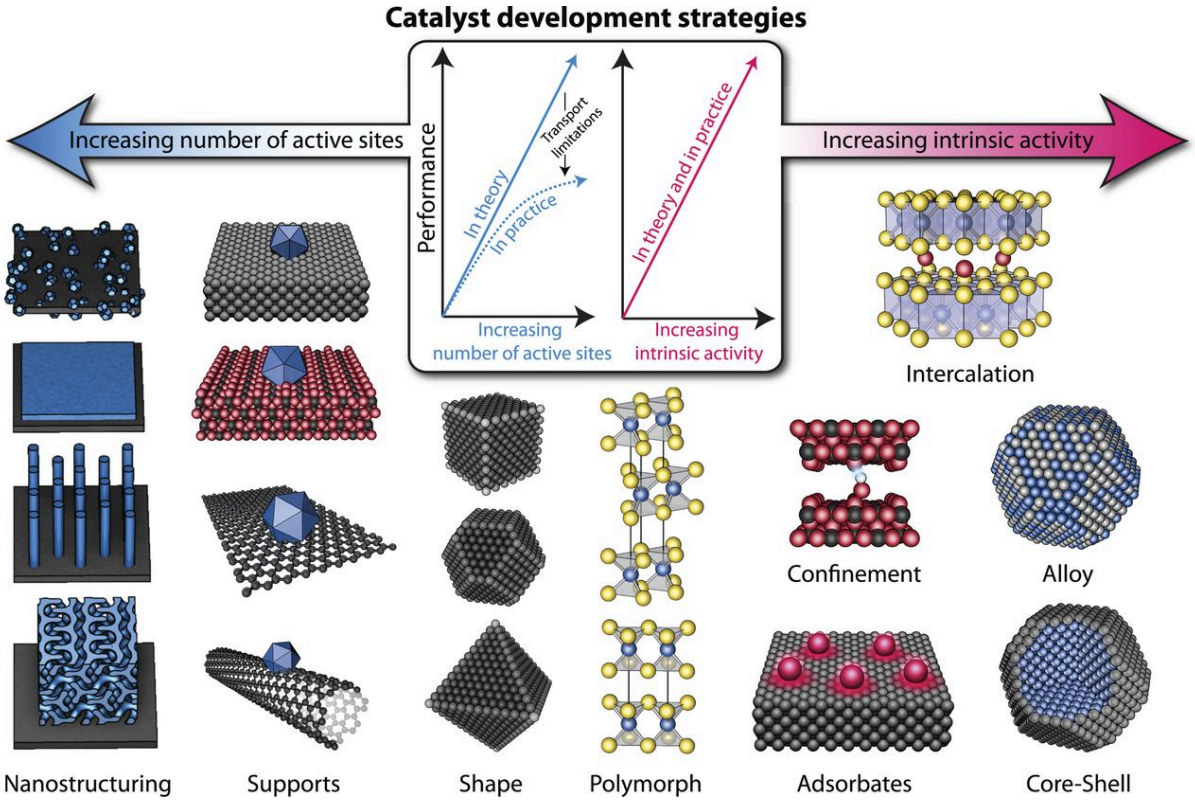

Figure 6. Various (photo)electrocatalyst development strategies employed in literature targeting more selective, active and durable catalysts for green energy applications. Reprinted with permission from Seh *et al.*[43] Copyright © 2017, AAAS.

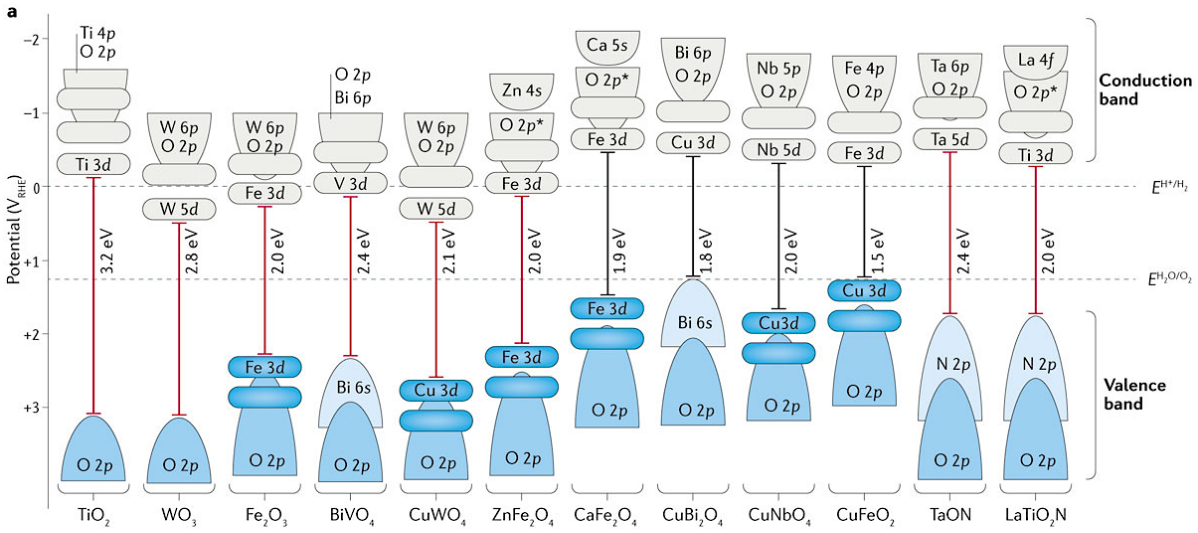

Figure 7. Band gap structure and selected crystal structures of oxide (and oxynitride) semiconductors for PEC applications. Reprinted with permission from Sivula *et al.*[17] Copyright © 2016, Springer Nature.

1.4.1. TiO_2

Various surface modification, nanostructuring and doping approaches have been employed targeting reduction of the TiO_2 band gap and the rate of charge carrier recombination.[44-47] For instance, Liu *et al.* demonstrated the single-pot hydrothermal synthesis of N-doped anatase TiO_2 sheets with a high proportion of (001) facets and enhanced visible light absorption, due to the presence of localised inter-band states due to N-doping, with a slight decrease in the anatase band gap determined by UV-visible absorption spectroscopy (3.11 eV).[48] This work was later supplemented by investigation of the effect of tuning the relative ratios of (001), (101) and (010) facets on undoped anatase TiO_2 particles, where a cooperative mechanism of surface atomic structure and surface electronic structure was proposed to explain the better PEC photocatalysis towards HER observed for the catalyst with the greater ratio of (010).[49] Similarly, Gordon *et al.* presented surface engineered anatase TiO_2 crystals on the nanometre regime via a seeded growth method with TiX_4 precursors (where X = F^- and/or Cl^-), generating O^{2-} vacancies in the presence of F^-.[50] Their results suggest that a high proportion of (101) facets generates more PEC active anatase TiO_2.

The most active TiO_2 surface morphology reported via the above surface engineering methodologies utilising the same surfactants conflict each other. Further, the presence of strongly adsorbed F at the surfaces altered the surface energy and reduced activity.[49] Therefore, to address the reliance on HF to impose morphological control on anatase TiO_2 surfaces, Lee *et al.* employed a vapor-solid reaction growth method with $TiCl_4$ and $Ca(OH)_2$/CaO to produce truncated octahedral bipyramids with highly exposed (001) and (101) facets.[51] With a (001)/(101) ratio > 0.75 Lee *et al.* observed that the surface heterojunctions formed between the two phases was advantageous to increase e^-/h^+ separation leading to enhanced photocatalytic performance towards PEC methyl blue degradation. The modification of particle size with vaporisation temperature was also presented.

Doping of TiO_2 thin films, often generated via atomic deposition techniques, has also been employed in the search for enhanced catalyst properties for PEC applications. Radecka *et al.* found that doping TiO_2 with 2.8 atomic% Cr^{3+} has a significant effect on the flat band potential, an important material parameter to PEC heterogeneous catalysis.[52] However, PEC activity was hindered by the presence of Cr^{3+} serving as recombination centres.

1.4.2. $BiVO_4$

Similar approaches to the modification of TiO_2 PEC catalysts have also been applied to $BiVO_4$. As in the case of TiO_2, modification of the surface properties of particulate $BiVO_4$ has been investigated via facet engineering where it has been reported, with reasonable agreement in the literature, that exposed (010) facets at $BiVO_4$ surfaces demonstrate enhanced photocatalytic OER activity.[53-55]

The impact of particle size effects has also been reported. Tan *et al.* observed an increase in measured PEC OER current density with decreasing particle size that was attributed to the greater contact between individual particles and the particles and the substrate, leading to improved charge transport and collection efficiency.[56]

Regarding $BiVO_4$ thin films, doping and nanostructuring are two commonly investigated pathways in the development of more active OER photoanodes. Parmar *et al.* screened the impact of 12 different metal dopants (including Ti, W, Fe and Pt) to the PEC OER activity of $BiVO_4$.[57] Only W and Mo were found to display enhanced photocatalytic activity relative to the undoped catalyst. The enhancements were due to reduction in charge-transfer resistance and increase in electron donation to V sites by W/Mo. Indeed, Mo was determined to be the more efficient electron donor, particularly important for $BiVO_4$ thin films where it has been reported previously that e^- transport is slower than for h^+.[58]

Kim *et al.* demonstrated the enhanced suppression of bulk charge carrier recombination by the utilisation of nanoporous $BiVO_4$ thin films in the presence of Na_2SO_3, a hole scavenger that prevents surface recombination by the rapid consumption of h^+.[59] However, under PEC water splitting conditions and in the absence of the hole scavenger catalytic performance was hampered by surface recombination if charge carriers, prompting the deposition of thin layers of earth-abundant OER electrocatalyst (namely FeOOH and NiOOH) to promote water splitting activity. Likewise, Thalluri *et al.* demonstrated that PEC performance can be improved by inducing porosity to $BiVO_4$ thin films.[60] They observed a two orders of magnitude increase in PEC OER photocurrent density at 1.23 V *vs.* RHE following treatment of the as-prepared $BiVO_4$ that removed impurities, producing a more exposed film surface and decreasing the overall film thickness from 400 nm to 280 nm.

1.5. Electrochemical reduction of CO_2 (CO_2RR)

In addition to the realisation of (photo)electrocatalytic energy production and storage applications that limit the use of fossil fuels and the emission of CO_2, the capture and reuse of atmospheric CO_2 is a promising pathway to enhance the decrease in net CO_2 emissions and prevent exceeding the 1.5 °C limit.[61, 62] In particular, the electrochemical conversion of CO_2 (CO_2RR) at ambient temperature to useful, value-added chemicals and polymer precursors is the subject of significant research effort because this avenue affords an opportunity to take advantage of electrical energy generated by wind, water and solar.[43, 62-65] Under this scenario the build-up of anthropogenic CO_2 creates an inexpensive, highly abundant carbon resource.

The enthusiasm amongst researchers for this environmental remediation pathway was stimulated by the work of Hori *et al.* in the late 1980s,[66-75] with a combined sum of 2448 citations at time of writing, who explored the products of CO_2RR on metallic catalysts, motivating more than 8700 publications dedicated to the subject over the last 30 years. The specific chemical and physical properties of the catalyst plays a significant role in CO_2RR. Among all monometallic catalysts, only Cu and Cu oxide-derived surfaces have been shown to electrochemically convert CO_2 to high value and energy dense multi-carbon ($C2_+$) products, with at least 16 total products accessible.[76] Although it is not currently fully understand why Cu surfaces display such outstanding CO_2RR capability, Bagger *et al*. recently presented the classification of monometallic catalysts and their major products under CO_2RR conditions (**Figure 8**) by the respective binding energies of adsorbed intermediates CO (CO*) and (H*).[77] Through this analysis Cu exists in its own class (**Figure 8B**), thereby providing some explanation for the observed C_{2+} product formation.

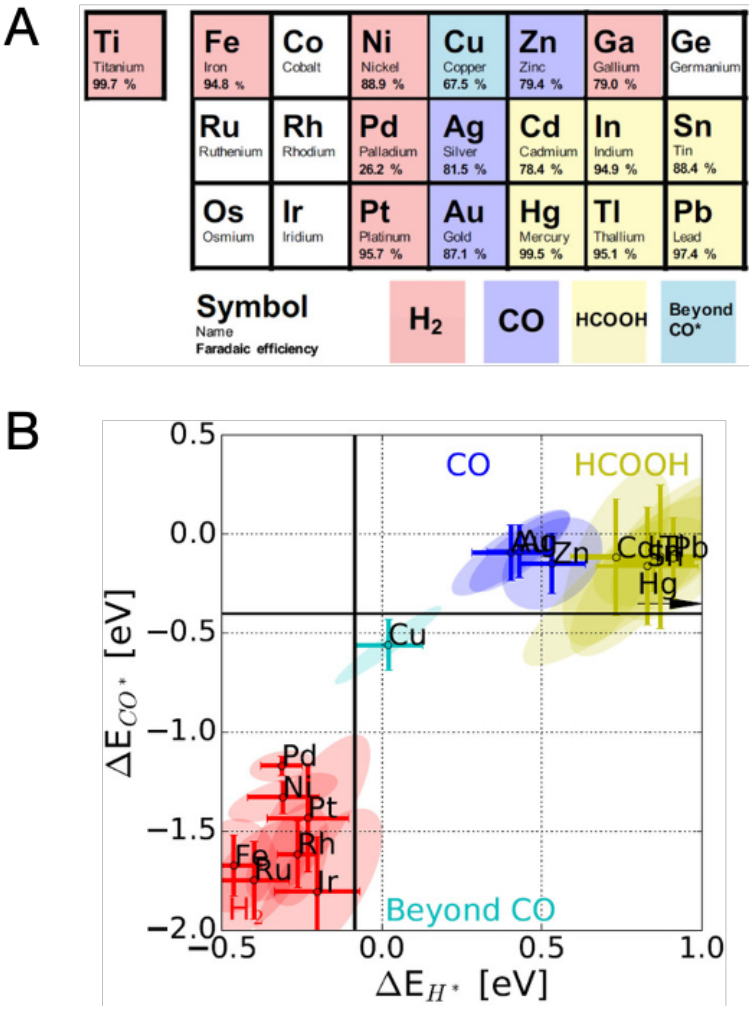

Figure 8. (A) Periodic table exert showing the major products under CO2RR conditions for various monometallic transition metal electrocatalysts based on data collected by Hori *et al*.[78] The Faradaic efficiency of major product formation is presented under each metal. (B) Binding energies of CO* and H* reaction intermediates with various monometallic metals. Colours correspond to the major product classifications. Reprinted with permission from Bagger *et al*.[77] Copyright © 2017, John Wiley and Sons.

Table 1. Products accessible via electrochemical reduction of CO_2 (CO_2RR) at polycrystalline Cu catalysts. Number of electrons required and standard reduction potential at neutral pH are also shown. Reprinted with permission from Kuhl *et al*.[76] Copyright © 2012, Royal Society of Chemistry.

Product	# e⁻	E	Product	# e⁻	E
Formate 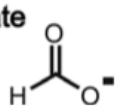	2	−0.02	Acetaldehyde 	10	0.05
Carbon monoxide 	2	−0.10	Ethanol 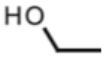	12	0.09
Methanol 	6	0.03	Ethylene	12	0.08
Glyoxal 	6	−0.16	Hydroxyacetone 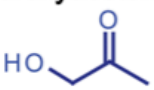	14	0.46
Methane 	8	0.17	Acetone 	16	−0.14
Acetate 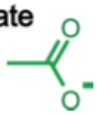	8	−0.26	Allyl alcohol 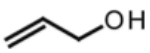	16	0.11
Glycolaldehyde 	8	−0.03	Propionaldehyde 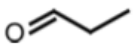	16	0.14
Ethylene glycol 	10	0.20	1-Propanol 	18	0.21

Table 1 presents the 16 CO_2RR products reported alongside the standard reduction potential at pH 6.8 and required number of electrons to facilitate the product generation. The generation of valuable industrial chemicals, such as methane, acetaldehyde and ethylene, is kinetically demanding, requiring the transfer of 8, 10 and 12 electrons, respectively. Furthermore, the standard reduction potential for the majority of CO_2RR products falls within the HER range. Thus, CO_2RR is hampered by poor product selectivity compounded by competition with HER activity. In response, various factors have been explored to address

the selectivity and efficiency, including catalyst surface geometry,[79, 80] oxidation state,[81, 82] particle size,[83, 84] morphology[85-87] and electrolyte composition.[88, 89]

Several reports on the increased selectivity towards C_{2+} products over CH_4 through use of oxidised Cu surfaces and so called oxide-derived (OD) Cu catalysts have been published of late.[81, 90-92] One of the most controversial aspects when studying the selectivity of the Cu catalyst is the presence of surface and subsurface oxides.[93-96] While some reports suggest that Cu oxides, at the surface or subsurface, are stable at the potentials where the CO_2RR takes place and its presence results in changes in the product selectivity, others claim that the copper oxide derivates fully reduce to copper during the CO_2RR and that it is the change of the surface structure which defines the changes in the product selectivity.[97]

Li *et al.* observed that the small Cu nanoparticles (NPs) generated *in situ* via the CO_2RR at micrometre thick Cu_2O films possessed enhanced activity at lower applied potentials, with increased selectivity towards C_{2+} products and considerably improved stability relative to polycrystalline Cu.[98] Electrochemical reduction of oxidised Cu is kinetically more favourable than CO_2RR hence always preceding the catalytic formation of products.[99] Subsequent investigation of the impact of the OD-Cu forming process, whether electrochemically or thermochemically, on the activity of the catalyst towards electrochemical CO reduction (CORR) determined that the electrochemical route afforded a significantly more roughened surface with smaller reduced Cu NPs.[100] The enhancement in CORR activity at OD-Cu surfaces was ascribed to the formation of a high number of highly active sites at nanocrystallite grain boundaries, not obtained via other NP synthesis routes.

Electrochemical surface activation has also been achieved by the use of potential pulses. It was reported that anodic pulse voltammetry could be used to successfully reproduce the initial surface conditions of Cu single crystal electrodes and that the selectivity towards C_{2+} products at Cu(100) and Cu(111) was associated to the presence of oxygen species adsorbed

during the anodic pulses.[95] While previous reports asserted that any Cu^+ detected at OD-Cu following CO_2RR was caused by oxidation upon exposure of the catalyst to air and that all Cu atoms are reduced under CO_2RR conditions, use of *operando* X-ray absorption spectroscopy (XAS) during CO_2RR with an OD-Cu catalyst determined the presence of Cu(I) and oxygen coordination environments after 1 hr electrolysis at -0.91 V *vs.* RHE.[81] Interestingly, the nature of the catalyst support was shown to impact on the stability of the OD-Cu catalyst and the reduction of Cu^+, with poorer stability obtained when Cu_2O nanocubes were deposited on C as opposed to a Cu foil.[83]

Thus, strategies for stabilising Cu^+ are desirable. Zhou *et al.* demonstrated the enhanced selectivity towards C_2 products through modifying the Cu electronic structure through doping with boron. The B-doped Cu possessed an average Cu valence of +0.35, achieving 80% Faradaic efficiency (FE) for C_2 product formation at up to 40 hrs catalysis.[101]

1.5.1. CO_2RR at transition metal oxides

For completeness I will briefly discuss the role of transition metal oxides as CO_2RR catalysts. Taking lessons from the insights gained from research on electrocatalytic water splitting,[102] studies on the CO_2RR at OER metal oxide anodes have been of interest due to their stability in aqueous environments over a wide potential range. Bandi investigated the CO_2RR activity of a series of composite metal oxide catalysts of Ru, Ti, Sn, Mo and Co.[103] It was demonstrated that RuO_2-TiO_2 catalysts were active CO_2RR cathodes, able to reduce CO_2 with greater selectivity towards C_1 products, CH_3OH and HCOOH (and H_2) with low overpotentials.[103, 104] Indeed, a decrease in Faradaic efficiency of CH_3OH was observed with increasing overpotential.[103] RuO_2 in particular has received much interest due to its enhanced selectivity towards CH_3OH over metal catalysts.[105-107]

Computational investigation of 12 rutile transition metal oxides towards CO_2RR suggested that CrO_2, PtO_2 and RhO_2 had smaller onset potentials (less -0.3 V *vs*. RHE), with CrO_2 and

RhO_2 having greater selectivity towards C_1 products.[108] Their experimental results demonstrated that in the -0.5 to -1.0 V (*vs.* RHE) applied potential range, RuO_2, IrO_2, and TiO_2 had enhanced selectivity towards CH_3OH.

1.5.1.1. Photoelectrochemical CO_2RR

Use of metal oxide semiconductor electrocatalysts for CO_2RR affords photocatalytic and PEC conversion routes.[109] The scope of the work undertaken as part of this thesis does not present any PEC CO_2RR. However, several oxide semiconductor catalyst materials have been investigated and reported that include, TiO_2, Cu_2O, WO_3, NiO, ZnO, Ta_2O_5, ZrO_2 and $BiVO_4$, with an extensive review published recently.[110]

1.6. Green energy landscape

Overall, (photo)electrochemistry affords multiple promising pathways to combat the existing reliance on fossil fuels for energy production and storage and to tackle the increase in anthropogenic CO_2 and other GHGs that contribute to global warming and extreme climate changes. The advancement of these electrocatalytic avenues at the industrial scale is one the key challenges of the present time but, once realised, the combination of the various green energy applications would provide a sustainable energy landscape. **Figure 9** illustrates the ideal green energy landscape driven by photoelectrochemistry and electrocatalysis.

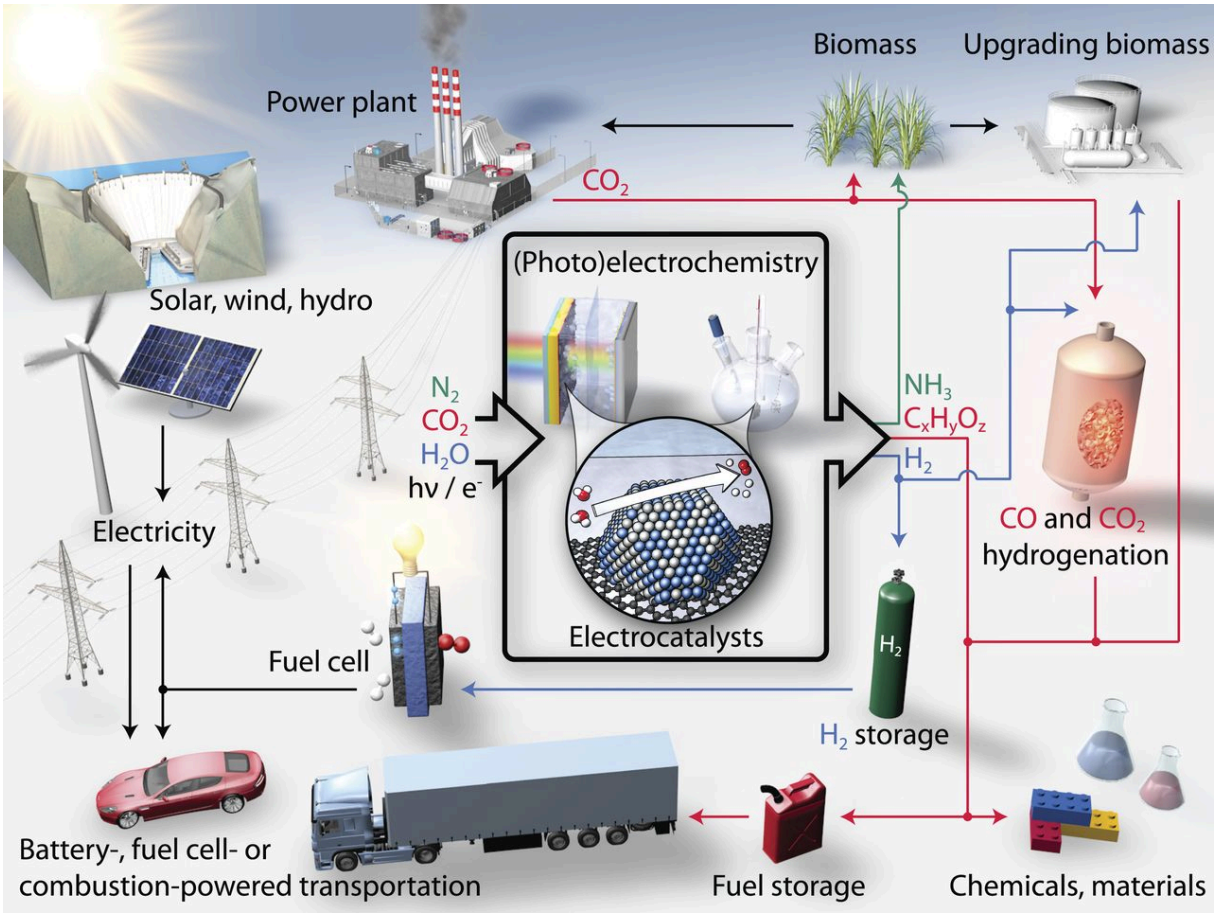

Figure 9. Schematic illustration of a desirable sustainable green energy landscape driven and supported by (photo)electrochemistry. Reprinted with permission from Seh *et al.*[43] Copyright © 2017, AAAS.

1.7. Electrocatalyst development via electrochemistry

An effective strategy towards tackling the issues that currently hinder the commercial and industrial application of the aforementioned green energy applications, catalysed by metal oxide (photo)electrocatalysts, would be the use of synthetic methods that target specific physical properties with: tunability, low cost, reproducibility, time efficiency and without the involvement of organic reagents that require significant cleaning protocols.

In the next chapter we will explore the role and advantages of electrochemistry in the investigation and preparation of nanostructured metal oxide catalysts for green energy applications.

References

1. N. S. Lewis and D. G. Nocera, *Proc. Natl. Acad. Sci. USA*, 2006, **103**, 15729-15735.

2. R. C. Allen, in *The British Industrial Revolution in Global Perspective*, Cambridge University Press, 2009, DOI: 10.1017/CBO9780511816680, ch. 7, pp. 156-181.

3. WCA, Coal & electricity, https://www.worldcoal.org/coal/uses-coal/coal-electricity, (accessed 7th July, 2020).

4. BGR, *Energy Study 2016. Reserves, Resources and Availability of Energy Resources*, Federal Institute for Geosciences and Natural Resources (BGR), Hannover, 2016.

5. R. Nataly Echevarria Huaman and T. Xiu Jun, *Renewable Sustainable Energy Rev.*, 2014, **31**, 368-385.

6. A. Zuttel, *Naturwissenschaften*, 2004, **91**, 157-172.

7. J. K. Meen, D. H. Eggler and J. C. Ayers, *Nature*, 1989, **340**, 301-303.

8. Climate Change Act 2008, c.27, https://www.legislation.gov.uk/ukpga/2008/27/contents, (accessed 12th July 2020, 2020).

9. U. N. F. C. o. C. Change, The Paris Agreement, https://unfccc.int/process-and-meetings/the-paris-agreement/the-paris-agreement, (accessed 12th July, 2020).

10. IPCC, *Summary for Policymakers*, International Panel on Climate Change, Geneva, Switzerland, 2018.

11. A. Midilli, I. Dincer and M. Ay, *Energy Policy*, 2006, **34**, 3623-3633.

12. L. M. Peter, *Electroanalysis*, 2015, **27**, 864-871.

13. J. R. Bolton, *Science*, 1978, **202**, 705-711.

14. G. Chen, J. Seo, C. Yang and P. N. Prasad, *Chem. Soc. Rev.*, 2013, **42**, 8304-8338.

15. K. Kalyanasundaram and M. Grätzel, *J. Mater. Chem.*, 2012, **22**, 24190-24194.

16. A. J. Nozik and J. Miller, *Chem. Rev.*, 2010, **110**, 6443-6445.

17. K. Sivula, F. Le Formal and M. Gratzel, *ChemSusChem*, 2011, **4**, 432-449.

18. A. J. Bard, *Science*, 1980, **207**, 139-144.

19. X. Chen, S. Shen, L. Guo and S. S. Mao, *Chem. Rev.*, 2010, **110**, 6503-6570.

20. J. Graetz, *Chem. Soc. Rev.*, 2009, **38**, 73-82.

21. S. Ramesohl and F. Merten, *Energy Policy*, 2006, **34**, 1251-1259.

22. P. P. Edwards, V. L. Kuznetsov, W. I. F. David and N. P. Brandon, *Energy Policy*, 2008, **36**, 4356-4362.

23. T. Jafari, E. Moharreri, A. S. Amin, R. Miao, W. Song and S. L. Suib, *Molecules*, 2016, DOI: 10.3390/molecules21070900.

24. E. Fabbri, A. Habereder, K. Waltar, R. Kötz and T. J. Schmidt, *Catal. Sci. Technol.*, 2014, **4**, 3800-3821.

25. H. Dau, C. Limberg, T. Reier, M. Risch, S. Roggan and P. Strasser, *ChemCatChem*, 2010, **2**, 724-761.

26. S. Trasatti, *Electrochim. Acta*, 1984, **29**, 1503-1512.

27. S. Park, Y. Shao, J. Liu and Y. Wang, *Energy Environ. Sci.*, 2012, **5**.

28. L. C. Seitz, C. F. Dickens, K. Nishio, Y. Hikita, J. Montoya, A. Doyle, C. Kirk, A. Vojvodic, H. Y. Hwang, J. K. Norskov and T. F. Jaramillo, *Science*, 2016, **353**, 1011-1014.

29. T. Shinagawa, M. T. Ng and K. Takanabe, *Angew. Chem., Int. Ed.*, 2017, **56**, 5061-5065.

30. Y. Pu, M. J. Lawrence, V. Celorrio, Q. Wang, M. Gu, Z. Sun, L. A. Jácome, A. E. Russell, L. Huang and P. Rodriguez, *J. Mater. Chem. A*, 2020, **8**, 13340-13350.

31. W. H. Brattain and C. G. B. Garrett, *Bell Syst. Tech. J.*, 1955, **34**, 129-176.

32. M. E. Becquerel, *C. R. Hebd. Seances Acad. Sci.*, 1839, **9**, 561-567.

33. P. Atkins and J. de Paula, in *Atkins' Physical Chemistry*, Oxford University Press, Oxford, 9th edn., 2010, ch. 19, pp. 722-723.

34. L. M. Peter, in *Photocatalysis: Fundamentals and Perspectives*, eds. J. Schneider, D. Bahnemann, J. Ye, G. Li Puma and D. D. Dionysiou, Royal Society of Chemistry, Cambridge, 2016, ch. 1, pp. 3-28.

35. A. J. Bard, *J. Photohem.*, 1979, **10**, 59-75.

36. R. L. Cummerow, *Phys. Rev.*, 1954, **95**, 16-21.

37. T. S. Jayadevaiah, *Appl. Phys. Lett.*, 1974, **25**, 399-400.

38. A. Fujishima and K. Honda, *Nature*, 1972, **238**, 37-38.

39. A. Fujishima, K. Kohayakawa and K. Honda, *Bull. Chem. Soc. Jpn.*, 1975, **48**, 1041-1042.

40. J. S. Jang, H. G. Kim and J. S. Lee, *Catal. Today*, 2012, **185**, 270-277.

41. K. Sivula and R. van de Krol, *Nat. Rev. Mater.*, 2016, **1**, 15010.

42. S. J. A. Moniz, S. A. Shevlin, D. J. Martin, Z.-X. Guo and J. Tang, *Energy Environ. Sci.*, 2015, **8**, 731-759.

43. Z. W. Seh, J. Kibsgaard, C. F. Dickens, I. Chorkendorff, J. K. Norskov and T. F. Jaramillo, *Science*, 2017, **355**.

44. W. Choi, A. Termin and M. R. Hoffmann, *Angew. Chem., Int. Ed.*, 1994, **33**, 1091-1092.

45. Z. Zhang, C.-C. Wang, R. Zakaria and J. Y. Ying, *J. Phys. Chem. B*, 1998, **102**, 10871-10878.

46. A. Tuan Vu, Q. Tuan Nguyen, T. H. Linh Bui, M. Cuong Tran, T. Phuong Dang and T. K. Hoa Tran, *Adv. Nat. Sci.: Nanosci. Nanotechnol.*, 2010, **1**.

47. J. Zhang, G. Xiao, F.-X. Xiao and B. Liu, *Mater. Chem. Front.*, 2017, **1**, 231-250.

48. G. Liu, H. G. Yang, S. Z. Qiao, C. H. Sun, Y. G. Jin, S. C. Smith, J. Zou, H. M. Cheng and G. Q. Lu, *J. Am. Chem. Soc.*, 2009, **131**, 4078-4083.

49. J. Pan, G. Liu, G. Q. Lu and H. M. Cheng, *Angew. Chem., Int. Ed.*, 2011, **50**, 2133-2137.

50. T. R. Gordon, M. Cargnello, T. Paik, F. Mangolini, R. T. Weber, P. Fornasiero and C. B. Murray, *J. Am. Chem. Soc.*, 2012, **134**, 6751-6761.

51. T. Y. Lee, C. Y. Lee and H. T. Chiu, *ACS Omega*, 2018, **3**, 10225-10232.

52. M. Radecka, M. Rekas, A. Trenczek-Zajac and K. Zakrzewska, *J. Power Sources*, 2 008, **181**, 46-55.

53. G. Xi and J. Ye, *Chem. Commun.*, 2010, **46**, 1893-1895.

54. D. Wang, H. Jiang, X. Zong, Q. Xu, Y. Ma, G. Li and C. Li, *Chemistry*, 2011, **17**, 1275-1282.

55. H. L. Tan, R. Amal and Y. H. Ng, *J. Mater. Chem. A*, 2017, **5**, 16498-16521.

56. H. L. Tan, R. Amal and Y. H. Ng, *ACS Appl. Mater. Interfaces*, 2016, **8**, 28607-28614.

57. K. P. Parmar, H. J. Kang, A. Bist, P. Dua, J. S. Jang and J. S. Lee, *ChemSusChem*, 2012, **5**, 1926-1934.

58. D. K. Zhong, S. Choi and D. R. Gamelin, *J. Am. Chem. Soc.*, 2011, **133**, 18370-18377.

59. T. W. Kim and K. S. Choi, *Science*, 2014, **343**, 990-994.

60. S. M. Thalluri, R. M. Rojas, O. D. Rivera, S. Hernandez, N. Russo and S. E. Rodil, *Phys. Chem. Chem. Phys.*, 2015, **17**, 17821-17827.

61. E. Alper and O. Yuksel Orhan, *Petroleum*, 2017, **3**, 109-126.

62. D. U. Nielsen, X.-M. Hu, K. Daasbjerg and T. Skrydstrup, *Nat. Catal.*, 2018, **1**, 244-254.

63. M. Schreier, F. Héroguel, L. Steier, S. Ahmad, J. S. Luterbacher, M. T. Mayer, J. Luo and M. Grätzel, *Nature Energy*, 2017, **2**, 17087.

64. J. H. Montoya, L. C. Seitz, P. Chakthranont, A. Vojvodic, T. F. Jaramillo and J. K. Norskov, *Nat. Mater.*, 2016, **16**, 70-81.

65. D. T. Whipple and P. J. A. Kenis, *J. Phys. Chem. Lett.*, 2010, **1**, 3451-3458.

66. Y. Hori, K. Kikuchi and S. Suzuki, *Chem. Lett.*, 1985, **14**, 1695-1698.

67. Y. Hori, K. Kikuchi, A. Murata and S. Suzuki, *Chem. Lett.*, 1986, **15**, 897-898.

68. Y. Hori, A. Murata, K. Kikuchi and S. Suzuki, *J. Chem. Soc., Chem. Commun.*, 1987, DOI: 10.1039/c39870000728, 728-729.

69. Y. Hori, A. Murata, R. Takahashi and S. Suzuki, *J. Am. Chem. Soc.*, 1987, **109**, 5022-5023.

70. Y. Hori, A. Murata, R. Takahashi and S. Suzuki, *Chem. Lett.*, 1987, **16**, 1665-1668.

71. Y. Hori, A. Murata, R. Takahashi and S. Suzuki, *J. Chem. Soc., Chem. Commun.*, 1988, DOI: 10.1039/c39880000017, 17-19.

72. Y. Hori, A. Murata, S.-y. Ito, Y. Yoshinami and O. Koga, *Chem. Lett.*, 1989, **18**, 1567-1570.

73. Y. Hori, A. Murata and R. Takahashi, *J. Chem. Soc., Faraday Trans. 1*, 1989, **85**.

74. Y. Hori and A. Murata, *Electrochim. Acta*, 1990, **35**, 1777-1780.

75. Y. Hori, A. Murata and S.-y. Ito, *Chem. Lett.*, 1990, **19**, 1231-1234.

76. K. P. Kuhl, E. R. Cave, D. N. Abram and T. F. Jaramillo, *Energy Environ. Sci.*, 2012, **5**.

77. A. Bagger, W. Ju, A. S. Varela, P. Strasser and J. Rossmeisl, *Chemphyschem*, 2017, **18**, 3266-3273.

78. Y. Hori, H. Wakebe, T. Tsukamoto and O. Koga, *Electrochim. Acta*, 1994, **39**, 1833-1839.

79. Y. Hori, I. Takahashi, O. Koga and N. Hoshi, *J. Phys. Chem. B*, 2002, **106**, 15-17.

80. I. Takahashi, O. Koga, N. Hoshi and Y. Hori, *J. Electroanal. Chem.*, 2002, **533**, 135-143.

81. H. Mistry, A. S. Varela, C. S. Bonifacio, I. Zegkinoglou, I. Sinev, Y. W. Choi, K. Kisslinger, E. A. Stach, J. C. Yang, P. Strasser and B. R. Cuenya, *Nat. Commun.*, 2016, **7**, 12123.

82. R. M. Arán-Ais, F. Scholten, S. Kunze, R. Rizo and B. Roldan Cuenya, *Nature Energy*, 2020, **5**, 317-325.

83. P. Grosse, D. Gao, F. Scholten, I. Sinev, H. Mistry and B. Roldan Cuenya, *Angew. Chem., Int. Ed.*, 2018, **57**, 6192-6197.

84. R. Reske, H. Mistry, F. Behafarid, B. Roldan Cuenya and P. Strasser, *J. Am. Chem. Soc.*, 2014, **136**, 6978-6986.

85. R. Kas, R. Kortlever, A. Milbrat, M. T. Koper, G. Mul and J. Baltrusaitis, *Phys. Chem. Chem. Phys.*, 2014, **16**, 12194-12201.

86. P. De Luna, R. Quintero-Bermudez, C.-T. Dinh, M. B. Ross, O. S. Bushuyev, P. Todorović, T. Regier, S. O. Kelley, P. Yang and E. H. Sargent, *Nat. Catal.*, 2018, **1**, 103-110.

87. D. Gao, I. Sinev, F. Scholten, R. M. Aran-Ais, N. J. Divins, K. Kvashnina, J. Timoshenko and B. Roldan Cuenya, *Angew. Chem., Int. Ed.*, 2019, **58**, 17047-17053.

88. A. S. Varela, M. Kroschel, T. Reier and P. Strasser, *Catalysis Today*, 2016, **260**, 8-13.

89. V. Colic, M. D. Pohl, D. Scieszka and A. S. Bandarenka, *Catalysis Today*, 2016, **262**, 24-35.

90. D. Ren, Y. Deng, A. D. Handoko, C. S. Chen, S. Malkhandi and B. S. Yeo, *ACS Catal.*, 2015, **5**, 2814-2821.

91. X. Wang, A. S. Varela, A. Bergmann, S. Kuhl and P. Strasser, *ChemSusChem*, 2017, **10**, 4642-4649.

92. H. Ning, X. Wang, W. Wang, Q. Mao, Z. Yang, Q. Zhao, Y. Song and M. Wu, *Carbon*, 2019, **146**, 218-223.

93. M. Favaro, H. Xiao, T. Cheng, W. A. Goddard, 3rd, J. Yano and E. J. Crumlin, *Proc. Natl. Acad. Sci. USA*, 2017, **114**, 6706-6711.

94. A. Eilert, F. Cavalca, F. S. Roberts, J. Osterwalder, C. Liu, M. Favaro, E. J. Crumlin, H. Ogasawara, D. Friebel, L. G. Pettersson and A. Nilsson, *J. Phys. Chem. Lett.*, 2017, **8**, 285-290.

95. C. S. Le Duff, M. J. Lawrence and P. Rodriguez, *Angew. Chem., Int. Ed.*, 2017, **56**, 12919-12924.

96. A. J. Garza, A. T. Bell and M. Head-Gordon, *J. Phys. Chem. Lett.*, 2018, **9**, 601-606.

97. S. B. Scott, T. V. Hogg, A. T. Landers, T. Maagaard, E. Bertheussen, J. C. Lin, R. C. Davis, J. W. Beeman, D. Higgins, W. S. Drisdell, C. Hahn, A. Mehta, B. Seger, T. F. Jaramillo and I. Chorkendorff, *ACS Energy Lett.*, 2019, **4**, 803-804.

98. C. W. Li and M. W. Kanan, *J. Am. Chem. Soc.*, 2012, **134**, 7231-7234.

99. D. Gao, R. M. Arán-Ais, H. S. Jeon and B. Roldan Cuenya, *Nature Catalysis*, 2019, **2**, 198-210.

100. C. W. Li, J. Ciston and M. W. Kanan, *Nature*, 2014, **508**, 504-507.

101. Y. Zhou, F. Che, M. Liu, C. Zou, Z. Liang, P. De Luna, H. Yuan, J. Li, Z. Wang, H. Xie, H. Li, P. Chen, E. Bladt, R. Quintero-Bermudez, T. K. Sham, S. Bals, J. Hofkens, D. Sinton, G. Chen and E. H. Sargent, *Nat Chem*, 2018, **10**, 974-980.

102. A. J. Martín, G. O. Larrazábal and J. Pérez-Ramírez, *Green Chemistry*, 2015, **17**, 5114-5130.

103. A. Bandi, *J. Electrochem. Soc.*, 1990, **137**, 2157-2160.

104. A. Bandi and H. M. Kühne, *J. Electrochem. Soc.*, 1992, **139**, 1605-1610.

105. J. Qu, X. Zhang, Y. Wang and C. Xie, *Electrochim. Acta*, 2005, **50**, 3576-3580.

106. N. Spataru, K. Tokuhiro, C. Terashima, T. N. Rao and A. Fujishima, *J. Appl. Electrochem.*, 2003, **33**, 1205-1210.

107. E. Tayyebi, J. Hussain and E. Skúlason, *Chem. Sci.*, 2020, **11**, 9542-9553.

108. E. Tayyebi, J. Hussain, Y. Abghoui and E. Skúlason, *J. Phys. Chem. C*, 2018, **122**, 10078-10087.

109. B. Aurian-Blajeni, M. Halmann and J. Manassen, *Solar Energy*, 1980, **25**, 165-170.

110. J. L. White, M. F. Baruch, J. E. Pander Iii, Y. Hu, I. C. Fortmeyer, J. E. Park, T. Zhang, K. Liao, J. Gu, Y. Yan, T. W. Shaw, E. Abelev and A. B. Bocarsly, *Chem. Rev.*, 2015, **115**, 12888-12935.

Preface to Chapter 2

Format: Published review article manuscript.

Some references have been updated during incorporation into this thesis and may appear to be discrepancies compared to the published article. However, no references have been added or removed and no changes to article content have been made.

Article information: M. J. Lawrence, A. Kolodziej and P. Rodriguez, *Curr. Opin. Electrochem.*, 2018, **10**, 7-15. DOI: 10.1016/j.coelec.2018.03.014. A contribution to a themed issue on *Innovative Methods in Electrochemistry*, edited by Frank Merken. Published by Elsevier,

Overview: This review presents a series of electrochemical techniques that have been demonstrated to be powerful tools in the production of metal oxide, hydroxide and oxyhydroxide nanostructures, of particular importance to the field of electrocatalysis and renewable energy technologies, and explores recent significant developments regarding how various types of nanostructuring can be achieved through the versatility of said techniques. As discussed in Chapter 1, the nanostructuring of catalysts is desirable due to the significant increase in ECSA and surface to bulk atomic ratios that subsequently leads to greater exposure of active sites and increased mass efficiency. Electrochemical techniques afford an unparalleled ability to tune both the composition and structure of metal oxide nanostructures via low energy input pathways, essential for scale-up and industrial commercialisation.

ED of aqueous metal species onto conductive substrates has been widely used over the last few decades. Advances in the use of both cathodic and anodic ED of aqueous metals to generate multi-metallic (oxyhydr-)oxide thin films with compositional control and AC ED to control the morphology of deposited thin films are presented. The anodization of metal foils

to generate uniform 2D nanostructures with long range order continues to receive increasing attention, particularly due to the ability to detach the structures from substrates whilst maintaining the integrity of the oxide material. We highlight what we believe have been the key most recent advances in this specific area of ED.

The room-temperature cathodic corrosion of metals to in an aqueous conductive electrolyte has been demonstrated to produce well-defined oxide NPs in the absence of surfactants and offers a unique alternative route towards the generation of active oxide catalysts for energy applications that does not involve a metal deposition step. Here we present recent examples of the effective use of cathodic corrosion to generate metal oxide NPs with tuneable size and/or morphology.

The formation of metal oxide nanostructures via GRR is another alternative electrochemical technique. The driving force behind such transformations is the difference in chemical potential of the metal species rather than any applied potential. We discuss the different types of nanostructures that have been produced via this method with controllable size, shape and composition.

Finally, we provide our personal, critical view regarding the advantages and challenges of the methods presented upon potential commercialisation.

Author Contributions: M.J.L prepared the sections on ED, anodization, cathodic corrosion and the final versions of all figures for publication. A.K. contributed significantly to the introduction of the article and was responsible for the section: ‘Synthesis of nanostructured metal oxides by galvanic exchange’, including the initial production of the galvanic exchange schematic illustration in Figure 3. All authors contributed to the drafting and revision of the article.

2. CONTROLLABLE SYNTHESIS OF NANOSTRUCTURED METAL OXIDE AND OXYHYDROXIDE MATERIALS VIA ELECTROCHEMICAL METHODS

2.1. Introduction

Metal oxides and metal oxyhydroxide nanoparticles play a central role in many areas of chemistry, physics, biology and materials science due to their vast number of applications such as catalysis, electronics, photonics, drug delivery, optics, sensing, environmental remediation, and energy storage/conversion applications.[1-8]

Such nanostructures, however, exhibit different physiochemical properties depending on the particle size, the structural geometries and level of crystallinity. Metal oxide and metal oxyhydroxide nanoparticles of the same material but different structure or particle size might show different optical, thermal, electrical and chemical properties. In particular it is well known that the size and surface structure play an important role in the photoelectrocatalytic processes.[9, 10] Therefore, special attention should be paid to the selection of the synthesis method, taking into account the close connection between the chosen pathway and the size/shape/crystallinity of resulting oxide and oxyhydroxide nanostructures.

Many chemical and physical synthetic pathways have been explored for the preparation of metal oxide nanomaterials and more recently metal oxyhydroxide nanomaterials with exercisable control over size, shape and composition of mixed metal oxides.[11-16] The most utilised approaches are sol-gel and hydro/solvo-thermal methods, which have been found to be extremely versatile when it comes to the scope of products.[17-20] Nevertheless, the utilization of the organic solvents/surfactants increases the cost, complexity, and likelihood of surface contamination by adsorbing species. In addition, such methods quite often require the implementation of high temperatures reaching over 1000 °C which result in the sintering

of the nanostructures with lower of control over the size and shape of the resulting nanomaterials. These two methods, although very useful in the preparation of single metal oxide particles, do not provide many opportunities to prepare mixed metal oxide nanomaterials, an emerging class of materials with outstanding properties. Mixed metal oxides can be prepared via a microemulsion method,[21, 22] which also provides tools to control size, shape, and composition. However, emulsion formation requires the use of surfactants – molecules that are prone to adsorb on the surface of particles and decrease their activity due to the blocking of active sites.

Electrochemical routes have been shown to be powerful methods for synthesis of metal oxides and oxyhydroxides nanostructures and more recent improvements in the methodologies have demonstrated the potential to control the composition and/or morphological features in the absence of adsorbing capping agents.[23-26]

The purpose of this short review is to highlight some of new electrochemical methods of synthesis of metal oxides and oxyhydroxide nanomaterials. It does not aim to cover all the methods of synthesis but to provide a personal view of notable methods that, given their advantages, could potentially be commercialized. Specifically, we cover three synthetic routes, namely electrochemical deposition (both cathodic and anodic), cathodic corrosion, and galvanic exchange reactions. In addition, we will briefly discuss the impact of the morphology and size of the metal oxides and metal oxyhydroxide nanoparticles prepared by these routes in their (photo)catalytic activity.

2.2. Electrodeposition of nanostructured thin-film metal oxides

The generation of conductive metal oxides and oxyhydroxides via electrodeposition (ED) has long been shown to be a useful synthetic route. ED is a highly versatile technique that: allows for deposition under fixed potential or voltammetric conditions; operates at ambient/low

temperatures; has great potential for industrial scale-up due to simplistic setup and mechanism; can be easily modified by variation of the substrate, operating potentials and/or electrolyte constituents.

Early examples of the ED of oxyhydroxides involved the anodic deposition of aqueous solution species, most commonly containing transition metal 2+ cations (M^{2+}), onto conductive metal substrates under potentiostatic control to generate oxide thin films for (photo)electrocatalysis applications.[27, 28] Cathodic ED is facilitated by pH changes local to the working electrode (WE) due to the hydrogen evolution reaction (HER) increasing the concentration of hydroxide ions, which subsequently react with M^{2+} to precipitate and deposit metal hydroxide species, $M(OH)_2$, as thin films which can be further oxidised to the desired metal oxide.[29-32] Homogeneous cathodic deposition of the (oxyhydr-)oxide is only achieved provided that the reduction potential of M^{2+}/M^0 is sufficiently more negative than that of H^+/H_2, otherwise the metallic form, M^0, would be formed before the formation of the $M(OH)_2$ complex in the presence of liberated OH^-. Other reduction pathways such as nitrate and nitrite reduction have been used as a precursors for the generation of OH^- during the cathodic ED of metal oxides and oxyhydroxides.[23, 27, 29-31]

ED of mixed oxides has been of particular interest in recent years due to their enhanced stability and activity. Sayeed and O'Mullane demonstrated the use of cathodic ED to synthesise single, binary and ternary oxides of Fe, Co and Ni utilising the hydrogen evolution reaction (HER) as the avenue for OH^- generation and equimolar concentrations of the metal salts.[29] Compositional analysis of the electrodeposited films, both before and after oxygen evolution reaction (OER) activity evaluation, highlighted the less favourable deposition of $Fe(OH)_2$ under cathodic conditions compared to the other metals due to lower observed Fe content. Under anodic deposition conditions, Fe deposition is more favourable, again hindering the transferal of stoichiometry from equimolar electrolytes to the resulting thin film.

Hu et al. addressed this issue by replacing Fe^{2+} with Fe^{3+} in the deposition solution, leading to in-situ generation of Fe^{2+} by reduction at the CE, thereby counteracting preferential Fe deposition under anodic deposition conditions.[23]

The physical and electrochemical properties of the deposited oxyhydroxides is strongly dependent on the substrate and the additives used for its ED as demonstrated by Lin et al. The authors used a 3D porous Ni foam as substrate for the co-precipitation and deposition of Ni and Co and NiCo mixed oxyhydroxides (**Figure 1A(i)**).[30] The combination of a 3D substrate and introduction of oxygen vacancies in the crystalline structure via oxidation/reduction steps using temperature annealing and reduction with ($NaBH_4$), resulted in an increase of the catalytic activity due to the increase of the surface area and active sites. Similar synthetic routes were employed to co-deposit $La(OH)_3$ and $Fe(OH)_2$ to yield $LaFeO_3$ after annealing,[31] however, none of these studies have shown evidence for control of oxide size, shape or morphology. Improvement of the methodology to allow further control of the porous size and surface structure expose would be highly relevant in the development of this type of catalyst.

Investigations into the controllable synthesis of nanostructured copper oxide (Cu_xO) have been of particular interest in recent years due to the various applications in which these materials have found use including the upraising investigation of the conversion of CO_2 into fuel.[33-37] Li et al. conducted a comprehensive study on the nanostructures of Cu_2O formed by surfactant-assisted ED and observed that cubic structures are formed in the absence of the sodium dodecyl sulfate (SDS) surfactant, while increasing the SDS concentration served to reduce the cubic nature of the deposited oxide film, generating flower-like structures and, finally, amorphous nanostructures under identical electrochemical conditions.[38] While the presence of the surfactant in the reaction media seems to be relevant in the control of the surface structure and particle size of the nanostructures, the adsorption of organic molecules

on the surface of the nanostructures might be a disadvantage in the utilization of this materials for catalysis due to the decrease of the available active sites.

The preparation of oxide nanostructure thin films can be achieved by underpotential deposition of metals under an oxygen atmosphere or electrodeposition/electrooxidation of the surface.[32, 39, 40] Demir et al. demonstrated the capabilities of this method to prepare Cu_2O and/or CuO over Au surfaces.[24] As can be seen in **Figure 1A(ii-iv**), the concentration of O_2 influenced not only the composition and termination of the copper oxides but also the structure of the nanostructures. The Cu nanostructure deposited with low oxygen (O_2) flow rate resulted in the formation of cubic Cu_2O (**Figure 1A(ii)**) while those films deposited under a high O_2 flow rate displayed flower-like, dendritic CuO nanostructures (**Figure 1A(iii)**). Variation of the O_2 flow rate during deposition, increasing from the lower to the higher rate after 30 min, facilitated the formation dendritic CuO atop cubic Cu_2O, evidenced by **Figure 1A(iv)**, demonstrating the tunability of the process. The authors also showed the versatility of the method by preparing the Cu_xO nanostructures onto ITO substrates, indicating that the process is not substrate dependent.

Pritzker et al. employed AC ED onto deposit Cu_2O thin films onto FTO substrates and demonstrated how the parameters of the square waveform such as frequency can be used to tuned the nanostructure of Cu_2O deposits (**Figure 1B**).[25] The authors demonstrated that morphological changes – cubic to spherical/amorphous nanostructures – could be obtained by varying: the frequency, the amplitude and the duty cycle of the square wave, the pH of the solution and the Cu^{2+} concentration. However, in all cases it appears that changes in the square wave parameters served to change the equilibrium between the two morphologies, i.e. only fluctuations between cubic and spherical particles are observed. Even though this work has shown the capabilities of the method to prepare Cu_2O nanostructures with defined nanostructure, further studies are needed to demonstrate its versatility in preparing a wider

range of materials and fine control over the structure and size of the nanomaterials as a function of the pH, temperature and more importantly, the underlying substrate.

The cathodic ED has been also used to prepare other highly ordered, crystalline, uniform hierarchical metal oxide nanostructures such as ZnO nanostructures (**Figure 1A(v-vi)**).[41, 42] These hierarchical nanostructures were shown to possess improved activity towards the electrochemical oxidation and sensing of hydrazine molecules compared to non-hierarchical ZnO, with the observed improvement in sensing ability attributable to the significant increase in the electrochemical surface area.[42]

Template-assisted ED is another route that has been shown to generate metal oxide nanostructures by depositing the oxyhydroxide material into well-defined pore channels. Use of porous templates was pioneered in the 1990s,[43-45] with reports on the ED of metal oxides onto porous templates emerging at the turn of the 21st century.[46-49] Anodized aluminium oxide (AAO) templates, commonly used materials generated by the anodization of metallic aluminium, can be tuned to generate a variety of pore sizes, from a myriad of electrolyte, applied potential and temperature systems.[50] The anodization of metals to generate porous metal oxide nanostructures, i.e. nanotubes, has also been exploited for different metals, particularly for self-ordered TiO_2 nanotube arrays (TNTAs) since this type of material is useful for several applications; a comprehensive review of TNTAs can be found in reference [[51]]. Most commonly, a 2-step anodization procedure is employed to generate the TNTAs (**Figure 1C**), with homogeneous tube spacing and pore sizes observed at the end of synthesis (**Figure 1C(i-ii)**). TiO_2 has long been known to be an active material for photoelectrochemical water splitting,[52, 53] with the anatase form being more active than rutile or brookite, reported to be due to the presence of an indirect band gap which leads to a relative increase in the lifetime of photogenerated charge carriers compared to rutile/brookite systems, which have direct band gaps that facilitate a higher rate of charge carrier recombination.[54] In the direct band

gap materials, the electron wave vectors of the valence band maximum and conduction band minimum are equivalent, resulting in direct recombination with photo-generated holes. The non-equivalence of these two electron wave vectors in direct band gap materials requires a transfer of momentum to occur before recombination. Thus, the effective lifetime of the charge carriers is increased in indirect band gap semiconductors.

Conversion of detached amorphous TNTAs to anatase by annealing at high temperature would present the possibility of a flow-through water splitting system. However, the annealing process introduces defects, namely bending and cracks, disrupting the tubular channels. Schmuki and co-workers have addressed this issue in a series of reports published in the last 2 years. They found that the inclusion of lactic acid in the anodization electrolyte allowed for defect-free, TNTAs to be formed after annealing of the detached amorphous membrane at temperatures >450 °C, generating crystalline anatase phases.[55] Further investigations revealed that the anodization of Ti in organic electrolytes generates core-shell structure, where a carbon-rich core is formed within the TiO_x-rich shell, but the inner core could be removed via a chemical dissolution step.[56] The effects of anodization potential and anodization time(Figure 1C), electrolyte, H_2O content and temperature on the resultant TNTAs has been also investigated.[55-59] It was found that the applied voltage and electrolyte temperatures were the most significant parameters in the production of spaced TNTAs at a fast rate.

Schmuki et al. have also extended the versatility of anodization to generate conductive core-shell nanotubes of TiO_2, and also MoO_x-MoS_2; the first demonstration of the formation of self-ordered MoO_3 arrays.[58, 59] Self-ordered anodization offers an electrochemical pathway toward the generation of high surface area oxide materials that can be tuned to produce, single-walled, double-walled, tube-in-tube and core-shell nanostructures, with the potential to be used in many applications.

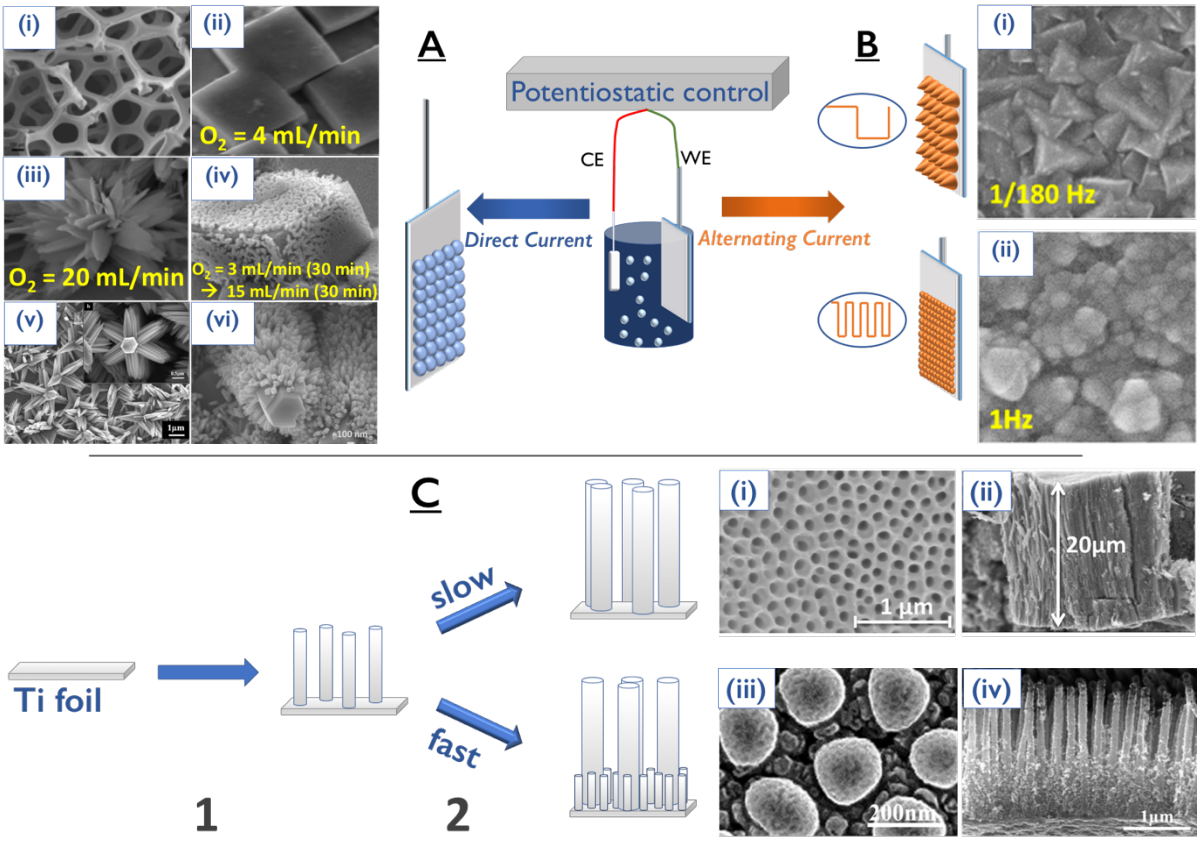

Figure 1. Schematic illustration of a 2-electrode setup for electrochemical deposition of aqueous species onto a conductive substrate under (A) applied direct current and (B) applied alternating current. Representative SEM images of: (A)(i) $NiCo_2O_4$ electrodeposited onto a 3D porous Ni foam substrate, adapted from Ref. [30] with permission from Wiley; (ii-iv) nanostructure of cubic, flower-like and flower-like covered cubes of Cu_xO produced via under potential deposition under various O_2 flow rates (annotated), adapted with permission from Ref. [24]. Copyright (2017) American Chemical Society; (v) hierarchical ZnO nanoneedle-on-nanoneedle structures with 6-fold symmetry, adapted with permission from Ref. [41]. Copyright (2007) American Chemical Society; (vi) hierarchical hexagonal nanorod-on-nanorod ZnO structures, adapted from Ref. [42] with permission from Elsevier; (B)(i-ii) the change in Cu_2O nanostructure due to changes in the applied square waveform frequency, adapted from Ref. [25] with permission from Elsevier. (C) Schematic illustration and accompanying SEM images of 2-step anodization processes applied to a Ti foil to generate self-ordered TiO_2 nanotubes (TNTAs); (i) top-view and (ii) side-view of TiO_2 membrane generated via a "slow" second anodization process, adapted from Ref. [58] with permission from Elsevier (iii) bottom-view and (iv) side-view of spaced TNTAs generated via a "fast" secondary anodization step, adapted from Ref. [57] with permission from Elsevier.

2.3. Electrochemical synthesis of metal oxide nanoparticles via cathodic corrosion

Many examples of the electrochemical synthesis of nanostructured metal oxides often involve the deposition of a thin film on a substrate, as either the main step or an inclusive step. Here we present cathodic corrosion as an alternative electrochemical method, in that, the nanostructures are produced as suspended particles rather than a thin film.[60, 61] Cathodic corrosion is a powerful tool for the facile electrochemical synthesis of metallic and alloy nanoparticles (NPs). The method involves the application of strong cathodic alternating current to electrochemically etch the WE in a conductive electrolyte. During cathodic corrosion, highly reactive intermediate anionic metal species are formed. These anionic intermediates are not stable and subsequently react via chemical oxidation, facilitated by aqueous oxygen species, to form metal nanoparticles. These metal clusters/nanoparticles can further oxidize, forming metal oxide nanoparticles. Early studies demonstrated the capabilities of the cathodic corrosion method to produce suspensions of crystalline core-shell Sn-SnO_2 nanoparticles as lithium-ion battery anode materials and amorphous TiO_2 nanowires as supports for Au nanocatalyst.[62-64] Recently, Rodriguez's group reported a more extensive description of the synthesis of TiO_2 nanowires, crystalline $BiVO_4$ nano-stars and crystalline H_2WO_4 nanorods using the cathodic corrosion method at room temperature, in the absence of organic solvents or surfactants (Figure 2).[26] The authors demonstrated for the first time that the size and shape of the oxide nanostructures can be controlled by variation of the applied square wave frequency as highlighted by the SEM/TEM images (**Figure 2A-B**). Early results have also shown that the particle size of the oxide nanoparticles increases with the concentration of the electrolyte in the same fashion as was reported for metal nanoparticles.[65] Preliminary data show that TiO_2 nanowires can be prepared in 10 M NaOH,[64] while small round TiO_2 nanoparticles can be obtained under similar conditions of applied voltage and frequency, but by reducing the concentration of the electrolyte to 2 M (**Figure 2C**). Such differences on

size and shape are highly relevant on the photoelectrochemical activity of the oxides towards water splitting.[26]

Similar pulse potential methods for the electrochemical synthesis of metal oxide NPs have been reported. Such methods compromise the reduction of the electrodes and oxidation of the electro-generated species by use of identical-sized working and counter electrodes. In terms of particle shape and size control, the produced ZnO nanorods suffered from poor size and shape homogeneity, whilst the TiO_2 lacked well-defined nanostructure, even in the presence of a capping agent.[66] Similarly, the as-produced Co oxyhydroxide material suffered from poor nanostructure homogeneity.[67]

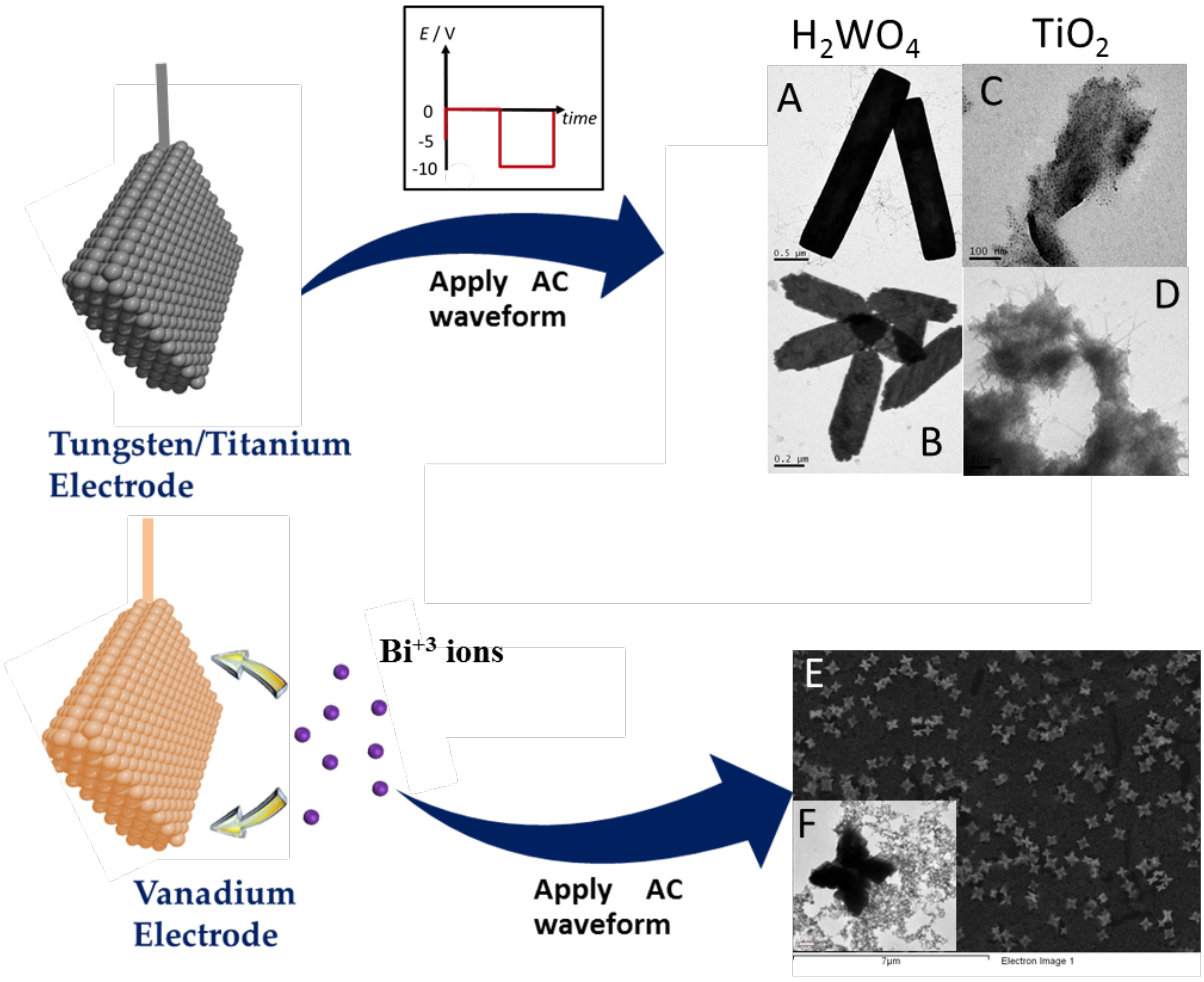

Figure 2. Schematic illustration of the formation of metal oxide nanoparticles via cathodic corrosion; pure metallic electrodes are electrochemically etched to produce a suspension of metal oxide nanoparticles, with controllable size and shape. TEM images of H_2WO_4 nanorods synthesized by application of a square waveform at (A) 100 Hz and (B) 1000 Hz, respectively. (C-D) TEM images demonstrating the effect of electrolyte concentration and applied potential on the morphology of TiO_2 nanowires synthesized via cathodic corrosion in (C) 2 M NaOH and (D) 10 M NaOH. (E) SEM and (F) TEM images of $BiVO_4$ nano-stars synthesized via cathodic corrosion. Adapted with permission from Ref. [26]. Copyright (2017) American Chemical Society.

2.4. Synthesis of nanostructured metal oxides by galvanic exchange

The majority of electrosynthetic pathways towards the formation of metallic oxides involve a substantial driving force to push the reaction to a state far from equilibrium. As an alternative to this, Oh et al.[68] have proposed an elegant way to prepare metal oxide nanostructures via the galvanic replacement reaction (GRR). GRR is a spontaneously occurring process at the open circuit potential (OCP) which is driven by a difference in electrochemical potentials between an oxide-confined metal and a free metal ion. As in a typical Galvani cell, this thermodynamic bias is diminished by a tendency of the system to reach equilibrium conditions, and eventually – a substitution of a cation in the oxide lattice.

Although this synthetic strategy has not been extensively studied, it has already brought a few advances to the field. First of all, the formation of core@shell nanoparticles is relatively straight-forward as it involves the addition of a foreign metal, which subsequently substitutes the outermost layers of the native metal within the oxide lattice (**Figure 3A)**.[69-71] Additionally, it has been shown that the ratio between core and shell thickness can be modulated while maintaining the particle diameter.[70] However, the main drawback is the lack of homogeneity in the deeper layers due to diffusional limitations of the metal in the solid. In addition, the morphology of prepared nanoparticles was not well defined due to the so-called Kirkendall effect that gives origin to hollow structures (**Figure 3B**).[71, 72] The formation of hollow structures via the Kirkendall effect has attracted substantial attention.[73-75] Many different hollow nano-forms, including rattles, boxes, bowls, spheres, and particles of various shapes, have been reported using GRR; **Figure 3C(i-iv)** shows the progressive change of the shape of the nanostructures during the synthesis of the nanobox.[69, 76, 77]

The GRR has been also employed in the preparation of exfoliated, 2D, layered metal oxide nanosheets. The authors reported the GRR of exfoliated MnO_2 nanosheets by Fe^{2+} or Sn^{2+}

ions resulting in highly anisotropic Fe- or Sn-oxide nanosheets.[78] These resulting materials are very relevant for lithium ion batteries and have potential as catalysts for the OER.

Further improvements of the GRR methodology include fine control of the shape and structure of the particles. In this case, GRR has been implemented on metal oxide nanoparticles with well-defined shape as a sacrificial-template to grow particles of other metal oxides (**Figure 3D**).[77] The importance of particle shape control has been extensively described in the literature with a particular interest in electrocatalysis.[79] Therefore, some attention has been paid to the factors determining the shape of particles of metal oxides[76] and oxyhydroxides[80] applicable in the field of energy conversion.

The early stages of galvanic replacement reactions in metal oxide structures raise a promise of a facile way to prepare these structures with a certain degree of control over the size, shape and composition. Nevertheless, the GRR approach is yet applicable to a very few types of metal oxides of the highest reactivity. Moreover, the relatively slow kinetics require the use of moderately elevated temperature, what may be considered as a drawback when compared to the classical electrochemical methods. Finally, a clear understanding of the galvanic exchange process within metal oxides is needed in order to rationally explore the scope of the method.[81-83]

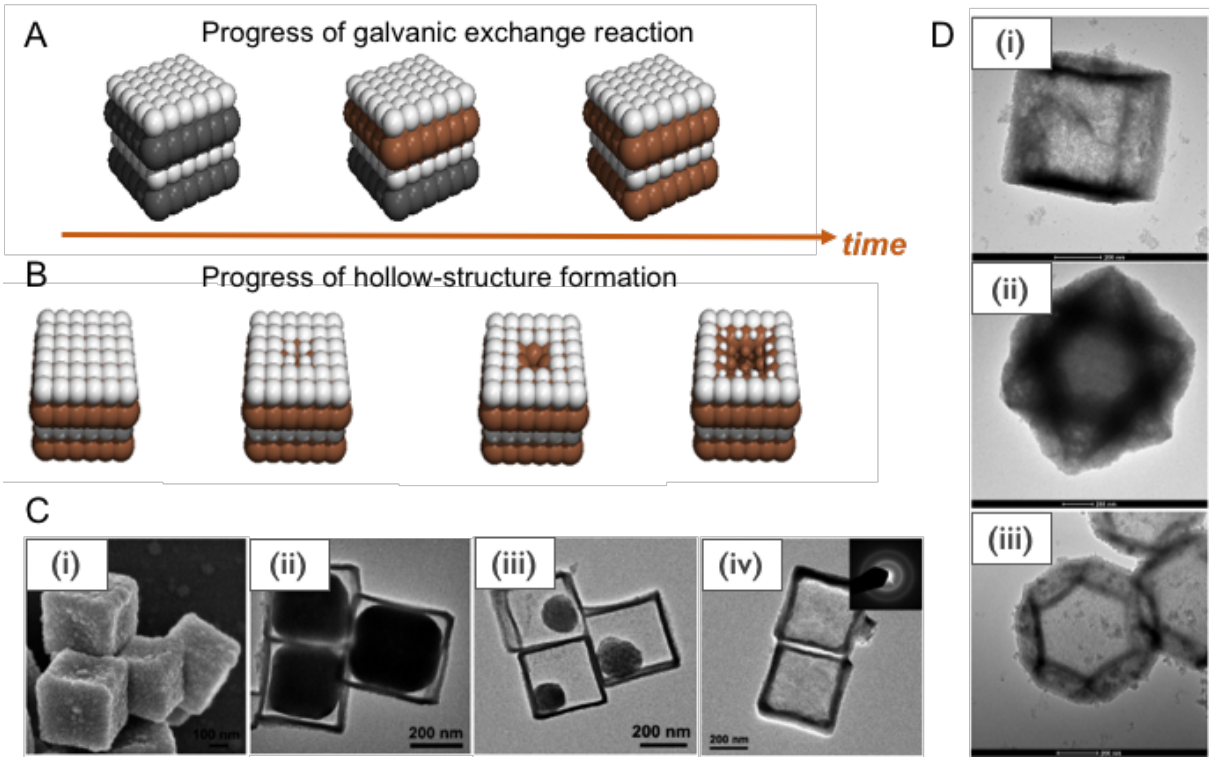

Figure 3. (A) Schematic representation of the galvanic exchange reaction and (B) hollow-structure formation where grey spheres represent the native metal; white – oxygen; brown – incoming metal. (C)(i) SEM and (ii-iv) TEM study of the evolution of $Cu_2O@Fe(OH)_x$ over time to form a nanobox. Adapted with permission from Ref. [69]. Copyright (2010) American Chemical Society (D) High-resolution TEM images of (i) cubic (ii) octahedral and (iii) dodecahedral NiO particles grown on a sacrificial Cu_2O substrate. Adapted from Ref. [77] with permission from Elsevier.

2.5. Conclusions

With this review, we have made an effort to highlight the more recent contributions and progress in the area of electrochemical methods for synthesis of metal oxide and oxyhydroxide nanoparticles. Each of the methods clearly present a number of advantages and disadvantages based on: the versatility of the materials that can be prepared with said method, the control over the structure and morphology, the time and cost of the method, scalability for industrial applications and, of course, the application, i.e. whether the final nanostructure is an electrodeposited thin film or a dispersion of nanoparticles.

In the search for new nanostructured materials with enhanced (photo)catalytic properties, desired composition and structural characteristics, electrochemical methods are indeed powerful tools and the new advances in the control of the structure and size are very encouraging. The electrochemical synthesis of the metal oxides and oxyhydroxides is ecologically friendly and the preparation quite often is inexpensive, providing a more efficient route for the generation of a variety of highly active materials.

2.6. Acknowledgments

M.J.L., and A.K. acknowledge the University of Birmingham for financial support through PhD scholarships at the School of Chemistry.

References

1. S. D. Jackson and J. S. J. Hargreaves, *Metal Oxide Catalysis*, Wiley-VCH, 2008.

2. J. Meyer, S. Hamwi, M. Kroger, W. Kowalsky, T. Riedl and A. Kahn, *Adv. Mater.*, 2012, **24**, 5408-5427.

3. J. E. G. J. Wijnhoven and W. L. Vos, *Science*, 1998, **281**, 802-804.

4. C. Barbé, J. Bartlett, L. Kong, K. Finnie, H. Q. Lin, M. Larkin, S. Calleja, A. Bush and G. Calleja, *Adv. Mater.*, 2004, **16**, 1959-1966.

5. E. Comini, *Anal. Chim. Acta*, 2006, **568**, 28-40.

6. J. Jiang, Y. Li, J. Liu, X. Huang, C. Yuan and X. W. Lou, *Adv. Mater.*, 2012, **24**, 5166-5180.

7. W. T. Hong, M. Risch, K. A. Stoerzinger, A. Grimaud, J. Suntivich and Y. Shao-Horn, *Energy Environ. Sci.*, 2015, **8**, 1404-1427.

8. S. Liu, H. Zhang, L. Sviridov, L. Huang, X. Liu, J. Samson, D. Akins, J. Li and S. O'Brien, *J. Mater. Chem*, 2012, **22**, 21862-21870.

9. D. Li and H. Haneda, *Chemosphere*, 2003, **51**, 129-137.

10. S. A. Bilmes, P. Mandelbaum, F. Alvarez and N. M. Victoria, *J. Phys. Chem. B*, 2000, **104**, 9851-9858.

11. L. Yu, L. Zhang, H. B. Wu, G. Zhang and X. W. Lou, *Energy Environ. Sci.*, 2013, **6**, 2664-2671.

12. Y.-w. Jun, J.-s. Choi and J. Cheon, *Angew. Chem., Int. Ed.*, 2006, **45**, 3414-3439.

13. S. Sun and H. Zeng, *J. Am. Chem. Soc.*, 2002, **124**, 8204-8205.

14. Y. Zhao, R. L. Frost, J. Yang and W. N. Martens, *J. Phys. Chem. C*, 2008, **112**, 3568-3579.

15. X. Liang, X. Wang, J. Zhuang, Y. Chen, D. Wang and Y. Li, *Adv. Funct. Mater.*, 2006, **16**, 1805-1813.

16. D. Fu, P. G. Keech, X. Sun and J. C. Wren, *Phys. Chem. Chem. Phys.*, 2011, **13**, 18523-18529.

17. M.-M. Titirici, M. Antonietti and A. Thomas, *Chem. Mater.*, 2006, **18**, 3808-3812.

18. M. Niederberger and G. Garnweitner, *Chem. - Eur. J.*, 2006, **12**, 7282-7302.

19. S. Liu, L. Huang, W. Li, X. Liu, S. Jing, J. Li and S. O'Brien, *Nanoscale*, 2015, **7**, 11766-11776.

20. Z. Chen, L. Huang, J. He, Y. Zhu and S. O'Brien, *J. Mater. Res.*, 2011, **21**, 3187-3195.

21. A. J. Zarur and J. Y. Ying, *Nature*, 2000, **403**, 65-67.

22. L. M. Gan, L. H. Zhang, H. S. O. Chan, C. H. Chew and B. H. Loo, *J. Mater. Sci.*, 1996, **31**, 1071-1079.

23. C. G. Morales-Guio, L. Liardet and X. Hu, *J. Am. Chem. Soc.*, 2016, **138**, 8946-8957.

24. C. Kartal, Y. Hanedar, T. Öznülüer and Ü. Demir, *Langmuir*, 2017, **33**, 3960-3967.

25. Y. Yang, Y. Li and M. Pritzker, *Electrochim. Acta*, 2016, **213**, 225-235.

26. M. L. Kromer, J. Monzó, M. J. Lawrence, A. Kolodziej, Z. T. Gossage, B. H. Simpson, S. Morandi, A. Yanson, J. Rodríguez-López and P. Rodríguez, *Langmuir*, 2017, **33**, 13295-13302.

27. D. Tench and L. F. Warren, *J. Electrochem. Soc.*, 1983, **130**, 869-872.

28. D. P. Anderson and L. F. Warren, *J. Electrochem. Soc.*, 1984, **131**, 347-349.

29. M. A. Sayeed and A. P. O'Mullane, *RSC Adv.*, 2017, **7**, 43083-43089.

30. C. Zhu, S. Fu, D. Du and Y. Lin, *Chem. - Eur. J.*, 2016, **22**, 4000-4007.

31. G. P. Wheeler and K.-S. Choi, *ACS Energy Lett.*, 2017, **2**, 2378-2382.

32. A. C. Cardiel, K. J. McDonald and K.-S. Choi, *Langmuir*, 2017, **33**, 9262-9270.

33. D. Gao, I. Zegkinoglou, N. J. Divins, F. Scholten, I. Sinev, P. Grosse and B. Roldan Cuenya, *ACS Nano*, 2017, **11**, 4825-4831.

34. R. Kas, R. Kortlever, A. Milbrat, M. T. M. Koper, G. Mul and J. Baltrusaitis, *Phys. Chem. Chem. Phys.*, 2014, **16**, 12194-12201.

35. C. S. Le Duff, M. J. Lawrence and P. Rodriguez, *Angew. Chem., Int. Ed.*, 2017, **56**, 12919-12924.

36. Y. Lum and J. W. Ager, *Angew. Chem., Int. Ed.*, 2018, **57**, 551-554.

37. J. Monzó, Y. Malewski, R. Kortlever, F. J. Vidal-Iglesias, J. Solla-Gullón, M. T. M. Koper and P. Rodriguez, *J. Mater. Chem. A*, 2015, **3**, 23690-23698.

38. J. Li, Y. Shi, Q. Cai, Q. Sun, H. Li, X. Chen, X. Wang, Y. Yan and E. G. Vrieling, *Cryst. Growth Des.*, 2008, **8**, 2652-2659.

39. C. Borrás, P. Rodríguez, T. Laredo, J. Mostany and B. R. Scharifker, *J. Appl. Electrochem.*, 2004, **34**, 583-589.

40. W. R. LaCourse, Y.-L. Hsiao and D. C. Johnson, *J. Electrochem. Soc.*, 1989, **136**, 3714-3719.

41. L. Xu, Q. Chen and D. Xu, *J. Phys. Chem. C*, 2007, **111**, 11560-11565.

42. J. Hu, Z. Zhao, Y. Sun, Y. Wang, P. Li, W. Zhang and K. Lian, *Appl. Surf. Sci.*, 2016, **364**, 434-441.

43. T. M. Whitney, J. S. Jiang, P. C. Searson and C. L. Chien, *Science*, 1993, **261**, 1316-1319.

44. C. R. Martin, *Science*, 1994, **266**, 1961.

45. J. C. Hulteen and C. R. Martin, *J. Mater. Chem*, 1997, **7**, 1075-1087.

46. D. Xu, D. Chen, Y. Xu, X. Shi, G. Guo, L. Gui and Y. Tang, *Pure Appl. Chem.*, 2000, **72**, 127-135.

47. M. J. Zheng, L. D. Zhang, G. H. Li and W. Z. Shen, *Chem. Phys. Lett.*, 2002, **363**, 123-128.

48. K. Takahashi, S. J. Limmer, Y. Wang and G. Cao, *J. Phys. Chem. B*, 2004, **108**, 9795-9800.

49. J. González-García, F. Gallud, J. Iniesta, V. Montiel, A. Aldaz and A. Lasia, *J. Electrochem. Soc.*, 2000, **147**.

50. X.-J. Wu, F. Zhu, C. Mu, Y. Liang, L. Xu, Q. Chen, R. Chen and D. Xu, *Coord. Chem. Rev.*, 2010, **254**, 1135-1150.

51. K. Lee, A. Mazare and P. Schmuki, *Chem. Rev*, 2014, **114**, 9385-9454.

52. A. Fujishima and K. Honda, *Nature*, 1972, **238**, 37-38.

53. A. Fujishima, K. Kohayakawa and K. Honda, *Bull. Chem. Soc. Jpn.*, 1975, **48**, 1041-1042.

54. J. Zhang, P. Zhou, J. Liu and J. Yu, *Phys. Chem. Chem. Phys.*, 2014, **16**, 20382-20386.

55. S. So, I. Hwang, F. Riboni, J. Yoo and P. Schmuki, *Electrochem. Commun.*, 2016, **71**, 73-78.

56. S. So, F. Riboni, I. Hwang, D. Paul, J. Hammond, O. Tomanec, R. Zboril, D. R. Sadoway and P. Schmuki, *Electrochim. Acta*, 2017, **231**, 721-731.

57. S. Ozkan, N. T. Nguyen, A. Mazare, R. Hahn, I. Cerri and P. Schmuki, *Electrochem. Commun.*, 2017, **77**, 98-102.

58. S. Mohajernia, S. Hejazi, A. Mazare, N. T. Nguyen, I. Hwang, S. Kment, G. Zoppellaro, O. Tomanec, R. Zboril and P. Schmuki, *Mater. Today Energy*, 2017, **6**, 46-52.

59. B. Jin, X. Zhou, L. Huang, M. Lickleder, M. Yang and P. Schmuki, *Angew. Chem., Int. Ed.*, 2016, **55**, 12252-12256.

60. A. I. Yanson, P. Rodrigez, N. Garcia-Araez, R. V. Mom, F. D. Tichelaar and M. T. M. Koper, *Angew. Chem., Int. Ed.*, 2011, **50**, 6346-6350.

61. P. Rodriguez, F. D. Tichelaar, M. T. M. Koper and A. I. Yanson, *J. Am. Chem. Soc.*, 2011, **133**, 17626-17629.

62. F. Lu, X. Ji, Y. Yang, W. Deng and C. E. Banks, *RSC Adv.*, 2013, **3**, 18791.

63. A. B. Kuriganova, C. A. Vlaic, S. Ivanov, D. V. Leontyeva, A. Bund and N. V. Smirnova, *J. Appl. Electrochem.*, 2016, **46**, 527-538.

64. P. Rodriguez, D. Plana, D. J. Fermin and M. T. M. Koper, *J. Catal.*, 2014, **311**, 182-189.

65. A. I. Yanson, P. V. Antonov, Y. I. Yanson and M. T. M. Koper, *Electrochim. Acta*, 2013, **110**, 796-800.

66. J. E. Cloud, T. S. Yoder, N. K. Harvey, K. Snow and Y. Yang, *Nanoscale*, 2013, **5**, 7368-7378.

67. M. Jing, Y. Yang, Y. Zhu, H. Hou, Z. Wu and X. Ji, *Electrochim. Acta*, 2014, **141**, 234-240.

68. M. H. Oh, T. Yu, S.-H. Yu, B. Lim, K.-T. Ko, M.-G. Willinger, D.-H. Seo, B. H. Kim, M. G. Cho, J.-H. Park, K. Kang, Y.-E. Sung, N. Pinna and T. Hyeon, *Science*, 2013, **340**, 964-968.

69. Z. Wang, D. Luan, C. M. Li, F. Su, S. Madhavi, F. Y. Boey and X. W. Lou, *J. Am. Chem. Soc.*, 2010, **132**, 16271-16277.

70. H.-M. Jeong, J.-H. Kim, S.-Y. Jeong, C.-H. Kwak and J.-H. Lee, *ACS Appl. Mater. Interfaces*, 2016, **8**, 7877-7883.

71. A. López-Ortega, A. G. Roca, P. Torruella, M. Petrecca, S. Estradé, F. Peiró, V. Puntes and J. Nogués, *Chem. Mater.*, 2016, **28**, 8025-8031.

72. Y. Yin, R. M. Rioux, C. K. Erdonmez, S. Hughes, G. A. Somorjai and A. P. Alivisatos, *Science*, 2004, **304**, 711-714.

73. A. A. El Mel, M. Buffiere, P. Y. Tessier, S. Konstantinidis, W. Xu, K. Du, I. Wathuthanthri, C. H. Choi, C. Bittencourt and R. Snyders, *Small*, 2013, **9**, 2838-2843.

74. H. J. Fan, U. Gosele and M. Zacharias, *Small*, 2007, **3**, 1660-1671.

75. S. J. P. Varapragasam, C. Balasanthiran, A. Gurung, Q. Qiao, R. M. Rioux and J. D. Hoefelmeyer, *J. Phys. Chem. C*, 2017, **121**, 11089-11099.

76. T. S. Rodrigues, A. G. M. da Silva, R. S. Alves, I. C. de Freitas, D. C. Oliveira and P. H. C. Camargo, *Part. Part. Syst. Charact.*, 2017, DOI: 10.1002/ppsc.201700175.

77. F. Lin, H. Wang and G. Wang, *Electrochim. Acta*, 2016, **211**, 207-216.

78. J. Lim, J. M. Lee, B. Park, X. Jin and S.-J. Hwang, *Nanoscale*, 2017, **9**, 792-801.

79. M. A. Montiel, F. J. Vidal-Iglesias, V. Montiel and J. Solla-Gullón, *Curr. Opin. Electrochem.*, 2017, **1**, 34-39.

80. M. Diab and T. Mokari, *Cryst. Growth Des.*, 2017, **17**, 527-533.

81. N. Comisso, L. Armelao, S. Cattarin, P. Guerriero, L. Mattarozzi, M. Musiani, M. Rancan, L. Vázquez-Gómez and E. Verlato, *Electrochim. Acta*, 2017, **253**, 11-20.

82. D. Kriegner, M. Sytnyk, H. Groiss, M. Yarema, W. Grafeneder, P. Walter, A.-C. Dippel, M. Meffert, D. Gerthsen, J. Stangl and W. Heiss, *J. Phys. Chem. C*, 2016, **120**, 19848-19855.

83. Y. Yao, C. Patzig, Y. Hu and R. W. J. Scott, *J. Phys. Chem. C*, 2017, **121**, 19735-19742.

3. AIMS AND OBJECTIVES

In the previous 2 chapters the current energy landscape was described, outlining the pervading global use of fossil fuels and the adverse environmental effects imposed by their use.

The ever increasing importance of green energy applications, such as water splitting and electrochemical reduction of CO_2, and the key role of nanostructured metal oxide catalysts to the realisation of these technologies, was described. Taking advantage of the electrical energy generated by wind, solar and wave technologies, (photo)electrocatalysis provides a route to further close the anthropogenic carbon cycle, thereby reducing reliance on fossil fuels for energy production and proactively combatting existing environmental deterioration trends.

As was also mentioned in **Chapter 1**, one of the main limitations to the extensive market implementation of these technologies is the lack of active, selective and durable oxide catalysts. Electrochemistry has provided the means to produce active (photo)electrocatalysts, particularly transition metal oxides and oxyhydroxides, with fine control over size, structure and elemental composition.

The aim of this thesis was to demonstrate that cathodic corrosion can be an important, versatile synthetic tool in the design, preparation and screening of intrinsically active metal oxide (photo)electrocatalysts. The following experimental chapters, **Chapters 5-7**, address specific objectives related to the preparation and characterization of transition metal oxide nanocatalysts using cathodic corrosion and the evaluation of such catalysts towards two key reactions: the photoelectrochemical oxygen evolution reaction (OER) and the electrochemical reduction of CO_2 (CO_2RR). The specific objectives of each chapter are:

Chapter 5

Aim - Investigation of the use of cathodic corrosion in the preparation of stable state-of-the-art binary and ternary metal oxide catalysts for photoelectrochemical water oxidation via:

- demonstration of the effective use of cathodic corrosion for the preparation of key OER metal oxide photoelectrocatalyst nanoparticles: $BiVO_4$, WO_3 and TiO_2.
- physical and photoelectrochemical characterisation of as-prepared oxide nanostructures
- demonstration of the tuning of nanoparticle shape and/or size by varying cathodic corrosion parameters
- evaluation of the photoelectrochemical activity of the as-prepared nanostructures in comparison to state-of-the-art catalysts.

Chapter 6

Aim - Exploration of the compositional retention of mixed metal oxide nanostructures generated by cathodic corrosion of alloys via:

- single-step preparation of nanostructured mixed metal oxides from homogeneous Ti alloys, without additive electrolyte cations
- extensive physical and morphological characterisation of the as-prepared nanostructures to probe mixed metal ratios and homogeneity, affording comparison to parent alloy composition and evaluation of alloy retention
- structural characterisation of the mixed metal oxide nanostructures via X-ray absorption spectroscopy (XAS) to determine oxidation state and local coordination environment of metal cations
- evaluation of the intrinsic effect of doped transition metal cations on photoelectrochemical water oxidation performance of nanostructured titanates.

Chapter 7

Aim - Evaluation of the effect of the local copper coordination environment on CO_2RR product selectivity in near-neutral aqueous media via:

- preparation of discrete Cu(II) oxide nanostructures via cathodic corrosion

- *ex-situ* physical and morphological characterisation of the prepared nanostructures
- electrochemical characterisation and evaluation of CO_2RR activity for each material in near-neutral phosphate buffer electrolyte
- CO_2RR product characterisation via on-line electrochemical mass spectrometry and ^{1}H NMR
- *in-situ* XAS characterisation under CO_2RR conditions to relate changes in Cu oxidation state and coordination environment to observed product selectivity.

4. EXPERIMENTAL METHODS

In this chapter the basic operating principles of the various experimental techniques employed for sample preparation, physical/structural and electrochemical characterisation in the subsequent chapters are presented. In **Chapters 5 – 7** the key results of the experimental work conducted over the course of this PhD research project are presented, with specific corresponding experimental details.

4.1. Catalyst preparation

4.1.1. Cathodic corrosion: Operating Principles & Experimental Setup

As was discussed in **Chapter 2**, cathodic corrosion is an electrochemical etching technique, performed in aqueous conductive electrolyte, atomising bulk metals/alloys to aqueous suspensions of metal and metal oxide nanoparticles in a single step, in contrast to the typical electrochemical preparation techniques that involve the deposition of thin films onto a substrate. The preparation of nanoparticles via cathodic corrosion is rapid and occurs over timescales on the order of minutes at room temperature, as opposed to hours at elevated temperature.[1] Control over particle size, alloy composition and surface orientation can be effected by appropriately tuning the electrochemical conditions employed.[2-4] That this process is able to produce stable and homogenous nanoparticles in the absence of organic capping reagents and surfactants removes the need for laborious cleaning steps, affording a clean and efficient synthetic route for the screening and discovery of new (photo)electrocatalyst materials for green energy applications.

The mechanism of action has been previously reported.[1] Cathodic corrosion is initiated by applying a strong negative alternating current (a.c.) voltage across the working electrode (WE) and counter electrode (CE) submerged in an aqueous conductive electrolyte.

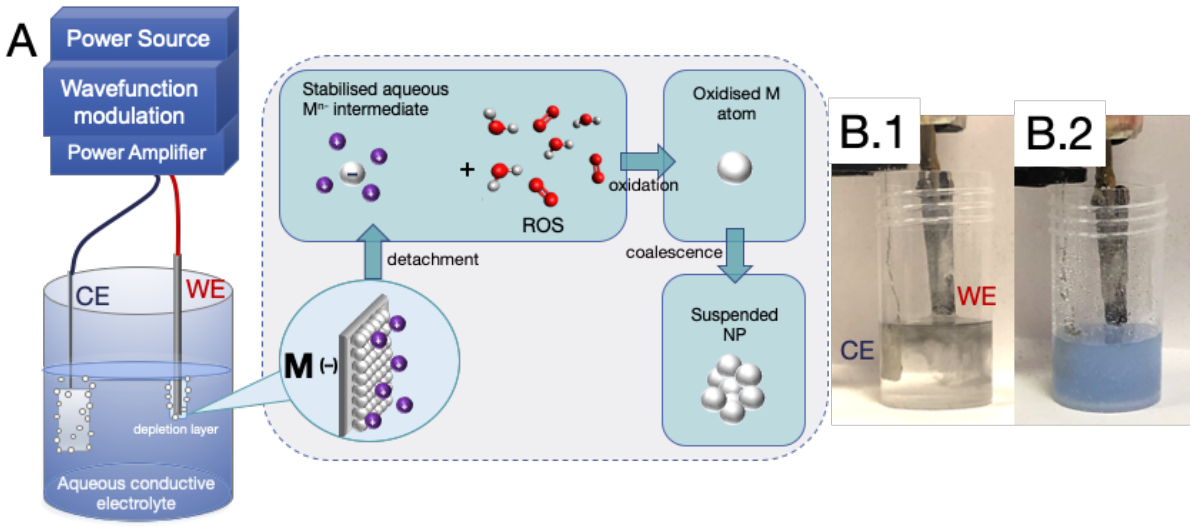

Figure 1. (A) Schematic illustration of a 2-electrode cathodic corrosion setup and the mechanism of nanoparticle (NP) formation. The power source, wavefunction modulation and power amplifier are used to generate the strong negative a.c. voltage across the working electrode (WE) and counter electrode (CE), causing the evolution of H_2 and O_2 at the WE and CE, respectively. The high pH depletion layer formed immediately local to the WE affords the formation of metal surface anionic species (M^-) stabilised by electrolyte cations. Through the action of the a.c. voltage, anionic surface species detach from the WE and are oxidised through interaction with reactive oxygen species (ROS) outside of the depletion layer and coalesce to form suspended NPs due to the high surface energy of the single metal atoms. Snapshots captured (B.1) during and (B.2) immediately following cathodic corrosion of a CuTi alloy in 10 M NaOH, oscillating between 0 and -10 V, showing the formation of metallic and oxide NP suspensions.

A high pH H^+/H_2O-free depletion layer is generated immediately local to the WE surface due to the vigorous HER occurring under the strong cathodic applied potential. The metallic electrode is reduced to its anionic form under the harsh experimental conditions, stabilised by the presence and adsorption of electrolyte cations. Recent studies have explored the effect of varying the electrolyte cation on the metal surface etching pit geometries, providing support for the importance of the adsorbed solution cations to the cathodic corrosion process.[5-7] Through the switching action of the a.c voltage the anionic species detach from the WE surface and are oxidised upon escaping the depletion layer by chemical reaction with H_2O

and reactive oxygen species (ROS) generated *in situ* at the CE via OER. The oxidised free atoms possess high surface energy leading to coalescence and the formation of freely suspended nanoparticles in the electrolyte.

It should be also noted that cathodic corrosion utilising direct current (d.c.) voltage is possible. Under this regime the anionic species do not detach from the WE, rather, nanoparticles form at the electrode surface.[1] This has been demonstrated as an effective route for enhancing the catalytic activity of bulk metal surfaces by increasing the electrochemical surface area (ECSA).[7]

Cathodic corrosion can be performed using either a 2-electrode or 3-electrode configuration.[7, 8] All cathodic corrosion experiments performed and reported as part of this thesis were conducted utilising the 2-electrode configuration (**Figure 1A**). Provided that a high purity (≥98%) metal or alloy WE precursor is to be employed in the cathodic corrosion process no specific additional preparatory steps are required. It is good practice, however, to briefly polish the metal/alloy wire with high grit polish paper prior to electrochemical etching to remove any surface oxides generated by exposure to air or for a length of wire which has previously been subject to cathodic corrosion, followed by dispersion by ultrasonication in water. Use of high grit paper prevents significant surface roughening prior to cathodic corrosion, which could affect the homogeneity of the etching process. Electrolyte solutions were prepared using high purity salts (≥97% purity) dissolved in milli-Q water to produce the desired molarity and transferred to the reaction beaker/flask via a micropipette. A high surface area Pt foil CE was employed in all cathodic corrosion syntheses presented. Prior to use, the CE was rinsed with ultrapure (milli-Q) water (18.2 MΩ•cm), flame-annealed using a propane/butane torch, to remove any organic surface species that would otherwise contaminate the electrochemical system upon immersion in the aqueous electrolyte, and immediately rinsed with milli-Q water to cool before transferring to the reaction vessel. The

CE was fully immersed in the electrolyte (**Figure 1B**) to afford as large a surface area as possible that would prevent the kinetics of the CE reaction limiting the supply of electrons to the WE.

To obtain the desired length of wire or depth of alloy immersed in the electrolyte, the WE was first lowered so that it just in contacted the electrolyte surface, then the desired depth was achieved through use of a micrometre screw, as described previously.[9]

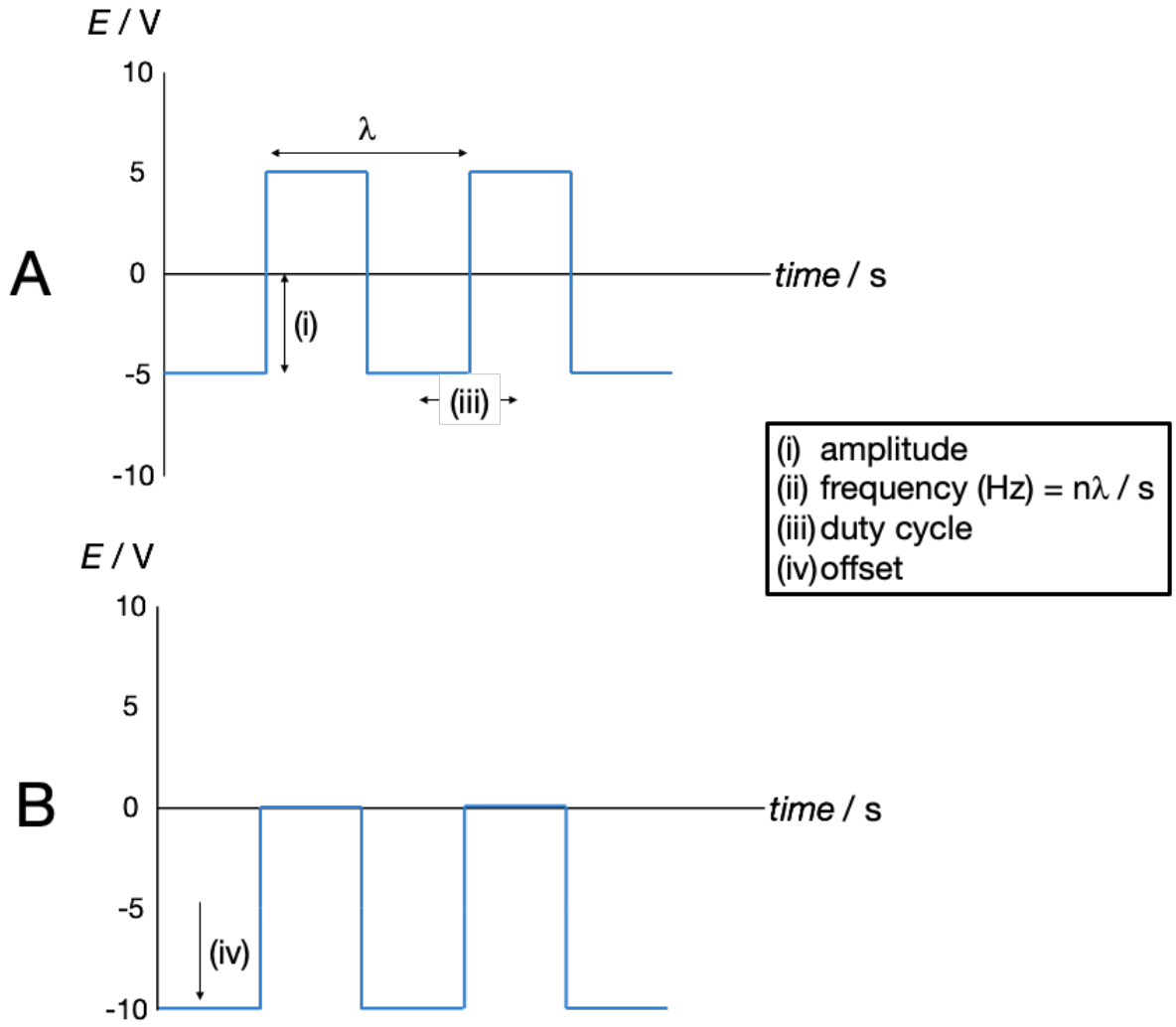

Figure 2. Illustrative square wave forms (blue lines) used to generate the a.c. voltage for cathodic corrosion and the effect of the square wave offset. Parameters: (A) amplitude = 5 V; frequency = 100 Hz; duty cycle = 50%; offset = 0 V. (B) amplitude = 5 V; frequency = 100 Hz; duty cycle = 50%; offset = -5 V.

The a.c. voltage was generated via a square wave form using LabVIEW hardware connected to a power amplifier and the current-time data was monitored using a National Instruments DAQ module. The key parameters used to define and control the a.c. voltage are: *(i)* amplitude, *(ii)* frequency, *(iii)* duty cycle and *(iv)* offset (**Figure 2**). Typically, the amplitude, frequency, duty cycle and offset conditions employed in the work presented in this thesis were 5 V, 100 Hz, 50% and -5V, respectively, generating an a.c. voltage oscillating between 0 and -10 V. The duty cycle refers to the ratio of time at the positive and negative maxima of the square waveform per wavelength, *i.e.* 50% equal time at the upper and lower limit (**Figure 2Aiii**).The offset potential is used to ensure that the a.c. voltage is cathodic for the duration of the process (**Figure 2B**).

Following the complete etching of the desired amount of metal/alloy, the electrolyte and nanoparticle suspension were separated by dilution and centrifugation with milli-Q water. The suspensions were subject to repeated 15 min cycles at 4000 rpm, followed by removal of the supernatant via micropipette and further dilution with milli-Q water until the pH of the supernatant was neutral. Nanoparticle samples were left suspended in milli-Q water prior to characterisation and analysis.

4.1.2. Suspended Droplet Alloying (SDA)

In **Chapters 6 & 7** the cathodic corrosion of Ti alloys is presented and explored for the preparation of metal oxide (photo)electrocatalysts without additive solution species. All alloys presented in the subsequent work were prepared via SDA.

SDA is a laser-assisted combinatorial alloy fabrication technique that has been demonstrated to be a useful and efficient method in the preparation of binary, ternary and quaternary alloys.[10-12] Aiming to improve on the inhomogeneity and inefficiency produced via direct laser deposition of alloys using metal powders,[13] SDA utilises multiple wires as the feedstock for alloy fabrication. The wires are fed and aligned into the focal point of a high energy laser via

a specially designed head where the tips of the wires are melted by the laser. As the wires continue to be fed into the focal point, the droplets at the ends of the wires grow such that a suspended alloy droplet forms which subsequently detaches from the tips of the wires when its mass is sufficiently large, falling onto the substrate below. Whilst the formation of the subsequent alloy droplet commences the head height is raised to allow the top of the detached droplet to be remelted to maintain the homogeneity of the detached alloy sample (**Figure 3**).[12] The process is performed in an Ar-filled chamber to prevent the formation of surface oxides via the melting process. SDA affords the possibility of specifically tuning the composition of the prepared alloys by precise control over the feed rate of each individual wire and via use of specific wire diameters. The complexity of the alloys can be further enhanced by use of coated wires and/or alloy wires, provided that pure wires can be sourced.

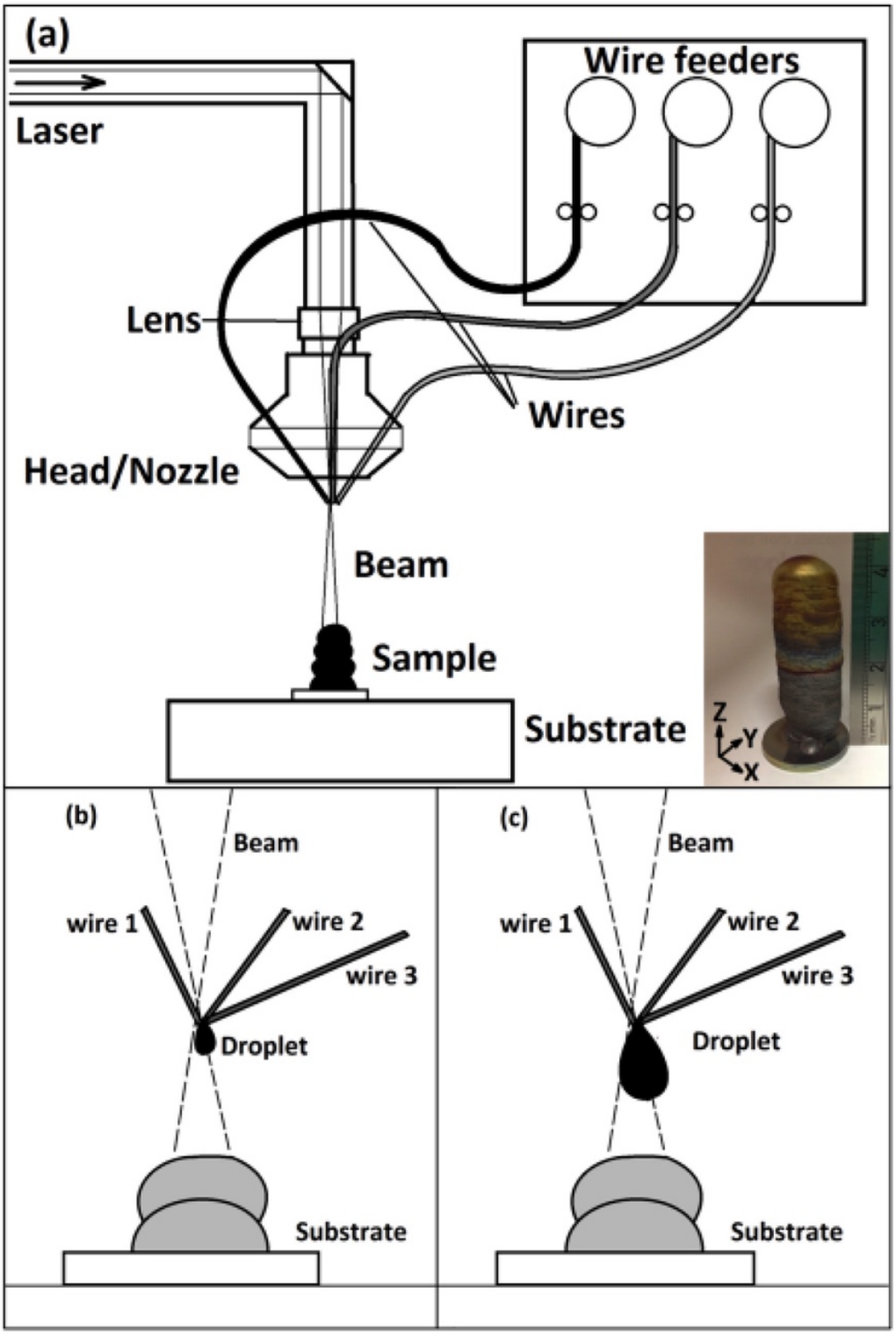

Figure 3. Schematic illustration of the suspended droplet alloying configuration. (a) Wire-feeding system (*inset*) photograph of a produced alloy button. (b) and (c) illustrate alloy droplet formation. Reprinted with permission from Li *et al*.[12] Copyright © 2018, Elsevier.

4.2. Physical and Structural Characterisation

Following production of nanoparticle samples via cathodic corrosion a variety of characterisation techniques were employed to investigate the composition, crystal and morphological structure and optical properties of the as-prepared materials. The techniques have been categorised by radiation type.

4.2.1. X-ray techniques

X-rays are transverse waves that are part of the higher energy portion of the electromagnetic spectrum, with wavelengths that range from 0.01 to 10 nm, that have found application in several materials characterisation techniques due to the similarity in wavelengths to interatomic distances and bond lengths.[14-16] The relative high energy of the x-rays allows for deep, non-destructive penetration of solid materials, useful for bulk characterisation techniques.

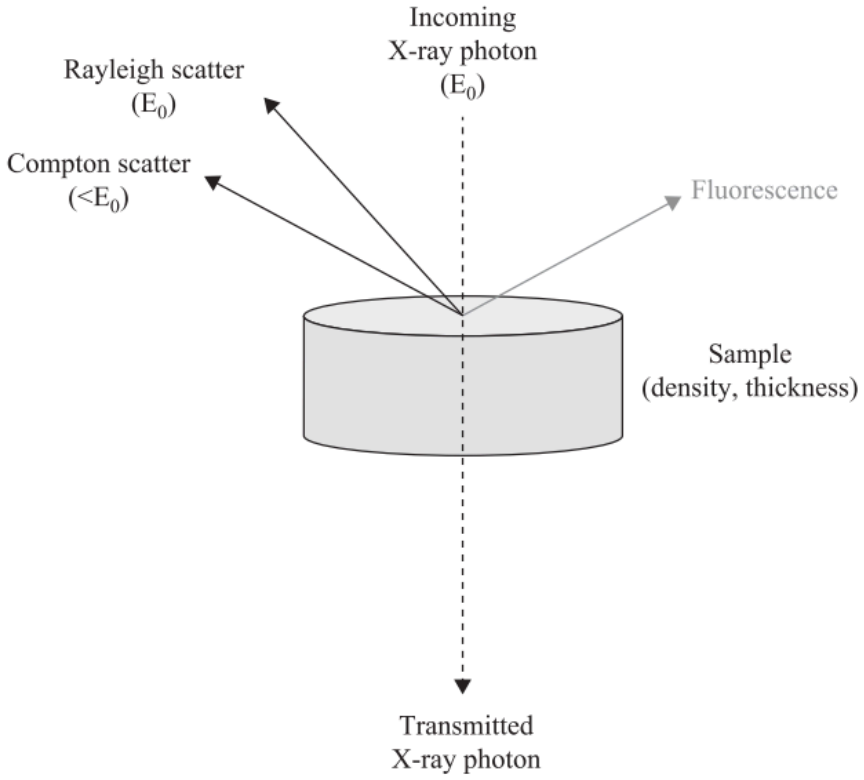

Figure 4. X-ray interactions with matter. Reprinted from ref. [14]. Copyright © 2013, Momentum Press.

There are multiple interactions that can occur whenever x-rays are incident on matter: scattering, fluorescence and transmission (**Figure 4**). X-rays are scattered by the atomic electrons and there are two main types of scattering interaction. Rayleigh (coherent) scattering is a form of elastic scattering, where no energy losses occur. Compton (incoherent) scattering is the product of secondary scattering interactions where energy is lost from the incident x-ray photon.

Below, the uses of the different x-ray interactions for materials characterisation are discussed.

4.2.1.1. X-ray diffraction (XRD)

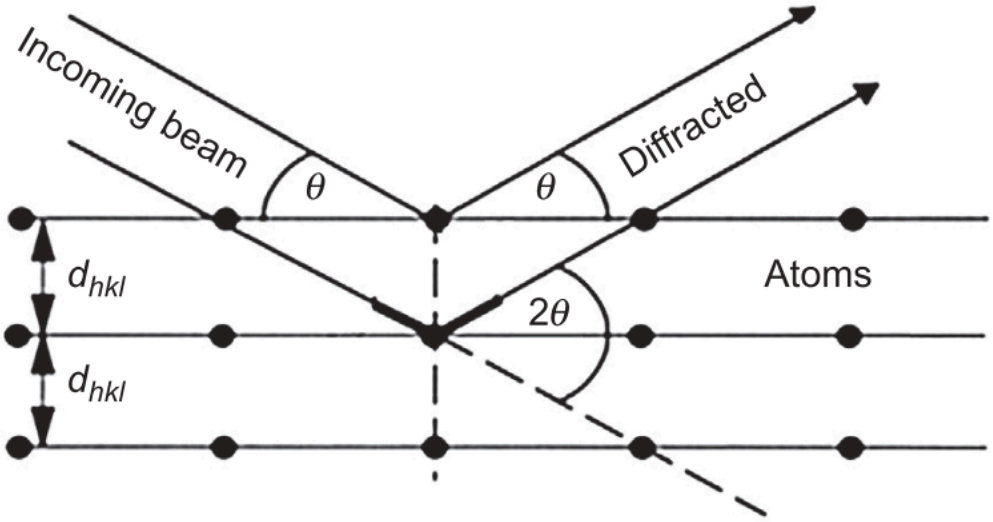

Figure 5. Schematic illustration of the geometrical condition for X-ray diffraction from lattice planes. Reprinted from ref. [16]. Copyright © 2016, Elsevier.

XRD utilises x-rays in the 0.5 to 2.5 Å regime to ascertain crystallographic information about the subject material using Rayleigh scattering.[15] Materials with periodic crystal lattices facilitate constructive (and destructive) interference of the scattered waves at specific incident angles, resulting in characteristic diffraction (**Figure 5**). The characteristic diffraction features can be used to determine the crystal structure, phase purity and interatomic distances, as expressed by Bragg's Law (**Equation 1**), where n the order of diffraction (an integer), λ is the incident x-ray wavelength (in nm), d_{hkl} is the lattice spacing (in nm) and θ is the incident angle

(in degrees). Diffraction patterns are collected and analysed to determine the crystallography of the material.

$$n\lambda = 2d_{hkl}sin\theta \quad (1)$$

4.2.1.2. X-ray fluorescence (XRF)

An incident x-ray photon with energy sufficient to overcome the binding energy of an inner-shell electron can be absorbed, causing ejection of the electron and creating an ionised atom with an electron vacancy. Two competing processes can occur to fill the vacancy and return the ionised atom to its original state. The Auger effect, or Auger decay, is a phenomenon where the filling of the inner-shell electron results in the emission of a photoelectron from an electron shell of higher energy.[14] The alternative competing process results in the emission of characteristic secondary x-rays equal to the difference in energy between the outer-shell and inner-shell electrons (**Figure 6**). The fluorescence spectrum obtained of the energy of the secondary x-rays can be used to identify and quantify the specific constituent elements in a material.

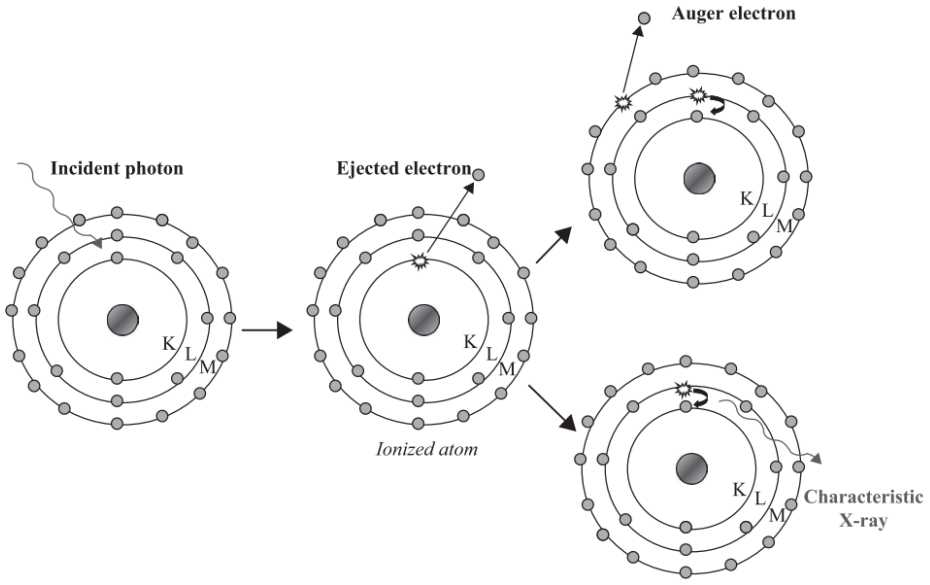

Figure 6. Schematic illustration of atomic ionisation and competing relaxation pathways generating either Auger electrons via Auger decay or characteristic x-rays via fluorescence. Reprinted from ref. [14]. Copyright © 2013, Momentum Press.

4.2.1.3. X-ray absorption spectroscopy (XAS)

XAS is analogous to XRF in that the photoelectric effect induced by the absorption of a photon causes excitation of a core electron, creating an excited state which can relax by the two emission pathways discussed above. An important distinction, however, is the use of synchrotron x-rays with very high energy that minimises signal to noise ratio in order to extract reliable long range structural information.

Absorption events exponentially reduce the total x-ray flux transmitted through a material (**Equation 2**)

$$I_t / I_0 = e^{-\mu L} \qquad (2)$$

where I_0 and I_t are the intensities of the incident and transmitted x-ray flux, respectively, μ is the linear absorption coefficient and L is the length of the sample. The absorption properties of elements vary according to atomic number (Z). Higher Z elements, with a greater number of electrons, have stronger interactions with incident x-rays. In XAS, the absorption edge is a sharp increase in absorption that occurs when the energy of incident photons corresponds to the binding energy of a core electron.[17] Absorption edges are labelled according to the principal quantum number (n) of the electron orbital, *i.e.* K for n = 1. The K-edge always denotes a transition from a 1s-orbital. All the XAS spectra measured and presented in this thesis were recorded at the corresponding K-edge of the subject element. Herein, the edge position is defined as the maximum of the first derivative.

In XAS characterisation two typical spectral regions and features are analysed: x-ray absorption near-edge structure (XANES) and extended x-ray absorption fine structure (EXAFS). These regions of the absorption spectrum arise due to either excitation to a valence orbital or ejection of the electron form the atom to the continuum as a wave, due to an excess in kinetic energy providing momentum to the photoelectron (**Figure 7**).[17]

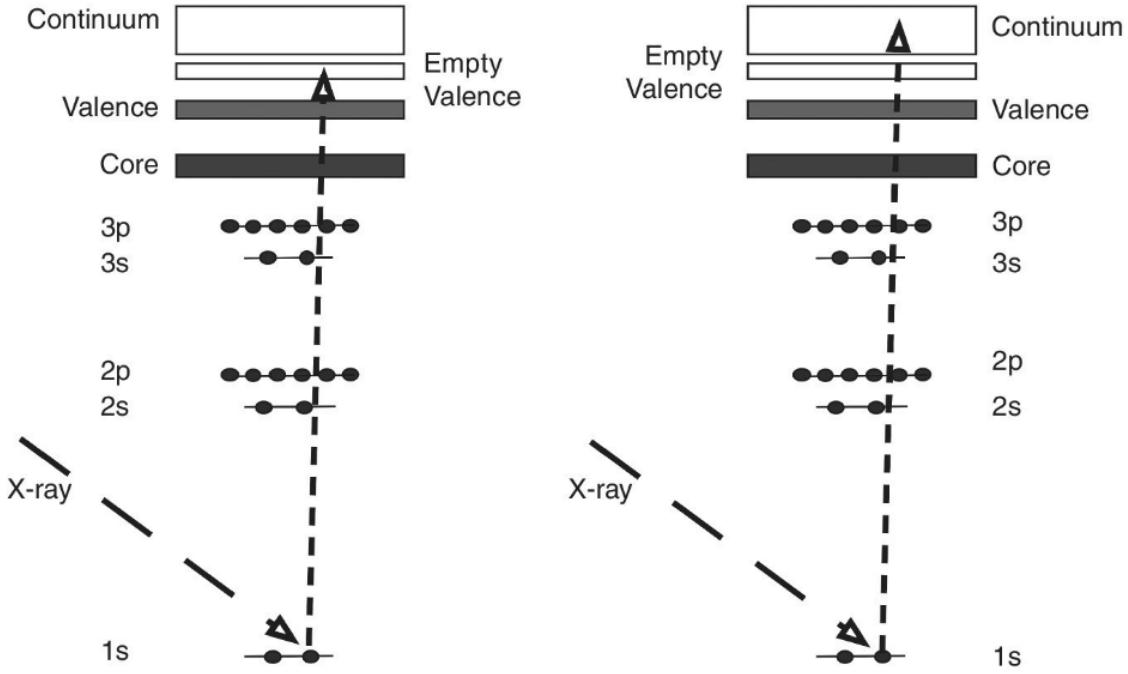

Figure 7. Illustration of the x-ray absorption electron excitation processes that give rise to XANES (*left*) and EXAFS (*right*) features. Reprinted from ref. [17]. Copyright © 2018, John Wiley & Sons.

Different structural information about the subject material can be obtained from XANES and EXAFS analyses, and typically both are performed to (*i*) gain a deeper understanding of the material properties and (*ii*) validate the conclusions reached by the other complimentary analysis. XANES features (pre-edge peaks and absorption edge position) are dependent on the local coordination environment and effective charge (Z_{eff}) of the absorbing atom, whereas EXAFS oscillations provide information on the geometry of the neighbouring atoms and interatomic distances. Combination of both XANES and EXAFS yields much greater understanding of the material.

The XAS spectra presented in this thesis were all measured in fluorescence mode (**Figure 8B**) on beamline B18 of Diamond Light Source (UK),[18] operating with a ring energy of 3 GeV and at a current of 300 mA. The monochromator comprises Si(111) crystals operating in Quick EXAFS mode. Calibration of the monochromator was carried out using the respective foils prior to the measurements.

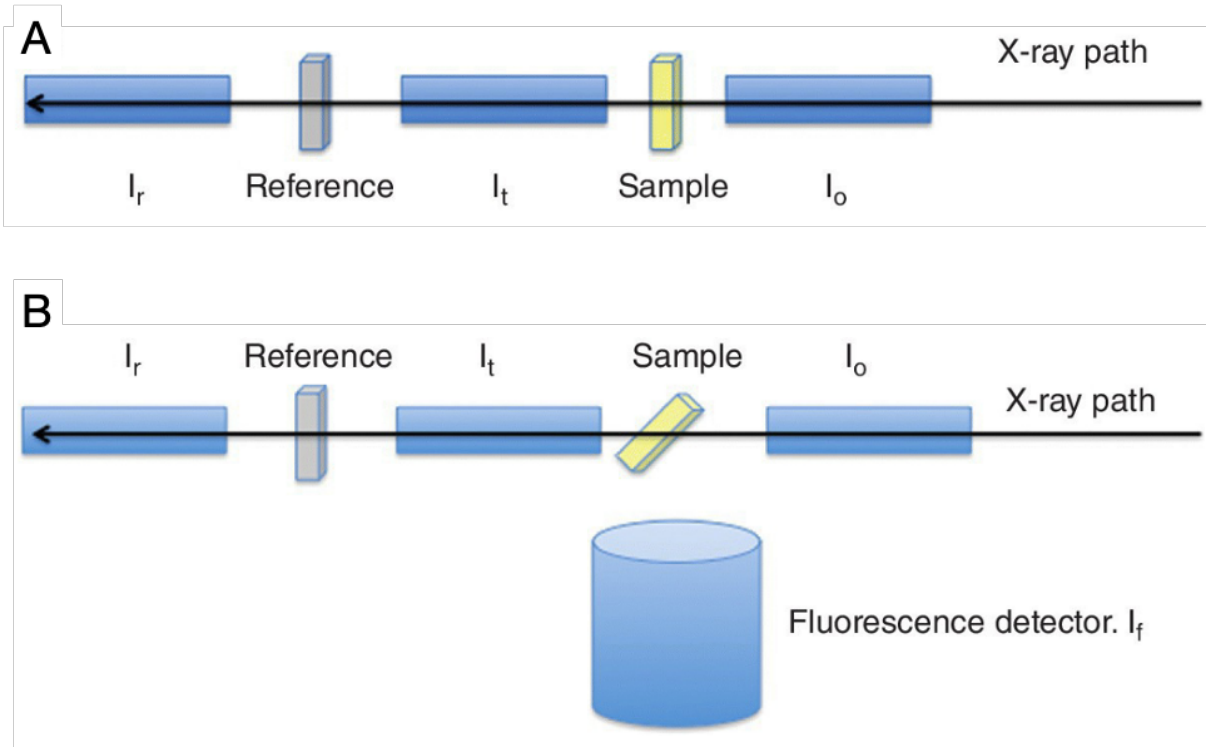

Figure 8. Schematic illustration of XAS signal collection configurations for (A) transmission and (B) fluorescence modes. Adapted from ref.[17]. Copyright © 2018, John Wiley & Sons.

The absorption coefficient energy dependence, $\mu(E)$, is determined for transmission and fluorescence modes, respectively, according to **Equation 3** and **Equation 4**,

$$\mu(E) = \ln {I_0}/{I_t} \tag{3}$$

$$\mu(E) \propto {I_f}/{I_0} \tag{4}$$

where I_f is the intensity of the monitored fluorescence line of the absorber.

During fluorescence XAS measurements the x-rays emitted from the sample not only contain the fluorescence of the absorber of interest, but also fluorescence lines from the rest of the sample in addition to scattered x-rays from the incident beam. However, due to the plane-polarised nature of the incident synchrotron beam, the fluorescence detector is placed perpendicular to the beam path, where the of elastic and Compton scattered x-rays are optimally suppressed (**Figure 8B**).

4.2.2. Electron microscopy

Electron microscopy (EM) techniques have become increasingly important for materials characterisation and to the field of catalysis given the intense focus on nanoparticles and nanostructured materials in recent decades. The advancement in electron microscopes has enabled the imaging of particles and films down to single atomic positions.[19] EM is key particularly to the field of electrocatalysis and materials synthesis because it enables high resolution imaging of the catalyst surface and morphology, which have been shown to be key factors to the activity and selectivity of OER and CO_2RR, comparable to non-destructive atomic force microscopy (AFM) and destructive secondary ion mass spectrometry (SIMS) (**Figure 9**).[19] The high magnification range, coupled with the accessible high image resolution, allows for characterisation at several size scales during a session, being both time and cost efficient. Furthermore, electron microscopes have been developed to be multifunctional. The strong interaction of the high energy electron beam (typically utilising accelerating voltages of 1 – 300 kV) affords spectroscopic analysis opportunities of emitted energy waves in tandem with imaging.[19] However, electron microscopes must be operated under vacuum to negate electron scattering interactions with air and the use of high energy electrons can lead to changes to the subject material via energy transfer. The oxide nanomaterials prepared via cathodic corrosion were characterised by EM.

There are generally two types of electron microscope with differences in the nature of the incident electron beam and the signal detection, as outlined below.

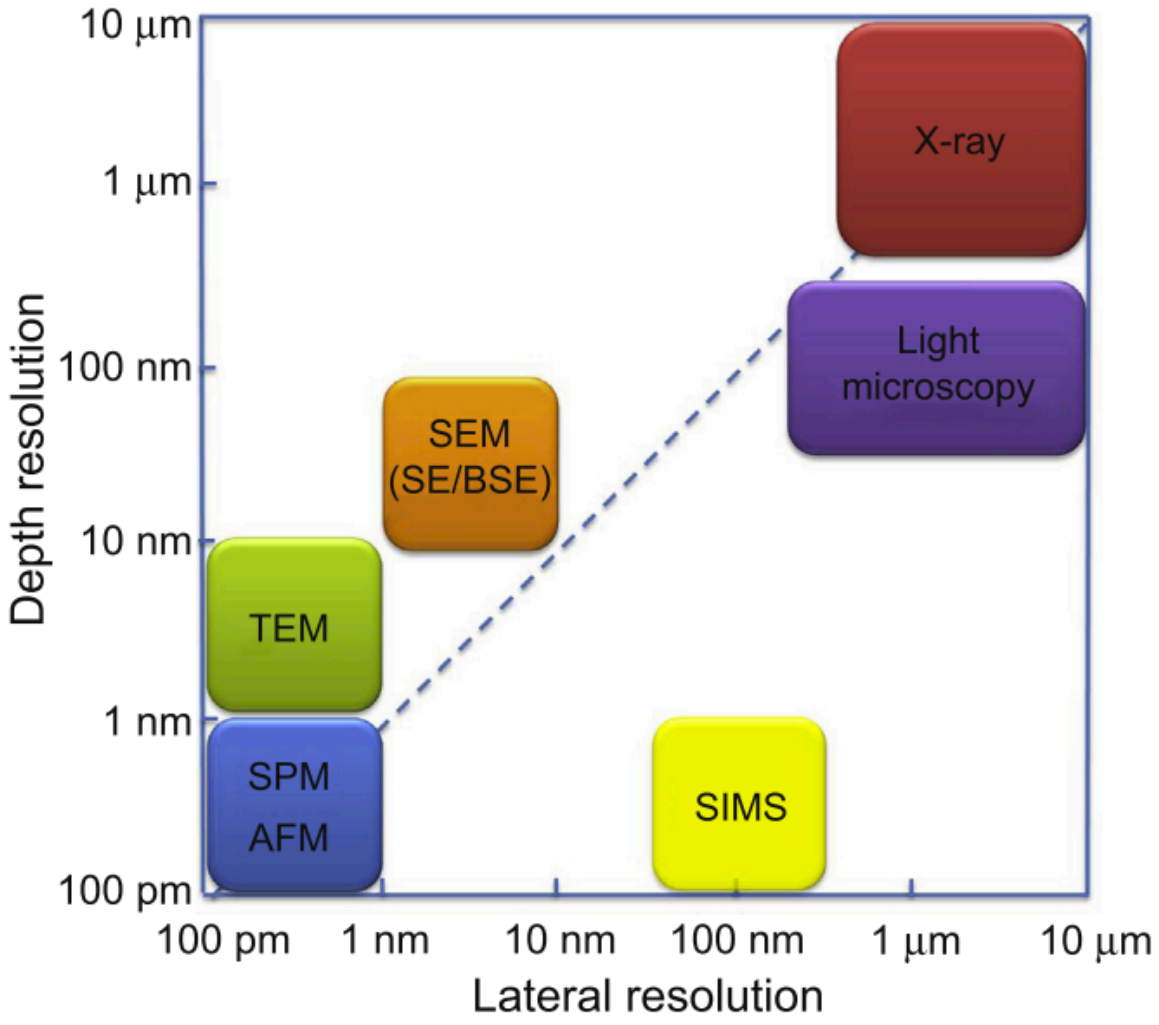

Figure 9. Depth and lateral resolution of various materials imaging techniques. Reprinted from ref.[19]. Copyright © 2016, Elsevier.

4.2.2.1. Scanning electron microscopy (SEM)

SEM is commonly used to image the size and shape, surface morphology and topography of a material. A focused electron beam (typically operating with an accelerating voltage of 1 – 30 kV) is scanned across the material and energy signals emitted from the material are detected in relation to the location of the electron beam (**Figure 10a**). Typically for SEM characterisation, secondary electrons, emitted from the sample following excitation via inelastic scattering events, are detected.[19] The accumulation of these detected electrons of differing energy provides pixel contrast which produces the overall image of the material surface. SEM was utilised in this work for size, shape and morphological characterisation of the as-prepared nanostructured oxides.

Furthermore, inelastic scattering of electrons can lead to the emission of characteristic x-rays from the sample, dependent on the constituent elements. Analogous to XRF, the emitted x-rays can be detected and analysed to quantify the relative atomic and mass ratios of the elements. This technique is called energy dispersive x-ray spectroscopy (EDX).

4.2.2.2. Transmission electron microscopy (TEM)

TEM is often used to image the microstructure of a sample, provided that the sample is thin enough (< 200 μm) to allow for electrons to be transmitted through to the detector (**Figure 10b**); the electron beam is typically generated using an accelerating voltage of 80 – 300 kV.[19] Unlike SEM, this technique employs a spread electron beam with rather than a focused beam. The pixel contrast built up at the detector is affected by the density of the sample. More dense areas do not transmit as many electrons and appear dark, while less dense areas transmit a greater proportion of the electron beam and appear lighter.

For very thin samples (< 100 nm thick) elastic scattering of incident electrons is the dominating electron-matter interaction. Electron diffraction patterns visible at magnifications > 400 k correspond to atom positions, generating high-resolution TEM (HRTEM) images.[19]

4.2.2.3. Scanning transmission electron microscopy (STEM)

As the name suggests, STEM can be considered as a hybrid of the previous two techniques. Like SEM a focused electron beam is scanned across the material, but in this case it is the transmitted electrons that are detected and compiled to produce the image pixels (**Figure 10c**). Like TEM is most effective when imaging a relatively thin sample.

In STEM mode, electrons incoherently scattered through very high angles can be collected using a high angle annular dark field (HAADF) detector affording images with very strong contrast changes due to local changes in *Z*, which can be used to elucidate elemental composition.

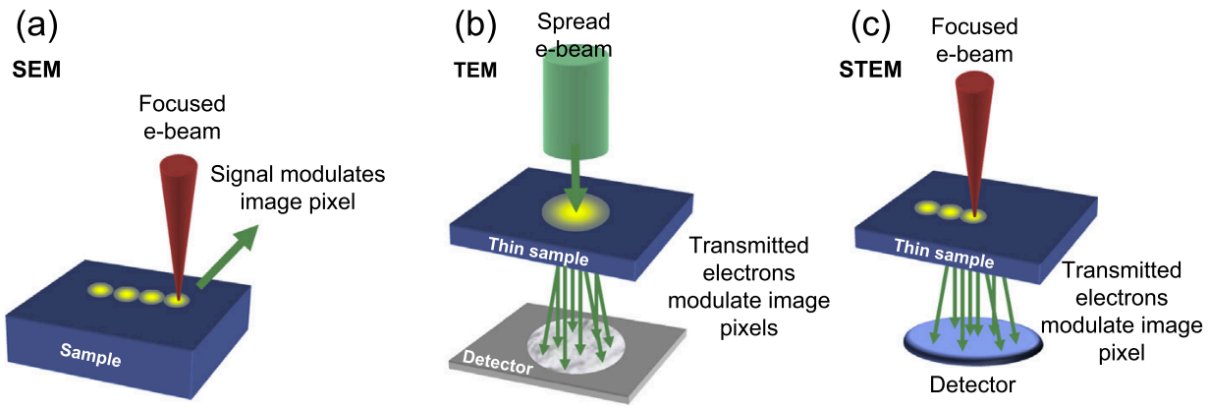

Figure 10. Schematic representation of the difference in electron beam and detection methods utilised in (a) SEM, (b) TEM and (c) STEM. Reprinted from ref. [19]. Copyright © 2016, Elsevier.

4.2.3. UV-visible absorption spectroscopy (UV-vis)

Light absorption of semiconductors is related to the band gap. UV-vis is commonly used when investigating semiconductors for PEC electrochemical applications because it indicates the wavelengths at which a particular semiconductor has greatest light absorption, which can

be used to estimate the band gap of the material; as discussed in **Chapter 1**, oxide semiconductors that absorb in the visible region (380 – 750 nm) are desirable.

4.3. Electrochemical Characterisation

Electrochemistry is the arm of the chemical sciences dedicated to the investigation of chemical changes induced by the movement of charge and the use of chemical reactions to generate electrical energy at the electrode-electrolyte interface.[20] Charge is carried through electrodes by electrons and holes (as described in **Chapter 1**) and by ions in the electrolyte. Generally electrochemical reactions fall under two classifications: inner-sphere and outer-sphere reactions. These concepts were first presented by Henry Taube[21] via the investigation of electron transfer reactions of complex ions in solution and have since been applied to heterogeneous electrode reactions.[22] The differences between the two classes is based on the distances involved in the electron transfer reaction. The reactants, intermediates and products in outer-sphere reactions do not possess strong interactions with the electrode and electron transfer occurs via tunnelling across at least one monolayer of solvent.[22] These reactions are generally independent of the electrode material. The reactants, intermediates and products of heterogeneous inner-sphere reactions are typically specifically adsorbed to the electrode surface and often the reaction is specifically affected by the electrode material.[22] The reactions presented within this thesis are all inner sphere reactions.

As this thesis utilises an alternative format whereby the experimental work presented is from published articles, full experimental details are included therein.

Below the key electrochemical techniques used are outlined.

4.3.1. Cyclic voltammetry (CV)

CV is an electrochemical analytical technique where the current response to a linear change in applied potential between the WE and CE is recorded against the RE over time. The applied

potential and current measurements are performed with a potentiostat. The key parameters that define the CV process are the start, end and switching potentials and the scan rate. The scan rate determines the rate of change in applied potential, with units V s^{-1}.

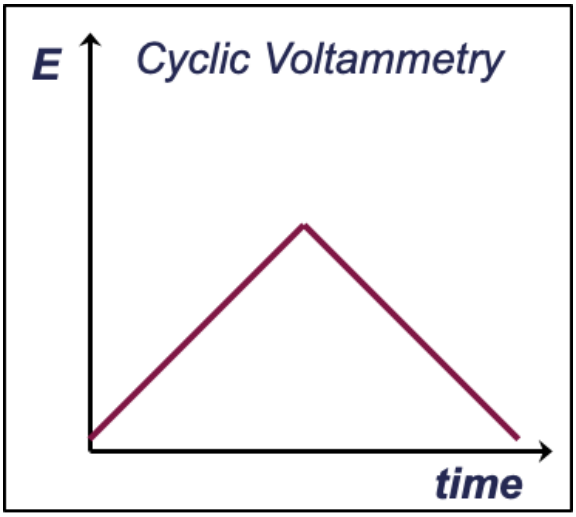

Figure 11. Schematic *E-t* graph showing the linear change in applied potential with time for cyclic voltammetry measurements.

4.3.2. Chronoamperometry

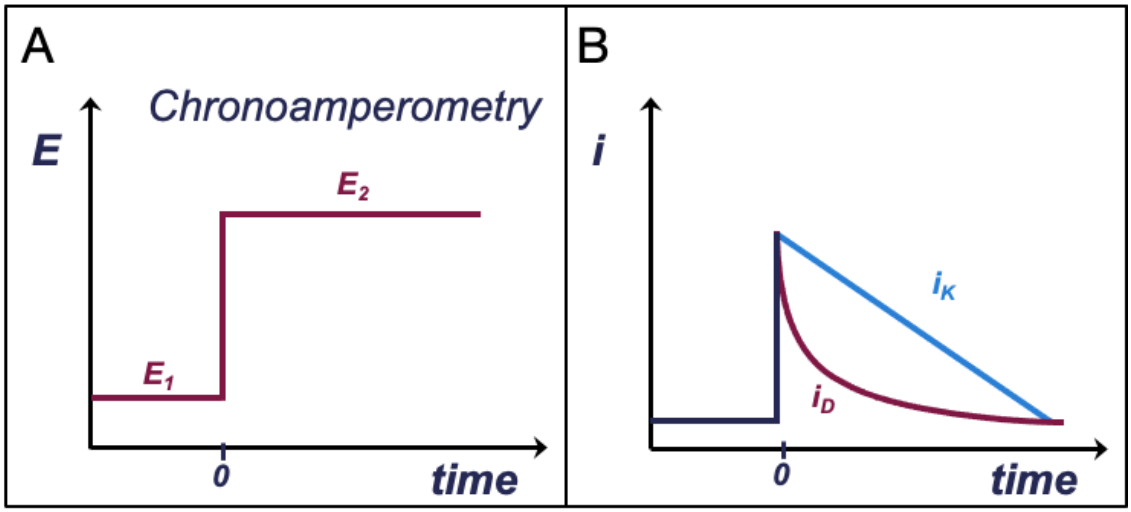

Figure 12. (A) Schematic illustration of the potential waveform (*E-t* graph) utilised during chronoamperometry measurements. A potential step is used to transition from the initial potential (E_1), a potential at which no Faradaic current flows, to the potential at which the electroactive species of interest results in the flow of Faradaic current (E_2). (B) Illustrative current-time (*i-t*) profiles following the potential step for diffusion-controlled (i_D) and kinetically-controlled (i_K) electrochemical processes.

References

1. A. I. Yanson, P. Rodrigez, N. Garcia-Araez, R. V. Mom, F. D. Tichelaar and M. T. M. Koper, *Angew. Chem., Int. Ed.*, 2011, **50**, 6346-6350.

2. A. I. Yanson, P. V. Antonov, P. Rodriguez and M. T. M. Koper, *Electrochim. Acta*, 2013, **112**, 913-918.

3. P. Rodriguez, F. D. Tichelaar, M. T. Koper and A. I. Yanson, *J. Am. Chem. Soc.*, 2011, **133**, 17626-17629.

4. E. Bennett, J. Monzó, J. Humphrey, D. Plana, M. Walker, C. McConville, D. Fermin, A. Yanson and P. Rodriguez, *ACS Catal.*, 2016, **6**, 1533-1539.

5. T. J. Hersbach, A. I. Yanson and M. T. Koper, *Nat. Commun.*, 2016, **7**, 12653.

6. T. J. P. Hersbach, V. A. Mints, F. Calle-Vallejo, A. I. Yanson and M. T. M. Koper, *Faraday Discussions*, 2016, **193**, 207-222.

7. T. J. P. Hersbach, I. T. McCrum, D. Anastasiadou, R. Wever, F. Calle-Vallejo and M. T. M. Koper, *ACS Appl. Mater. Interfaces*, 2018, **10**, 39363-39379.

8. A. I. Yanson and Y. I. Yanson, *Low Temp. Phys.*, 2013, **39**, 312-317.

9. P. Rodriguez, F. D. Tichelaar, M. T. M. Koper and A. I. Yanson, *J. Am. Chem. Soc.*, 2011, **133**, 17626-17629.

10. J. Garcia-Canadas, N. J. Adkins, S. McCain, B. Hauptstein, A. Brew, D. J. Jarvis and G. Min, *ACS Comb. Sci.*, 2016, **18**, 314-319.

11. S. Liu, Ph.D., University of Birmingham, 2017.

12. S. Li, N. J. E. Adkins, S. McCain and M. M. Attallah, *J. Alloys Compd.*, 2018, **768**, 392-398.

13. N. Shamsaei, A. Yadollahi, L. Bian and S. M. Thompson, *Addit. Manuf.*, 2015, **8**, 12-35.

14. E. Margui and R. Van Grieken, *X-Ray Fluorescence Spectrometry and Related Techniques : An Introduction*, Momentum Press, New York, UNITED STATES, 2013.

15. A. Guinier, *X-Ray Diffraction: In Crystals, Imperfect Crystals, and Amorphous Bodies*, Dover Publications, 2013.

16. J. Epp, in *Materials Characterization Using Nondestructive Evaluation (NDE) Methods*, 2016, DOI: 10.1016/b978-0-08-100040-3.00004-3, pp. 81-124.

17. J. Evans, *X-Ray Absorption Spectroscopy for the Chemical and Materials Sciences*, John Wiley & Sons, Incorporated, Newark, UNITED KINGDOM, 2018.

18. A. J. Dent, G. Cibin, S. Ramos, A. D. Smith, S. M. Scott, L. Varandas, M. R. Pearson, N. A. Krumpa, C. P. Jones and P. E. Robbins, *J. Phys.: Conf. Ser.*, 2009, **190**.

19. B. J. Inkson, in *Materials Characterization Using Nondestructive Evaluation (NDE) Methods*, 2016, DOI: 10.1016/b978-0-08-100040-3.00002-x, pp. 17-43.

20. A. J. Bard and L. R. Faulkner, *Electrochemical methods: fundamentals and applications*, Wiley, New York, 2nd edn., 2001.

21. H. Taube, *Electron transfer reactions of complex ions in solution*, London Academic Press, New York, 1970.

22. A. J. Bard, *J. Am. Chem. Soc.*, 2010, **132**, 7559-7567.

Preface to Chapter 5

Format: Published article manuscript.

The formatting of the manuscript and supporting information have been updated in keeping with the style of this thesis. Thus, references and references styles have been updated. Crucially, no changes to the written content of the published article have been made. **Figure 1** has been updated to show the distinction between the 3 metal electrode precursors and mention of the formation of metallic Ti nanoparticles as key intermediates in the formation of the oxides.

Article Information: M. L. Kromer, J. Monzo, M. J. Lawrence, A. Kolodziej, Z. T. Gossage, B. H. Simpson, S. Morandi, A. Yanson, J. Rodriguez-Lopez and P. Rodriguez, *Langmuir*, 2017, **33**, 13295-13302, DOI: 10.1021/acs.langmuir.7b02465. Published by the American Chemical Society.

Overview: Nanoparticle metal oxide photocatalysts are attractive because of their increased reactivity and ease of processing into versatile electrode formats; however, their preparation is cumbersome. We report on the rapid bulk synthesis of photocatalytic nanoparticles with homogeneous shape and size via the cathodic corrosion method, a simple electrochemical approach applied for the first time to the versatile preparation of complex metal oxides. Nanoparticles consisting of tungsten oxide (H_2WO_4) nanoplates, titanium oxide (TiO_2) nanowires, and symmetric star-shaped bismuth vanadate ($BiVO_4$) were prepared conveniently using tungsten, titanium, and vanadium wires as a starting material. Each of the particles were extremely rapid to produce. In addition to the preparation, physical and photoelectrochemical characterisation of the nanomaterials, we probe the ability to effectively tune the particle size of the oxides through controlling cathodic corrosion parameters, in this instance, applied square wave frequency.

All crystalline H_2WO_4 and $BiVO_4$ particles and amorphous TiO_2 were photoelectrochemically active toward the water oxidation reaction. Additionally, the BiVO4 particles showed enhanced photocurrent in the visible region toward the oxidation of a sacrificial sulfite reagent. This synthetic method provides an inexpensive alternative to conventional fabrication techniques and is potentially applicable to a wide variety of metal oxides, making the rapid fabrication of active photocatalysts with controlled crystallinity.

Author Contributions: M.L.K., J.M., A.K. and M.J.L are co-first authors of this article. J.M. and P.R. conducted the initial development of the metal oxide syntheses. J.M. prepared the H_2WO_4, TiO_x and $BiVO_4$ particles and conducted physical characterisation (XRD, XRF, SEM, TEM). A.K. prepared TiO_x and $BiVO_4$ particles. A.K. and P.R. performed AFM measurements. M.J.L. prepared H_2WO_4 particles, performed the frequency-particle size investigations, conducted physical characterisation (SEM and TEM) and contributed significantly to the final revisions of the published manuscript. Photoelectrochemical characterization of the nanoparticles was performed by M.L.K. All authors contributed to the analysis of the results, discussion, writing and revision of the manuscript.

5. High Throughput Preparation of Metal Oxide Nanocrystals by Cathodic Corrosion and their Use as Active Photocatalysts

5.1. Introduction

Water splitting via semiconductor photocatalysts presents a promising means to store solar energy in the form of renewable fuels.[1-3] However, implementing this technology faces important challenges in materials design, engineering, and fabrication. Among the challenges for materials scientists is identifying an inexpensive material that combines excellent visible light absorption, efficient conversion, and long-term stability. The study of the impact of structural parameters on the photocatalytic performance of nano- and microparticles creates opportunities in increasing their efficiency by decreasing charge carrier diffusion lengths and therefore decreasing recombination.[4] Furthermore, the control of surface orientation, particle shape, and particle morphology enables the exploration of emerging chemical properties.[5] The use of photoactive particles also enhances the processability of large-area photoelectrodes by means of their assembly using discrete, well-defined constituent entities.

The widespread use and commercialization of semiconductor photocatalysts requires high-throughput, robust, efficient, safe, and inexpensive fabrication procedures.[6]. To date, the most common ways to prepare photocatalysts for water oxidation are solution based methods such as solvothermal syntheses[7-10] and electrodeposition.[11,12] In the case of solvothermal methods, time consuming synthesis procedures are usually required, and low yields are common. Such methods commonly demand the utilization of organic solvents, surfactants, or capping materials that add complexity and cost. The use of capping agents can also negatively affect the catalytic activity by blocking active sites.[13] In addition, these methods implement high temperature protocols which can result in large particle size

distribution and a lack in control of the surface structure.[9] Solvothermal methods are particularly prevalent in the synthesis of various nanostructured forms of tungsten oxide and titanium dioxide. In one study, this method was employed to prepare tungstic acid hydrate nanotubes without the use of any template, [14] but the synthesis required 12 h of drying at 60ºC.[14]. The solvothermal method has been used to produce TiO_2 nanosheets with preferentially oriented surfaces.[15] This synthesis required the use of hazardous precursors (TiF_4 and HF), and took 5.5-44 h to complete, with a yield of 34.8%.[15] Conversely, electrodeposition methods while offering morphological versatility,[16] suffer from low throughput. Examples of a high degree of morphological control include the use of photolithographic patterning of Cu_2O,[17] and electrodeposition of Si nanowires followed by generation of a catalyst layer.[18] In these cases, a general strategy for applying the synthesis methods to a variety of materials is lacking. A summary of recent methods for the preparation of H_2WO_4, $BiVO_4$ and TiO_2, including synthesis time, advantages and disadvantages is shown in the Supporting Information Table S1. These examples underscore the opportunity for developing methods capable of creating complex photocatalytic materials with high throughput and in a timely manner.

Here we report the utilization of the cathodic corrosion method[19, 20] for the preparation of metal oxide and mixed metal oxide photocatalysts. This method has shown the potential to prepare metal and metal alloy nanoparticles with high morphological homogeneity and well-defined composition.[19-21] Additionally, it has the capability to modulate particle size and shape by means of versatile adjustments of the potential waveform applied to the electrode. An early report demonstrated that the cathodic corrosion method can be used in the preparation of TiO_2 nanoparticles. However, these nanomaterials were used as support for Au nanocatalyst and not directly as a photoactive material.[22] Since the method does not require the utilization of organic solvents, surfactants, or capping ligands, metal nanocatalysts produced through

this method have shown extraordinary catalytic activity.[21] In this report, we take a step forward and demonstrate the utility of cathodic corrosion as a synthetic method to prepare complex oxide nanoparticles of H_2WO_4, TiO_2, and $BiVO_4$ with unprecedented simplicity and particle size homogeneity. All of the syntheses were done on the order of minutes, making this method far superior in terms of time to any of the more commonly used synthetic methods for preparing nanoparticulate photocatalysts. In addition, the control achieved over the crystallinity of the H_2WO_4 nanoparticles is indicative that such control could be also achieved on other metal oxides by changing electronic parameters such as amplitude or frequency of the AC wave, or by changing chemical parameters such as concentration or nature of the cation.

5.2. Experimental

Synthesis and Characterization of Particles

The method by which these particles were synthesized is summarized in Figure 1. For the synthesis of H_2WO_4 particles, 2.5 mm of a tungsten wire (diameter of 0.127 mm, Rembar Co. LLC, USA) was submerged in a 1 M solution of $KHSO_4$. A square wave voltage in the range of 0 V to -10 V was applied between a W wire (working electrode) and a high surface area Pt foil (counter electrode) resulting in the instantaneous formation of the nanoparticles. The TiO_2 nanowires were prepared with a 0.2 mm diameter titanium wire that was subjected to an AC square wave in the range of 0 V to -10 V with a frequency of 100 Hz while immersed in a 10 M NaOH solution. The $BiVO_4$ nanoparticles were synthesized using a vanadium wire with diameter of 0.15 mm (99.8 % Alfa Aesar). This wire was immersed in 10 mL of a mixture (1:1 by volume) of saturated $CaCl_2$ solution and MilliQ water (Elga, 18.2 MΩ cm, 1 ppb total organic carbon), in which 750 µL of a saturated Bi_2O_3 solution was subsequently added. The synthesis was successfully achieved by applying a square wave voltage in a range of -8 V to 2 V. In each of the syntheses, current and time was monitored using a National Instruments DAQ module (NI-6211). Once synthesized, the resulting suspensions of nanoparticles were centrifuged at 3000 rpm for 20 minutes and suspended in ElgaPure water to remove the excess electrolyte. UV-vis spectroscopy was employed to elucidate species present in $KHSO_4$ solution immediately after cathodic corrosion of W wire and in the resultant supernatant solution after centrifugation at 4000 RPM for 3 minutes, using a Varian Cary 50 UV-Vis Spectrophotometer.

The crystal structures of the prepared particles were determined using a BRUKER D2 Phaser powder X-ray diffractometer operating at 30 kV, 10 mA and a Co-Kα (0.179 nm) radiation source. The X-ray diffraction (XRD) data are reported on a 2θ angle scale of a Co-Kα radiation source for an appropriate comparison with values from the JCPDS database. The samples

were prepared by depositing 25 µL of the aqueous nanoparticle suspensions on a zero background SiO (MTI) holder and dried under air atmosphere.

The particle size distribution and shape of the particles were determined by transmission electron microscopy (TEM) using a JEOL JEM 1200 EX MKI instrument and the particle thickness was determined by contact mode atomic force microscopy (AFM), obtained under ambient pressure and temperature conditions, using an AFM microscope Veeco metrology, equipped with a NanoScope IIIa controller and using a 200 µm cantilever with a pyramidal silicon nitride tip (spring constant 0.12 Nm^{-2}). Compositional analysis was determined by X-ray fluorescence (XRF) using a Bruker S8 Tiger 4 kW spectrometer under a helium atmosphere. The particle morphology and composition was confirmed by scanning electron microscopy (SEM) in a JEOL 2100 Scanning electron microscope instrument coupled with energy dispersive X-ray spectroscopy (EDX).

Photoelectrochemical Measurements

In order to study the photoactivity of the particles, they were first integrated into a photoelectrode. The suspended particles were drop cast in volumes of 20 µL onto an indium tin oxide (ITO) cover slip (SPI Instruments 15-30 Ω). Next, 100 µL of 5 wt% Nafion® perfluorinated resin solution (Sigma Aldrich) were spun-cast onto the particles at 1200 rpm for 3 minutes to prevent the particles from detaching from the ITO when immersed in solution. Electrical connection was made to the ITO slide by using copper tape (3M Electrical Products). In the case of $BiVO_4$, particles were drop cast as 3 layers of 20 µL to increase the overall particle concentration on the surface of the ITO cover slip. The photoelectrochemical measurements were carried out in a custom made 3 mL Teflon cell and the potential of the photoelectrodes was controlled via either CHI760E or 920D workstations (CHI Instruments) in a three-electrode setup. The reference electrode used was a Ag/AgCl (3M KCl) with a $NaClO_4$ agar salt bridge and all potentials reported are versus Ag/AgCl unless otherwise

stated. The counter electrode was 1 mm diameter Pt wire. All measurements were performed in 0.1 M NaOH under illumination from a 6258 Oriel Xe lamp. Incident photon-to-electron conversion efficiency (IPCE) spectra were taken by filtering this source using a Newport Oriel 1/8m Cornerstone monochromator.

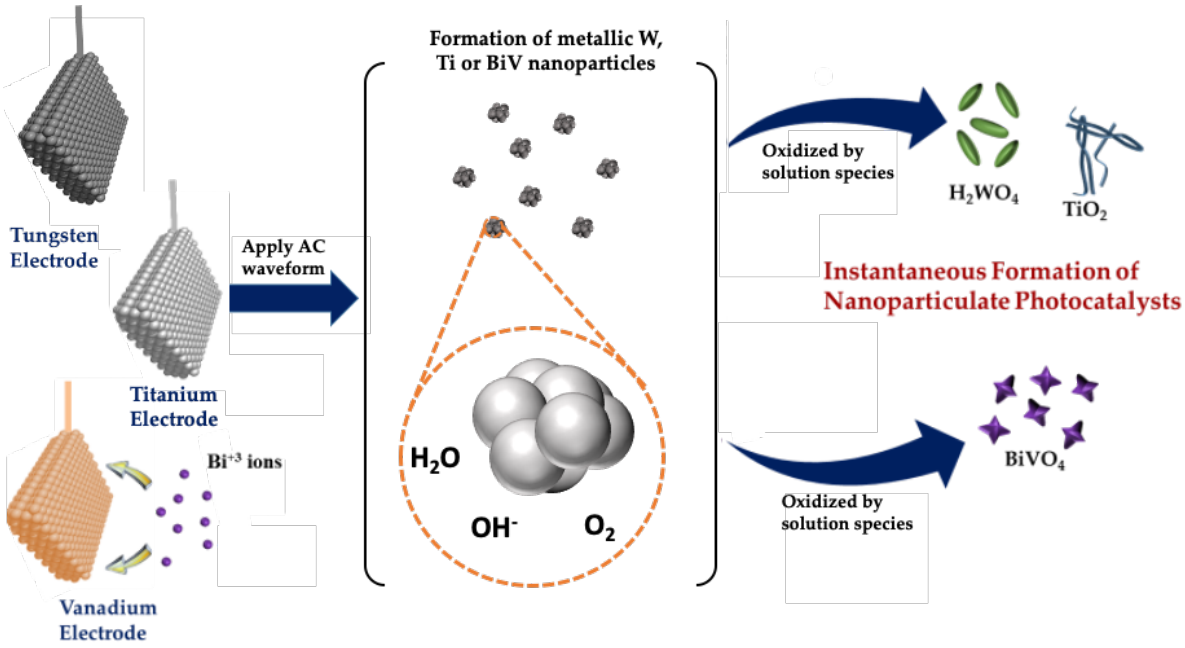

Figure 1. Schematic depicting how cathodic corrosion was used to prepare H_2WO_4, TiO_2, and $BiVO_4$ photocatalysts.

5.3. Results and Discussion

The reaction mechanism of the cathodic corrosion method for the formation of the nanoparticles proceeds via the formation of the metal anion stabilized by the cations, rather than the protons, present in the solution. In order to confirm this reaction mechanism in the formation of the tungsten nanoparticles via cathodic corrosion, a tungsten wire was immersed in a solution of 0.1 M H_2SO_4 and a AC wave form between 0 and -10 V with a frequency of 100 Hz was applied during 120 s. Under these conditions, only hydrogen evolution was observed. In contrast, when the same AC wave form conditions were applied in a solution containing 1 M $KHSO_4$, the reaction resulted in an aqueous nanoparticle dispersion. Given that the electrochemical conditions are identical and the pH in both solutions is similar, we

conclude that the presence of the metal cation is requisite for the formation of the nanoparticles and therefore the cathodic corrosion is the dominant reaction mechanism. Furthermore, we propose that the formation of metallic tungsten nanoparticles proceed via the formation of an anion intermediate stabilized by the cation in solution and the oxidation of these intermediates to tungsten nanoparticles. The tungsten nanoparticles are prompt to oxidation in water,[23] resulting in the formation of WO_2 and subsequently to WO_3 and H_2WO_4.[24] In a similar fashion, previous work has shown the synthesis of SnO_2 nanoparticles via a two-step process involving the cathodic corrosion.[25] We propose that the formation of $BiVO_4$ nanoparticles proceeds via the formation of a multimetallic anion intermediate $(BiV)^{-n}$ on the surface of the vanadium upon the reduction of the Bi^{+3} similar to the reaction mechanism proposed for the formation of PtBi nanoparticles.[21] However, we do not discard the possibility that the positive potential applied during the square wave program may influence the reaction mechanism and final geometry of the nanoparticles.

We analysed a freshly-prepared solution and its supernatant via UV-Vis in order to discard the presence of ionic W species. As can be seen in Figure S1, the spectra of the freshly prepared solution shows one broad adsorption band between 200 nm and 400 nm, associated to the presence of WO_2/WO_3 colloidal nanoparticles. After the nanoparticles were centrifuged, the supernatant did not show any adsorption band. Therefore, the presence of dissolved cationic tungsten species was discarded.

5.3.1. Morphological Characterization

After the synthesis of the nanoparticles of H_2WO_4 and $BiVO_4$ by cathodic corrosion, their crystal structure, composition, and particle size were studied by XRD, SEM-EDX, and TEM, as shown in Figure 2 and by XRF, as shown in Figure S3. XRD patterns for representative H_2WO_4 particles obtained at a frequency of 100 Hz are shown in Figure 2A. The 2θ angle at 14.8° indicates a preferential orientation along the (010) plane (JCPDS no. 18-1420). In the

case of H_2WO_4, a colloidal suspension was always observed after cathodic corrosion, although the XRD pattern exhibited an evolution in time, as shown in Figure S2. The SEM and TEM images of the H_2WO_4 show the presence of H_2WO_4 nanorods/nanoplates with homogenous size and consistent shape (Figure 2B). The particle size distribution (Figure S4) was found to be 2.7 ± 0.2 μm in length and 0.5 ± 0.1 μm in width. In addition to the particle size obtained by TEM and SEM measurements, the AFM measurements (Figure S5) have shown that the H_2WO_4 nanoparticles have 61±10 nm height. One of the most interesting aspects that we found for the cathodic corrosion synthesis of H_2WO_4 was its versatility for controlling the size and shape of the particles. Even though, the control on the size and shape has been probed for the synthesis of platinum nanoparticles,[26, 27] the control of the size and shape of metal oxides open a new dimension of application of these materials. Until now, such control was limited by the application of high temperatures during the synthesis protocol and due to harsh conditions used to clean the capping materials and surfactants. As shown in Figure 3, the shape and size of the nanoparticles was tuned by simply changing the frequency of the square wave voltage. Choosing this external input allows us to change the size of the H_2WO_4 nanorods by an order of magnitude from hundreds of nanometers to few microns (Figure 3).

Figure 2C shows the X-ray pattern of the $BiVO_4$ nanoparticles which indicates the presence of (040) preferential orientation (JCPDS no. 14-0688). The SEM and TEM images show star-like shape nanoparticles with homogenous size of 1.1 ± 0.1 μm. The AFM cross section of the $BiVO_4$ nanoparticles (Figure S6) shows that the particles are 35 ± 12 nm height. The composition of the $BiVO_4$ nanoparticles was confirmed by XRF and EDX analysis (Figure S4). Synthesis of $BiVO_4$ has demonstrated the capabilities of the cathodic corrosion method to prepare complex oxides by the addition of solution-phase components in the synthesis media. Future work will contemplate the control of the particle size, shape and composition

as a function of chemical and electrochemical parameters such as amplitude and cation concentration. Although it is difficult to estimate the Faradaic yield for any of the samples prepared, the obtained powders exhibited only slight amounts of the V_2O_5 phase, displaying largely the correct crystal structure for $BiVO_4$.[28, 29] Finally, the characterization by TEM of the TiO_2 nanoparticles is presented in Figure 4. The size of the TiO_2 nanowires was approximately 500-800 nm in length and 4-8 nm in diameter. Despite the morphological conservation among the TiO_2 nanowires, there was no periodic crystal structure which resulted in the absence of any XRD pattern.

Under the conditions presented here, the rate of formation of particles was the highest for the H_2WO_4, taking ~60–100 s to etch 2.5 mm of wire (Figure S6). The $BiVO_4$ took a similar time of 100–160 s to etch 2.5 mm of wire, and the TiO_2 took a longer time of 250–320 s to also etch the same amount of wire. The nanoparticles were collected by centrifugation, as described in the Experimental Section, after etching 5–7.5 mm of the wires and we observed that quantities on the order of milligrams could be produced from all samples. Yields of 38 ± 9%, 61 ± 7%, and 66 ± 10% have been achieved for H_2WO_4, $BiVO_4$, and TiO_2. Losses in mass of the nanoparticles take place during the synthesis process by attachment of the nanoparticles to the counter electrode and during the process of centrifugation and removal of the excess of electrolyte. It has been also observed that TiO_2 nanoparticles lack stability in concentrated NaOH solution; therefore, a quick washing procedure is required to avoid major losses due to dissolution of the TiO_2 nanoparticles.

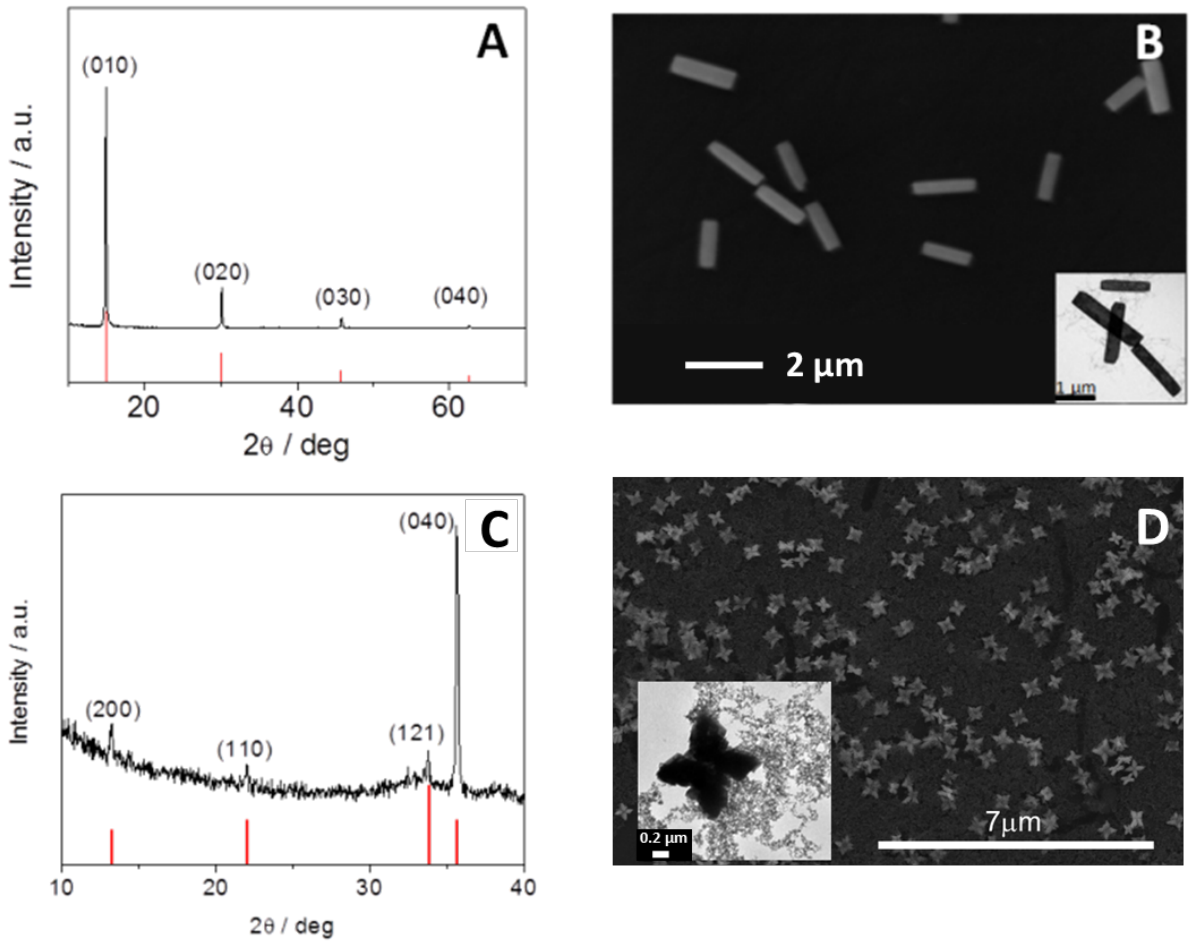

Figure 2. X-ray diffraction patterns and SEM images of (A, B) H_2WO_4 and (C, D) $BiVO_4$. The insets on the SEM images correspond to the high magnification TEM images of the nanoparticles.

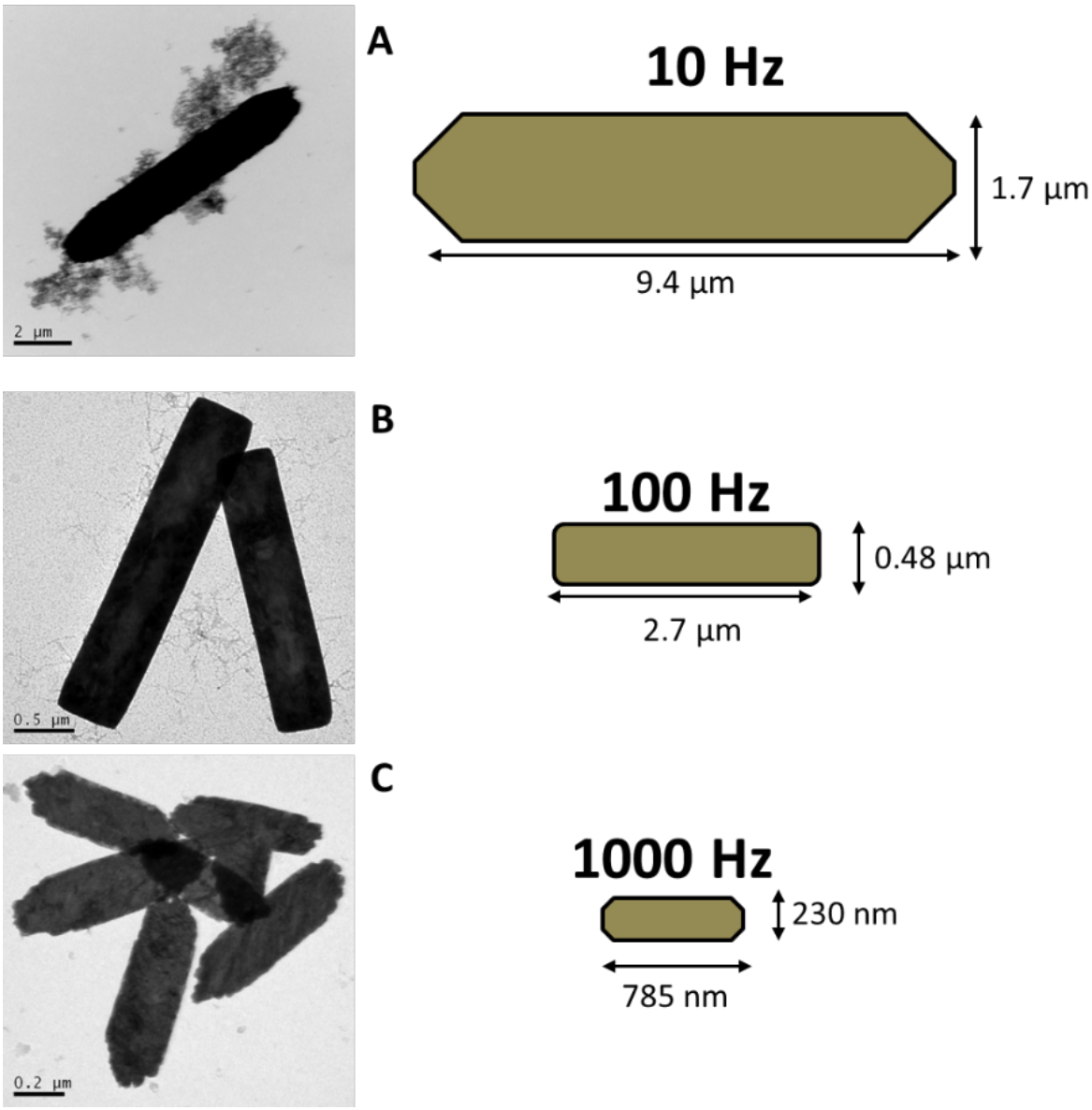

Figure 3. TEM images and schematic of the H_2WO_4 particles prepared by cathodic corrosion in a 1 M solution of $KHSO_4$ with a square wave voltage between 0 V to -10 V and different frequencies (A) 10 Hz, (B) 100 Hz and (C) 1000 Hz.

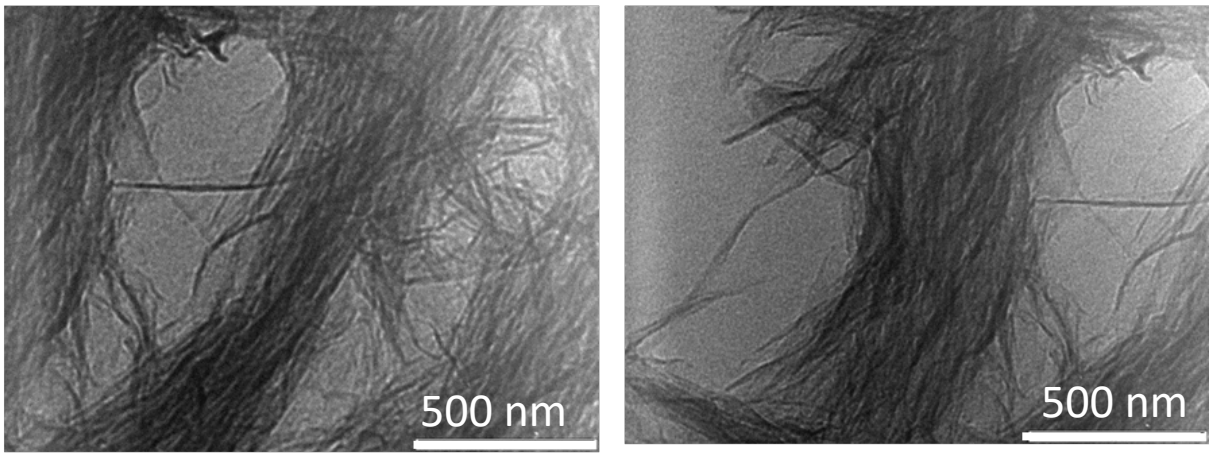

Figure 4. TEM of TiO_2 nanoparticles prepared by cathodic corrosion from a Ti wire in a 10 M NaOH solution using an AC square wave between -10 and 0 V with 100Hz frequency.

Because of the different synthesis conditions and varying sizes of the metal wires, it is difficult to draw comparisons between each of the nanoparticles. Despite the successful preparation of oxide particles from various parent metals, there are several aspects yet to be understood about the cathodic corrosion method applied to these samples, including the etching time and its relationship with the resulting particle size and crystallinity of the sample. We propose that the changes in size and shape of the H_2WO_4 particles are influenced by the concentration of intermediate species (anionic and/or metallic) in solution. This intermediate species concentration is modified by changes in the frequency and amplitude of the applied waveform, as well as by the stabilizing cation concentration in solution (here, K^+). Similar changes in size and shape were also observed during the formation of Pt, Au and Rh nanoparticles as a function of these factors.[26, 27, 30] Furthermore, it is plausible that the kinetics of nanoparticle oxidation ($W \rightarrow WO_x$) will be affected by the size of the particles generated after cathodic corrosion.[23] In addition, other factors such as changes in zeta potential may occur. Therefore, we postulate that differences in nanoparticle shape and size are induced by chemical processes that take place after the electrochemical etching step, but that nonetheless are a product of the chosen cathodic corrosion parameters.

Other than the frequency of the waveform, we are currently investigating other parameters that govern the etching time, size, shape, and composition of the particles. Currently our groups are studying the effect of electrolyte composition and potential thresholds during cathodic corrosion on particle size and shape and this will be subject of a forthcoming publication.

5.3.2. Electrochemical Characterization

We now turn to evaluate the photoelectrochemical reactivity of the obtained particles. Chopped light linear sweep voltammetry was used to determine the relative activation of the particles towards water oxidation and is shown in Figures 5A and 5B. Due to the relatively low surface coverage and the Nafion® partially covering some of the particles, the photocurrent density scale is fairly low for the H_2WO_4/ITO, $BiVO_4$/ITO, and TiO_2/ITO electrodes. However, as a reference point unsintered semiconductor particle films yield photocurrents on the order of $\mu A\ cm^{-2}$.[31] The H_2WO_4 and TiO_2 particles, prepared with a square wave function at 100 Hz, yielded photocurrent values on the same order of magnitude, and the $BiVO_4$ resulted in the lowest activity. The photocurrent shown by TiO_2 nanowires, despite having no defined crystal structure, is strongly suggestive of a mixture of photoactive crystal domains. As stated earlier, the crystallinity of nanoparticles may be dependent on the rate of corrosion, and if so, then we hypothesize that highly crystalline TiO_2 photocatalysts can also be prepared. Despite the higher crystallinity of the obtained samples for $BiVO_4$, its low activity toward water oxidation has been well-documented,[32, 33] where the addition of Na_2SO_3 acting as a hole scavenger improved the current magnitude significantly. As shown in Figure 5C, the presence of Na_2SO_3 increased the photocurrent of $BiVO_4$ to be comparable to the H_2WO_4 nanoparticles and TiO_2 nanowires. This demonstrates that these photocatalysts all possess relatively similar activity so long as they are carrying out a kinetically facile reaction – sulfite oxidation in the case of $BiVO_4$. We have successfully demonstrated the preparation of photoactive $BiVO_4$ particles

through cathodic corrosion, but the challenge remains to fabricate $BiVO_4$ that is highly active toward water splitting. This will most likely be enabled through the inclusion of dopants in solution during the synthesis that are known to enhance the adsorption and interfacial charge transfer kinetics between $BiVO_4$ and H_2O to form O_2.[34, 35]

Chronoamperometry of H_2WO_4 and $BiVO_4$ nanoparticles was utilized to investigate the presence of transient processes upon illumination. In the case of H_2WO_4, there is an initial decrease in current under illumination at high activation (Figure 6A). This decrease in current is likely due to charge recombination in the H_2WO_4 particles. This current transient is not observed for $BiVO_4$ and is likely due to the size difference between the particles. The H_2WO_4 particles are larger than the $BiVO_4$, which results in longer distances for holes to reach the surface. Since the $BiVO_4$ particles are much smaller than the H_2WO_4 particles, there is no observable charge recombination occurring. While seemingly detrimental to photocatalyst performance, this recombination is not too concerning since it only occurred at large applied biases. We tested the spectral response of the obtained particles. Figure 6C shows the chopped chronoamperometry with the $BiVO_4$ particles under illumination through a 405 nm cutoff filter. We observed that the $BiVO_4$ retained about half of the current density when only illuminated with visible light. Chopped chronoamperometry under visible light was also collected for the H_2WO_4 particles, but large activity was not observed (Figure S8) due to the relatively small amount of visible light that H_2WO_4 can be expected to absorb. We hypothesize that cathodic corrosion could also be used to incorporate dopants for increasing the visible light response of the resulting nanoparticles. Certain dopants have already been shown in the literature to red shift the band edge of WO_3,[36-38] and could bolster the visible activity of H_2WO_4 particles.

Because crystalline $BiVO_4$ and H_2WO_4 particles absorb some portion of visible light, an IPCE spectrum was obtained for each to determine the wavelength cutoff of their band edges

(Figure 7). A spectrum was acquired for each in the presence and absence of Na_2SO_3, which acted as a hole scavenger. The IPCE spectra for the H_2WO_4/ITO shows a cutoff around 440 nm, which is similar to what is expected for an electrodeposited film of H_2WO_4.[12,39] It also shows very slight differences in the presence of a hole scavenger, thus suggesting that interfacial charge transfer is not limiting in these particles. Additionally, the IPCE for H_2WO_4 shows a marked increase from 550 nm to 650 nm, which may be due to the presence of defects in the crystal structure. These defects reside at an energy in between the conduction and valence band, which results in electrons occupying these states to be excited by longer wavelengths of light.[40, 41] In the absence of a hole scavenger, a poor IPCE spectrum was obtained for $BiVO_4$, which is due to very slow reaction kinetics to carry out water oxidation. In contrast, upon addition of Na_2SO_3, the IPCE for the $BiVO_4$ particles showed a band edge around 510 nm, which corresponds well with what has been reported in the literature.[28, 29] Altogether these measurements confirm the ability of the cathodic corrosion method to yield photoactive metal oxides with unique morphologies using a simple synthetic approach.

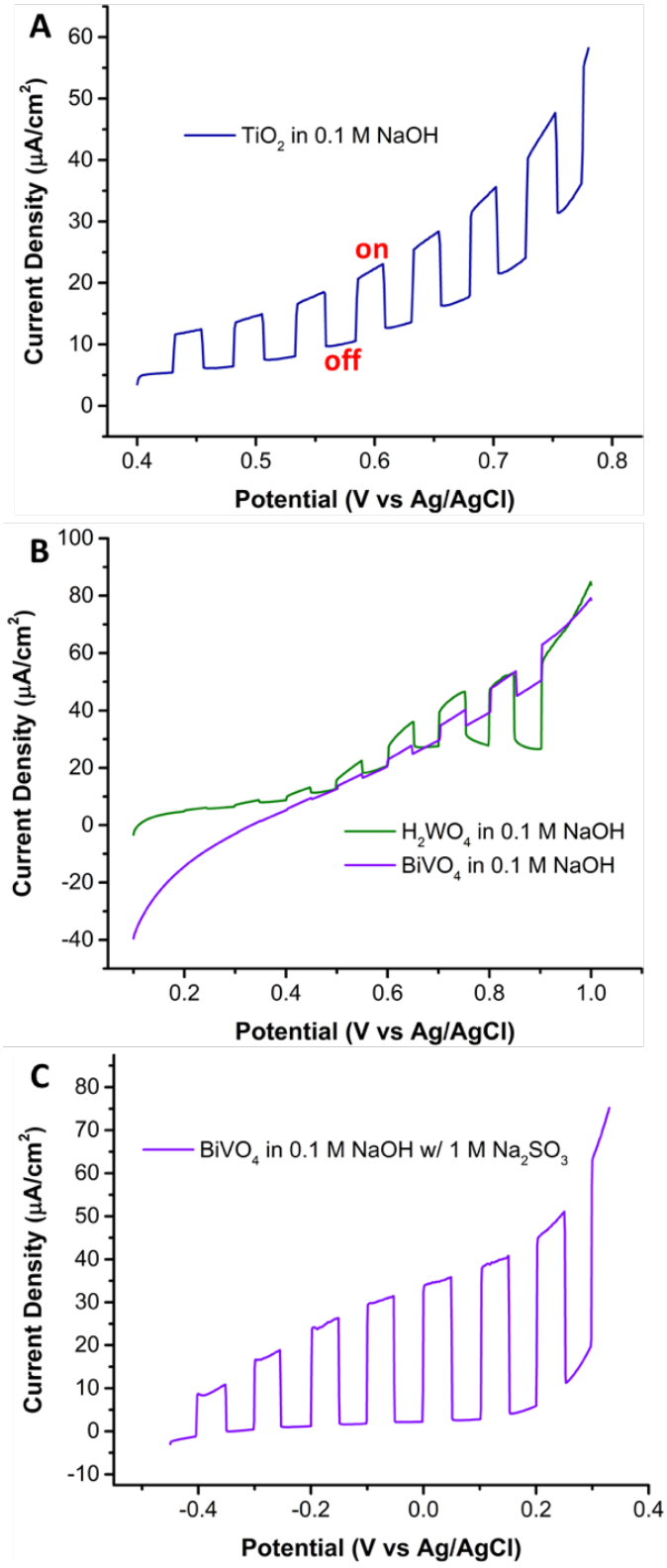

Figure 5. Chopped light linear sweep voltammograms of the nanoparticulate photocatalysts prepared through cathodic corrosion. A) Linear sweep voltammogram for TiO_2 in 0.1 M NaOH. B) Linear sweep voltammogram for the 100 Hz H_2WO_4 and $BiVO_4$ particles in 0.1 M NaOH. C) The same experiment shown in A repeated for $BiVO_4$ in 1 M Na_2SO_3.

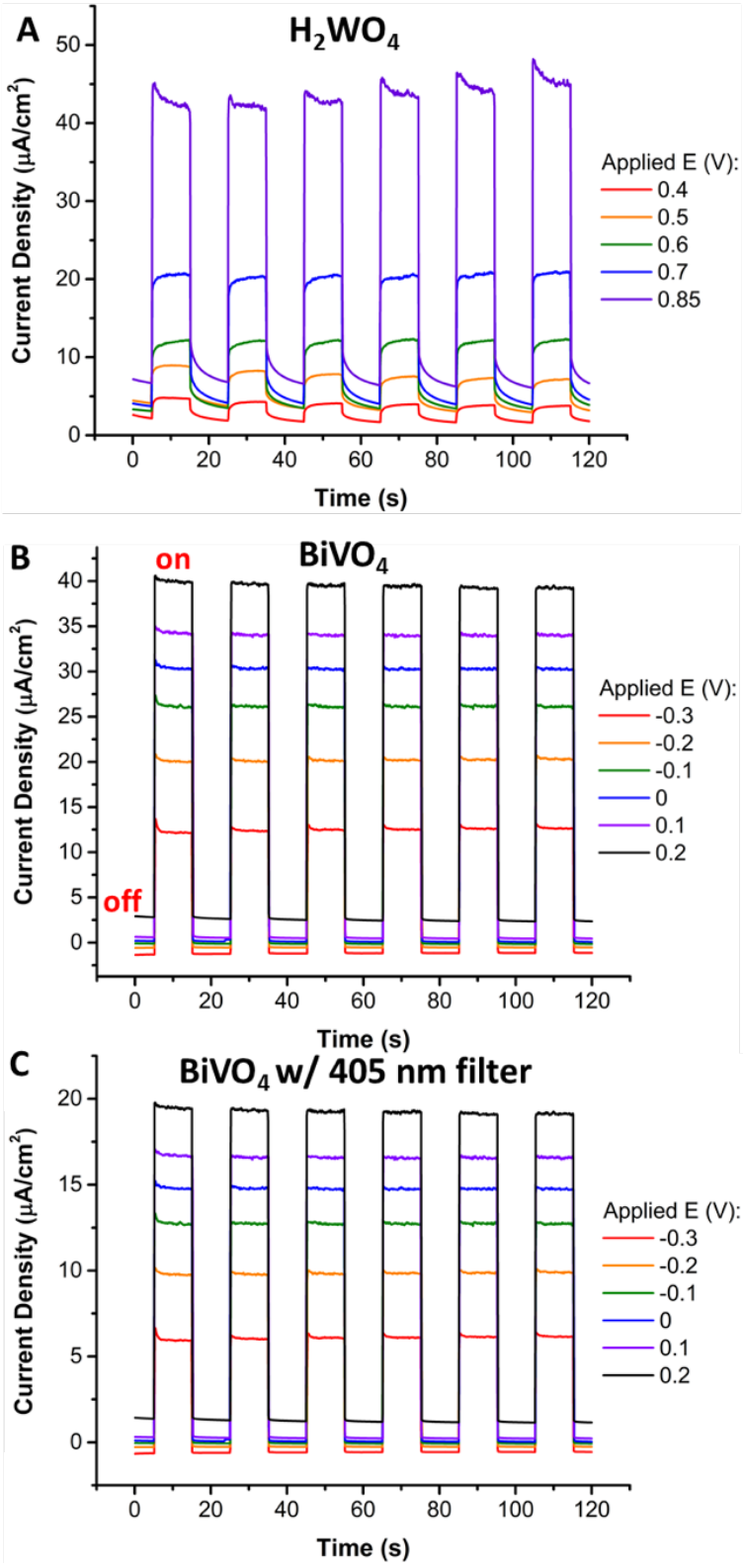

Figure 6. Photocurrent as a function of potential for the H_2WO_4 (A) and $BiVO_4$ (B) particles, respectively, prepared via cathodic corrosion. The chronoamperometry in (C) is the same $BiVO_4$ particles being illuminated with only visible light. Measurements were taken in 1 M Na_2SO_3 for $BiVO_4$ and 0.1 M NaOH for H_2WO_4 and both were illuminated with 60 mW/cm^2 for the chronoamperometry experiments.

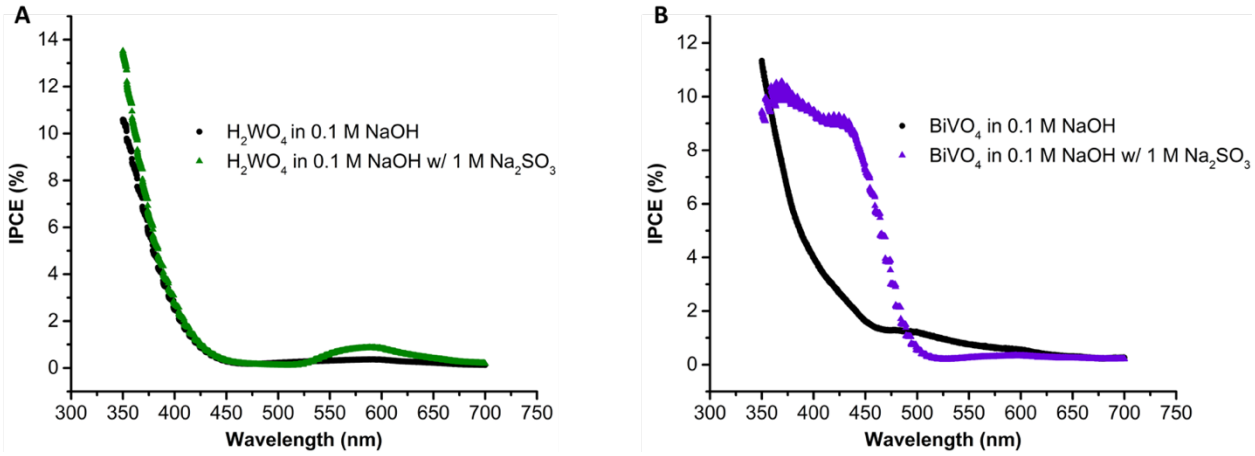

Figure 7. IPCE spectra for the H_2WO_4 (A) and $BiVO_4$ (B) particles depicting an appropriate band edge for each. Measurements were taken in 0.1 M NaOH with and without 1 M Na_2SO_3.

5.4. Conclusions

We show for the first time the application of cathodic corrosion to produce metal oxides and mixed metal oxide nanoparticles with an outstanding homogeneity of particle size and shape. All of the particles studied here were made on the order of minutes, which greatly improves upon standard photocatalyst nanoparticle synthesis procedures. Amorphous TiO_2, and crystalline H_2WO_4 and $BiVO_4$ nanoparticles were prepared with preferential crystallographic orientation starting from the base metal as the reactant. In all cases, we observed the successful incorporation of oxygen the lattice as confirmed via XRD and EDX. We also illustrated for H_2WO_4 that the frequency of the excitation waveform can greatly impact the particle size. The cathodic corrosion method can be very easily modified to produce particles with a variety of sizes. In addition, the successful preparation of $BiVO_4$ underscores the exciting possibilities for the synthesis of multi-metallic oxides and the incorporation of dopants using simple solution precursors. Although the TiO_2 did not possess a high degree of crystallinity, it was nonetheless photoactive toward water oxidation. The H_2WO_4 and $BiVO_4$ both were crystalline, and H_2WO_4 carried out water oxidation under illumination. The $BiVO_4$ prepared with cathodic corrosion was not able to appreciably carry out water splitting but

displayed facile conversion of sulfite under both UV-vis and visible only illumination. This ability for $BiVO_4$ to effectively facilitate photochemical oxidation of sulfite under only visible light was displayed through chopped light chronoamperometry and the obtained IPCE spectrum. Future work will investigate alternatives to adhering particles to a surface that do not alter morphology or crystal orientation.[42, 43]

We demonstrated the potential of the cathodic corrosion method for the straightforward synthesis of particles with well-defined morphology and composition. This creates opportunity in the low-cost production of large quantities of processable particles that can streamline the preparation of efficient electrodes for photocatalysis. The cathodic corrosion method is prompt for industrial scale up: the method avoids large volumes of organic solvents and the ensuing large investments in heating and cleaning treatment and safety and disposal issues. Finally, the time of synthesis of the catalyst is an important parameter to consider for further industrial applications. While other methods might require several hours or days of preparations, we have shown the time-effectiveness of the method to prepare particles in minutes. There is still much work to be done toward the effect that various parameters such as etching time or solution composition have on the resulting particles. Despite this, cathodic corrosion was shown here to be a facile alternative method for producing metal oxide nanoparticles.

Acknowledgements

We acknowledge support from the Transatlantic Collaboration Fund and the BRIDGE program between the University of Illinois and the University of Birmingham. P.R. acknowledges the University of Birmingham for the financial support through the Birmingham fellowship program. J.M., M.J.L., and A.K. acknowledge the University of Birmingham for financial support through PhD scholarships at the School of Chemistry.

References

1. M. Gratzel, Nature, 2001, 414, 338-344.

2. J. R. Bolton, Solar Energy, 1996, 57, 37-50.

3. D. Gust, T. A. Moore and A. L. Moore, Acc. Chem. Res., 2009, 42, 1890-1898.

4. R. Memming, Electron Transfer I, 1994, 169, 105-181.

5. D. Li and H. Haneda, Chemosphere, 2003, 51, 129-137.

6. N. S. Lewis, Science, 2016, 351, aad1920.

7. H. G. Choi, Y. H. Jung and D. K. Kim, J. Am. Ceram. Soc., 2005, 88, 1684-1686.

8. Z. H. Jiao, J. M. Wang, L. Ke, X. W. Sun and H. V. Demir, ACS Appl. Mater. Interfaces, 2011, 3, 229-236.

9. M. R. Waller, T. K. Townsend, J. Zhao, E. M. Sabio, R. L. Chamousis, N. D. Browning and F. E. Osterloh, Chem. Mater., 2012, 24, 698-704.

10. K. Lee, W. S. Seo and J. T. Park, J Am Chem Soc, 2003, 125, 3408-3409.

11. S. H. Baeck, T. Jaramillo, G. D. Stucky and E. W. McFarland, Nano Lett., 2002, 2, 831-834.

12. L. Su, L. Zhang, J. Fang, M. Xu and Z. Lu, Sol. Energy Mater. Sol. Cells, 1999, 58, 133-140.

13. C. Kim and H. Lee, Catal. Commun., 2009, 10, 1305-1309.

14. Z. G. Zhao and M. Miyauchi, Angew. Chem., Int. Ed., 2008, 47, 7051-7055.

15. H. G. Yang, G. Liu, S. Z. Qiao, C. H. Sun, Y. G. Jin, S. C. Smith, J. Zou, H. M. Cheng and G. Q. Lu, J. Am. Chem. Soc., 2009, 131, 4078-4083.

16. M. J. Siegfried and K. S. Choi, J. Am. Chem. Soc., 2006, 128, 10356-10357.

17. A. W. Maijenburg, A. N. Hattori, M. De Respinis, C. M. McShane, K. S. Choi, B. Dam, H. Tanaka and J. E. ten Elshof, ACS Appl. Mater. Interfaces, 2013, 5, 10938-10945.

18. L. Y. Ma, S. Lee, J. DeMuth and S. Maldonado, RSC Adv., 2016, 6, 78818-78825.

19. A. I. Yanson, P. Rodriguez, N. Garcia-Araez, R. V. Mom, F. D. Tichelaar and M. T. M. Koper, Angew. Chem., Int. Ed., 2011, 50, 6346-6350.

20. P. Rodriguez, F. D. Tichelaar, M. T. M. Koper and A. I. Yanson, J. Am. Chem. Soc., 2011, 133, 17626-17629.

21. E. Bennett, J. Monzo, J. Humphrey, D. Plana, M. Walker, C. McConville, D. Fermin, A. Yanson and P. Rodriguez, ACS Catal., 2016, 6, 1533-1539.

22. P. Rodriguez, D. Plana, D. J. Fermin and M. T. M. Koper, J. Catal., 2014, 311, 182-189.

23. S. E. S. Elwakkad, H. A. Rizk and I. G. Ebaid, J. Phys. Chem., 1955, 59, 1004-1008.

24. M. S. Elbasiouny, S. A. Hassan and M. M. Hefny, Corrosion Science, 1980, 20, 909-917.

25. F. Lu, X. B. Ji, Y. C. Yang, W. T. Deng and C. E. Banks, RSC Adv., 2013, 3, 18791-18793.

26. A. I. Yanson, P. V. Antonov, P. Rodriguez and M. T. M. Koper, Electrochim. Acta, 2013, 112, 913-918.

27. M. Duca, P. Rodriguez, A. I. Yanson and M. T. M. Koper, Top. Catal., 2014, 57, 255-264.

28. J. A. Seabold, K. Zhu and N. R. Neale, Phys. Chem. Chem. Phys., 2014, 16, 1121-1131.

29. Y. H. Ng, A. Iwase, A. Kudo and R. Amal, J. Phys. Chem. Lett., 2010, 1, 2607-2612.

30. T. J. P. Hersbach, V. A. Mints, F. Calle-Vallejo, A. I. Yanson and M. T. M. Koper, Faraday Discuss., 2016, 193, 207-222.

31. T. K. Townsend, E. M. Sabio, N. D. Browning and F. E. Osterloh, ChemSusChem, 2011, 4, 185-190.

32. J. A. Seabold and K. S. Choi, J. Am. Chem. Soc., 2012, 134, 2186-2192.

33. D. K. Zhong, S. Choi and D. R. Gamelin, J. Am. Chem. Soc., 2011, 133, 18370-18377.

34. H. S. Park, K. E. Kweon, H. Ye, E. Paek, G. S. Hwang and A. J. Bard, J. Phys. Chem. C, 2011, 115, 17870-17879.

35. L. Chen, F. M. Toma, J. K. Cooper, A. Lyon, Y. J. Lin, I. D. Sharp and J. W. Ager, ChemSusChem, 2015, 8, 1066-1071.

36. C. X. Feng, S. Z. Wang and B. Y. Geng, Nanoscale, 2011, 3, 3695-3699.

37. J. Theerthagiri, R. A. Senthil, A. Malathi, A. Selvi, J. Madhavan and M. Ashokkumar, RSC Adv., 2015, 5, 52718-52725.

38. S. L. Liew, Z. Zhang, T. W. G. Goh, G. S. Subramanian, H. L. D. Seng, T. S. A. Hor, H. K. Luo and D. Z. Chi, Int. J. Hydrogen Energy, 2014, 39, 4291-4298.

39. M. Radecka, P. Sobas, M. Wimbicka and M. Rekas, Phys. B (Amsterdam, Neth.), 2005, 364, 85-92.

40. I. N. Martyanov, S. Uma, S. Rodrigues and K. J. Klabunde, Chem. Commun., 2004, DOI: 10.1039/b409730k, 2476-2477.

41. J. D. Zhuang, W. X. Dai, Q. F. Tian, Z. H. Li, L. Y. Xie, J. X. Wang, P. Liu, X. C. Shi and D. H. Wang, Langmuir, 2010, 26, 9686-9694.

42. B. A. Helms, T. E. Williams, R. Buonsanti and D. J. Milliron, Adv. Mater., 2015, 27, 5820-5829.

43. A. Singh, B. A. Lindquist, G. K. Ong, R. B. Jadrich, H. Ha, C. J. Ellison, T. M. Truskett and D. J. Milliron, Angew. Chem., Int. Ed., 2015, 54, 14840-14844.

5.5. Supporting Information

High throughput preparation of metal oxides and mixed oxides nanocrystals by cathodic corrosion and their use as active photocatalysts

Matthew L. Kromer,[†,⊥] Javier Monzó,[‡,⊥] Matthew J. Lawrence,[‡,⊥] Adam Kolodziej,[‡,⊥] Zachary T. Gossage,[†] Burton H. Simpson,[†] Sara Morandi,[§] Alex Yanson,[∥] Joaquín Rodríguez-López*[,†,#] and Paramaconi Rodríguez*[,‡]

[†]Department of Chemistry and [#]Beckman Institute for Science and Technology, University of Illinois at Urbana–Champaign, Urbana, Illinois 61801, United States

[‡]School of Chemistry, University of Birmingham, Edgbaston Birmingham B15 2TT, United Kingdom

[§]Dipartimento di Chimica, Università degli Studi di Milano, via Golgi 19, 20133 Milano, Italy

[∥]Cosine Measurement Systems, Oosteinde 36, 2361 HE, Leiden, The Netherlands

*Correspondence should be addressed to: joaquinr@illinois.edu; p.b.rodriguez@bham.ac.uk

Contents

Table S1. Summary of the recent protocols for the synthesis of H2WO4, WO3, BiVO4 and TiO2 particles.

Material	Synthetic Method	Reactants	Notes About Synthesis	Reference
H_2WO_4 nanotubes	Solvothermal	WCl_6, Urea Ethanol	12 h reaction time at 180 °C Dried at 60 °C for 12 h	1
WO_3 nanoparticles	Reverse microemulsion method	Tungsten isopropoxide Triton X-100 (surfactant) n-heptane	Aging step took 4-96 h 200-500 °C heat treatment for 2 h Post-treatment: the nanoparticles were first heated to 300 °C in air for 1 h to remove residual organics followed by a heat treatment under flowing pure H2 or a mixture of H2/N2 (1:5 v/v) at temperatures between 500 and 650 °C No morphology control	2
$BiVO_4$ thin film	Metal organic decomposition	Bismuth nitrate hexahydrate Vanadyl acetylacetonate	~10 h annealing at 500 °C, No morphology control	3
Nanoporous $BiVO_4$	Electrodeposition/ solvothermal	BiOI Vanadyl acetylacetonate	2-step electrodeposition method Calcination process at 450 °C for 2 h, No size and morphology control	4
TiO_2 nanorods	Solvothermal	TiF_4, 2-propanol, HF	Calcination at 180 °C for 5.5-44 h Fluoride removal requires further heating to 600 °C for 1.5 h 34.8% yield of anatase TiO_2	5

TiO_2 nanorods	Sol-gel	Oleic acid Oleylamine Titanium isopropoxide CTAB	~4 h reaction time at 80°C - 260°C. Multiple purification steps including centrifugation with cyclohexane Monodisperse Very good morphology control	6
H_2WO_4	Cathodic corrosion	W wire K_2SO_4 Water	Reaction time < 2 min Room temperature Control on size and shape	*This work*
$BiVO_4$	Cathodic corrosion	V wire Bi_2O_3 $CaCl_2$ Water	Reaction time < 2min Room temperature	*This work*
TiO_2	Cathodic corrosion	Ti wire NaOH Water	Reaction time < 2min Room temperature	*This work*

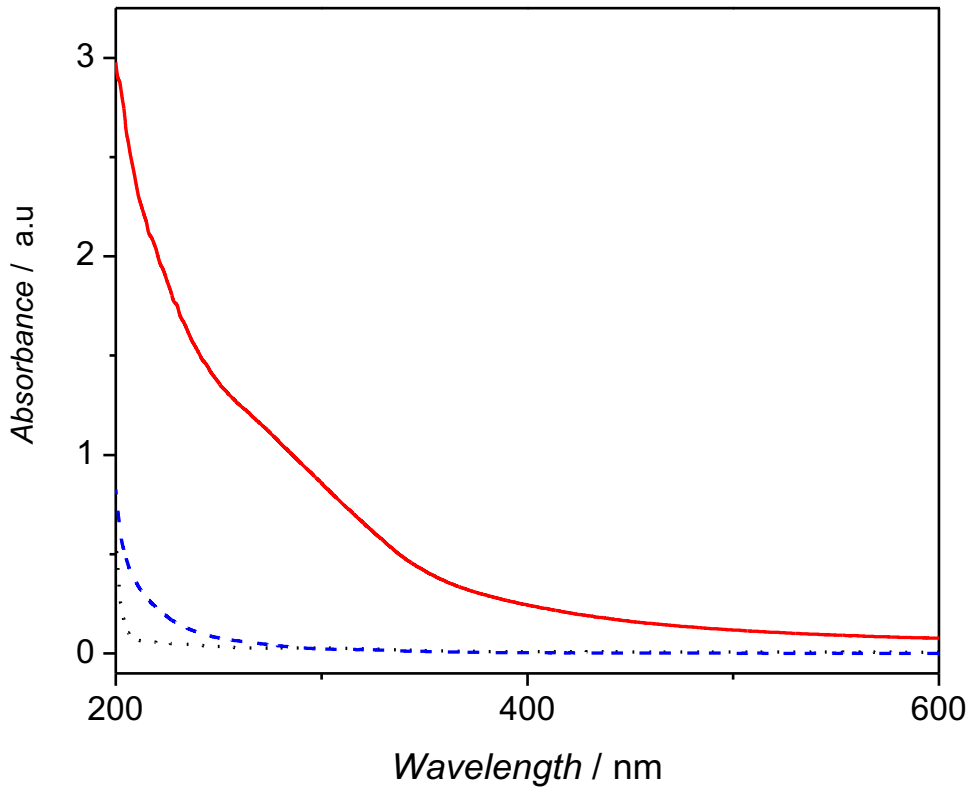

Figure S1. UV–Vis absorption spectra of freshly prepared WO_2/WO_3 samples in $KHSO_4$ solution (red line) and supernatant $KHSO_4$ solution after centrifugation at 4000 RPM for 3 minutes (dashed blue line). The UV-Vis adsorption spectra of the $KHSO_4$ solution has been also included (dotted black line).

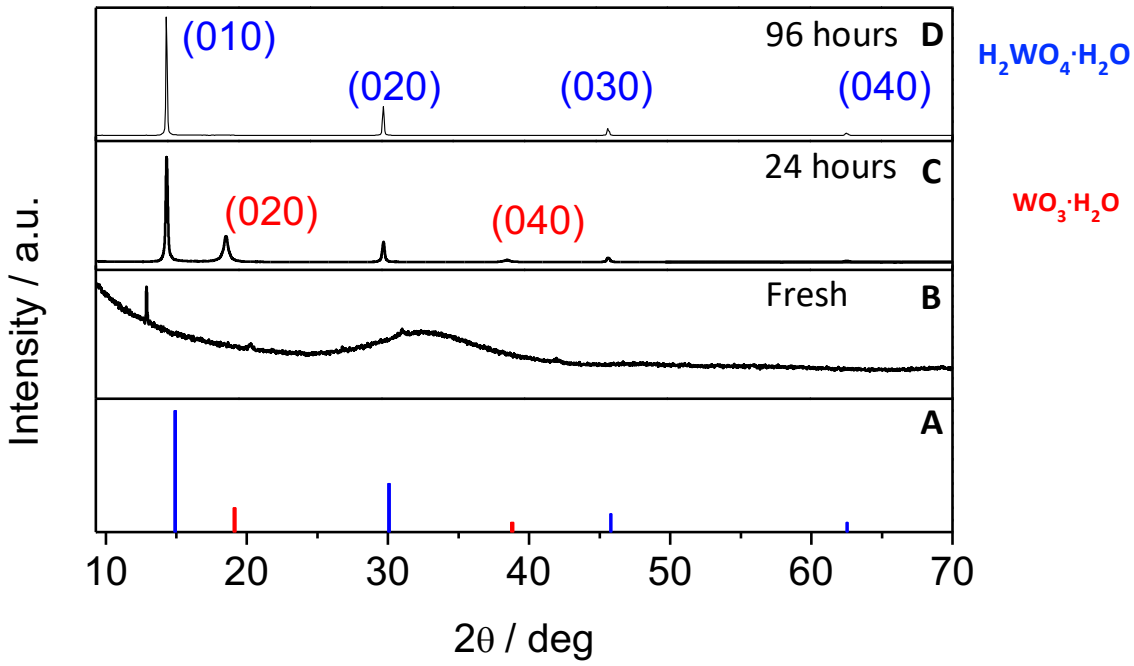

Figure S2. (A) XRD pattern of $H_2WO_4 \cdot H_2O$ (blue lines; JCPDS database no. 18-1420) and $WO_3 \cdot H_2O$ (red lines; JCPDS database no. 43-0679) and XRD patterns of WO_x nanoparticles as a function of the ageing time in water (B) freshly prepared (C) after 24 hours (D) after 96 hours.

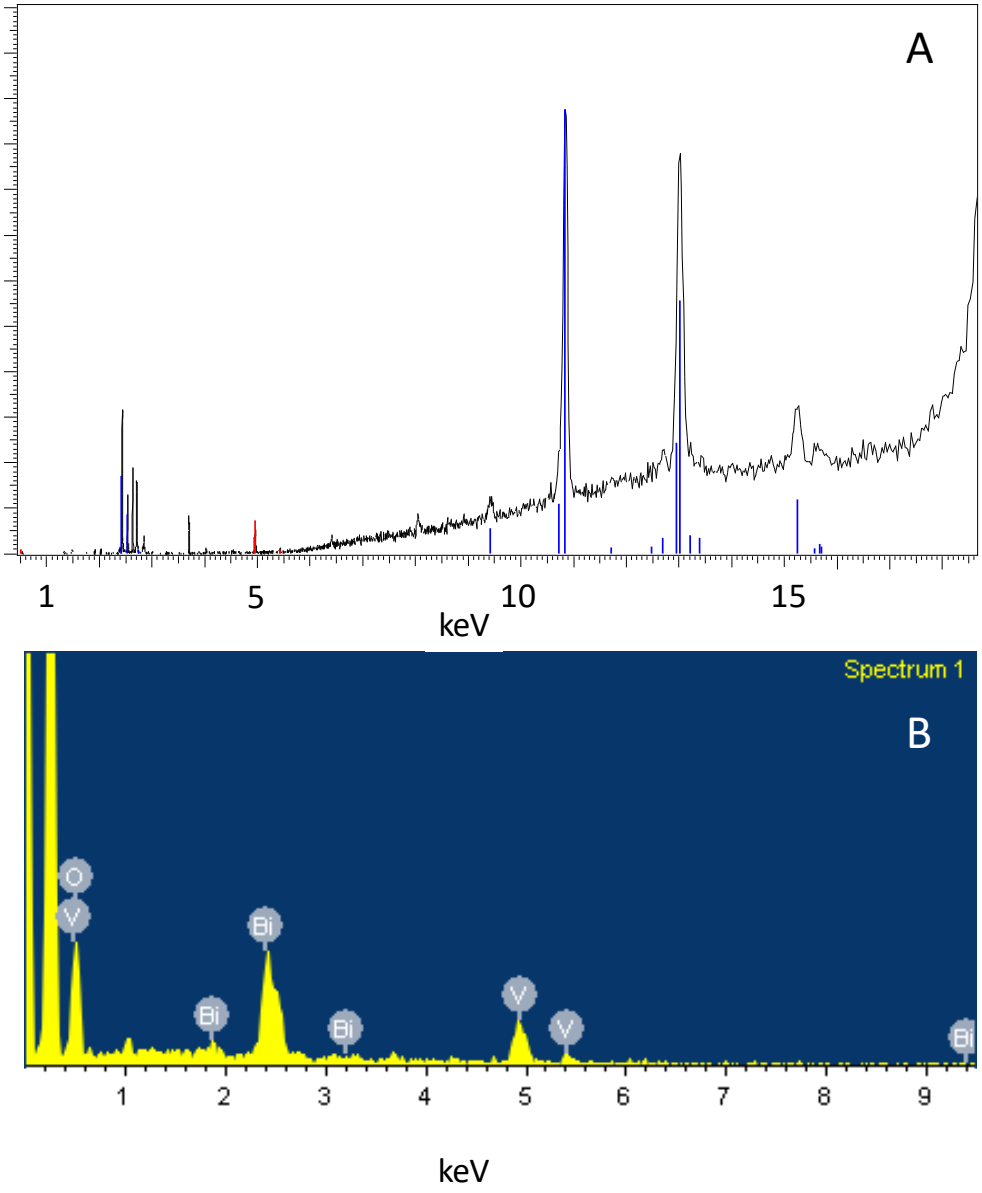

Figure S3. (A) XRF spectrum of $BiVO_4$ nanoparticles; red and blue lines indicate V and Bi content, respectively (B)EDX spectrum of $BiVO_4$ nanoparticles. Quantitative analysis reveals nanoparticle composition to be 56:44 (XRF) and 58:42 (EDX) for Bi:V content.

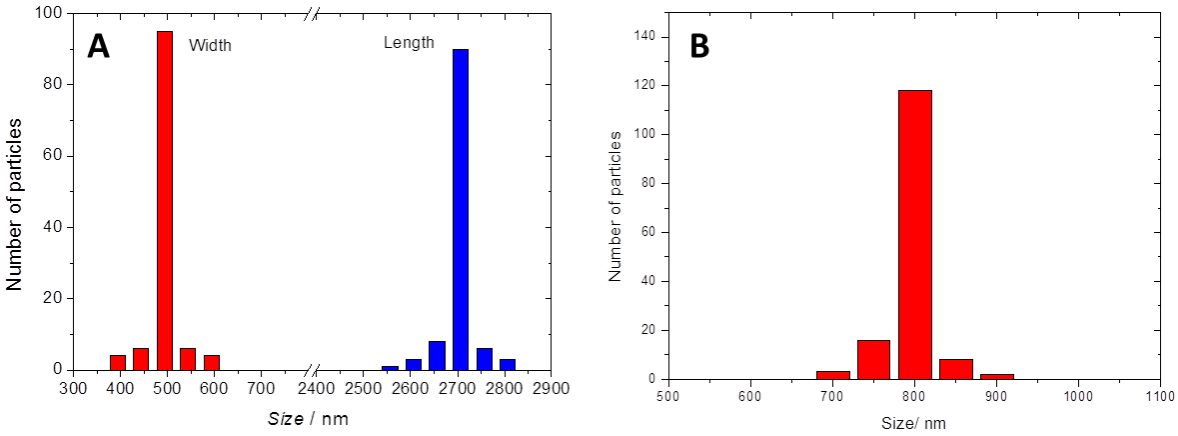

Figure S4. Particle size distribution of (A) H_2WO_4 and (B) $BiVO_4$ obtained from TEM measurements accordingly. The relative abundance of each particle size was calculated from a total of >150 nanoparticles.

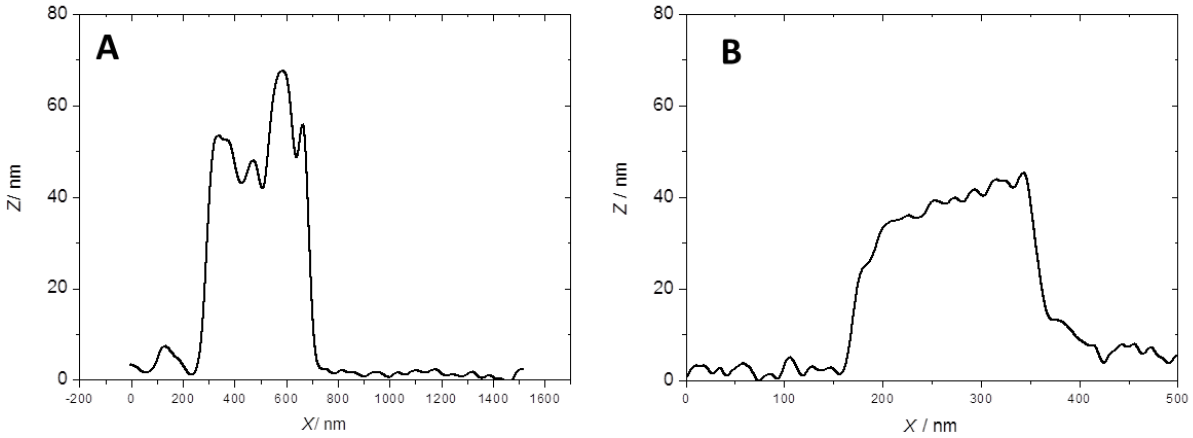

Figure S5. Cross section of a AFM measurement over a single (A) H_2WO_4 nanoparticle and (B)$BiVO_4$ nanoparticle.

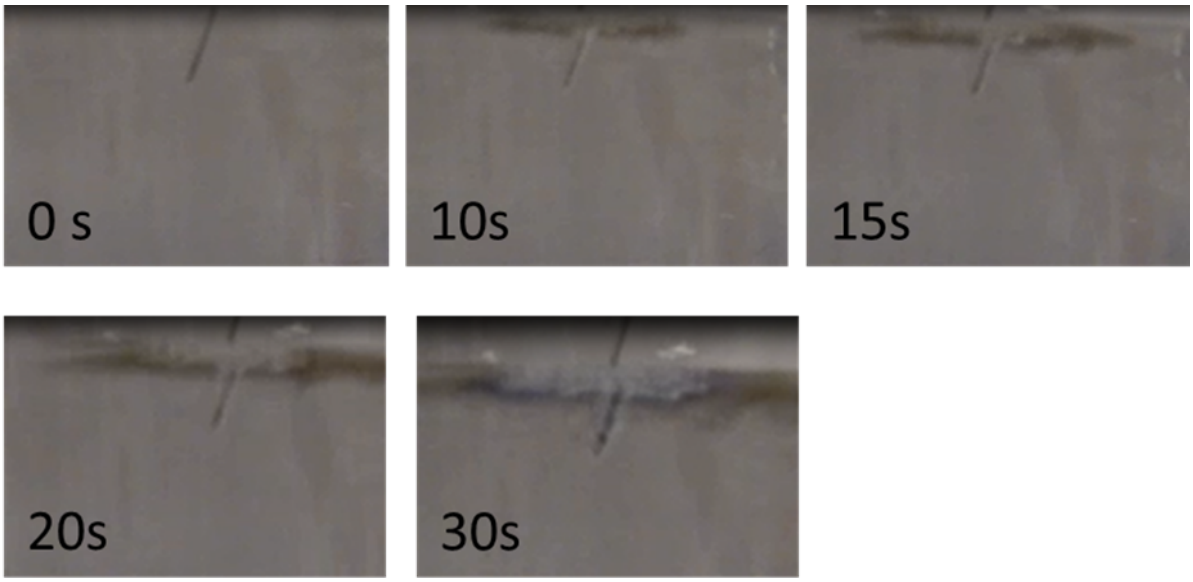

Figure S6. Snapshots at different timepoints during the cathodic corrosion process. As the etching proceeds, a dark cloud of colloidal nanoparticles forms in solution immediately surrounding the metal wire.

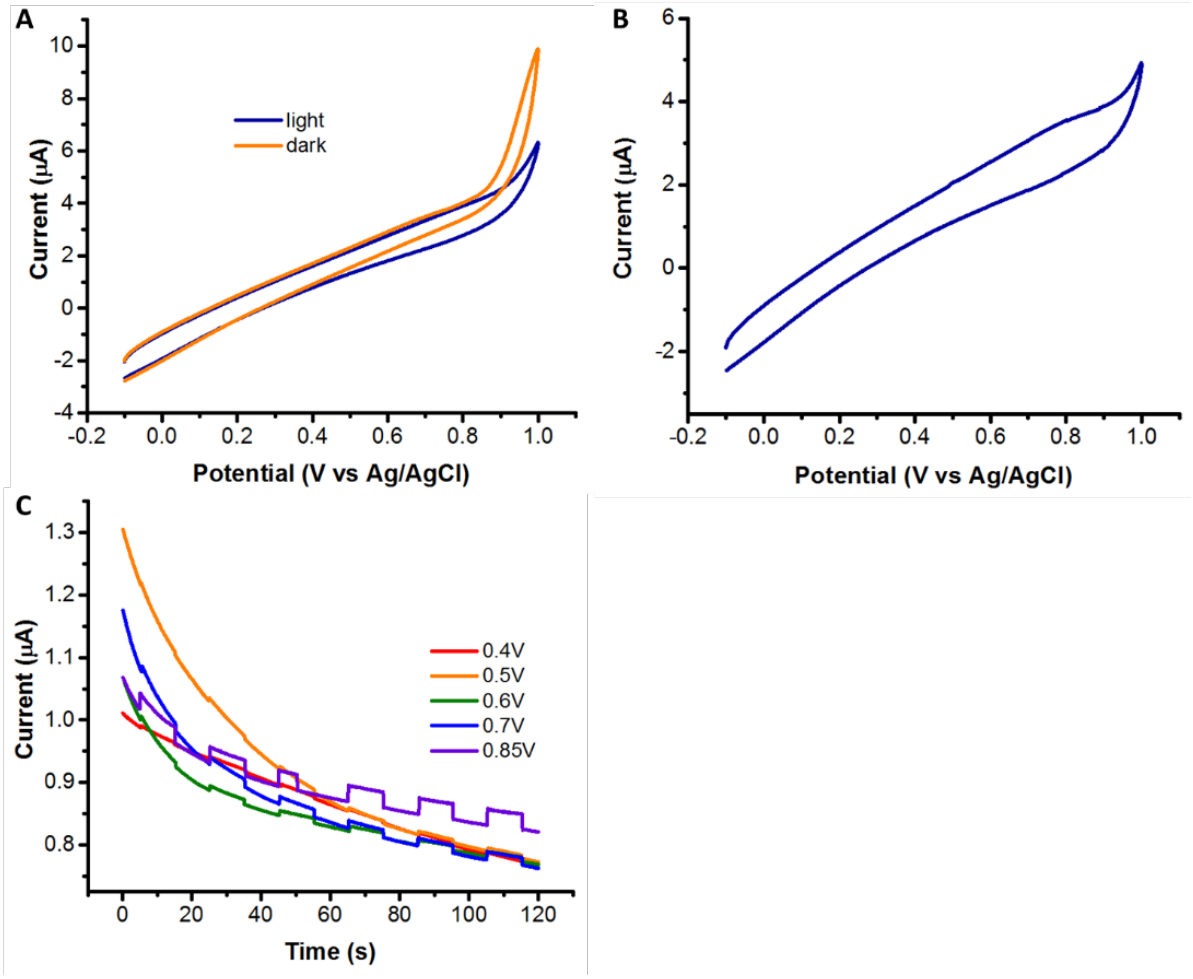

Figure S7. Blank measurements were taken of an ITO cover slip with a thin layer of Nafion® spin coated onto it. The data suggest some photocurrent in the absence of any photocatalyst particles, but significantly less compared to an ITO slide with photocatalytic particles on it. A) A cyclic voltammogram in dark and a cyclic voltammogram in light showing very little difference when the sample was illuminated. B) A cyclic voltammogram in which the light was chopped, which also shows very little change in current in dark compared to when illuminated. C) Chronoamperometry that clearly depicts the low values of photocurrent for the blank sample.

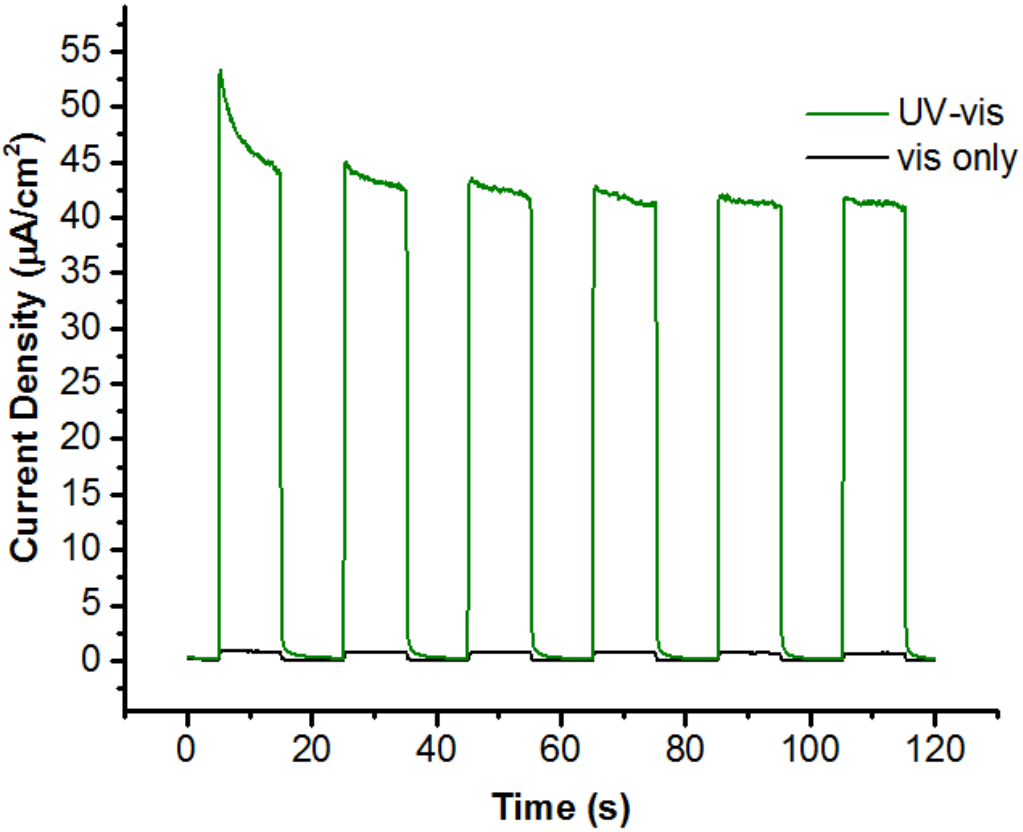

Figure S8. When exposed to only visible light, the H_2WO_4 displayed much lower activity. This is due to the relatively high band edge for H_2WO_4 which results in poor conversion of visible light. Sample was biased to 0.85V vs Ag/AgCl.

References

1. Z. G. Zhao and M. Miyauchi, *Angew. Chem., Int. Ed.*, 2008, **47**, 7051-7055.

2. L. Xiong and T. He, *Chem. Mater.*, 2006, **18**, 2211-2218.

3. D. K. Zhong, S. Choi and D. R. Gamelin, *J. Am. Chem. Soc.*, 2011, **133**, 18370-18377.

4. T. W. Kim and K. S. Choi, *Science*, 2014, **343**, 990-994.

5. H. G. Yang, G. Liu, S. Z. Qiao, C. H. Sun, Y. G. Jin, S. C. Smith, J. Zou, H. M. Cheng and G. Q. Lu, *J. Am. Chem. Soc.*, 2009, **131**, 4078-4083.

6. Z. Zhang, X. Zhong, S. Liu, D. Li and M. Han, *Angew. Chem., Int. Ed.*, 2005, **44**, 3466-3470.

5.6. Addendum

Chapter 5 presents the nanostructured material produced via cathodic corrosion of Ti wire in 10 M NaOH as amorphous TiO_2. However, subsequent work led to a more accurate understanding of the chemical composition and structure of the product, presented herein.

An initial XRD pattern of the as-produced material is presented in **Figure A1**. The diffraction pattern presents a number of broad bands with low peak intensities between 2θ = 25 – 80° and appears to suggest the formation of a highly amorphous mixed TiO_2 phase when compared to the ICSC database patterns of anatase and rutile (**Figure A1A**). However, the poor signal-to-noise ratio did not allow sufficient peak resolution to justifiably attribute the material to either of the predominant TiO_2 polymorphs of anatase and rutile.

In attempts to improve the signal-to-noise ratio of the diffraction pattern, measurements were repeated employing a greater measurement time (by decreasing the number of 2θ steps per second). Furthermore, the 2θ range employed in the measurements was increased to 20 – 100°. The resulting diffraction pattern is presented in **Figure A1B**; both the as-measured diffraction pattern data and the background-subtracted data are presented. Again, comparison to the anatase and rutile database patterns suggested the presence of a mixed phase with low crystallinity.

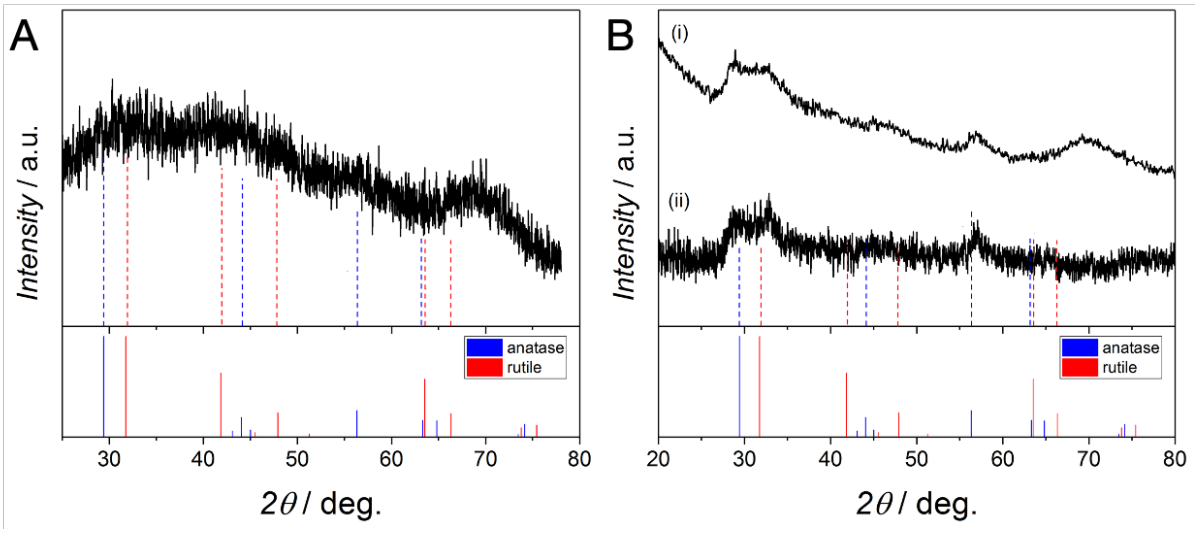

Figure A1. XRD pattern of TiO_x nanoparticles produced via cathodic corrosion of a Ti wire in 10 M NaOH between 0 and -10 V; $f_{square\ waveform}$ = 100 Hz. (A) Diffraction pattern measured during 45 min (B)(i)as-measured and (ii) background-subtracted diffraction patterns measured during 2 hrs.

However, further scrutiny of this conclusion regarding the chemical structure and composition of the Ti cathodic corrosion product determined that it was not able to account for the Na content detected via EDX,[1] even after thorough cleaning and dilution of the product. In addition, the application of XAS (presented in detail in **Chapter 6**) provided greater evidence against the product being a mixture of TiO_2 polymorphs, or TiO_2 at all.

Survey of the literature for nanostructured Ti oxides produced via hydrothermal and sol-gel routes involving high molarity NaOH solutions provided strong evidence to suggest that the product of cathodic corrosion of Ti in 10 M NaOH was in fact $Na_2Ti_3O_7$.[2-6] The layered nature of the $Na_2Ti_3O_7$ material results in the appearance of an intense diffraction peaks at low 2θ at *ca.* 10°. Thus, the XRD diffraction patterns were obtained for the cathodic corrosion product utilising a scan range starting at 2θ = 5° (**Figure A2**). There was good agreement between the nanostructured cathodic corrosion product in comparison to the ICSD database pattern for bulk $Na_2Ti_3O_7$ and was in harmony with those presented in existing works.[5, 6]

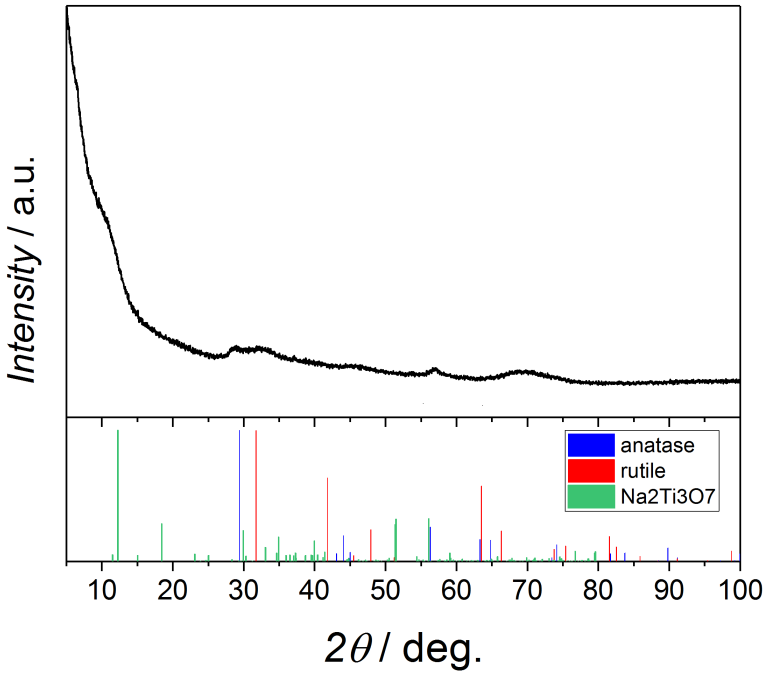

Figure A2. XRD pattern recorded during 15 hrs of nanostructured material produced via cathodic corrosion of Ti wire in 10 M NaOH at room temperature.

References

1. Rodriguez, P.; Plana, D.; Fermin, D. J.; Koper, M. T. M. *J. Catal.* **2014,** 311, 182-189.

2. Guo, Y.; Lee, N.-H.; Oh, H.-J.; Yoon, C.-R.; Park, K.-S.; Lee, H.-G.; Lee, K.-S.; Kim, S.-J. *Nanotechnology* **2007,** 18, (29).

3. Ferreira, O. P.; Souza Filho, A. G.; Mendes Filho, J.; Alves, O. L. *J. Braz. Chem. Soc.* **2006,** 17, (2), 393-402.

4. Du, G. H.; Chen, Q.; Che, R. C.; Yuan, Z. Y.; Peng, L. M. *Appl. Phys. Lett.* **2001,** 79, (22), 3702-3704.

5. dos Santos, N. M.; Rocha, J. M.; Matos, J. M. E.; Ferreira, O. P.; Filho, J. M.; Viana, B. C.; Oliveira, A. C. *Appl. Catal., A* **2013,** 454, 74-80.

6. Umek, P.; Bittencourt, C.; Gloter, A.; Dominko, R.; Jagličić, Z.; Cevc, P.; Arčon, D. *J. Phys. Chem. C* **2012,** 116, (20), 11357-11363.

Preface to Chapter 6

Format: Published article manuscript.

The formatting of the manuscript and supporting information have been updated in keeping with the style of this thesis. Thus, references and reference styles have been updated. Importantly, no changes to the specific content of the published article have been made.

Article information: M. J. Lawrence, V. Celorrio, X. Shi, Q. Wang, A. Yanson, N. J. E. Adkins, M. Gu, J. Rodríguez-López and P. Rodriguez, *ACS Appl. Energy Mater*., 2018, **1**, 5233-5244, DOI: 10.1021/acsaem.8b00873. Published by the American Chemical Society.

Overview: In this chapter our aim was to further develop the cathodic corrosion method and to showcase its integral versatility and wider applicability to the production of metal oxides for green energy applications. The ideology was simple: combining two of its key selling points, (i) retention of alloy composition from a bulk to material to NPs and (ii) the production of (photo)electrochemically active metal oxides.

Mixed and doped metal oxides are excellent candidates for commercial energy applications such as batteries, supercapacitors, solar cells, and photocatalysts due to their activity, stability, tailorable band edge and bandgaps, and low cost. However, the routes commonly employed in their synthesis present synthetic bottlenecks with reliance on sacrificial materials, the use of high temperatures, long reaction times, and little ability to control morphology, thus compromising their scale- up. Herein, we present the single-pot, electrochemical synthesis of high surface area, doped metal titanate nanostructures, including $Na_2Ti_3O_7$ (NTO), 25 wt.% Sn:NTO, 5 wt.% Fe:NTO, and 3 wt.% Cu:NTO. The synergistic use of the cathodic corrosion method with suspended droplet alloying (SDA) led to materials with excellent homogeneity, presenting a promising route for the screening, production, and discovery of electroactive materials.

As proof of concept of the synthetic control and impact on reactivity, we found that the photoanodic oxygen evolution activity of the nanomaterials was adversely affected by Fe and Sn doping into NTO while Cu doping, at 3 wt.%, displayed significant improvement. This work demonstrates the ability of the cathodic corrosion method to obtain compositionally and structurally controlled mixed-metal oxides in a rapid fashion, thus creating new opportunities in the field of materials engineering and the systematic study of compositional gradients on the (photo)electrochemical performance of metal oxide nanoparticles.

Author Contributions: M.J.L. performed the preparation, physical, optical and (photo)electrochemical characterization of the nanoparticles. V.C. and P.R.. performed XANES and EXAFS characterization and analyses. X.S. and Q.W. performed the initial HRTEM, STEM and HAADF-EDS experiments and analyses. N.J.E.A. prepared the laser-fabricated alloys. All authors contributed to the analysis of the results, discussion, writing and revision of the manuscript.

6. ELECTROCHEMICAL SYNTHESIS OF NANOSTRUCTURED METAL-DOPED TITANATES AND INVESTIGATION OF THEIR ACTIVITY AS OXYGEN EVOLUTION PHOTOANODES

6.1. Introduction

Addressing fundamental kinetic and efficiency challenges of electrochemical renewable energy technologies is crucial towards making them more economically viable, thus contributing to the transition from fossil fuel dependence.[1] A major drawback associated with solar and wind technologies is the intermittent nature of these resources, making the conversion of electrical to chemical energy and its subsequent storage the preferred route.[2-4] In this regard, nanostructured titanium oxides and titanates are an ever increasingly important class of semiconductor materials for energy storage and conversion, due to their high surface areas, natural abundance, low toxicity, and excellent stability,[5-7] which have led to their investigation for a myriad of applications, such as carbon capture technologies,[8] batteries,[9, 10] supercapacitors,[11-13] solar cells[14-16] and photocatalysis.[17, 18]

As proof of concept of the impact of compositional control on the electroactivity of metal oxide nanoparticles, we explore the activity of doped titanate particles towards photoelectrochemical (PEC) water oxidation. The prospect of converting solar light and electrical energy has resulted in a wealth of literature dedicated to gaining a fundamental understanding of the materials capable of performing PEC reactions, in addition to the development of new materials synthesis strategies.[19]The PEC oxygen evolution reaction (OER), where the absorption of light by semiconductors with band gap >1.23 eV generates reactive charge carriers in order to drive uphill electrochemical reactions, is the rate-determining process for PEC cells.[20] The relatively large band gap of Ti-based oxides (~3 eV) renders them unable to absorb any significant portion of the solar spectrum. Common

avenues explored in attempts to extend the visible light absorption properties of the oxides to harness greater portions of the solar spectrum include surface sensitization, via decoration with plasmonic particles and/or narrow band gap semiconductors, as well as the introduction of dopants.[18, 21, 22] Doping with earth-abundant metals, especially Cu, Fe and Sn, has been shown to enhance visible light absorption via band gap narrowing and reduced rates of surface recombination.[23-31] Furthermore, nanostructuring and morphological tuning further enhance physical properties through quantum confinement.[17, 32, 33] Nanostructuring has emerged as a promising pathway for materials preparation because of the improved physiochemical properties relative to conventional nanoparticles.[6] In particular, nano-wires/rods/tubes/ribbons benefit from more efficient light absorption, longer charge carrier diffusion lengths due to increased length-to-diameter ratios and increases in specific surface area and the number of active sites.[5, 6]

Current approaches for the production of titanate nanomaterials can be categorized into four groups: (i) solid state, (ii) template-assisted, (iii) hydrothermal and (iv) electrochemical. Solid state syntheses involve the calcination of metal powders for long time periods, typically at least 12 hours, with the ability to introduce dopants with a suitable precursor.[34] However, this methodology does not allow for control over the shape, size or morphology of the products. Template-assisted syntheses employ the use of well-ordered, nanostructured substrates onto which the titanates are grown or deposited, commonly via sol-gel methods, chemical vapor deposition or atomic layer deposition (ALD).[35] The sol-gel route involves the deposition of polymer sols onto the substrate and calcination to yield the (doped) titanate product.[15, 26, 29] ALD generates a uniform film over large areas of the template surface, allows for fine control over the thickness and composition of the as-deposited film and can be used to generate three-dimensional structures.[9, 36] The template-assisted methodology is heavily reliant on the underlying template, which is often a sacrificial component of the synthetic process, as in the

case of anodized alumina, for determining the shape, size, and morphology of the titanates. This makes the screening and discovery of new materials costly and inconvenient.

By far, the hydrothermal synthesis of nanostructured titanates is the most common approach reported in the literature, after Kasuga et al. first demonstrated the formation of titanate nanotubes in a one-pot procedure without the need for a sacrificial template.[37] Since then, it has been successfully applied to the formation of transition metal-doped titantes.[31, 38, 39] Typically, a Ti precursor is reacted with a high molarity NaOH solution, at elevated temperatures and pressures, in a one-pot synthesis, to yield one-dimensional titanate nanostructures, with near complete conversion of the precursor. The structure of the titanates can be varied by choice of solvent, the reaction time, temperature and pressure.[7] However, long reaction times (>24 hours) are typical of such syntheses due to the slow reaction kinetics and room-temperature syntheses require much longer synthesis times (72 hours).[40] Overall, the aforementioned routes are cumbersome due to multiple reaction steps, energy inefficient due to the high temperatures involved in their synthesis, and chemically inefficient due to the use of organic additives, which require additional purification or sacrificial templates and are not cost effective for scale-up.

In contrast, electrochemical routes have been shown to greatly reduce the time taken to produce nanostructured titanate catalysts.[41, 42] Electrodeposition is a one-pot technique that enables: (i) control over deposition thicknesses, (ii) direct deposition of the catalyst onto the conductive substrate, maximizing the electrical connection, (iii) ease of access to multi-component, mixed metal oxide materials.[42-44] Unfortunately, control over the uniform morphology of the electrodeposits is lacking. Electrochemical anodization of Ti foils addresses these morphology issues by the generation of titanate nanotube arrays with uniform pore sizes and lengths that can be varied by adjusting the synthetic parameters, such as temperature, electrolyte and anodization potential and duration.[5, 42, 45] However, the

syntheses involve the use of organic solvents and demonstration of the production of homogeneously metal-doped titanates via anodization is yet to be reported.

Here we present a new approach for the facile preparation of metal-doped sodium titanate, $Na_2Ti_3O_7$, (M:NTO) nanomaterials through the combination of two versatile synthetic techniques: combinatorial alloy laser fabrication[46, 47] and cathodic corrosion (Figure 1A-B).[48, 49] The synergy of these techniques resides on the ability of obtaining compositionally and structurally well-defined nanomaterials from a small portion of an alloy sample. Combinatorial alloy laser fabrication significantly reduces the time taken to generate these alloys and affords the ability to fine tune their composition by variation of wire feed rates and diameters. Utilization of a high-power laser and suspended droplet alloying (SDA) allowed the formation of an alloy from thin wires only at the laser focal point, minimized domain segregation and removed the need to melt bulk materials, thus improving the cost and energy efficiency.[47] Subsequent electrochemical synthesis was performed via cathodic corrosion[48] to generate suspended nanoparticles of the metal alloys, in the absence of surfactants, to yield clean, useable materials.

Cathodic corrosion, is a versatile electrochemical synthetic tool (**Figure 1B**) that has been demonstrated in both aqueous and organic media, used for the synthesis of both pure metallic and alloy nanomaterials, with exercisable control, resulting in homogenous particle size and alloy composition.[50-52] In this method, when the cathodic potential is applied to the working electrode (WE) the metal is reduced to metal anions stabilized by cations from the electrolyte, different from protons. This intermediate is relatively stable in the absence of an oxidant, but in the presence of water, oxygen or reactive oxygen species generated in-*situ* at the counter electrode (CE), the metal anion intermediate is oxidized, forming metal nanoparticles.[53-55] These nanoparticles can be further oxidized, depending on the electrolyte or metal, resulting into metal oxide nanoparticles as described here. Recently, we demonstrated the synthesis

of photoactive metal oxides, including $BiVO_4$ and H_2WO_4 and presented the variation of particle size with the frequency of the applied AC voltage.[41] We now expand to the synergy of this technique with SDA for obtaining compositionally and structurally well-defined nanomaterials. Here, we show that cathodic corrosion of homogenous Ti-based metal alloys results in homogenous, high surface area, doped titanate photocatalysts and investigate their activity towards the PEC OER.

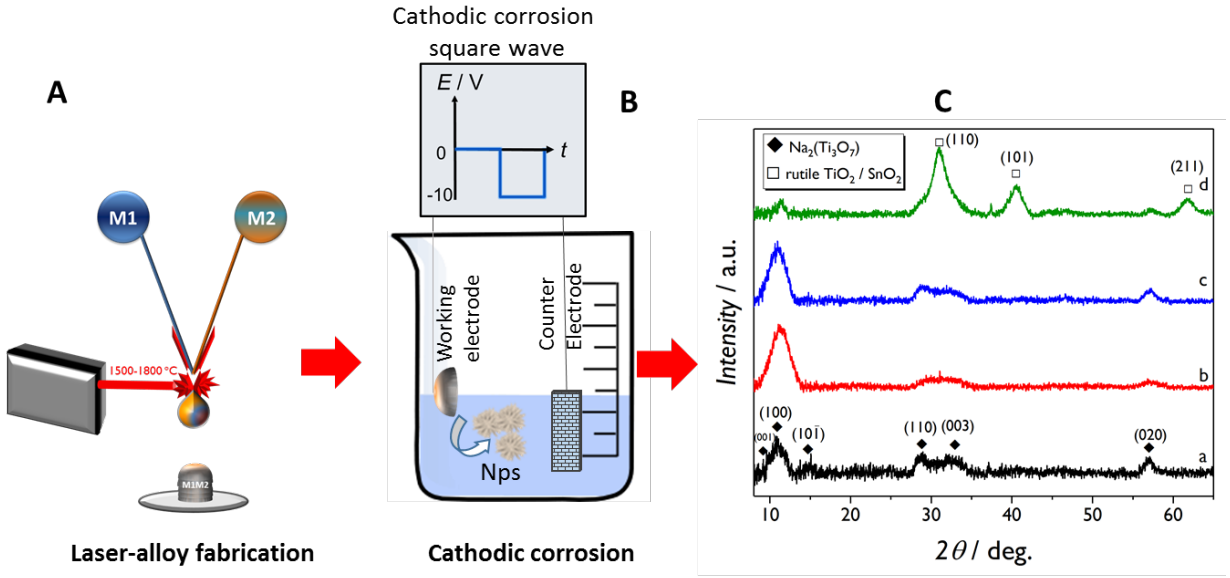

Figure 1. (A-B) Schematic representation of alloy and nanoparticle fabrication via the combination of laser combinatorial facility and cathodic corrosion (C) X-ray diffraction patterns of (a) NTO, (b) 5 wt.% Fe:NTO, (c) 3 wt.% Cu:NTO, (d) 25 wt.% Sn:NTO nanoparticles obtained via cathodic corrosion of a Ti wire and $Fe_{8.82}Ti_{91.28}$, $Cu_{6.38}Ti_{93.72}$ and $Sn_{42.82}Ti_{57.18}$. The position and assignment of Miller indices were obtained via PDF card no. 01-072-0148 ($Na_2Ti_3O_7$), JCPDS card no. 21-1276 (rutile TiO_2) and JCPDS card no. 41-1445 (rutile-type SnO_2).

6.2. Experimental

Alloy laser fabrication

Homogeneous bulk alloys were prepared via a laser combinatorial facility, as described in a previous report,[47] modified for the production of binary rather than ternary alloys. Pure elemental wires (Advent Research Materials, UK) were aligned into the focal point of a high energy laser beam within a deoxygenated chamber (Ar; flow rate=5 L min^{-1}, oxygen level below 50ppm), where alloys were formed through the melting of the wire tips and mixing of the elements, as suspended droplets. Continuous feeding of each wire into the focal point increased the size of the alloy droplet until the mass was great enough so that the gravitational force acting upon it overcame the surface tension of the droplet, causing detachment of the alloy droplet from the wires, causing it to fall onto a stainless-steel substrate (430 grade) positioned below the focal point. Wires were continuously fed into the focal point until the desired amount of alloy was produced, at which point the wire feeding mechanism was shut off and the alloy was allowed to cool in the argon-filled chamber. The typical synthesis time was 2 min. After cooling, alloys were retrieved, removed from the stainless-steel substrates, cut into narrow discs/rods with width ~2 mm by electrical discharge machining (EDM) and then mechanically polished.

Cathodic corrosion synthesis

For the preparation of the nanoparticles the cathodic corrosion method was implemented.[48] Nanoparticles of NTO and M:NTO (M =Fe, Cu or Sn) were synthesized by applying an AC voltage of 0 to -10 V between the WE (Ti wire of 0.25 mm diameter or laser-fabricated Ti-alloy) and a flame-annealed, high surface area Pt flag used as counter electrode, in 10 mL of 10 M NaOH (Merck, ≥99%) solution. Flame annealing is a common terminology used to describe a cleaning process of certain metal electrodes such as Pt, Au or Pd. A propane/butane torch is used to increase the temperature of the electrode and at these temperatures all organic

contaminants are removed from the electrode thus avoiding contaminating the electrochemical measurements. Typically, syntheses were conducted for 1 hour to collect sufficient quantities for all the characterization and the electrocatalytic assessments. The 100 Hz square wave signal was generated by LabVIEW / National Instruments hardware and amplified by a power amplifier. A suspension of oxide particles was formed at the WE in each synthesis. After the synthesis, the nanoparticles were separated by centrifugation and decanting the supernatant. The process was repeated until the removed supernatant was of neutral pH; the oxides were left suspended in milli-Q water (PURELAB Ultra, 18.2 MΩ.cm).

Physical Characterization

The crystal structure of the metal oxides was investigated by X-ray diffraction (XRD) via a Bruker D2 Phaser Powder X-ray diffractometer (Co Kα radiation source, λ=1.78897 Å; 30 kV operating voltage; 10 mA). Aqueous oxide suspensions were drop-cast onto a quartz crystal in 25 μL increments and the water was evaporated in a fan oven (60 °C). Diffraction patterns were recorded for >12 hours.

Particle morphology was analyzed by scanning electron microscopy (SEM) using a Philips XL-30 ESEM instrument. Compositional analyses were conducted via energy dispersive X-ray spectroscopy (EDX/EDS) coupled to the SEM microscope and X-ray fluorescence spectroscopy (XRF) (Bruker S8 Tiger 4 kW spectrometer; He atmosphere). Transmission electron microscopy (TEM) was performed on FEI Themis G2 microscopes, with double Cs-correctors, operating at 300 kV, in scanning transmission electron microscopy (STEM) mode with both bright field and high-angle annular dark field (HAADF) images recorded. The microscopes were also equipped with super-X EDS detectors, which facilitate the acquisition of EDS maps with 50 times higher signal collection efficiency than normal EDS detectors. A theoretical model was employed to calculate the specific surface areas for each sample (*see Supporting Information*).

X-ray absorption spectroscopy (XAS) measurements were recorded on the B18 beamline at Diamond Light Source operating with a ring energy of 3 GeV and at a current of 300 mA.[56] The monochromator comprises Si(111) crystals operating in Quick EXAFS mode. Calibration of the monochromator was carried out using the respective foils prior to the measurements. Pellets of the different samples were collected in fluorescence mode at the Ti K-edge (4965 eV), Fe K-edge (7111 eV), Cu K-edge (8979 eV) and Sn K-edge (29200 eV), simultaneously with the metallic foils. The data was analyzed using Athena and Arthemis programs which implement the FEFF6 and IFEFFIT codes.[57, 58]

Optical property characterization was conducted using a Varian Cary 50 UV-Vis spectrophotometer (*see Supporting Information*).

Photoelectrochemical characterization

Electrodes were prepared by drop-cast deposition of nanoparticle suspensions onto indium tin oxide (ITO) slides (SPI Instruments, 15–30 Ω) in volumes of 10-20 μL to generate a photoelectrode; electrical contact to the ITO slide was achieved by securing indium wire to the edge of the conductive face of the slide with conductive copper tape (3 M Electrical Products). The photoelectrode was assembled into a Teflon electrochemical cell (~3mL volume) as the WE in a 3-electrode electrochemical setup. A flame annealed Pt wire (1 mm diameter) and Ag/AgCl (3 M KCl) with a $NaClO_4$ salt bridge were employed as the counter and reference electrodes, respectively, with 0.1 M NaOH (pH = 12.7) serving as electrolyte. All measurements were conducted at ambient temperature in a dark room. PEC measurements were conducted under illumination by incident polychromatic white light (UV and visible), generated by a 300 W, 6258 Oriel Xe arc lamp (incident light power ~180 mW cm^{-2}). Electrode potential and current measurements were controlled and recorded using CHI920D potentiostats (CHI Instruments). Measured potentials were converted to the reversible hydrogen electrode (RHE) via the Nernst equation.

6.3. Results and Discussion

Prior to the synthesis of the nanoparticles the composition of the alloys used as starting materials was fully characterized by XRD, XRF and EDX (see the SI). The analyses confirm that the atomic composition of the starting alloys were: $Fe_{8.81}Ti_{91.18}$, $Cu_{6.28}Ti_{93.72}$ and $Sn_{42.82}Ti_{57.18}$.

After applying the cathodic AC voltage to the starting alloys, white suspensions of nanoparticles were collected from the FeTi and the CuTi samples, whilst a light-grey suspension was observed for SnTi.

6.3.1. X-ray Diffraction

Figure 1C shows the XRD patterns of the nanowires (NWs) prepared by cathodic corrosion. As curve (a) shows, the diffraction pattern of the titanate nanoparticles present broad peaks at 2θ=10.96°, 14.75°, 28.68°, 32.37° and 56.98° which correspond to the (100), (10$\bar{1}$), (110), (003) and (020) planes of sodium titanate, $Na_2Ti_3O_7$ (NTO), in agreement with reports on the generation of NTO nanotubes via other synthetic routes.[38, 39, 59, 60] The NTO crystal structure (PDF no. 01-072-0148) consists of zig-zagging layers of edge-shared TiO_6 octahedra, with ionically bonded, intercalated Na^+ ions (**Figure 2B**).[61] The observed peak broadening is associated to the low crystallinity and nanostructuring of the NWs. In the case of the Fe:NTO (**Figure 1C.b**) and Cu:NTO (**Figure 1C.c**), a decrease in intensity for the (10$\bar{1}$), (110), (003) and (020) signals is observed relative to the (100) signal at ~11° whilst no additional signals are observed, suggestive of successful doping due to a disruption in recurring crystallinity. The decrease in crystallinity can be associated to the Cu and Fe incorporation. Cu^{2+} dopant species intercalate between the layers of TiO_6 octahedra in titanate nanotubes and the number of Cu^{2+} intercalated per unit cell is half that of Na^+, primarily due to adherence to charge neutrality laws (**Figure 2B**).[38, 60]

Assuming that the same intercalation process occurs in the case of Fe, the substitution of Na^+ for Fe^{n+}, where $n \geq 2$, would cause a contraction of the unit cell. Indeed, shifts in (100) peak position were observed for Fe:NTO and Cu:NTO from 2θ=10.96° to 11.25° and 11.00°, respectively, indicative of a decrease in lattice parameter, in agreement with literature.[31] This effect is not as pronounced in the case of Cu:NTO due to the low Cu concentration (~ 1 at.%). Furthermore, previous reports have shown that the incorporation of Fe and Cu as a dopant in the crystalline structure of TiO_2 does not result in additional XRD signals, in agreement with our results.[29, 62]

Contrastingly, the XRD pattern of the nanoparticles prepared from $Sn_{42.82}Ti_{57.18}$ shows additional intense peaks at 2θ=30.94°, 40.64° and 61.84° which could be associated to the (110), (101) and (211) planes of rutile TiO_2 (**Figure 1C.d**). The positions of these signals, however, are slightly shifted to lower 2θ values, suggesting an increase in lattice parameter as a result of Sn-doping. On the other hand, the rutile phase of SnO_2 also presents signals at similar 2θ angles (**Figure S3**), therefore the presence of SnO_2 was not discarded.[63] Comparison of the diffraction pattern to previously reported Sn-doped titanate materials synthesized by alternative methods suggest that Sn-rich areas exist in and facilitate formation of a predominant rutile phase (**Figure S4**).[64]

6.3.2. Morphological and elemental analyses

In order to determine morphology and chemical composition of the samples, SEM-EDX and HAADF STEM-EDS were conducted. Both STEM (**Figure 2**) and SEM (**Figure S5**) demonstrated the presence of aggregated NWs for all the samples, in agreement with previous reports on TiO_x nanoparticle production via cathodic corrosion,[41, 65] providing evidence for the ability of cathodic corrosion to produce nanostructured titanate materials in the absence of capping agents or surfactants, at ambient temperatures. While surfactants may favor the dispersion of the materials,[66] the presence of surface ligands might strongly

affect the catalytic activity, further complicating particle purification.[67-69] The TEM images show that no significant morphological variation between the undoped (**Figure 2A**) and doped (**Figure 2C-E**) materials was observed.

Analysis of the electron micrographs indicated that the diameters of the individual NW samples were 12.35 ± 1.92 nm, 7.49 ± 1.04 nm, 11.74 ± 1.92 nm and 10.62 ± 1.55 nm for NTO, Fe:NTO, Cu:NTO and Sn:NTO, respectively (Figure S6). Due to the aggregated nature of the nanoparticles, the lengths of the NWs were difficult to determine with precision. The apparent lengths were on the order of few hundreds of nanometers. The calculated surface areas were 90.1, 154.7, 96.8 and 107.1 m^2 g^{-1}, respectively, for NTO, Fe:NTO, Cu:NTO and Sn:NTO, in reasonable agreement with BET values reported in the literature for analogous nanostructures (see Supporting Information).[39]

We used STEM-EDS analyses (Figure S7) to identify the composition of constituent elements, in addition to the relative metal atomic composition to evaluate the transfer of initial alloy composition to the oxide NWs (**Tables S2 & S3**). The nanoparticles retained the relative metal composition of the parent alloys, particularly well in the case of 5 wt.% Fe:NTO and 3 wt.% Cu:NTO. While STEM-EDS spectra alone do not provide unambiguous proof of the homogeneity of the samples, with preferential etching and phase segregation as potential masked effects, these experiments represented a first confirmation of the successful implementation of cathodic corrosion on SDA alloys.

For a stricter evaluation of the compositional effectiveness of the syntheses we turned to HAADF-EDS elemental mapping and to HRTEM. These analyses provided further evidence of the excellent homogeneity of constituent elements present in the doped titanate NWs synthesized by cathodic corrosion of laser-fabricated alloys (**Figure 2I-Q**). No areas of metal segregation or clustering were found within the materials, with both Ti and the dopant metal observed in all regions of the synthesized NWs.

Further HAADF-HRTEM images of 5 wt.% Fe:NTO NWs showed an interlayer distance of 0.75 nm (**Figure 2F**)., in agreement with literature.[70] This is a slight decrease in the NTO (100) interlayer distance relative to the database value, indicative of compression upon Fe intercalation, in agreement with XRD results Some isolated fringe regions with amorphous structures and the presence of small, spherical crystalline nanoparticles with d-spacing of 0.21 nm, which can be attributed to the (420) plane of Fe_2O_3, were observed (**Figure S9**). Bright field STEM and HRTEM images of 3 wt.% Cu:NTO show that the sample solely consisted of crystalline NWs, with no other morphology observed (**Figure 2D,G**). An interlayer distance of 0.747 nm was observed, corresponding to the compressed (100) plane of NTO, similar to that of 5 wt.% Fe:NTO NWs. On the other hand, the 25 wt.% Sn:NTO NWs show an interlayer distance of 0.77 nm for the (100) plane (**Figure 2H**). This increase in d-spacing relative to the Fe- and Cu-doped NWs is rationalized by the increased size of Sn ions relative to Fe and Cu (**Figure 2B**) and to the higher concentration of the Sn-dopant in this sample. Additionally, cubic planes with interlayer distances of 0.26 nm and 0.35 nm were observed via atomic STEM, corresponding to the (101) and (110) planes of rutile SnO_2, respectively – JCPDS no. 41-1445 – providing further evidence of the existence of both Sn-doped titanate NWs and SnO_2 in the 25 wt.% Sn:NTO sample, in agreement with XRD results (**Figure S10**). Altogether, the observed crystallinity and interlayer distances of the doped NWs are in good agreement with analogous transition metal-doped nanostructured titanates synthesized by alternative routes,[71-74] showcasing the advantage of the use of cathodic corrosion to rapidly produce M:NTO nanostructures by the single-step, electrochemical etching of alloys at ambient temperature.

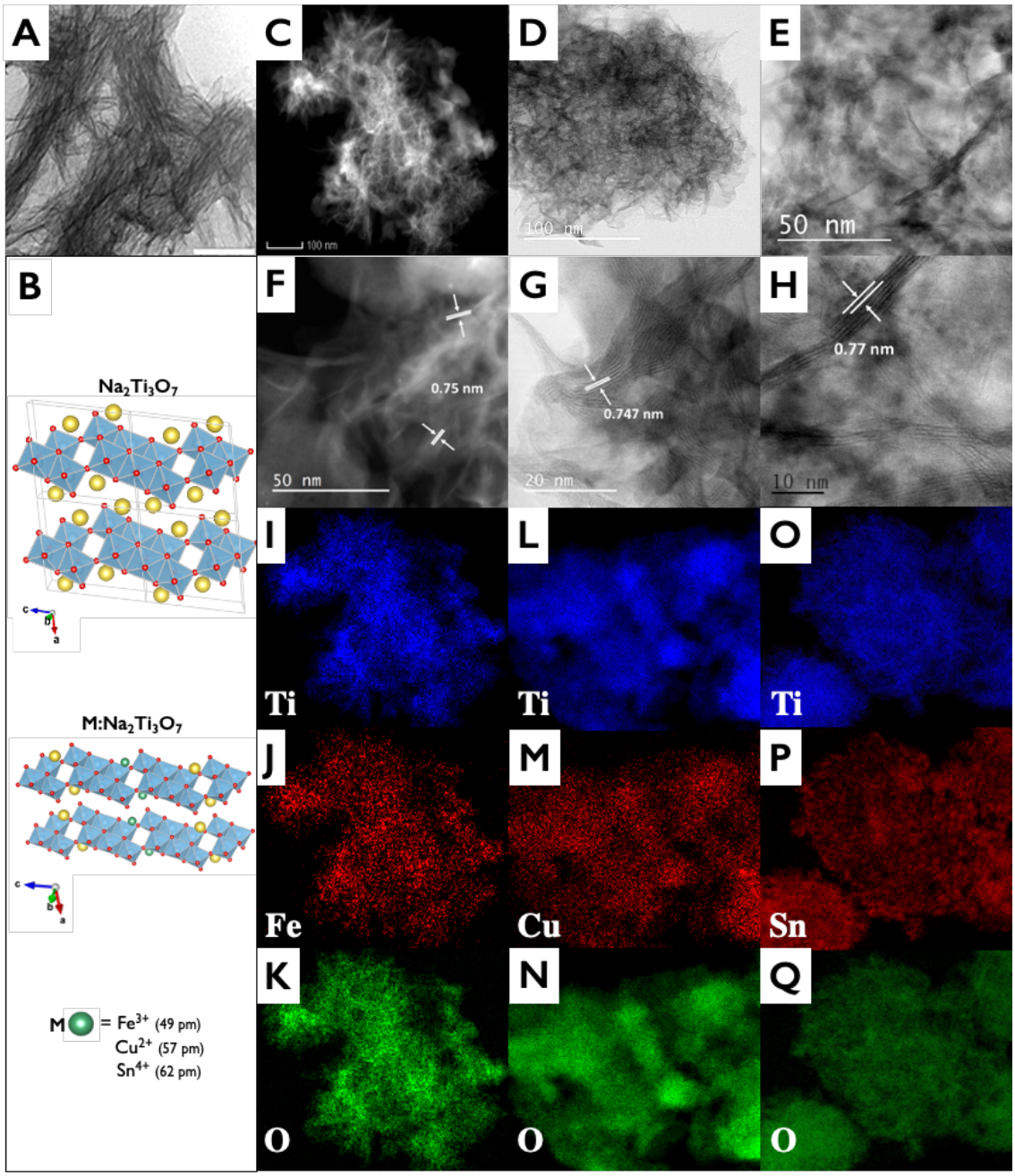

Figure 2. (A) Low magnification TEM image of NTO NWs. (B) Crystal structures of NTO and intercalated transition metal-doped analogues, M:NTO. (C) HAADF-STEM image of 5 wt.% Fe:NTO, (D-E) bright field STEM images of 3 wt.% Cu:NTO and 25 wt.% Sn:NTO NWs, respectively. (F) Dark field and (G-H) bright field HRTEM images of 5 wt.% Fe:NTO, 3 wt.% Cu:NTO and 25 wt.% Sn:NTO NWs, respectively. HAADF-EDS elemental mapping for (I-K) 5 wt.% Fe:NTO, (L-N) 3 wt.% Cu:NTO and (O-Q) 25 wt.% Sn:NTO.

6.3.3. X-ray Aborption Spectroscopy

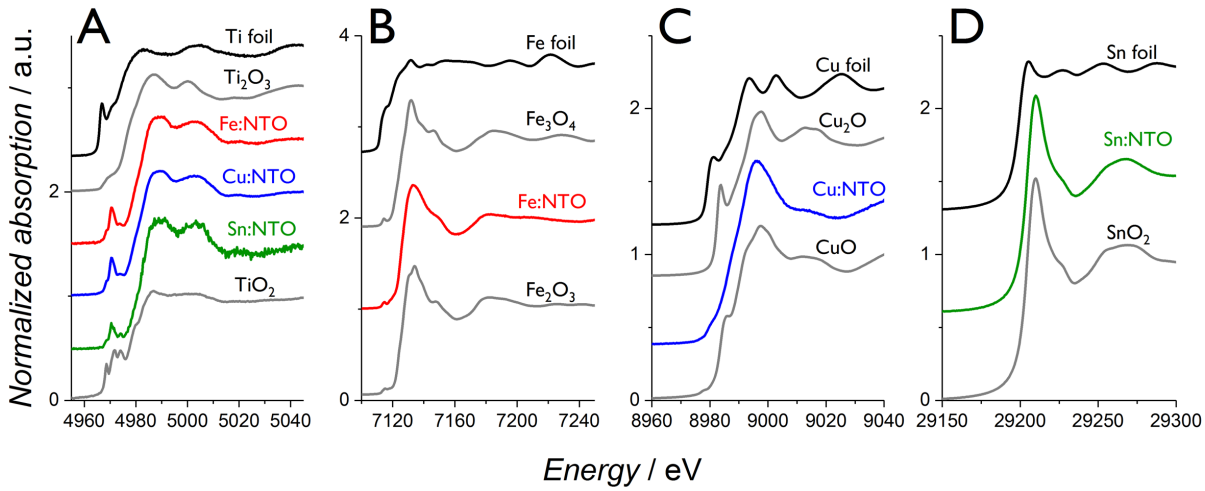

Figure 3. Normalized (A) Ti K-edge, (B) Fe K-edge, (C) Cu K-edge and (D) Sn K-edge XANES spectra of 5 wt.% Fe:NTO, 3 wt.% Cu:NTO and 25 wt.% Sn:NTO nanoparticles synthesized via cathodic corrosion of laser-fabricated alloys compared to the reference compounds; metallic foils and standard metal oxide compounds are represented by black lines and grey lines, respectively.

More detailed information about the bonding environment and the oxidation states of the metal constituents of the NWs formed via cathodic corrosion were determined by XAS. **Figure 3A** compares the normalized Ti K-edge XANES spectra of the synthesized M:NTO samples against Ti foil, Ti_2O_3, and TiO_2 standard compounds. Pre-edge features are sensitive to valence, occurring ~ 2.0 eV lower in Ti^{3+} samples compared to Ti^{4+}.[75] All the spectra show only a weak pre-edge peak relative to Ti foil due to the octahedral local structures around Ti ions.[76] Additionally, the pre-edge features observed for the M:NTO samples display the best agreement with features reported for titanate structures rather than for either anatase or rutile TiO_2.[75] It is challenging to deduce unambiguously the Ti valence because the pre-edge features vary as a function of Ti coordination. However, the edge positions, defined as the maximum of the first-derivative, suggest that Ti atoms in the M:NTO nanoparticles exist in a +4 oxidation state (**Figure S11A**). Furthermore, the emergence of the pre-edge feature at 4974 eV for 25 wt.% Sn:NTO corresponds to rutile TiO_2,[75] further suggesting the presence of the rutile phase in the sample, consistent with our XRD and SEM-EDX analyses.

Figure 3B shows the Fe K-edge XANES spectra of the reference foil and oxide compounds in comparison to the 5 wt.% Fe:NTO NWs. The first-derivative peak of the absorption coefficient appears at 7120.5 eV for Fe^{2+}, while that for Fe^{3+} appears at 7124 eV.[77] Interestingly, for 5 wt.% Fe:NTO, this first-derivative peak appears at around 7124.2 eV (**Figure S11B**), corresponding to a Fe oxidation state ≥ +3, which has been ascribed previously to an electronic inductive effect promoted by surrounding Ti^{4+} ions.[78]

Figure 3C illustrates the characteristic XANES spectra of Cu foil, Cu_2O and CuO standard compounds together with Cu K-edge of the synthesized 3 wt.% Cu:NTO NWs. The edge position was found to be 8979.0, 8980.6 and 8983.6 eV for Cu foil, Cu_2O, and CuO, respectively, in agreement with values reported in the literature.[79-81] The first-derivative peak for Cu:NTO indicated that Cu^{2+} is present (**Figure S11C**). However, the near edge structure did not allow for the unambiguous determination of the corresponding Cu coordination.

Finally, **Figure 3D** shows the Sn K-edge XANES spectra for 25 wt.% Sn:NTO as well as the reference spectra of Sn foil and SnO_2. The edge of the Sn foil was located at 29200 eV, in agreement with data in the literature.[82] The edge position of 25 wt.% Sn:NTO corresponds to 29204 eV, which is the value measured for the SnO_2 reference, indicating that the Sn exists as tetravalent Sn^{4+} ions (**Figure S11D**). The appearance of the 25 wt.% Sn:NTO spectra closely resembles that of SnO_2, suggesting that SnO_2 is present.

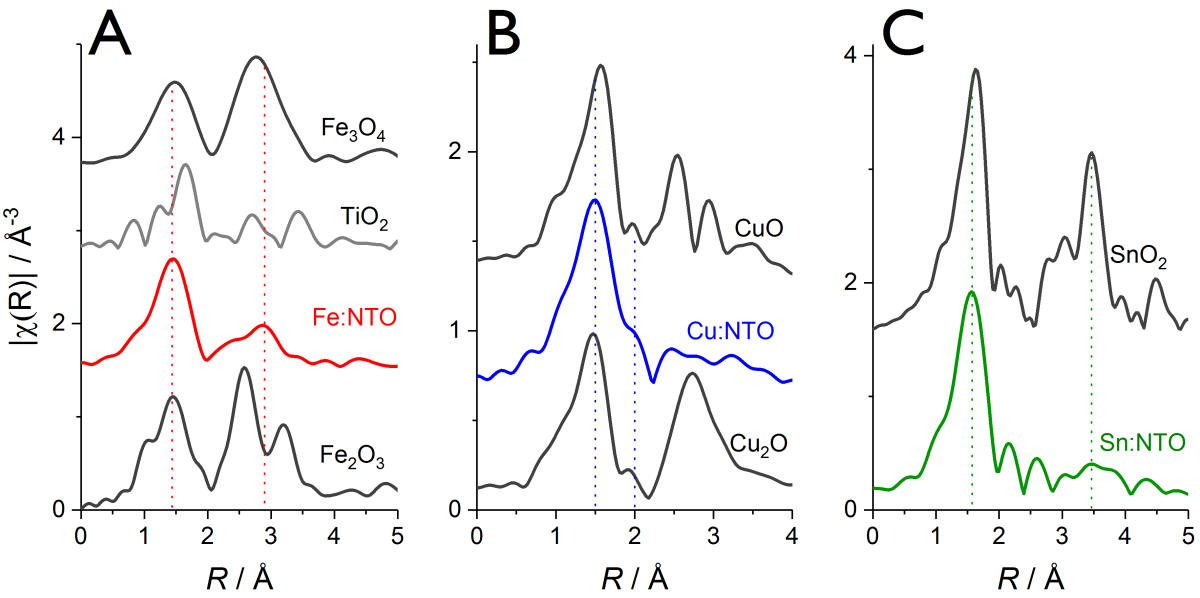

Figure 4. EXAFS Fourier Transforms of $k^2\chi(k)$ functions for (A) Fe K-edge, (B) Cu K-edge and (C) Sn K-edge. The spectra for the standard oxide compound references are shown for comparison.

Figure 4A shows the Fe K-edge EXAFS Fourier transforms (FTs) of 5 wt.% Fe:NTO in addition to the Fe_2O_3, Fe_3O_4 and TiO_2 standard compound references. The FT spectra show two strong peaks below 4 Å. The first, at around 1.5 Å (without phase correction), corresponds to the first coordination shell (Fe-O) and matches well with the first strong peak identifiable in the FT spectrum of Fe_3O_4. A quick first shell fit resulted in a coordination number of ~4 for the Fe-O path, and a bond distance of 1.94 Å. The second peak around 3 Å is associated with the second coordination shell, with potential Fe-Fe, Fe-Ti and Fe-O contributions together with multiple scattering paths. Looking at the data qualitatively, the formation of Fe_2O_3 and Fe_3O_4 can be ruled out as the FT of the NWs is quite different, particularly above 3 Å. Moreover, the position of the second shell peaks differs from that of Ti–Ti_1 for TiO_2, suggesting that the Fe atoms do not simply substitute for Ti. The fit data in *k*-space and the corresponding fitted parameters at the Fe K-edge are reported in **Figure S12(A,B)** and **Table S3**.

Figure 4B shows Cu K-edge EXAFS FTs of 3 wt.% Cu:NTO and the reference samples. The first peak at ~1.5 Å (phase shift was not corrected) is due to the Cu-O scattering in the first shell. The second coordination peaks – between 2 and 3 Å – are weak in comparison to the CuO reference but are not absent, suggesting a scattering from a heavier element. However, both SEM-EDS and TEM-EDS analyses rule out the presence of elements heavier than Cu in the sample. Additionally, it has been reported that a noticeable second shell EXAFS feature at ~ 2.4 Å is observed in CuO and Cu-doped titanate nanotubes, attributable to the presence of Cu-Cu bonding interactions. [83, 84] Comparison of our Cu K-edge EXAFS spectra to the literature indicate that Cu-Cu bonding in our sample is of low occurrence, as this feature is not present. Additionally, the poor resolution of the higher shell features, including Cu-Ti bonding (>3 Å), limit the depth of discussion.[83] A quick first shell fit was performed to the data using one oxygen scattering path (**Figure S12 C&D** and **Table S4**), resulting in a coordination number N=3.5 at Cu-O distance of 1.93 Å, suggesting that the Cu is in a tetrahedral coordination, in agreement with existing literature.[84]

At the Sn K-edge (**Figure 4C**), the EXAFS spectrum of 25 wt.% Sn:NTO is dominated by the Sn-O coordination, suggestive of the formation of either a SnO_2 layer or isolated SnO_2 particles, in agreement with XRD, SEM-EDX and STEM-EDS analysis. The Sn-Ti interaction was not detected, which could be attributed to the fact that it is too small compared with the Sn-O signal or non-existent. The EXAFS data and the corresponding fitted parameters at the Sn K-edge reported in **Figure S12(E,F)** and **Table S5**, confirmed an octahedral coordination of Sn. Unfortunately, the Ti K-edge EXAFS functions are not usable because of poor statistics.

6.3.4. Summary of physical characterization

The combination of the different physicochemical characterization techniques suggests that crystalline NTO NWs are synthesized by electrochemically etching Ti electrodes in 10 M NaOH under an applied AC voltage of 0 to -10 V. The NWs agglomerate to form discrete

particles with high surface area and metal doped titanates with analogous structure are produced when Ti alloys are employed. STEM-EDS and SEM-EDX confirm excellent homogeneity of constituent elements in all cases. XAS and XRD suggest that the dopant metal cations predominantly intercalate between Ti-O octahedral layers rather than substituting for Ti and that the binary oxides of the dopant metal are absent in the case of Fe and Cu. For 25 wt.% Sn:NTO, where the concentration of Sn in the parent alloy was > 40 at.%, XRD, XAS, SEM-EDX, STEM (Figure S8) and HRTEM all indicate the presence of rutile SnO_2 in addition to Sn-doped TiO_2 and titanate NWs, suggesting that non-trivial differences in the rate of chemical oxidation for atomized Ti and Sn exist.

6.3.5. Evaluation of PEC activity

Chronoamperometry (*I-t*) under interrupted illumination measurements were employed to determine the PEC properties of the oxide nanomaterials in aqueous 0.1 M NaOH. The selection of potential at which the photocurrents were measured was based on the comparison of CV response in the dark and under illumination (**Figure S14**). Figure 5 shows that charge-carrier recombination transients were observed during the 'on' portion of the chopped light cycles in all *I-t* curves, additional evidence of PEC activity.[32] At 1.5 V vs RHE the M:NTO samples did not display significant improvement towards OER in comparison with the undoped titanate nanocatalyst, in agreement with *J-E* curves under interrupted illumination (**Figure S15**). At a more oxidative potential (1.8 V vs RHE), reduced photocurrents were measured on 5 wt.% Fe:NTO and 25 wt.% Sn:NTO. The Fe(III) oxidation state, determined by XANES analysis, is reported to cause an increase in bulk photogenerated charge carrier recombination by serving as hole traps, thereby limiting the flux of holes to the surface to conduct the OER and reducing the relative magnitude of photocurrents measured.[85, 86] In the case of the Sn-doped titanate, because the Fermi level of SnO_2 is lower than that of TiO_2, it was expected that the photogenerated electrons would transfer from the

NTO to the SnO_2, resulting in a reduction of the number of photogenerated electrons on the surface of NTO and subsequent surface-recombination events. However, STEM characterization of the 25 wt.% Sn:NTO sample suggest that the SnO_2 present in the sample acts as a passivating shell atop the Sn:NTO NWs. In this scenario, the photogenerated holes that migrate to the surface of the Sn:NTO are prone to undergo annihilation with the increased electron occupancy of the SnO_2 shell conduction band, thereby decreasing the observed PEC activity.

Interestingly, 3 wt.% Cu:NTO nanoparticles demonstrated a significant increase in the steady-state photocurrent for the OER in comparison with the undoped titanate. UV-vis absorption spectroscopy indicated that 3 wt.% Cu:NTO possessed enhanced light absorption capabilities relative to NTO, in addition to enhanced absorption intensity in the visible region (Figure S13). Doping TiO_2 with Cu is reported to decrease the magnitude of its band gap by lowering the position of the conduction band and the introduction of inter-band levels by spin-up Cu 3d states.[38, 87] The combination of these two effects serves to increase the visible light absorption capabilities of TiO_2. Thus, we anticipate that an analogous effect is wrought in the case of NTO and is the main contributor to the observed relative increase in photocurrent upon doping with Cu^{2+}. The magnitude of the current transients were also larger indicating an increase in charge-carrier recombination, which can be attributed to an increase in electron flux due to the presence of Cu dopants. Increases in catalyst loading and subsequent increases in photocurrent and recombination transients, further demonstrated the PEC catalytic properties of 3 wt.% Cu:NTO towards the OER (**Figure S16**).

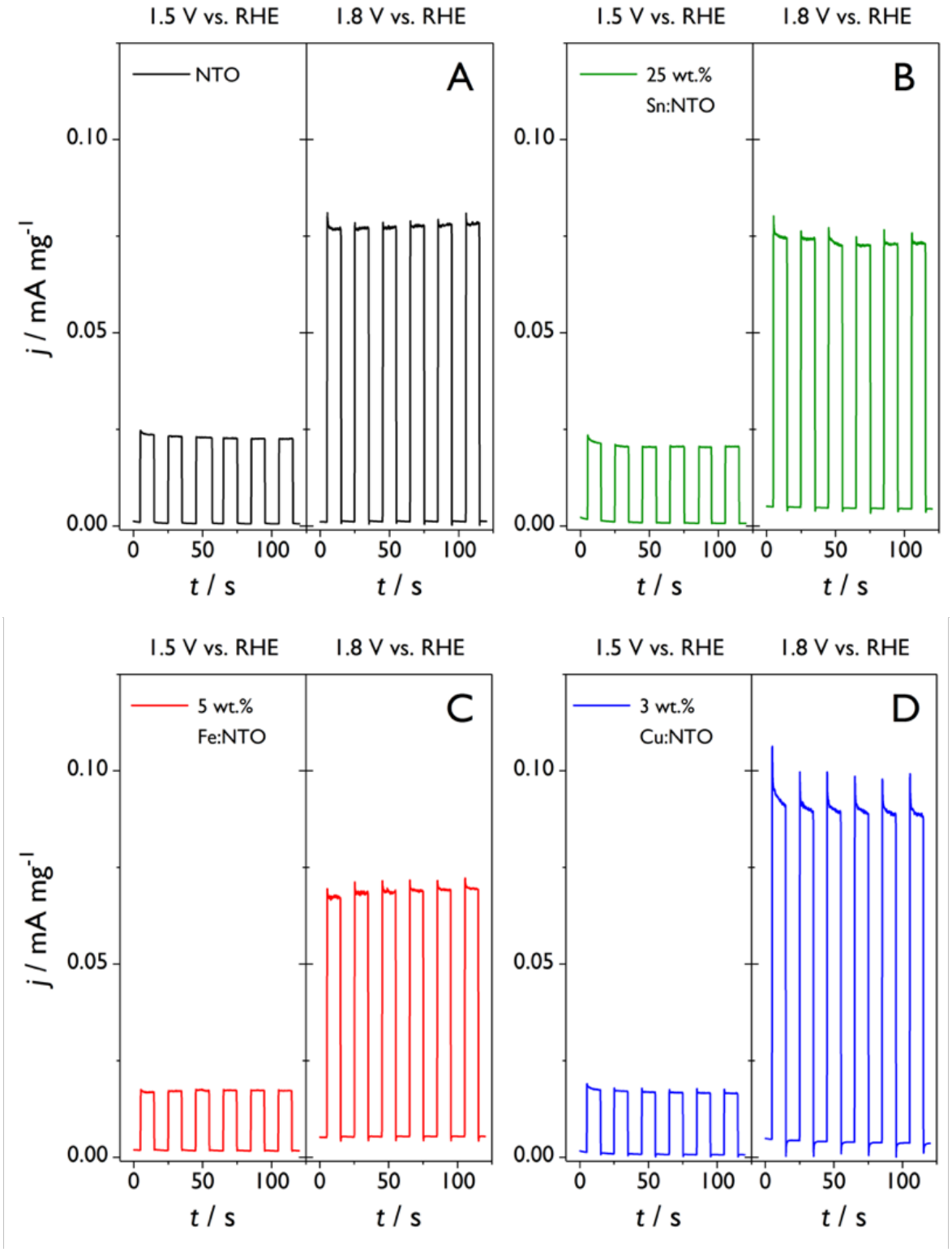

Figure 5. Chopped light *I-t* curves, at 1.5 V (η ~300 mV) and 1.8 V (η ~500 mV) vs. RHE in 0.1 M NaOH, of titanate nanoparticles synthesized via cathodic corrosion: (A) NTO, (B) 25 wt.% Sn:NTO, (C) 5 wt.% Fe:NTO and (D) 3 wt.% Cu:NTO. The potentials displayed correspond to OER overpotentials of ~300 mV and 500 mV, respectively.

The improvement in PEC activity for 3 wt.% Cu:NTO prompted investigation of the effect of increasing Cu content. Accordingly, a laser-fabricated $Cu_{19.31}Ti_{80.68}$ alloy was employed as WE. The suspension obtained from the electrochemical synthesis possessed a pale blue tint (**Figure S17**) which disappeared during the electrolyte removal centrifugation process. XRD patterns suggested that attempts to increase the Cu dopant concentration were successful. A shift in the NTO (100) peak position from 11.00° to 11.39°, relative to 3 wt.% Cu:NTO, indicated a decrease in lattice parameter whilst observed signal broadening was indicative of a decrease in long-range crystallinity (**Figure S18A**). STEM-EDS analyses (**Figure S18B**) revealed that aggregated NWs had been produced but the relative composition of Cu was noticeably lower in the titanate than in the parent alloy, 9 wt.% (4 at.%) (**Table S7**). Comparison of only the relative metal atomic ratios of Cu and Ti in the NWs and the alloy precursor revealed reasonable agreement between the parent alloy and the NWs (**Table S7**).

In order to investigate the cause of the blue tint observed in the 9 wt.% Cu:NTO suspension, a Cu wire was subjected to cathodic corrosion under identical conditions to the alloys. A clear, light-blue aqueous solution of $Cu(OH)_2/Cu(OH)_4^{2-}$ (**Figure S18C**) confirmed that Cu is susceptible to form aqueous metal complexes under the specific cathodic corrosion conditions employed (AC voltage between 0 and -10 V; 100 Hz squarewave; 10 M NaOH electrolyte) and provides a plausible explanation for the low Cu content observed in the nanoparticles. In addition, the presence of peaks at 2θ = 51.62° and 60.35° in the XRD pattern of the $Cu_{19.32}Ti_{80.68}$ alloy, corresponding to the (111) and (200) planes of fcc Cu, not observed for $Cu_{6.28}Ti_{93.72}$, suggest the presence of Cu and Ti metal segregation at higher alloying concentrations (Figure S18D). The reduced content of Cu in the 9 wt.% Cu:NTO NWs can be explained by the low limit of incorporation of Cu ions into TiO_2.[60, 62] Albeit a significantly larger concentration of copper was not achieved, the HAADF-STEM imaging and EDS elemental mapping demonstrated that the Cu and Ti were homogeneously distributed throughout the 9

wt.% Cu:NTO NWs (**Figure 6A**). Negligible differences in the Cu K-edge XANES (**Figure 6B**) and EXAFS (**Figure 6C**) spectra were observed. However, the second shell interactions observed at the Cu K-edge (Cu-Cu or Cu-Ti) have more resolved distances in the case of 9 wt.% Cu:NTO, where the Cu content is higher and thus the relative frequency of the interactions is increased. Additionally, FT EXAFS simulated fits for the sample with increased Cu content have a lower value for the R_{factor} (**Figure S19** and **Table S4**). Albeit that the visible light absorption intensity for 9 wt.% Cu:NTO was enhanced relative to NTO, 3 wt.% Cu:NTO possessed greater absorption at all wavelengths (**Figure S20**).

The PEC results (**Figure 7**) further demonstrated that Cu:NTO nanomaterials produced via cathodic corrosion of laser-fabricated alloys are photoelectrochemically active towards OER. However, increasing the relative Cu dopant concentration did not yield any increase in PEC activity, in agreement with the UV-vis analysis. Rather, photocurrent density was reduced while the magnitude of the photocurrent recombination transients increased and the oxidation onset potential was shifted by ~90 mV to a more oxidative potential (**Figure S21**), suggesting that increasing the concentration of Cu^{2+} increased the number of charge-carrier recombination sites and hindered the catalytic activity observed, in agreement with existing reports regarding Cu-doped TiO_2 for the photocatalytic oxidation of methylene blue.[62] Furthermore, it has been reported that the optimal Cu dopant concentration is ~ 0.5 at.%,[88] thus increasing the Cu concentration did not improve the PEC activity.

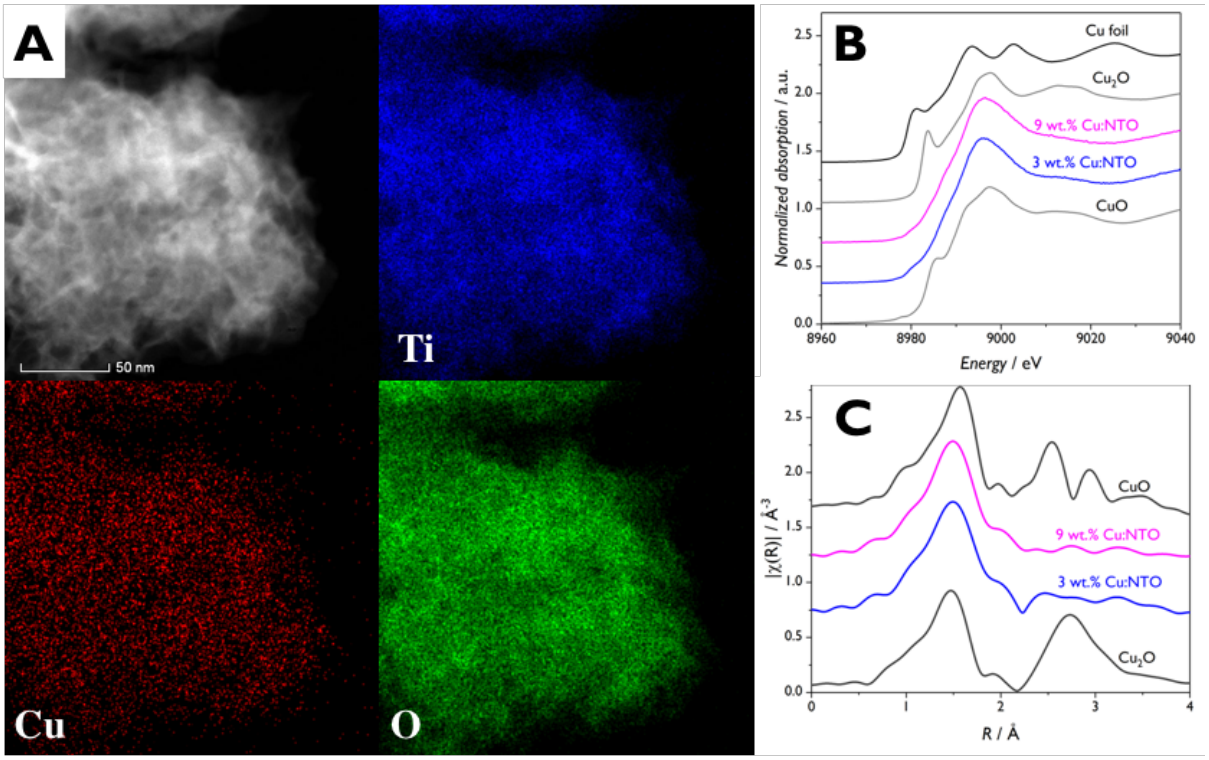

Figure 6. (A) HAADF-STEM and corresponding EDS elemental mapping of 9 wt.% Cu:NTO NWs synthesized by cathodic corrosion of $Cu_{19.32}Ti_{80.68}$ in 10 M NaOH. Comparative (B) normalized XANES and (C) EXAFS Fourier Transforms of $k^2\chi(k)$ functions for Cu:NTO NWs at the Cu K-edge; metallic foils and standard metal oxide compounds are represented by black lines and grey lines, respectively.

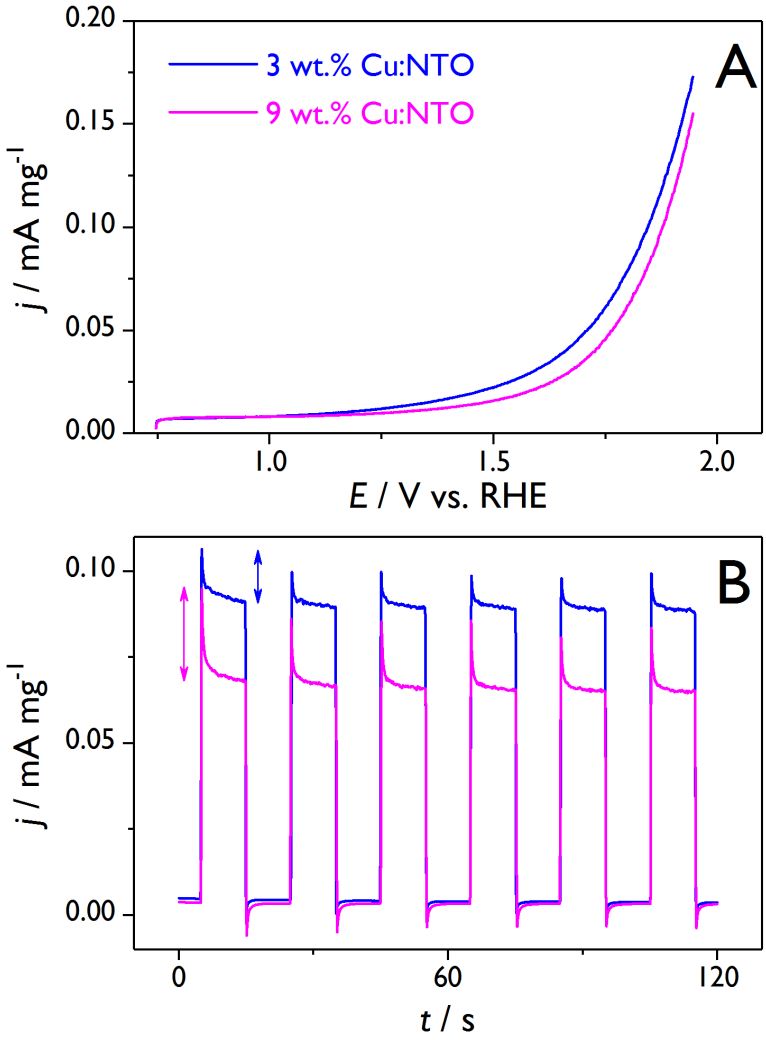

Figure 7. (A) Anodic voltammetric profiles of Cu:NTO NWs under incident white polychromatic light normalized by the mass loading of each photocatalyst; ν=20 mV s^{-1}. (B) Chopped light *I-t* curves at 1.8 V vs RHE; arrows correspond to the relative magnitude of recombination-transient photocurrent density for each material.

6.4. Conclusions

We successfully demonstrated the synthesis of mixed metal oxides via the cathodic corrosion of laser-fabricated alloy samples, providing a rapid, electrochemical route for the production, screening and discovery of high surface area nanomaterials with controlled composition. Specifically, we synthesized NTO and M:NTO nanomaterials, where M (= Fe, Cu or Sn) was incorporated into nanowires that agglomerated to generate higher surface area particles.

We explored the synergy between cathodic corrosion and SDA to produce nanostructured mixed metal oxide materials in a single step without the addition of dopant-metal precursors in the electrolyte. The retention of the relative composition of the alloys was best achieved in the FeTi system, which was essentially identical to the parent alloy. Compositional retention was poorest in the case of SnTi, with noticeable difference between the parent alloy and 25 wt.% Sn:NTO, in addition to a significantly large value of standard deviation, due to the high dopant concentration and multiple crystalline phases of the alloy detected by XRD (**Figure S2**). A smaller value of standard deviation was observed for 3 wt.% Cu:NTO at the expense of poor retention of composition. Nevertheless, we were able to identify the source of this discrepancy, ascribed to the tendency of Cu ions to form soluble aqueous complexes in the presence of ^{-}OH and a maximum concentration of Cu intercalation in the oxide matrix. Good retention of starting relative composition is achieved when optimal cathodic corrosion conditions are employed, which requires consideration of the etching electrolyte is important to this effect.

XRD and HAADF EDS mapping demonstrated that the distribution of elements in the NWs synthesized by cathodic corrosion was homogenous for all samples, while HRTEM imaging demonstrated that the synthesized NWs were crystalline. SnO_2 rutile phase was observed in the XRD pattern of 25 wt.% Sn:NTO and was attributed to the varying etching rates of different SnTi phases but could be the result of different rates of chemical oxidation upon interaction with dissolved oxygen species. The wide range of relative metal compositions obtained by EDS was due to the presence of SnO_2 and Sn:NTO phases.

While all samples displayed PEC activity towards oxygen evolution under white light illumination, only 3 wt.% Cu:NTO NWs, displayed a higher activity than undoped NTO. To the best of our knowledge this was the first demonstration of the PEC activity of intercalated copper titanate nanomaterials towards the OER. Exploiting the newly developed ability to

modify the atomic percentage of Cu, we explored the effect of increasing it. However, increases in Cu concentration were detrimental to the OER activity. No improvement in PEC activity was observed for 5 wt.% Fe:NTO relative to the undoped NWs. This was attributed to the Fe(III) oxidation state in the nanostructures which serve as recombination centers for photogenerated charge carrier species.

In summary, this work showcases the ability of the cathodic corrosion method to rapidly produce metal-doped metal oxide nanostructures by the single-step electrochemical etching of alloys at ambient temperature. Future directions in our laboratories will explore the fine control over the size and structure of the nanoparticles, as well as the application of the methodology to a wider range of metal oxide systems and the inclusion of a variety of elements, with higher refinement of dopant concentration, for systematic studies on the impact of compositionally-controlled dopants on the electrochemical performance of metal oxide NWs for applications in energy technologies.

6.5. Acknowledgments

M.J.L. acknowledges the University of Birmingham for financial support through Ph.D. scholarships at the School of Chemistry. V.C. and P.R. are thankful to the UK Catalysis Hub (EPSRC Grants EP/K014706/1 and EP/K014714/1) for resources and support. We acknowledge Diamond Light Source for provision of beamtime (SP15151). X.S., Q.W., and M.G. acknowledge the SUSTech Pico Center that receives funding from the Shenzhen government, where the STEM analyses were conducted. M.J.L, P.R., and J.R.-L acknowledge financial support from the BRIDGE program between the University of Illinois and the University of Birmingham through the Transatlantic Collaboration Fund. P.R. acknowledges the University of Birmingham for financial support through the Birmingham fellowship program.

References

1. H. J. Neef, *Energy*, 2009, **34**, 327-333.

2. R. Amirante, E. Cassone, E. Distaso and P. Tamburrano, *Energy Convers. Manage.*, 2017, **132**, 372-387.

3. K. Liang, L. Li and Y. Yang, *ACS Energy Lett.*, 2017, **2**, 373-390.

4. J. K. Stolarczyk, S. Bhattacharyya, L. Polavarapu and J. Feldmann, *ACS Catal.*, 2018, **8**, 3602-3635.

5. K. Lee, A. Mazare and P. Schmuki, *Chem. Rev.*, 2014, **114**, 9385-9454.

6. J. Zhang, G. Xiao, F.-X. Xiao and B. Liu, *Mater. Chem. Front.*, 2017, **1**, 231-250.

7. M. Ge, C. Cao, J. Huang, S. Li, Z. Chen, K.-Q. Zhang, S. S. Al-Deyab and Y. Lai, *J. Mater. Chem. A*, 2016, **4**, 6772-6801.

8. M. Ota, Y. Hirota, Y. Uchida, Y. Sakamoto and N. Nishiyama, *Langmuir*, 2018, **34**, 6814-6819.

9. J. Liu, M. N. Banis, B. Xiao, Q. Sun, A. Lushington, R. Li, J. Guo, T.-K. Sham and X. Sun, *J. Mater. Chem. A*, 2015, **3**, 24281-24288.

10. Z. Chen, I. Belharouak, Y. K. Sun and K. Amine, *Adv. Funct. Mater.*, 2013, **23**, 959-969.

11. C. Li, Z. Wang, S. Li, J. Cheng, Y. Zhang, J. Zhou, D. Yang, D.-G. Tong and B. Wang, *ACS Appl. Mater. Interfaces*, 2018, **10**, 18390-18399.

12. X. Lu, G. Wang, T. Zhai, M. Yu, J. Gan, Y. Tong and Y. Li, *Nano Lett*, 2012, **12**, 1690-1696.

13. W. Zhou, X. Liu, Y. Sang, Z. Zhao, K. Zhou, H. Liu and S. Chen, *ACS Appl. Mater. Interfaces*, 2014, **6**, 4578-4586.

14. L. Chu, Z. Qin, J. Yang and X. a. Li, *Sci. Rep.*, 2015, **5**.

15. K. Sarkar, E. V. Braden, T. Fröschl, N. Hüsing and P. Müller-Buschbaum, *J. Mater. Chem. A*, 2014, **2**, 15008-15014.

16. K. Li, J. Xu, W. Shi, Y. Wang and T. Peng, *J. Mater. Chem. A*, 2014, **2**, 1886-1896.

17. Y. Ma, X. Wang, Y. Jia, X. Chen, H. Han and C. Li, *Chem. Rev.*, 2014, **114**, 9987-10043.

18. K. R. Reyes-Gil and D. B. Robinson, *ACS Appl. Mater. Interfaces*, 2013, **5**, 12400-12410.

19. B. H. Simpson and J. Rodríguez-López, *Analytical Methods*, 2015, **7**, 7029-7041.

20. X. Chen, S. Shen, L. Guo and S. S. Mao, *Chem. Rev.*, 2010, **110**, 6503-6570.

21. J. Cai, X. Wu, S. Li and F. Zheng, *ACS Sustainable Chem. Eng.*, 2016, **4**, 1581-1590.

22. X. Zhang, Y. Liu, S.-T. Lee, S. Yang and Z. Kang, *Energy Environ. Sci.*, 2014, **7**.

23. M. Graetzel and R. F. Howe, *J. Phys. Chem.*, 1990, **94**, 2566-2572.

24. W. Choi, A. Termin and M. R. Hoffmann, *Angew. Chem., Int. Ed.*, 1994, **33**, 1091-1092.

25. M. Khan, S. Woo and O. Yang, *Int. J. Hydrogen Energy*, 2008, **33**, 5345-5351.

26. I. Ganesh, P. P. Kumar, I. Annapoorna, J. M. Sumliner, M. Ramakrishna, N. Y. Hebalkar, G. Padmanabham and G. Sundararajan, *Appl. Surf. Sci.*, 2014, **293**, 229-247.

27. Y. Liu, W. Liang, W. Zhang, J. Zhang and P. Han, *Solid State Commun.*, 2013, **164**, 27-31.

28. R. T. Ako, P. Ekanayake, D. J. Young, J. Hobley, V. Chellappan, A. L. Tan, S. Gorelik, G. S. Subramanian and C. M. Lim, *Appl. Surf. Sci.*, 2015, **351**, 950-961.

29. H. Moradi, A. Eshaghi, S. R. Hosseini and K. Ghani, *Ultrason. Sonochem.*, 2016, **32**, 314-319.

30. Y. Duan, N. Fu, Q. Liu, Y. Fang, X. Zhou, J. Zhang and Y. Lin, *J. Phys. Chem. C*, 2012, **116**, 8888-8893.

31. E. Morgado, B. A. Marinkovic, P. M. Jardim, M. A. S. de Abreu, M. d. G. C. Rocha and P. Bargiela, *Mater. Chem. Phys.*, 2011, **126**, 118-127.

32. L. M. Peter and K. G. Upul Wijayantha, *ChemPhysChem*, 2014, **15**, 1983-1995.

33. D. L. Morgan, G. Triani, M. G. Blackford, N. A. Raftery, R. L. Frost and E. R. Waclawik, *J. Mater. Sci.*, 2011, **46**, 548-557.

34. J. Xia, H. Zhao, W. K. Pang, Z. Yin, B. Zhou, G. He, Z. Guo and Y. Du, *Chem. Sci.*, 2018, **9**, 3421-3425.

35. D. V. Bavykin, J. M. Friedrich and F. C. Walsh, *Adv. Mater.*, 2006, **18**, 2807-2824.

36. T. Aaltonen, M. Alnes, O. Nilsen, L. Costelle and H. Fjellvåg, *J. Mater. Chem.*, 2010, **20**.

37. T. Kasuga, M. Hiramatsu, A. Hoson, T. Sekino and K. Niihara, *Langmuir*, 1998, **14**, 3160-3163.

38. Y. An, Z. Li and J. Shen, *Phys. B (Amsterdam, Neth.)*, 2013, **429**, 127-132.

39. N. M. dos Santos, J. M. Rocha, J. M. E. Matos, O. P. Ferreira, J. M. Filho, B. C. Viana and A. C. Oliveira, *Appl. Catal., A*, 2013, **454**, 74-80.

40. W. Wen, J.-m. Wu, Y.-z. Jiang, S.-l. Yu, J.-q. Bai, M.-h. Cao and J. Cui, *Sci. Rep.*, 2015, **5**, 959-969.

41. M. L. Kromer, J. Monzo, M. J. Lawrence, A. Kolodziej, Z. T. Gossage, B. H. Simpson, S. Morandi, A. Yanson, J. Rodriguez-Lopez and P. Rodriguez, *Langmuir*, 2017, **33**, 13295-13302.

42. M. J. Lawrence, A. Kolodziej and P. Rodriguez, *Curr. Opin. Electrochem.*, 2018, **10**, 7-15.

43. B. Endrődi, E. Kecsenovity, K. Rajeshwar and C. Janáky, *ACS Appl. Energy Mater.*, 2018, **1**, 851-858.

44. T.-S. Su, Y.-S. Wu, Y.-L. Tung and T.-C. Wei, *ACS Appl. Energy Mater.*, 2018, **1**, 2429-2433.

45. N. T. Nguyen, I. Hwang, T. Kondo, T. Yanagishita, H. Masuda and P. Schmuki, *Electrochem. Commun.*, 2017, **79**, 46-50.

46. C. Qiu, G. A. Ravi, C. Dance, A. Ranson, S. Dilworth and M. M. Attallah, *J. Alloys Compd.*, 2015, **629**, 351-361.

47. J. Garcia-Canadas, N. J. Adkins, S. McCain, B. Hauptstein, A. Brew, D. J. Jarvis and G. Min, *ACS Comb. Sci.*, 2016, **18**, 314-319.

48. A. I. Yanson, P. Rodriguez, N. Garcia-Araez, R. V. Mom, F. D. Tichelaar and M. T. Koper, *Angew. Chem., Int. Ed.*, 2011, **50**, 6346-6350.

49. P. Rodriguez, F. D. Tichelaar, M. T. Koper and A. I. Yanson, *J. Am. Chem. Soc.*, 2011, **133**, 17626-17629.

50. B. Vanrenterghem, M. Bele, F. R. Zepeda, M. Šala, N. Hodnik and T. Breugelmans, *Appl. Catal., B*, 2018, **226**, 396-402.

51. A. I. Yanson, P. V. Antonov, P. Rodriguez and M. T. M. Koper, *Electrochim. Acta*, 2013, **112**, 913-918.

52. E. Bennett, J. Monzó, J. Humphrey, D. Plana, M. Walker, C. McConville, D. Fermin, A. Yanson and P. Rodriguez, *ACS Catal.*, 2016, **6**, 1533-1539.

53. J. Simonet, *Journal of Electroanalytical Chemistry*, 2006, **593**, 3-14.

54. J. Ghilane, M. Guilloux-Viry, C. Lagrost, J. Simonet and P. Hapiot, *J Am Chem Soc*, 2007, **129**, 6654-6661.

55. F. Lu, X. Ji, Y. Yang, W. Deng and C. E. Banks, *RSC Adv.*, 2013, **3**.

56. A. J. Dent, G. Cibin, S. Ramos, A. D. Smith, S. M. Scott, L. Varandas, M. R. Pearson, N. A. Krumpa, C. P. Jones and P. E. Robbins, *J. Phys.: Conf. Ser.*, 2009, **190**.

57. M. Newville, *J. Synchrotron Radiat.*, 2001, **8**, 96-100.

58. B. Ravel and M. Newville, *J. Synchrotron Radiat.*, 2005, **12**, 537-541.

59. G. H. Du, Q. Chen, R. C. Che, Z. Y. Yuan and L. M. Peng, *Appl. Phys. Lett.*, 2001, **79**, 3702-3704.

60. P. Umek, M. Pregelj, A. Gloter, P. Cevc, Z. Jagličić, M. Čeh, U. Pirnat and D. Arčon, *J. Phys. Chem. C*, 2008, **112**, 15311-15319.

61. A. Rudola, K. Saravanan, C. W. Mason and P. Balaya, *J. Mater. Chem. A*, 2013, **1**, 2653-2662.

62. F. Bensouici, M. Bououdina, A. A. Dakhel, R. Tala-Ighil, M. Tounane, A. Iratni, T. Souier, S. Liu and W. Cai, *Appl. Surf. Sci.*, 2017, **395**, 110-116.

63. T. Yamanaka, R. Kurashima and J. Mimaki, *Z. Kristallogr.*, 2000, **215**.

64. Y. Akila, N. Muthukumarasamy, S. Agilan, S. Senthilarasu and D. Velauthapillai, *Mater. Sci. Semicond. Process.*, 2017, **57**, 24-31.

65. P. Rodriguez, D. Plana, D. J. Fermin and M. T. M. Koper, *J. Catal.*, 2014, **311**, 182-189.

66. J. Feng, D. Chen, A. S. Sediq, S. Romeijn, F. D. Tichelaar, W. Jiskoot, J. Yang and M. T. M. Koper, *ACS Appl. Mater. Interfaces*, 2018, **10**, 9532-9540.

67. J. N. Kuhn, C.-K. Tsung, W. Huang and G. A. Somorjai, *J. Catal.*, 2009, **265**, 209-215.

68. F. J. Vidal-Iglesias, J. Solla-Gullón, E. Herrero, V. Montiel, A. Aldaz and J. M. Feliu, *Electrochem. Commun.*, 2011, **13**, 502-505.

69. J. Monzo, M. T. Koper and P. Rodriguez, *ChemPhysChem*, 2012, **13**, 709-715.

70. X. Ding, X. G. Xu, Q. Chen and L. M. Peng, *Nanotechnology*, 2006, **17**, 5423-5427.

71. C. Huang, X. Liu, L. Kong, W. Lan, Q. Su and Y. Wang, *Appl. Phys. A*, 2007, **87**, 781-786.

72. P. Kasian, T. Yamwong, P. Thongbai, S. Rujirawat, R. Yimnirun and S. Maensiri, *Jpn. J. Appl. Phys.*, 2014, **53**.

73. D. Wu, Y. Chen, J. Liu, X. Zhao, A. Li and N. Ming, *Appl. Phys. Lett.*, 2005, **87**.

74. P. Umek, C. Bittencourt, A. Gloter, R. Dominko, Z. Jagličić, P. Cevc and D. Arčon, *J. Phys. Chem. C*, 2012, **116**, 11357-11363.

75. G. A. Waychunas, *Am. Mineral.*, 1987, **72**, 89-101.

76. F. Farges, G. E. Brown and J. J. Rehr, *Phys. B (Amsterdam, Neth.)*, 1997, **56**, 1809-1819.

77. C. Piquer, M. A. Laguna-Marco, A. G. Roca, R. Boada, C. Guglieri and J. Chaboy, *J. Phys. Chem. C*, 2014, **118**, 1332-1346.

78. F. Liu, K. Asakura, P. Xie, J. Wang and H. He, *Catal. Today*, 2013, **201**, 131-138.

79. A. Gaur and B. D. Shrivastava, *Acta Phys. Pol., A*, 2012, **121**, 647-652.

80. C. S. Chen, C. C. Chen, T. W. Lai, J. H. Wu, C. H. Chen and J. F. Lee, *J. Phys. Chem. C*, 2011, **115**, 12891-12900.

81. C. S. Chen, T. C. Chen, C. C. Chen, Y. T. Lai, J. H. You, T. M. Chou, C. H. Chen and J. F. Lee, *Langmuir*, 2012, **28**, 9996-10006.

82. G. M. Dalpian, Q. Liu, C. C. Stoumpos, A. P. Douvalis, M. Balasubramanian, M. G. Kanatzidis and A. Zunger, *Phys. Rev. Mater.*, 2017, **1**.

83. P. Khemthong, P. Photai and N. Grisdanurak, *Int. J. Hydrogen Energy*, 2013, **38**, 15992-16001.

84. A. Sharma, M. Varshney, J. Park, T.-K. Ha, K.-H. Chae and H.-J. Shin, *RSC Adv.*, 2015, **5**, 21762-21771.

85. L. Kavan and M. Grätzel, *Electrochim. Acta*, 1995, **40**, 643-652.

86. Y. Wang, H. Cheng, Y. Hao, J. Ma, W. Li and S. Cai, *J. Mater. Sci.*, 1999, **34**, 3721-3729.

87. L. Zhou, L. Wei, Y. Yang, X. Xia, P. Wang, J. Yu and T. Luan, *Chemical Physics*, 2016, **475**, 1-8.

88. G. Colón, M. Maicu, M. C. Hidalgo and J. A. Navío, *Appl. Catal., B*, 2006, **67**, 41-51.

6.6. Supporting Information

Electrochemical Synthesis of Nanostructured Metal-Doped Titanates and Investigation of Their Activity as Oxygen Evolution Photoanodes

Matthew J. Lawrence,[†,‡] Veronica Celorrio,[∥,⊥] Xiaobo Shi,[#] Qi Wang,[#] Alex Yanson,[▽] Nicholas J. E. Adkins,[§] Meng Gu,[,#] Joaquín Rodríguez-López,[*,○] and Paramaconi Rodriguez[*,†,‡]*

[*]corresponding authors: *gum@sustc.edu.cn*, *joaquinr@illinois.edu*, *p.b.rodriguez@bham.ac.uk*

Alloy characterization

Compositional analyses of FeTi, CuTi, and SnTi alloys, obtained via XRF and EDS, are tabulated in **Table S1**. Differences in excitation radiation, X-rays for XRF and electrons for EDS, result in differences in penetration depth of the techniques, with EDS having greater penetration depth. Therefore, comparison of elemental compositions given by XRF and EDS is a useful indicator of differences in surface and bulk composition, respectively, providing a measure of the degree of segregation within the alloy.[1] The relative atomic compositions obtained by the different techniques are in good agreement, with small variations observed – <5 atomic% (at.%). For FeTi and SnTi alloys, a slight enrichment in the relative composition of the alloying metal, of 2-4 at.% is observed at the surface (XRF analysis) compared to the bulk (EDS analysis). For CuTi the opposite case is true; depletion of the alloying metal is observed at the surface relative to the bulk by ~4 at.%. Henceforth, the relative atomic composition of the bulk of the alloys, obtained by EDS, will be included in their discussion.

XRD patterns of the three alloys were recorded and compared to metallic Ti – JCPDS no. 441294 – (Figure S1). Shifts in 2θ position for all three samples relative to the database values were observed, indicative of successful alloy formation. Shifts to lower 2θ values, indicative of an increase in lattice spacing, were observed for $Fe_{8.82}Ti_{91.28}$ and $Sn_{42.82}Ti_{57.18}$, the two alloys with enriched surface dopant concentration relative to the bulk.

In the case of $Fe_{8.82}Ti_{91.28}$, the shift in 2θ position for the $(01\bar{1})$ peak is less significant, with Fe and Ti possessing similar atomic radii, but a decrease in peak intensities in conjunction with peak broadening is observed. The presence of a broad peak adjacent to the $(01\bar{1})$ peak is also observed. This suggests that the crystallinity of the Ti lattice is adversely affected by the formation of the Fe-containing alloy and slow cooling procedure. Metallic Fe and Ti have differing crystal structures, with body-centered cubic (bcc) and hexagonal close-packed (hcp) structures, respectively. Therefore, the formation of a hybridized FeTi crystal structure,

between the bcc and hcp structures, during the cooling of alloy droplets would explain the observed decrease in crystallinity relative to pure Ti and could explain the observed shift in 2θ position.

For $Cu_{6.38}Ti_{93.72}$, the sample with the lowest degree of alloying, the diffraction pattern closely reflects the pattern for alpha-Ti; no additional peaks are observed. Shifts to higher 2θ position for all peaks by ~0.8° are observed, indicative of a decrease in lattice parameter. The atomic radius of Cu is 4% smaller than Ti and its crystal structure, face-centered cubic (fcc), more closely resembles the hcp structure of Ti than the bcc structure of Fe. Therefore, the low degree of alloying, smaller atomic radius and fcc structure of Cu means that the Ti hcp structure is minimally disrupted by the formation of the $Cu_{6.38}Ti_{93.72}$ alloy.

The largest shift in 2θ position was observed for $Sn_{42.82}Ti_{57.18}$, rationalized by the fact that this sample had the highest degree of alloying and that the atomic radius of Sn is 4% larger than Ti.[2] A significant number of additional peaks can be observed in the diffraction pattern suggesting that the higher alloying content produced a mixture of metallic phases rather than a solid solution (Figure S2).

Table S1. Relative atomic compositions of Ti alloys synthesised by combinatorial facilty, obtained by energy dispersive X-ray spectroscopy (EDX) and X-ray fluorescence spectroscopy (XRF).

Alloy (M-Ti)	**XRF composition (atomic %)**		**EDX composition (atomic %)**	
	M	**Ti**	**M**	**Ti**
Fe-Ti	10.75	89.25	8.82	91.28
Cu-Ti	2.69	97.31	6.28	93.72
Sn-Ti	46.24	53.76	42.72	57.28

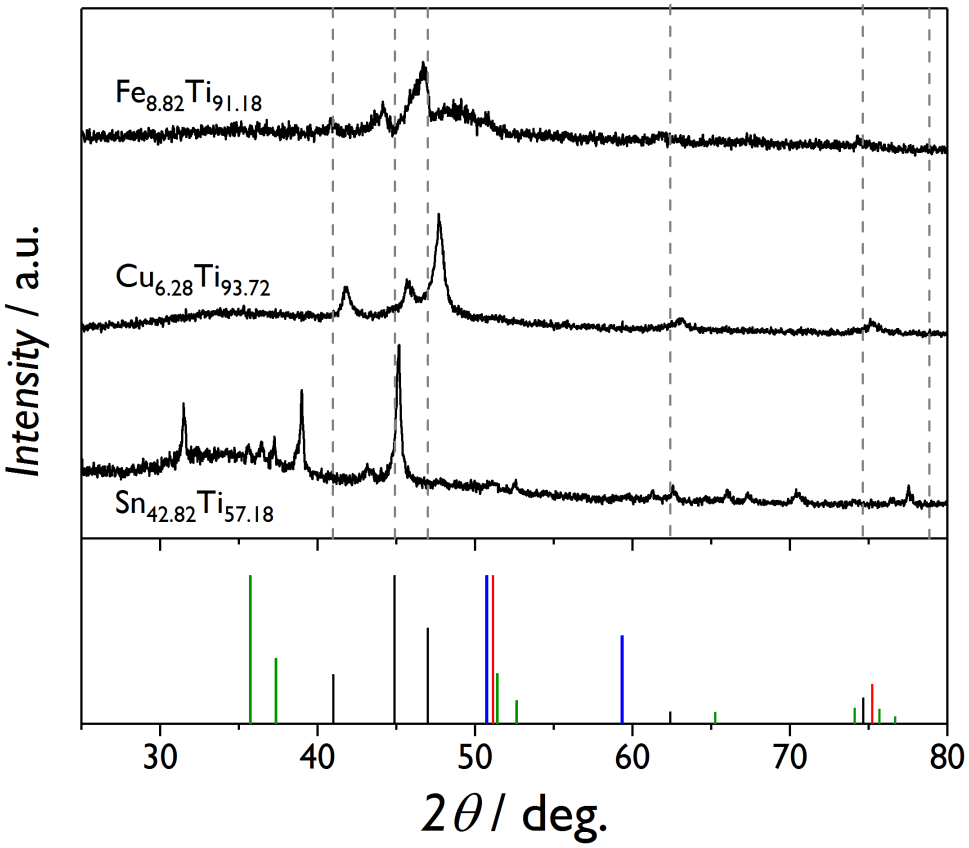

Figure S1. X-ray diffraction patterns of FeTi, CuTi and SnTi alloys synthesized by laser fabrication combinatorial facility. Peaks observed in the diffractograms of the alloys have been compared (dashed lines) to the relative 2θ positions of the Miller indices of alpha-Ti [JCPDS card no. 44-1294] (black lines). The diffraction peaks of metallic Fe (red) [JCPDS card no. 06-0696], Cu (blue) [JCPDS card no. 04-0836] and Sn (green) [JCPDS card no. 04-0673] are included for comparison.

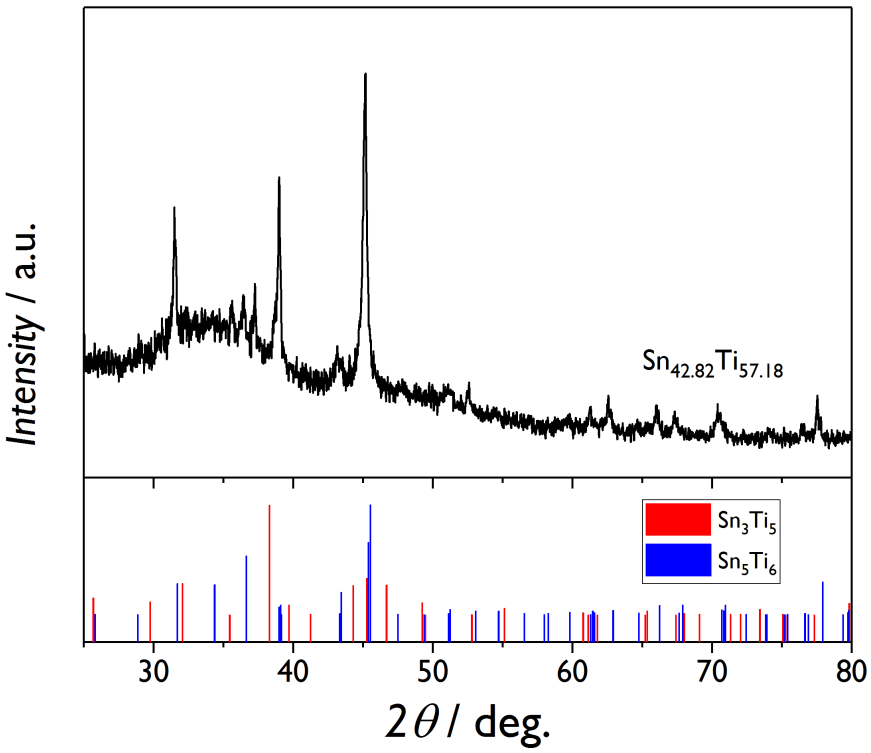

Figure S2. XRD pattern of SnTi alloy produced by combinatorial facility and comparison to diffraction patterns of Sn_3Ti_5 and Sn_5Ti_6 alloys reported in the literature.[3-4]

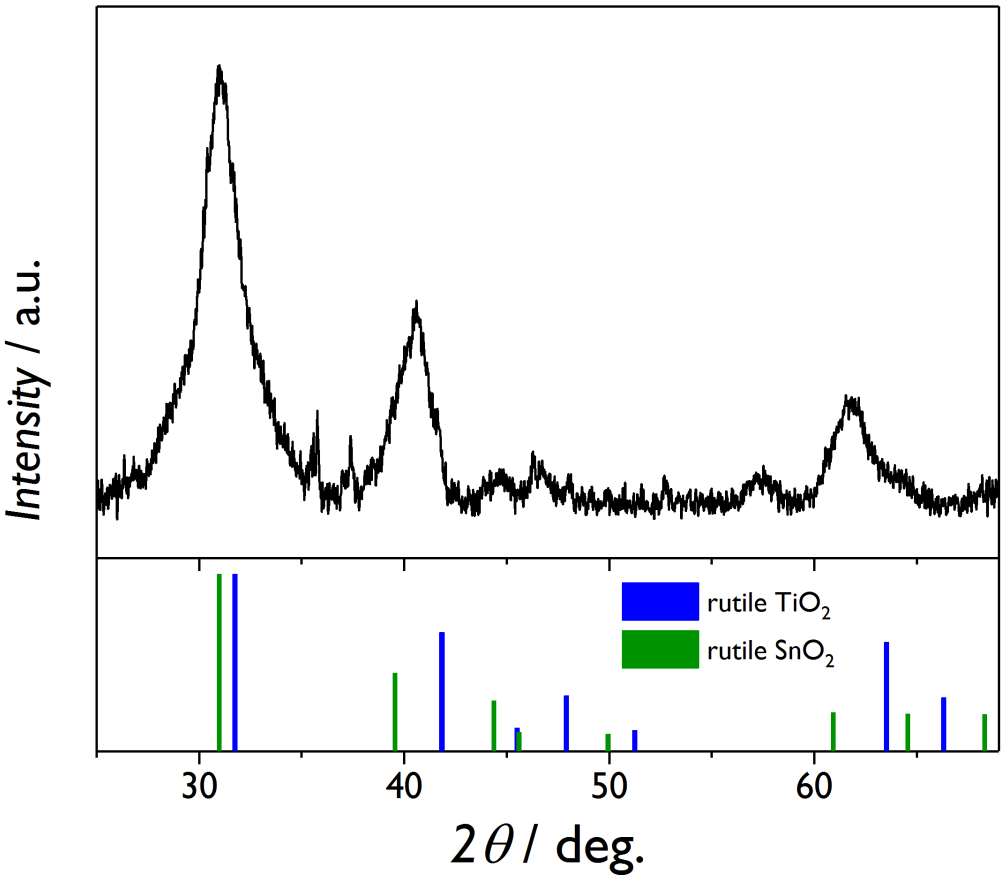

Figure S3. Comparison of XRD pattern recorded for 25 wt.% Sn:NTO nanoparticles and database patterns of rutile TiO_2 [JCPDS card no. 21-1276] (blue lines) and SnO_2 [JCPDS card no. 41-1445] (green lines), showing that rutile TiO_2 is the predominant phase while some rutile SnO_2 is also present.

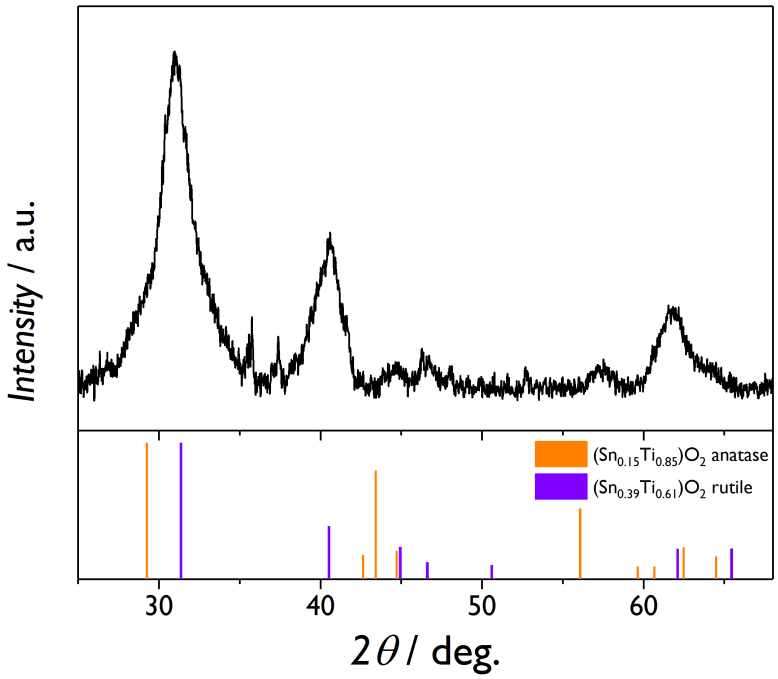

Figure S4. XRD pattern of 25 wt.% Sn:NTO nanoparticles prepared by cathodic corrosion of $Sn_{42.82}Ti_{57.18}$ alloy in comparison to previously reported Sn-doped titanate materials produced via alternative synthetic methods (orange[5] and purple[6] lines).

Anatase is the predominant crystal phase at low Sn-doping concentrations, while rutile phase is predominant at higher Sn-doping concentrations.

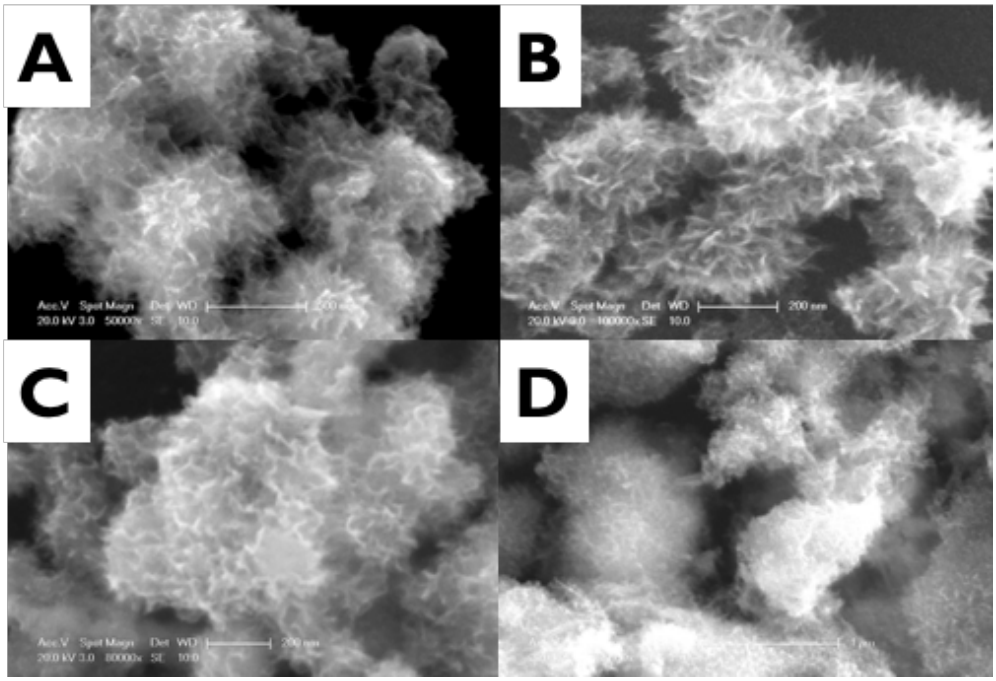

Figure S5. Scanning electron micrographs of (A) NTO, (B) 5 wt.% Fe:NTO, (C) 3 wt.% Cu:NTO and (D) 25 wt.% Sn:NTO NWs synthesized by the cathodic corrosion of Ti wire, $Fe_{8.81}Ti_{91.19}$, $Cu_{6.28}Ti_{93.72}$ and $Sn_{42.82}Ti_{57.18}$, respectively, in 10 M NaOH under an applied AC voltage between 0 and -10 V.

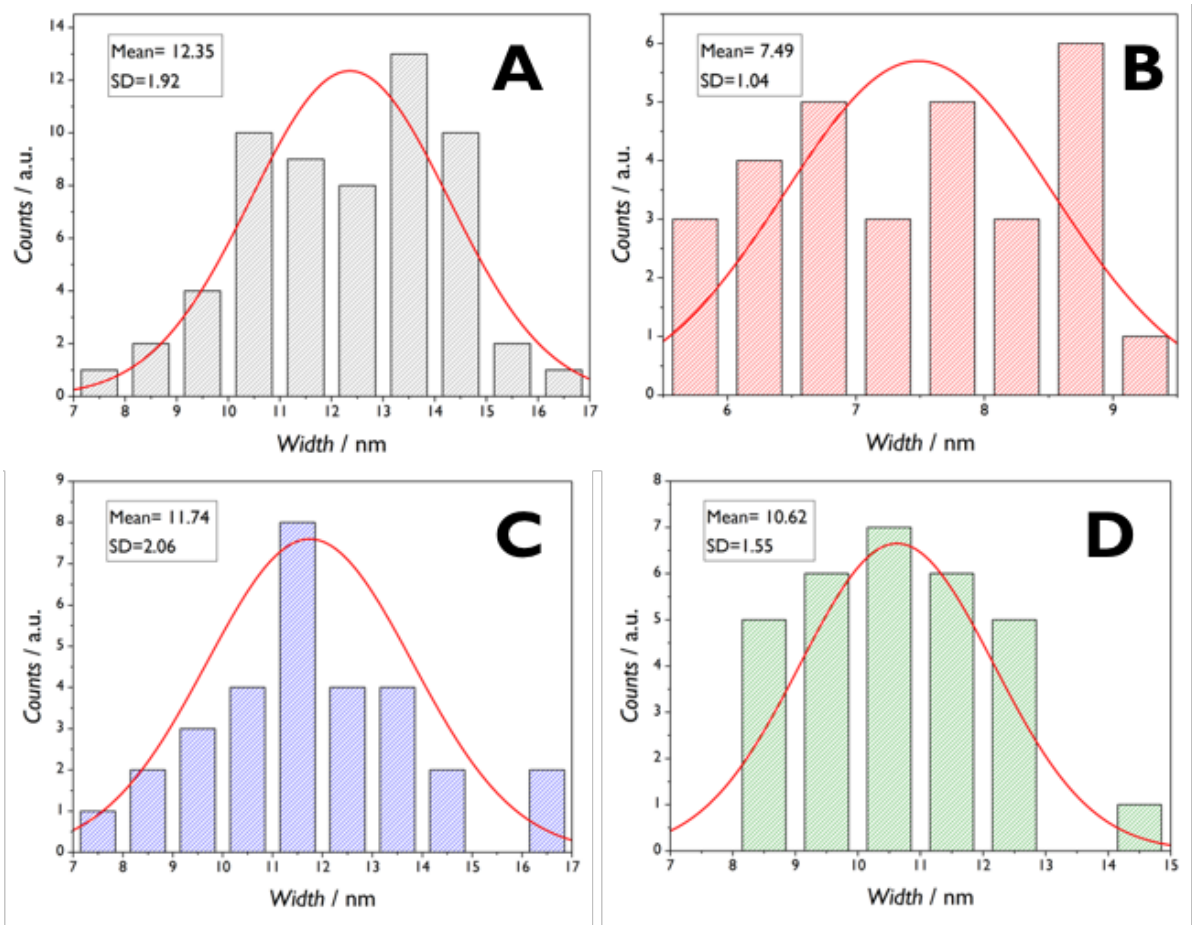

Figure S6. Size distribution plots displaying the mean and standard deviation widths for (A) NTO, (B) Fe:NTO, (C) Cu:NTO and (D) Sn:NTO NWs synthesized via cathodic corrosion of Ti wire, $Fe_{8.81}Ti_{91.19}$, $Cu_{6.28}Ti_{93.72}$ and $Sn_{42.82}Ti_{57.18}$, respectively, in 10 M NaOH under an applied AC voltage between 0 and -10 V. Sample populations were (A) 60 and (B-D) 30 NWs, respectively.

Specific surface area calculations

A theoretical model was employed to calculate the specific surface area of the NW samples (SA_{NW}). Assuming they possessed ideal cylindrical morphology,

$$m_{SNW} = V_{SNW} \times \rho_{NTO} \quad (1)$$

$$SA_{NW} = \frac{SA_{SNW}}{m_{SNW}} \quad (2)$$

where m_{SNW}, SA_{SNW} and V_{SNW} are the mass, surface area and volume of a single NW, respectively, and ρ_{NTO} is the density of NTO. The dimensions used in the calculations were obtained from electron microscopy measurements, with the widths taken from Figure S6 and representative short, median and long lengths implemented in order to obtain an average surface area value for each sample.

The specific surface areas obtained for NTO, Fe:NTO, Cu:NTO and Sn:NTO were 90.1, 154.7, 96.8 and 107.1 $m^2\ g^{-1}$, respectively. The values for the M:NTO NWs are in reasonable agreement with BET values reported in the literature for analogous nanostructures.[7]

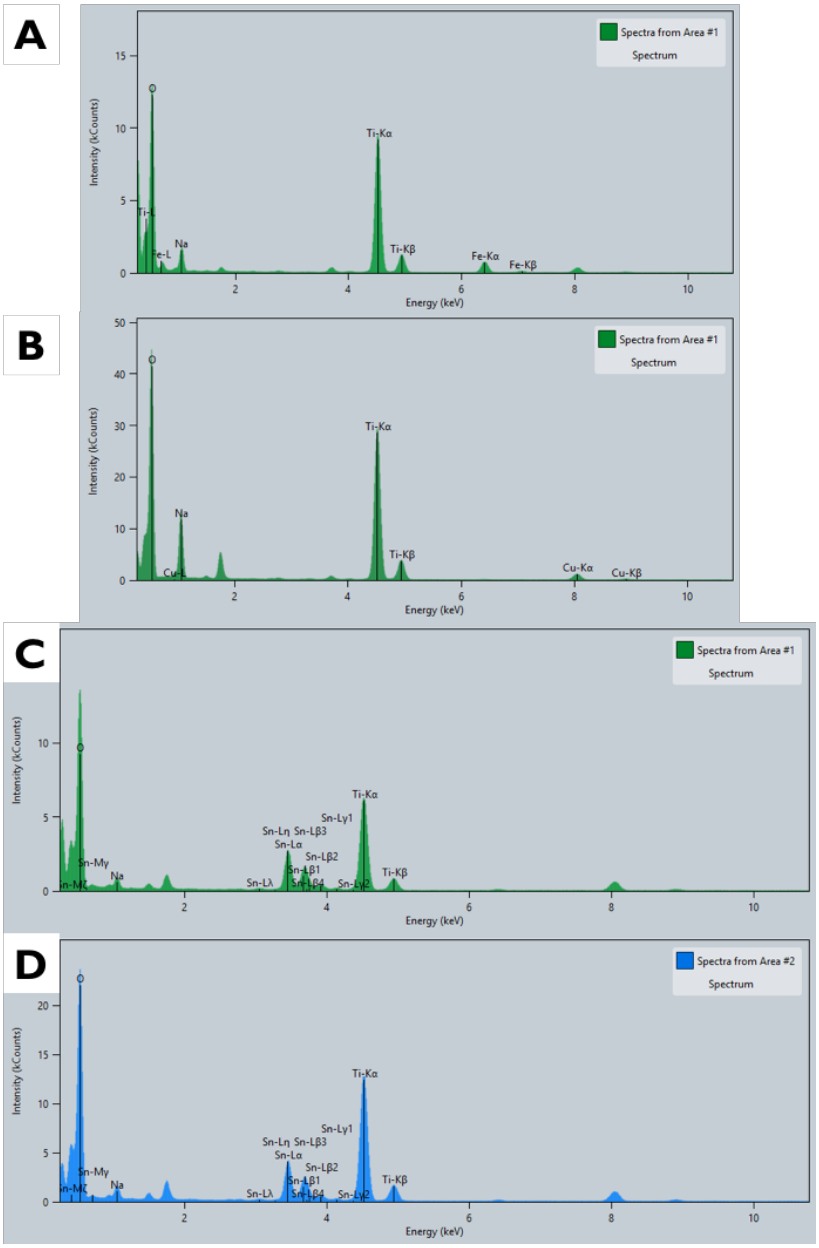

Figure S7. Representative EDS spectra of (A) 5 wt.% Fe:NTO (B) 3 wt.% Cu:NTO (C-D) 25 wt.% Sn:NTO nanoparticles synthesized by cathodic corrosion of laser-fabricated alloys in 10 M NaOH.

Table S2. Mean and standard deviation relative elemental composition of M:NTO nanoparticles, synthesized by cathodic corrosion of FeTi, CuTi and SnTi alloys, respectively, obtained via STEM-EDS analyses.

Atomic %						
	O	***Na***	***Ti***	***M***	***Ti***	***M***
Fe	60.26 ± 4.95	6.28 ± 1.35	30.76 ± 4.80	2.70 ± 0.42	91.92 ± 9.59	8.08 ± 1.27
Cu	58.04 ± 4.73	13.4 ± 2.87	27.20 ± 4.23	1.35 ± 0.21	95.27 ± 10.10	4.73 ± 0.75
Sn_{area1}	61.34 ± 4.37	3.22 ± 0.68	27.03 ± 4.07	8.41 ± 1.17	76.26 ± 8.00	23.74 ± 3.46
Sn_{area2}	65.44 ± 4.57	2.92 ± 0.61	25.92 ± 3.87	5.72 ± 0.79	81.91 ± 8.40	18.09 ± 2.61
Weight %						
Fe	37.87 ± 2.65	5.04 ± 1.06	51.82 ± 7.77	5.27 ± 0.79	90.77 ± 7.81	9.23 ± 1.34
Cu	37.99 ± 2.58	11.22 ± 2.35	47.74 ± 7.11	3.04 ± 0.45	94.01 ± 8.18	5.99 ± 0.87
Sn_{area1}	31.97 ± 1.93	2.15 ± 0.44	37.78 ± 5.51	28.11 ± 3.76	65.45 ± 5.09	34.55 ± 5.75
Sn_{area2}	37.31 ± 2.22	2.13 ± 0.44	39.64 ± 5.75	20.92 ± 2.78	81.91 ± 5.62	18.09 ± 4.59

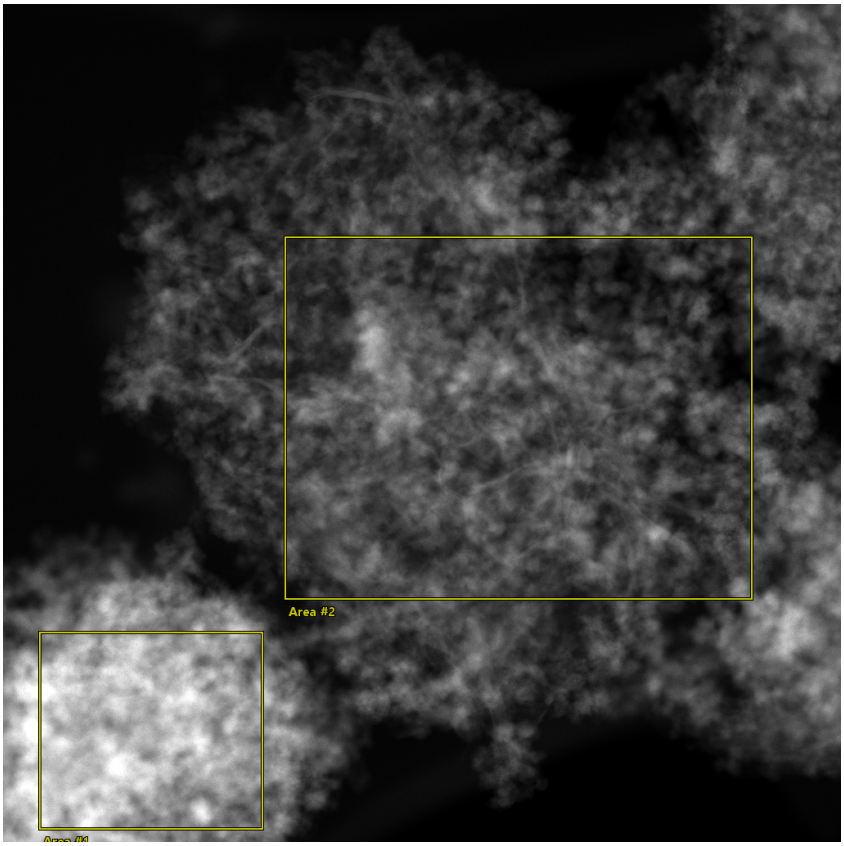

Figure S8. HAADF-STEM image showing two areas used in the acquisition of EDS spectra for 25 wt.% Sn:NTO NWs.

Table S3. Comparison of relative M-Ti compositions (atomic %) of M:NTO NWs and laser-fabricated alloy precursors.

	M:NTO		***Alloy***	
	M	***Ti***	***M***	***Ti***
Fe	9.27	91.92	8.82	91.18
Cu	4.73	95.27	6.28	93.72
Sn_{area1}	23.74	76.26	42.72	8.66
Sn_{area2}	18.09	81.91		

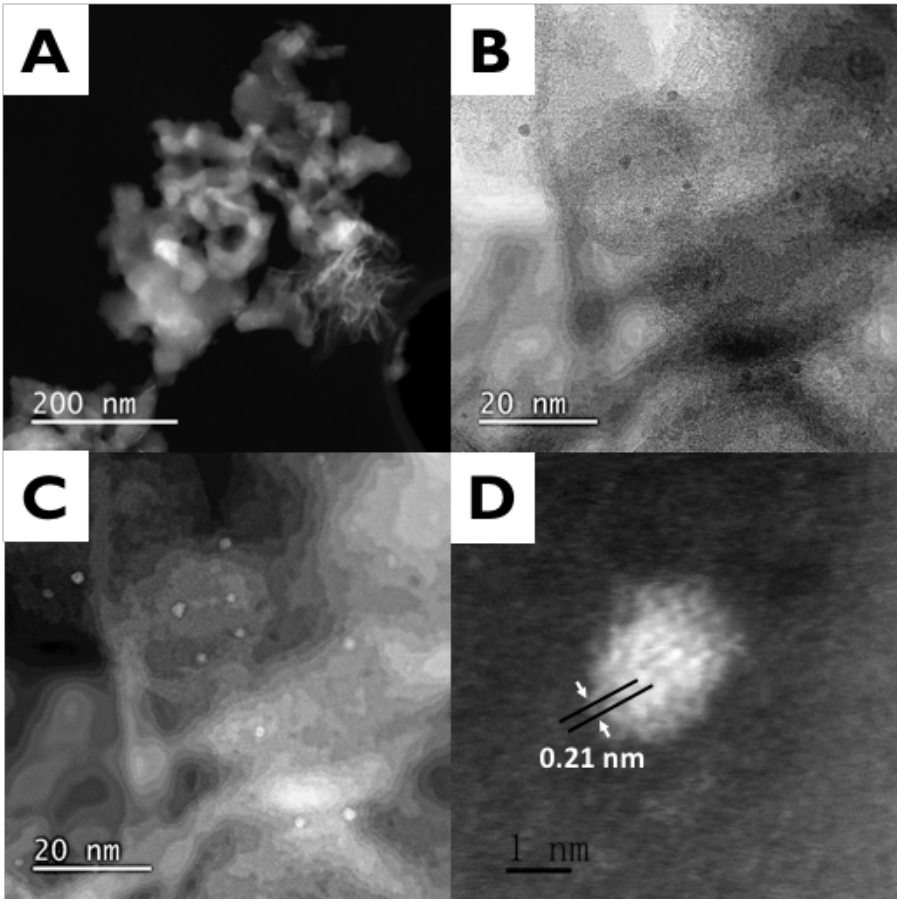

Figure S9. (A) HAADF image, (B) bright field and (C) dark field HRTEM images of 5 wt.% Fe:NTO amorphous phase. (D) HRTEM image of a crystalline Fe-rich oxide nanoparticle observed in the amorphous phase.

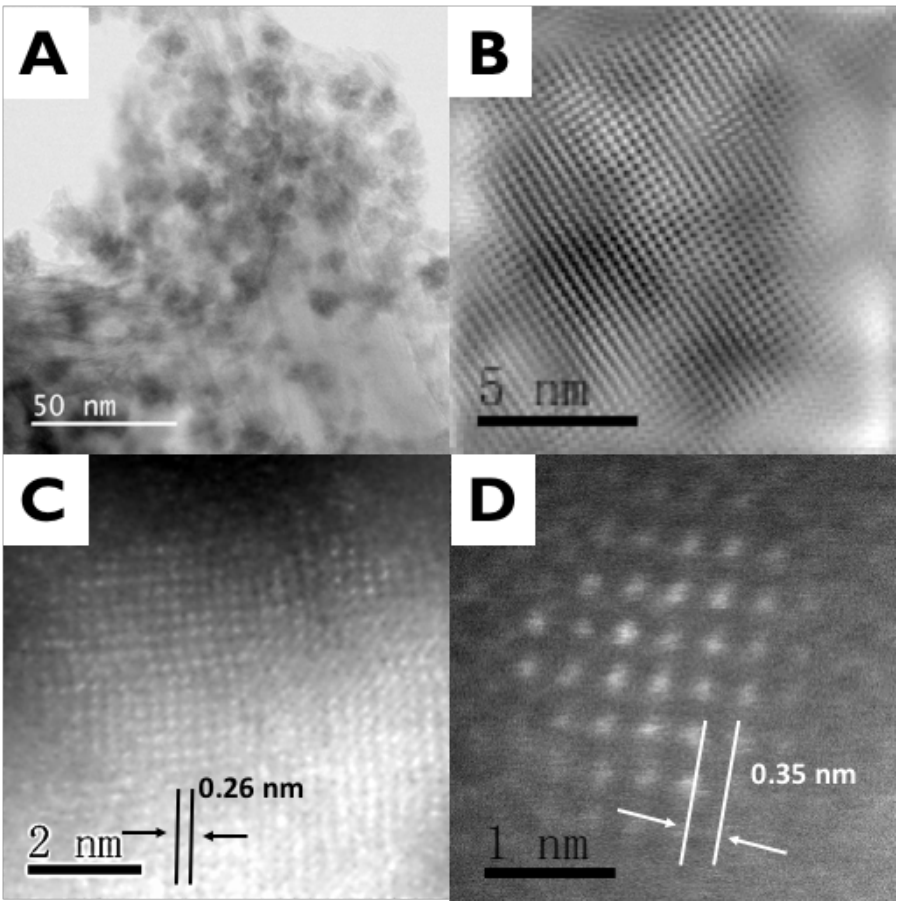

Figure S10. (A) Low magnification bright field STEM image and (B-D) corresponding dark field atomic STEM images of 25 wt.% Sn:NTO NWs.

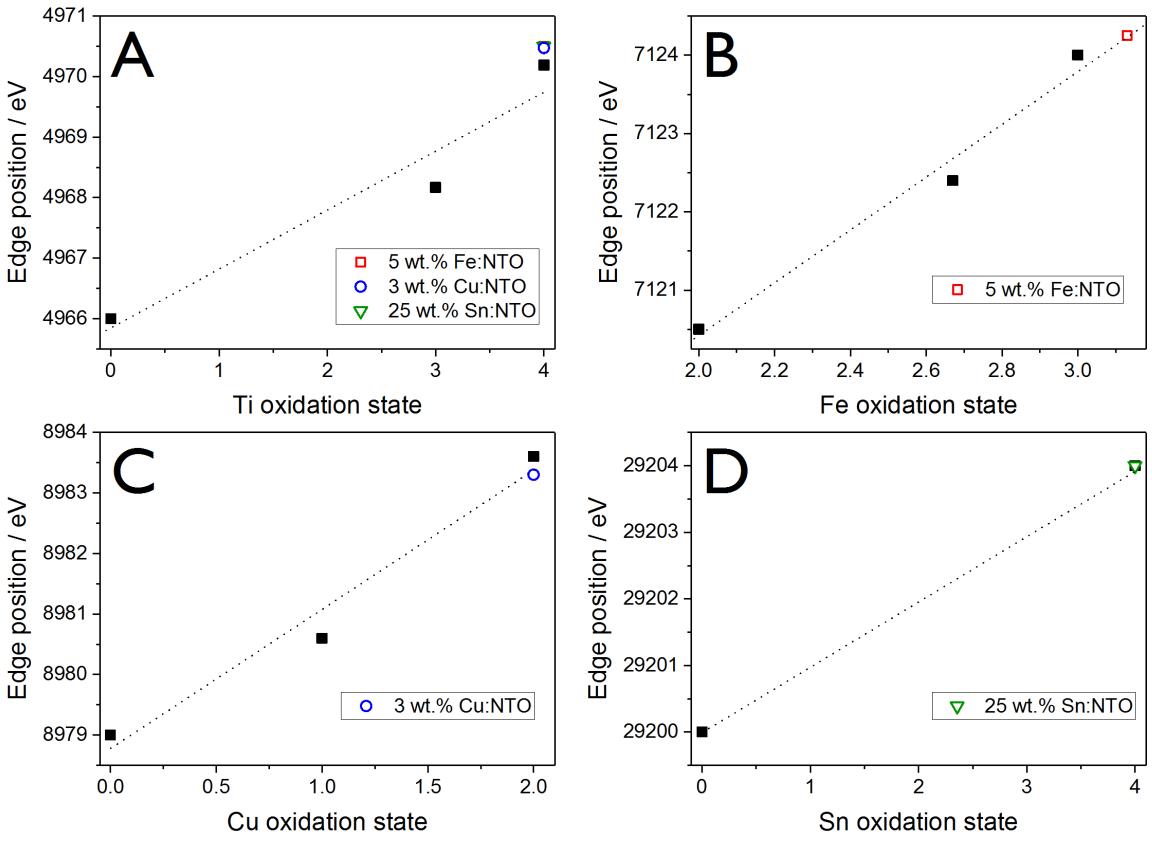

Figure S11. Mean (A) Ti, (B) Fe, (C) Cu and (D) Sn oxidation state as a function of the correspond M K-edge position for the prepared M:NTO catalysts, where M = Ti, Fe, Cu and Sn, respectively; black squares represent edge positions of corresponding oxidation states, as obtained from the standard reference compounds and foils. In the determination of Ti oxidation state (A) the edge positions overlap at +4 for all M:NTO samples.

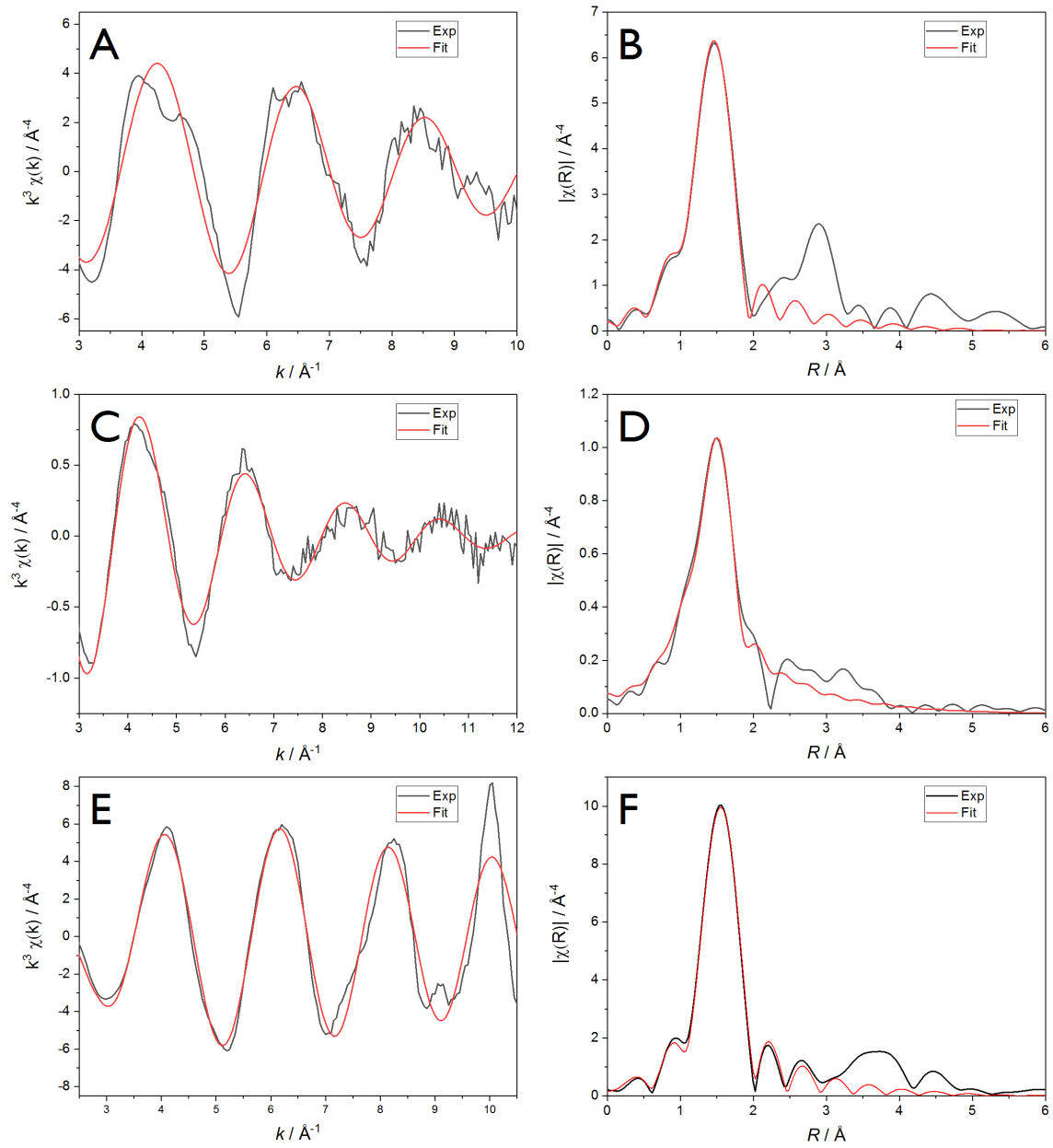

Figure S12. k^3 weighted χ data (left) and k^3 weighted Fourier transform EXAFS data (right) for the (A, B) 5 wt.% Fe:NTO (C, D) 3 wt.% Cu:NTO and (E, F) 25 wt.% Sn:NTO catalysts recorded at Fe, Cu and Sn K-edges, respectively. For each sample the red line represents the simulated fit.

Table S4. EXAFS distances and fitting parameters for the Fe:NTO catalyst. Fitting parameters: S_0^2 = 0.85 calculated using a Fe foil standard; fit range 3.0 < k < 10, 1 < R < 2.

Sample	**Scattering**	**CN**	**R / Å**	**σ^2 x 10^3 / Å^2**	**ΔE_0 / eV**	**R_{factor}**
5 wt.%	Fe–O	4.5 ± 0.8	1.94 ± 0.02	7.2 ± 3.0	-4.0 ± 2.8	0.003

Table S5. EXAFS distances and fitting parameters for the Cu:NTO catalysts. Fitting parameters: S_0^2 = 0.72 calculated using a Cu foil standard; fit range 3.0 < k < 12, 1 < R < 2

Sample	**Scattering**	**CN**	**R / Å**	**σ^2 x 10^3 / Å^2**	**ΔE_0 / eV**	**R_{factor}**
3 wt.%	Cu–O	3.5 ± 0.4	1.93 ± 0.02	5.8 ± 2.0	1.8 ± 1.6	0.008
9 wt.%	Cu–O	3.4 ± 0.3	1.93 ± 0.01	4.8 ± 1.0	1.8 ± 1.6	0.005

Table S6. EXAFS distances and fitting parameters for the Sn:NTO catalyst. Fitting parameters: S_0^2 = 0.85 calculated using a Sn foil standard; fit range 3.0 < k < 10, 1 < R < 3

Sample	**Scattering**	**CN**	**R / Å**	**σ^2 x 10^3 / Å^2**	**ΔE_0 / eV**	**R_{factor}**
25 wt.%	Sn–O	6.6 ± 0.4	2.05 ± 0.01	2.8 ± 0.8	5.3 ± 0.7	0.004

UV-vis absorption spectroscopy

Optical property characterisation was conducted by UV-visible (UV-vis) absorption spectroscopy. The results revealed that the titanates absorb strongly in the UV region (<400 nm), 5 wt.% Fe:NTO has poor relative light absorption properties to the undoped titanate in the visible region, but improved absorption in the UV region, Sn:NTO absorbs significantly poorly at all wavelengths and that Cu:NTO absorbs more strongly than undoped TiO_2 in both UV and visible regions (Figure S13). It has been reported that increasing Sn dopant concentration in TiO_2 causes significant blue shift at concentrations as low as 1 at.%.[8] Therefore, this effect is more pronounced for Sn:NTO NWs with a relative Sn concentration of 25 wt.% (~8 at.%). Additionally, the presence of apparent Sn:NTO@SnO_2 core@shell structure, indicated by STEM characterization (Figure S8), reduces the relative absorption of this sample due to the increased magnitude of the SnO_2 band gap that acts as a passivation layer.

Fe-doping in TiO_2, up to ~10 wt.%, is reported to increase absorption intensity in the visible region, whereas we observed an increase in UV absorption upon doping in NTO, suggestive of a relative increase in the Fe:NTO band gap.[9] For Cu:NTO, the observed increase in visible light absorption with a Cu concentration as low as 3 wt.% (~1 at.%) is in agreement with existing reports regarding Cu-doped titanate nanostructures.[10-11] Furthermore, the observed trend in absorption intensity for M:NTO nanoparticles synthesized by cathodic corrosion, M = Cu > Fe > Sn, is in agreement with existing literature.[12]

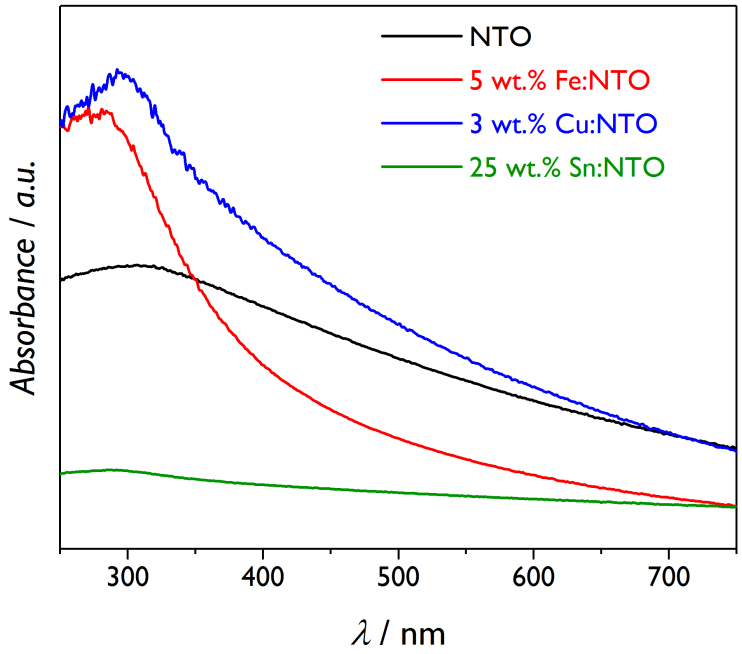

Figure S13. UV-vis absorption spectra of the titanate and doped titanate nanostructures as indicated in the figure synthesized via cathodic corrosion as described in the experimental section; absorbance measurements were normalized by the mass concentration of each material (mg mL^{-1}).

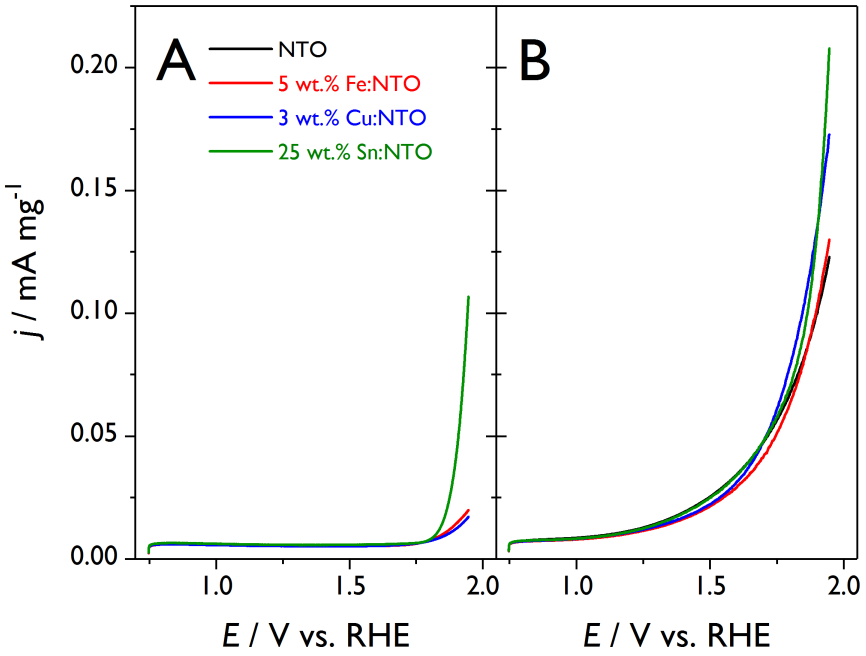

Figure S14. Anodic sweeps recorded of NTO (black), 5 wt.% Fe:NTO (red), 3 wt.% Cu:NTO (blue) and 25 wt,% Sn:NTO (green) in (A) the absence of light and (B) under incident white (UV and visible) light; ν=20 mV s^{-1}.

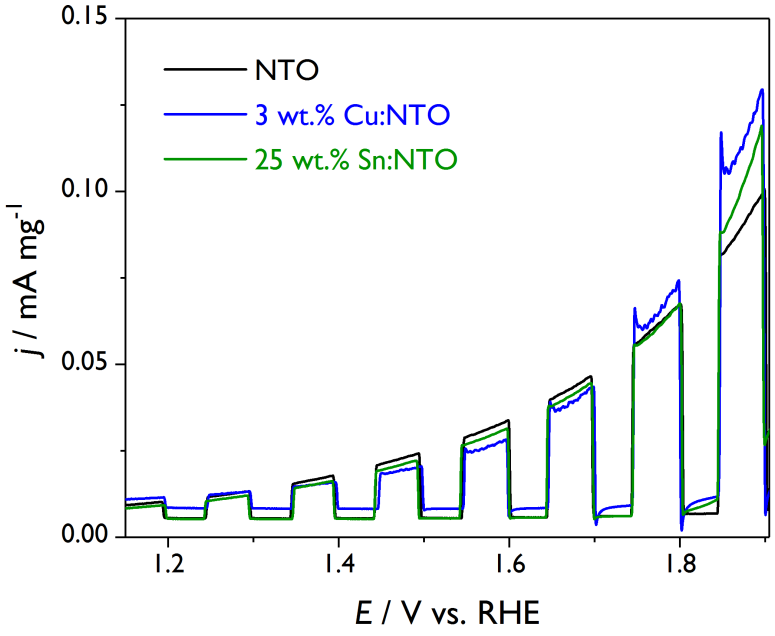

Figure S15. *J-E* curves under intermittent light illumination for NTO, 3 wt.% Cu:NTO and 25 wt.% NTO NWs synthesized via cathodic corrosion between 0 and -10 V in 10 M NaOH.

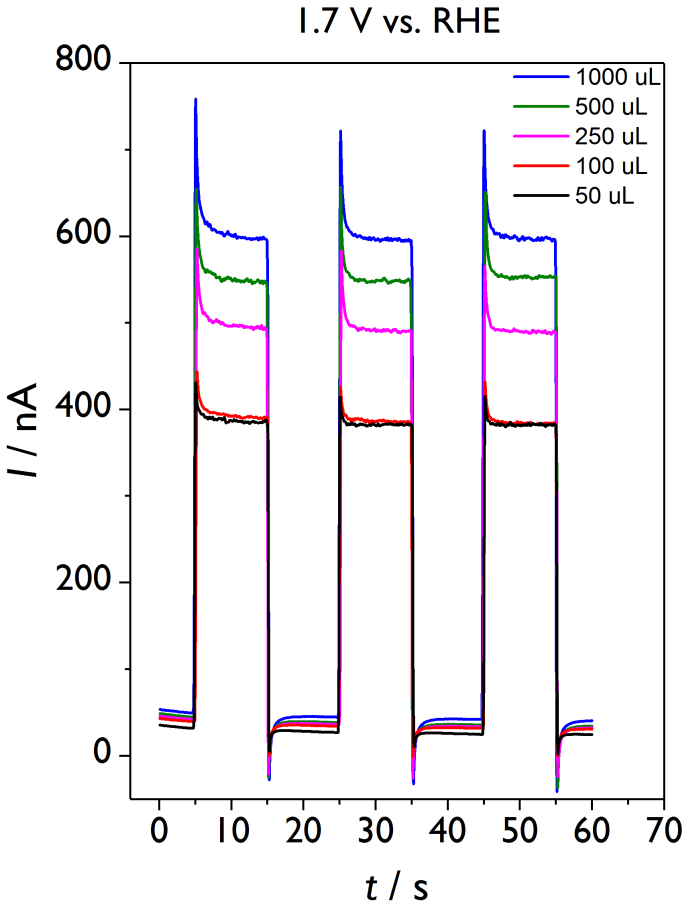

Figure S16. Chopped light *I-t* curves with increasing 3 wt.% Cu:NTO loading volume, recorded at 1.7 V vs. RHE in 0.1 M NaOH.

Figure S17. Photograph of the nanoparticle suspensions obtained from cathodic corrosion of $Cu_{6.28}Ti_{93.72}$ (left) and $Cu_{19.32}Ti_{80.68}$ (right).

Table S7. STEM-EDS compositional analysis of 9 wt.% Cu:NTO NWs synthesized by cathodic corrosion of $Cu_{19.32}Ti_{80.68}$ in 10 M NaOH solution.

	O	***Na***	***Ti***	***Cu***	***Ti***	***Cu***
Atomic %	58.92 ± 4.76	6.95 ± 1.49	30.08 ± 4.67	4.05 ± 0.63	91.92 ± 9.59	8.08 ± 1.27
Weight %	36.28 ± 2.48	5.47 ± 1.15	49.66 ± 7.40	8.58 ± 1.29	90.77 ± 7.81	9.23 ± 1.34

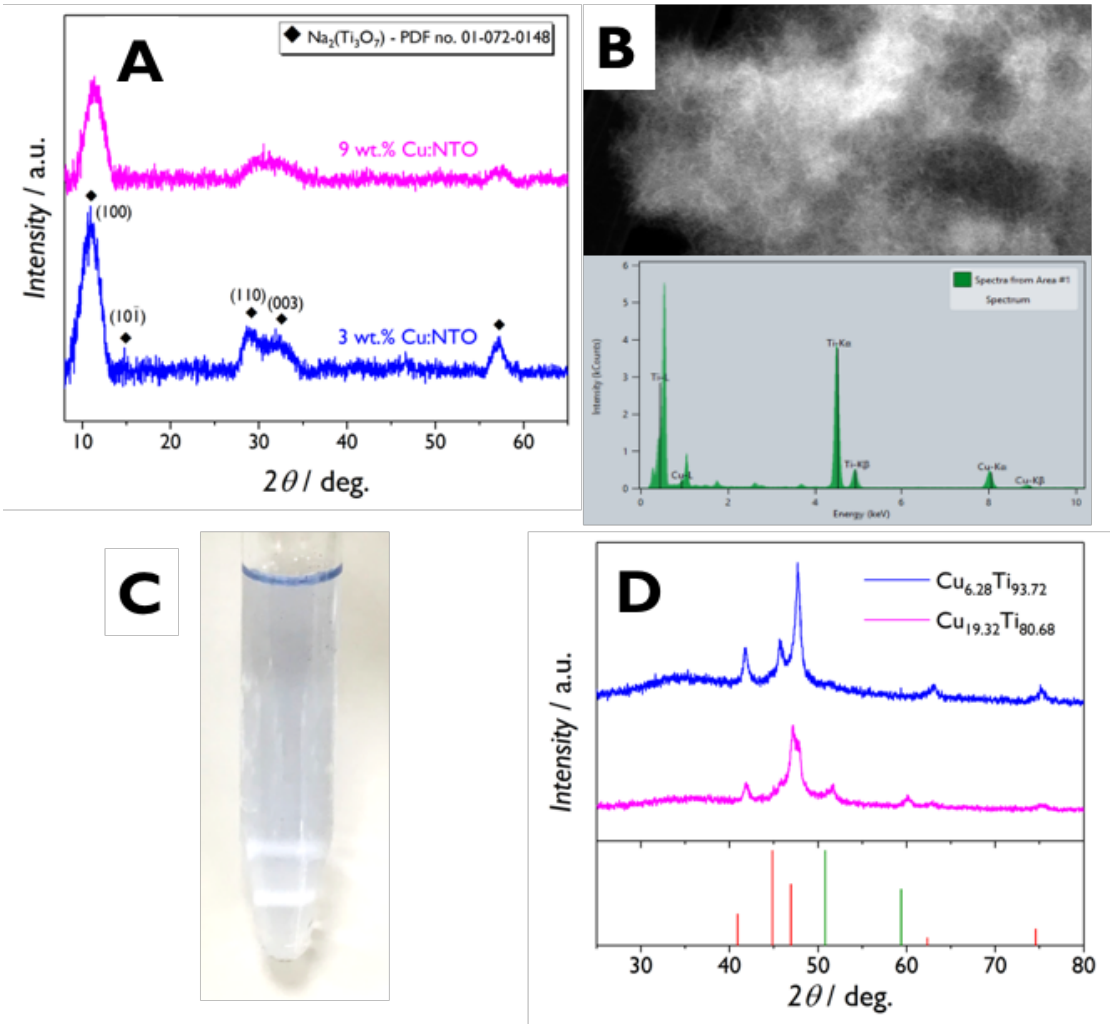

Figure S18. (A) Comparison of the XRD patterns of Cu:NTO NWs synthesized from alloys with varying Cu composition. (B) STEM image [top] and EDS spectrum [bottom] of 9 wt.% Cu:NTO synthesized by cathodic corrosion of $Cu_{19.32}Ti_{80.68}$ in 10 M NaOH solution. (C) Photograph of the aqueous solution obtained by cathodic corrosion of Cu wire in 10 M NaOH with an applied AC voltage between 0 V and -10 V. (D) XRD pattern of laser-fabricated CuTi alloys compared to the patterns of alpha-Ti [JCPDS card no. 44-1294] and fcc Cu [JCPDS card no. 04-0836].

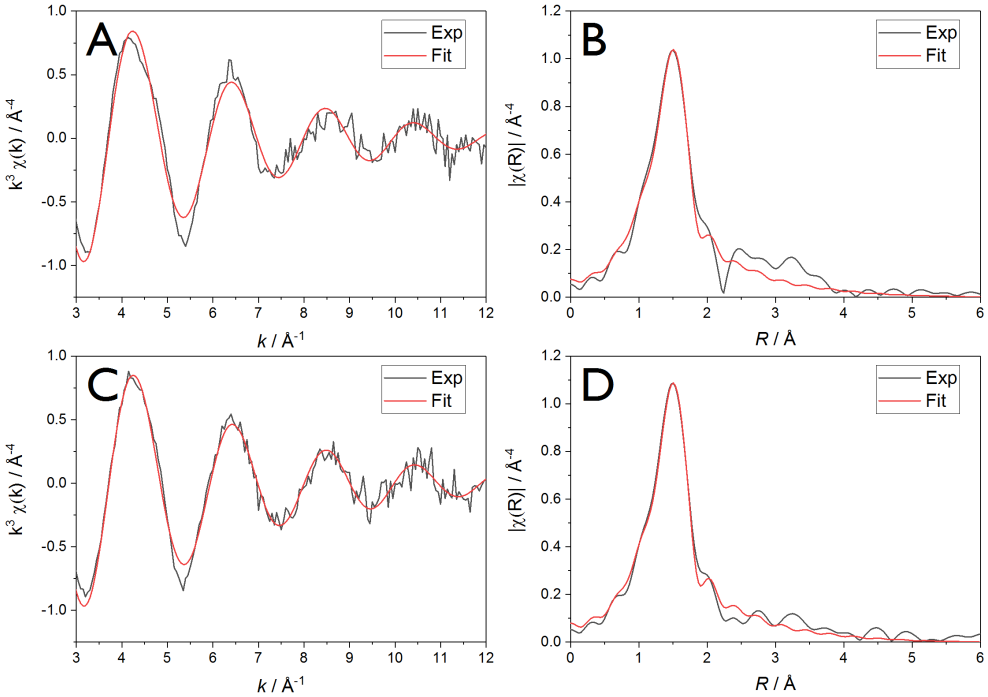

Figure S19. k^3 weighted χ data (left) and k^3 weighted Fourier transform EXAFS data (right) for the (A, B) 3 wt.% Cu:NTO and (C, D) 9 wt.% Cu:NTO catalysts recorded at Cu K-edge. For each sample the red line represents the simulated fit.

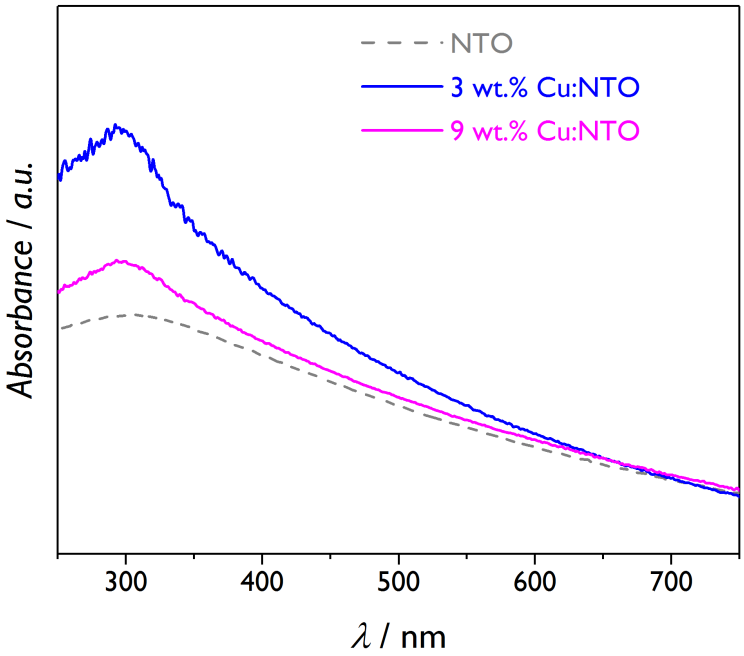

Figure S20. UV-vis absorption spectra for 3 wt.% and 9 wt.% Cu:NTO NWs compared to undoped NTO NWs.

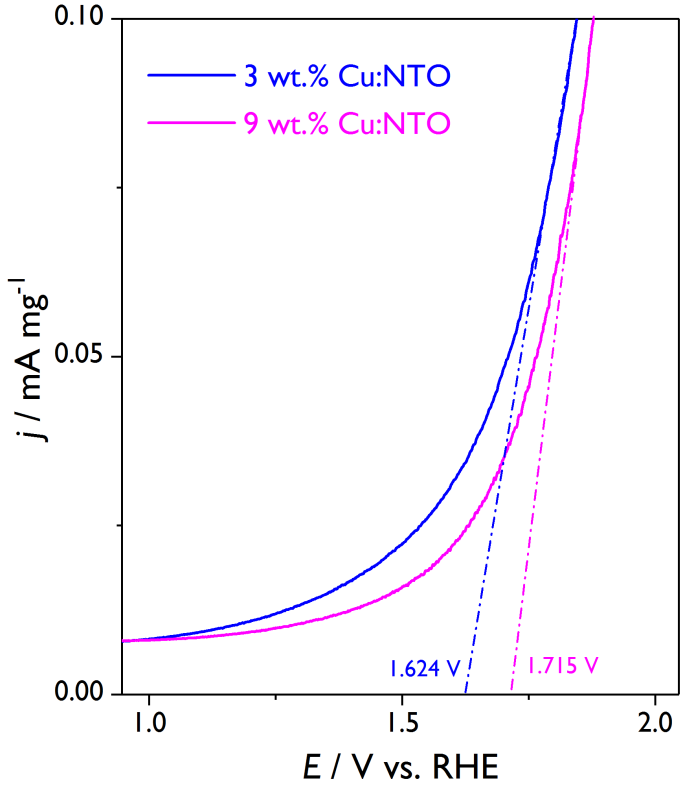

Figure S21. Anodic voltammetric profiles of Cu:NTO NWs under incident white polychromatic light (UV and visible) normalized by mass loading of each catalyst with approximate OER onset potentials annotated; ν=20 mV s^{-1}.

References

1. R. Linke and M. Schreiner, Microchim. Acta, 2000, 133, 165-170, DOI: 10.1007/s006040070087.
2. J. C. Slater, *J. Chem. Phys.*, 1964, **41**, 3199-3204, DOI: 10.1063/1.1725697.
3. P. Pietrokowsky and P. Duwez, *JOM*, 2017, **3**, 772-773, DOI: 10.1007/bf03397370.
4. K. Schubert, K. Frank, R. Gohle, A. Maldonado, H. G. Meissner, A. Raman and W. Rossteutscher, *Sci. Nat. (1913-2014)*, 1963, **50**, 41-41, DOI: 10.1007/bf00622812.
5. H. Yamane, B.-C. Young and T. Hirai, *J. Ceram. Soc. Jpn.*, 1992, **100**, 1473-1474. DOI: 10.2109/jcersj.100.1473.
6. Y. Xie, S. Yin, H. Yamane, T. Hashimoto, H. Machida and T. Sato, *Chem. Mater.*, 2008, **20**, 4931-4935, DOI: 10.1021/cm800277b.
7. N. M. dos Santos, J. M. Rocha, J. M. E. Matos, O. P. Ferreira, J. M. Filho, B. C. Viana and A. C. Oliveira, *Appl. Catal., A*, 2013, **454**, 74-80, DOI: 10.1016/j.apcata.2012.12.035.
8. Y. Akila, N. Muthukumarasamy, S. Agilan, S. Senthilarasu and D. Velauthapillai, *Mater. Sci. Semicond. Process.*, 2017, **57**, 24-31, DOI: 10.1016/j.mssp.2016.09.028.
9. H. Moradi, A. Eshaghi, S. R. Hosseini and K. Ghani, *Ultrason. Sonochem.*, 2016, **32**, 314-319, DOI: 10.1016/j.ultsonch.2016.03.025.
10. Y. An, Z. Li and J. Shen, *Mater. Lett.*, 2012, **74**, 65-67, DOI: 10.1016/j.matlet.2012.01.096.
11. Y. An, Z. Li and J. Shen, *Phys. B (Amsterdam, Neth.)*, 2013, **429**, 127-132, DOI: 10.1016/j.physb.2013.08.006.
12. R. T. Ako, P. Ekanayake, D. J. Young, J. Hobley, V. Chellappan, A. L. Tan, S. Gorelik, G. S. Subramanian and C. M. Lim, *Appl. Surf. Sci.*, 2015, **351**, 950-961, DOI: 10.1016/j.apsusc.2015.06.015.

Preface to Chapter 7

Format: Unpublished article manuscript.

Overview: The aim of this chapter was to investigate the activity of recently developed Cu-doped $Na_2Ti_3O_7$ (NTO) catalysts (presented in **Chapter 6**) towards CO_2RR, given the interesting reactive site presented by the confined nature of the Cu^{2+} ions. To compare, CuO@NTO was prepared, possessing a different local Cu coordination environment but with the same initial oxidation state. The activity and selectivity of the Cu-NTO catalysts was evaluated and contrasted via electrochemical methods, with products characterised *in situ* by OLEMS.

In situ XAS was performed to monitor and elucidate the Cu species composition during CO_2RR catalysis given that literature reports have debated on the feasibility of oxidised Cu species existing during and after CO_2RR.

Author Contributions: The experiments were devised by M.J.L and P.R. M.J.L performed the synthesis, physical and electrochemical characterisation of the materials and preparation of painted button electrodes for *in situ* XAS measurements. P.R. performed OLEMS characterisation and analyses. L.S. conducted NMR characterisation. M.J.L, V.C., P.R., L.S. and H.H. conducted the measurement of *in situ* XAS spectra. M.J.L. performed XANES analysis and V.C. performed EXAFS fit analyses. Y.Z. performed STEM HAADF-EDS.

7. INSIGHT INTO THE ACTIVITY AND SELECTIVITY OF NANOSTRUCTURED COPPER TITANATES DURING ELECTROCHEMICAL CONVERSION OF CO_2 AT NEUTRAL pH VIA *IN SITU* X-RAY ABSORPTION SPECTROSCOPY

7.1. Introduction

The impacts of climate change and global warming have become a topical subject in both the political and scientific landscapes in recent times. The significant increase of anthropogenic carbon dioxide (CO_2) in the atmosphere through the widespread use of fossil fuels to produce energy to meet the ever-increasing global demand and consumption of energy is of great concern.[1] The capture and recycling of atmospheric CO_2 is a promising pathway to address this global challenge.[2, 3] In particular, the electrochemical conversion of CO_2 (CO_2RR) to useful, value-added chemicals is the subject of significant research effort because this avenue affords an opportunity to take advantage of electrical energy generated by renewable sources such as wind, water and solar.[3-7]

The specific chemical and physical properties of the catalyst plays a significant role in CO_2RR. Among all monometallic catalysts, copper and copper oxide-derived surfaces are the only catalysts that can electrochemically convert CO_2 to high value and energy-dense C2 and C3 products.[8] Previous studies have demonstrated that surface geometry,[9, 10] oxidation state,[11, 12] particle size,[13, 14] morphology[15-17] and electrolyte composition[18, 19] impact the selectivity and efficiency of CO_2RR.

One of the most controversial aspects when studying the selectivity of the copper catalyst is the presence of surface and subsurface oxides.[20-23] However, while some reports suggest that copper oxides, at the surface or subsurface, are stable at the potentials where the CO_2RR takes place and its presence result in changes in the product selectivity, other researchers

claim that the copper oxide derivates fully reduce to copper during the CO_2RR and that it is the change of the surface structure which defines the changes in the product selectivity.[24] We recently demonstrated that the presence of surface oxides electrochemically generated via potential pulses, results in change of the product selectivity and the formation of oxygenated products.[22] Recently, further quasi *in-situ* studies by Roldan-Cuenya's group confirmed that the change in selectivity is associated to both changes in the surface structure and the presence of Cu(I) species.[12]

Even though electrochemical potential pulses are, from the fundamental point of view, suitable to generate Cu(I) species and thus change the selectivity, the application of the method in CO2 electrolysers is not easy. Therefore, strategies to supply and retain oxygen on the copper catalyst will be ideal for the implementation of CO_2RR.

Herein, we present the synthesis of a series of Cu-containing $Na_2Ti_3O_7$ (NTO) catalysts for CO_2RR in neutral aqueous phosphate electrolyte. The titanate motif was shown to be stable under CO_2RR conditions and facilitate strong adsorption and chemisorption pf CO_2 and CO_3^{2-}.[25] Two distinct Cu titanates were prepared for this investigation: Cu-intercalated NTO (Cu:NTO) and CuO nanoparticles mixed with NTO (CuO@NTO). The nanoparticles were prepared via cathodic corrosion,[26] which enables the single-step preparation of oxide nanoparticles dispersed in aqueous solution that can be directly used as catalyst without the need of additional chemical cleaning or baking steps.[27, 28]

The catalytic activity and selectivity for the CO_2RR was evaluated for all metal oxide catalysts used. *In situ* X-ray absorption spectroscopy (XAS) characterisation was used to determine the Cu oxidation state and local coordination environment at the relevant CO_2RR conditions and thus, establish a relationship between these parameters and the product selectivity determined by on-line electrochemical mass spectrometry (OLEMS) and NMR.

7.2. Experimental

Cathodic corrosion synthesis

A 2-electrode configuration was employed for cathodic corrosion synthesis, as described previously, using a LabVIEW/National Instruments hardware and a homebuilt power amplifier.[26, 27, 29, 30] NTO and Cu:NTO nanowires were prepared by applying a square waveform oscillating between 0 and -10 V at 100 Hz across the working electrode (WE) (Ti wire of 0.25 mm diameter and $Cu_{19}Ti_{81}$ alloy, respectively) and a high surface area Pt flag used as counter electrode (CE), submerged in 10 M NaOH (Merck, ≥99%) solution.[26] The $Cu_{19}Ti_{81}$ alloy was prepared via suspended droplet alloying[31, 32] (see Supporting Information for experimental details).

CuO nanoparticles were prepared by applying a square waveform oscillating between +4 and -4 V at 100 Hz across the working electrode (Cu wire of 0.41 mm) in 90% saturated $CaCl_2$ (Merck, anhydrous ≥93%).

The suspensions of nanoparticles were separated by repeated centrifugation at 4500 rpm and decanting of the supernatant until neutral pH was obtained. Catalysts were left suspended in Milli-Q water (PURELAB Ultra, 18.2 MΩ· cm) prior to physical and electrochemical investigations.

In order to normalise the catalytic activity per mass, the clean samples were dried at 75 °C and weighed. CuO@NTO was prepared by adding 10% by weight of the CuO to a known mass of NTO nanowires to produce the 10 wt.% CuO@NTO catalyst.

Physical characterisation

X-ray diffraction (XRD) patterns of the prepared nanomaterials were recorded using a Bruker D2 Phaser powder X-ray diffractometer (Co Kα radiation source, λ = 1.78897 Å; 30 kV operating voltage; 10 mA). The suspended aqueous oxide suspensions were drop-cast onto

a SiO_2 low diffraction background plate in 40 µL increments, and the water was evaporated. Diffraction patterns for NTO, Cu:NTO and CuO@NTO were recorded for >12 h, while the for CuO diffraction patterns were recorded over 90 mins.

Particle morphology was analysed by scanning electron microscopy (SEM) using a Philips XL-30 ESEM instrument. High resolution transmission electron microscopy (HRTEM) images were recorded using a JEOL JEM-2100F instrument operating at 200 kV. Scanning transmission electron microscopy (STEM) was performed on a FEI Talos 200 microscope, with double Cs correctors, operating at 200 kV recording high-angle annular dark field (HAADF) images. The microscope was equipped with super-X EDS detectors, which facilitate the acquisition of EDS maps with 50 times higher signal collection efficiency than normal EDS detectors.

Electrochemical characterisation

A standard 3-electrode configuration was employed for electrochemical measurements. The cyclic voltammetries (CVs) were measured under mass transport conditions using a rotating disk electrode (RDE). A glassy carbon (GC) disk support assembled into a Teflon RDE holder was used as a support for the catalyst and a high-surface area gold flag was used as a CE, with a Ag/AgCl (3 M NaCl) used as the reference electrode (RE). All the graphs are presented in respect to the reversible hydrogen electrode (RHE) scale. All the measurements were performed in 0.1 M phosphate buffer solution (pH 8) produced from K_2HPO_4 (Acros Organics, >98%) and KH_2PO_4 (Sigma, ≥99%).

Electrodes were prepared by drop-casting the catalyst suspension onto a glassy carbon substrate in volumes of 25 µL and drying in a fan oven at 75 °C until the total mass of the catalyst was 0.6 $mg \cdot cm^{-2}$. After drying, the catalysts were coated with 2 x 25 µL of Nafion D-521 solution (Alfa Aesar, 5% w/w in H_2O and 1-propanol) diluted in milli-Q water (1:10).

The uncompensated solution resistance was measured using the positive feedback mode of the potentiostat and all voltammetries have been corrected by the resistance.

Electrolysis measurements were obtained via chronoamperometry using a custom 3 compartment glass cell, separating the WE, gold flag CE and Ag/AgCl (3 M NaCl) RE, respectively. The 0.1 M phosphate buffer solution (pH 8) was added to the cell before purging with Ar to remove the oxygen from the electrolyte. The CO_2RR electrolysis was performed after saturating the solution with CO_2 (BOC, N5) during 30 min. During electrolysis, a slow stream of CO_2 was used to maintain the solution gas concentration.

Product Characterisation

On-line Electrochemical Mass Spectrometry (OLEMS) was used to detect the gaseous products formed during the reaction. The reaction products at the electrode interface were collected with a small tip positioned close to the electrode. The tip is a 2 mm diameter porous Teflon cylinder (Porex with an average pore size of 5 µm - 10 µm and 45% - 55% porosity) in a Kel-F holder. The tip configuration was cleaned overnight in a 2 M NaOH solution (VWR, EMSURE) and rinsed 5 times with ultrapure warm water before use. A secondary electron multiplier voltage of 1390 V was used, except for hydrogen (m/z =2) where a secondary electron multiplier voltage of 2100 V was used. The pressure was equilibrated for 1 h prior to each measurement. During each experiment, multi ion mass detection as a function of time was used. This program implies a progressive measuring of the different channels with a maximum of 6 channel detections and a time difference of 50 ms between the detection on each channel. One of the channels was used to follow the changes in the total pressure and the other five channels were used to measure the following fragments: m/z=1, m/z=15, m/z=18, m/z=26, m/z=28, corresponding to H_2, CH_4, H_2O, C_2H_4 and CO / N_2, respectively. In order to determine the quantitative distinction of CO (as a product), CO (as a fragment of CO_2)

and N_2 during the reduction of CO_2, the calibration method described by Binninger *et al*. was implemented.[33]

^{1}H NMR samples were prepared by collecting a 2 mL aliquot at a specific time point (30 min or 60 min), adding 100 μL D_2O, dispersing by ultrasonication and transferring 600 μL to a glass NMR tube. A Bruker AVANCE NEO spectrometer console with a 9.4 T superconducting magnet operating at a frequency of 400 MHz fitted with a 5 mm nitrogen-cooled BBFO "SMART" probe, at a calibrated temperature of 298 K was used to measure all ^{1}H NMR. 1D ^{1}H NMR spectra were acquired using a pulse sequence with excitation sculpting and gradients to suppress the water (H_2O) peak;[1] a spectral width of 15 ppm with 32K complex data points was measured. 400 scans were acquired for each sample to increase the signal-to-noise ratio so that quantification of the products was possible. A delay (d1) of 15 s between scans was used. Data were zero-filled to 32K using a line broadening of 0.3 Hz to provide a final spectra resolution of 0.19 Hz per point and chemical shifts were indirectly referenced to TMS at 0 ppm. All data were processed and plotted using TOPSPIN 4.0.6 software.

In situ XAS

Catalyst inks were prepared by adding 100 mg catalyst to 100 mg Vulcan, 200 mg Nafion and 1.5 mL of milli-Q water. The resultant mixtures were dispersed by ultrasonication until homogeneous inks were obtained. Button electrodes were prepared by painting the catalyst ink onto a carbon paper support (PTFE treated Toray Carbon Paper, Alfa Aesar) to generate a catalyst loading of 0.75 mg Cu cm^{-2}. The painted electrodes were hydrated in milli-Q water under vacuum prior to assembling into the *in situ* XAS cell. Spectra referred to as 'dry' were recorded free of any electrolyte solution and without any applied potential. Several scans were collected and merged.

All measurements were collected *in situ* at room temperature at the B18 beamline of Diamond Light Source (UK),[34] using our custom-designed electrochemical cells in a three-electrode configuration,[35] connected to an μAutolab Type III potentiostat. The painted button electrodes were used as the WE with a gold wire CE and RHE RE. Calibration of the monochromator was carried out using a Cu foil, and XAS spectra were recorded in fluorescence mode at the Cu K-edge (8979 eV). The data was analysed using Athena and Artemis programs, which implement the FEFF6 and IFEFFIT codes.[36] No data merge was performed with the *in situ operando* XAS spectra measured. For each catalyst and electrochemical environment a series of potentials was applied cathodically from +0.05 V to –0.75 V *vs*. RHE, in succession, before returning back to +0.05 V. Several spectra were recorded at each potential and the assigned times presented are based on the time elapsed from the initial recording of the *in situ operando* XAS spectra at +0.05 V. For the CO_2-saturated measurements the XAS spectra were recorded in a shortened energy range whilst scanning the monochromator in both directions to minimise the time between individual scans.

7.3. Results and Discussion

7.3.1. Physical characterization of the Cu:NTO and CuO@NTO catalysts

The SEM and TEM images of 9 wt.% Cu:NTO are presented in **Figure 1**. Discrete individual particles on the order of a few microns are observed that consist of aggregated nanowires (**Figure 1A**). The TEM images (**Figure 1B and C**) provide further evidence of the intertwined nature of the nanowires that give rise to the larger particles. Particle size analysis indicated that the diameter of the 9 wt.% Cu:NTO nanowires was 13.0 ± 2.6 nm (**Figure S1A**), in agreement with previous work.[26] HAADF-STEM EDS elemental mapping was performed to probe the homogeneity of metals within 9 wt.% Cu:NTO (**Figure 1D**). The homogeneous distribution of Na, Ti and Cu throughout the particles probes the suitability of this methodology in the preparation of mixed metal oxide layered nanomaterials. As can be seen

in **Figure 1E**, the diffraction pattern of the intercalated Cu:NTO sample, there is a relative decrease in 2θ position for the $Na_2Ti_3O_7$ (100) peak around 11° indicative of the lattice expansion produced by the intercalation of hydrated Cu cations between the layers of TiO_6 octahedra, expanding the unit cell. Furthermore, peak broadening was observed indicative of the low crystallinity of the nanostructured catalyst.

SEM images of the CuO particles obtained via cathodic corrosion (**Figure 2A**) show cubic particles with an average diameter of 527 ± 73 nm (**Figure S1B**). HRTEM imaging of the cubic particles show distinct lattice spacing of 0.28 nm (**Figure 2B**) which corresponds to the (110) plane of CuO. The XRD pattern of the cubic CuO particles is presented in **Figure S2**. The relatively narrow and intense diffraction peaks of the catalyst prepared in $CaCl_2$ are identical to the database pattern of monoclinic CuO and are indicative of the formation of a highly crystalline CuO particles under the cathodic corrosion parameters employed. The peaks at 2θ = 41.9°, 45.1°, 57.1° 63.1°, 68.6°, 72.8°, 78.2°, 79.0° and 80.9° correspond well with the (002) & ($11\bar{1}$), (111) & (200), ($20\bar{2}$), (020), (202),($11\bar{3}$), (022), ($31\bar{1}$) and (113) planes of CuO.

The diffraction pattern of 10 wt.% CuO@NTO shows broad signals at 2θ = 10.2°, 29.4°, 33.2° and 57.1° corresponding to the (100), (110), (111) and (020) planes of $Na_2Ti_3O_7$, respectively. Additional low intensity peaks can be observed at 2θ = 41.9° and 45.1°, corresponding to the overlapping (002) & ($11\bar{1}$) planes and (111) & (200) planes of crystalline CuO, respectively. For the undoped NTO nanowires, less broad diffractions peaks with greater relative intensity are observed, suggestive of greater crystallinity in the absence of intercalated transition metal ions. The peaks are in reasonable agreement with the database pattern of crystalline $Na_2Ti_3O_7$ [ICSD Coll Code 187821].

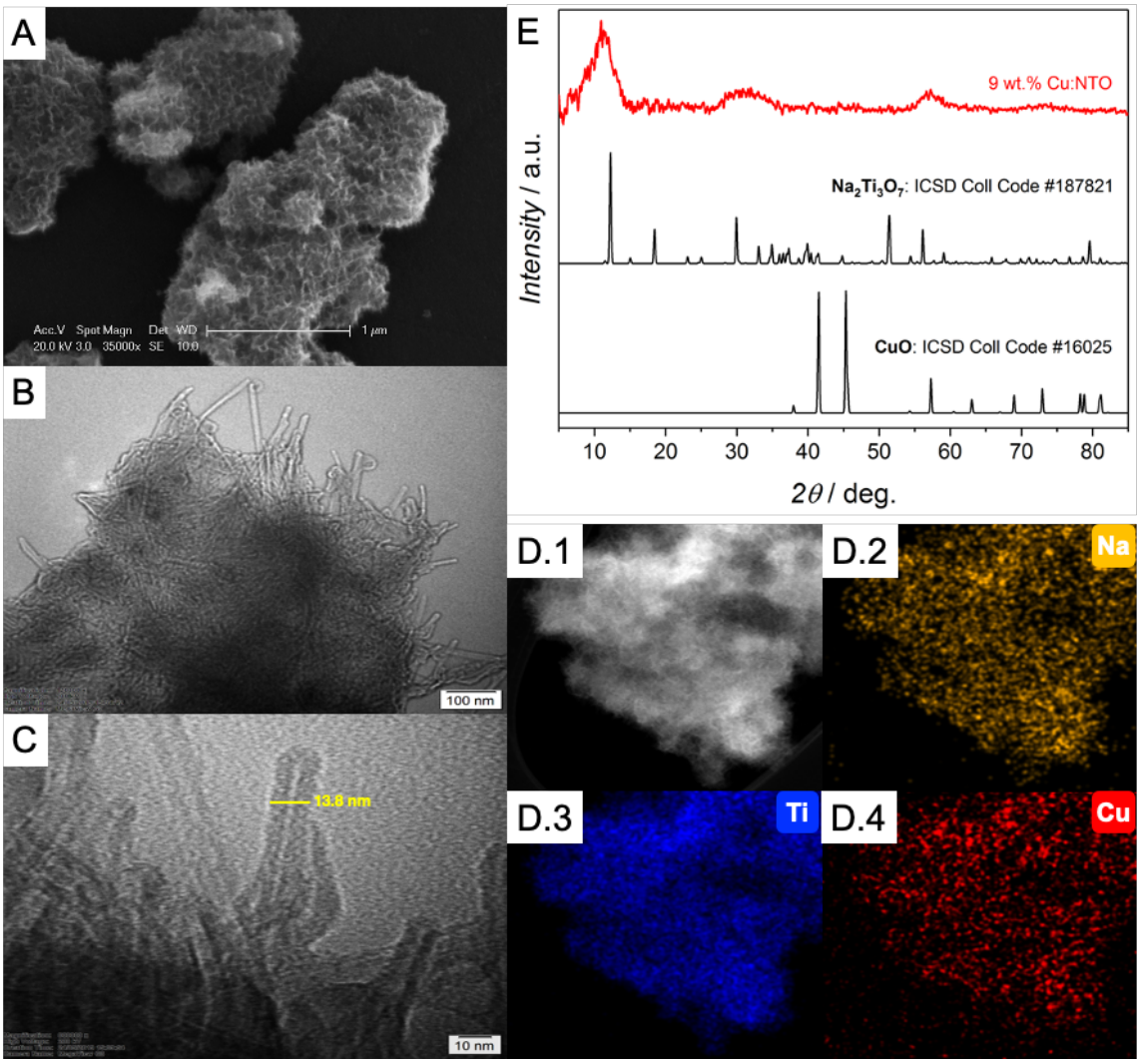

Figure 1. (A) SEM, (B) TEM, (C) HRTEM and (D) HAADF and corresponding EDS elemental mapping images of 9 wt.% Cu:NTO. (E) XRD pattern of 9 wt.% Cu:NTO. ICSD database patterns for $Na_2Ti_3O_7$ [Coll Code 187821] and CuO [Coll Code 16025] are shown for comparison.

The increase in the NTO (100) spacing indicated by the shift in 2θ is generated by the presence of hydrating water molecules within the titanate layers due to the low temperature production of layered titanate nanowires in an aqueous environment.[37]

Upon mixing NTO and the CuO nanocubes, the presence of both the cubic CuO particles and the aggregated NTO nanowires as separate phases were observed for the 10 wt.% CuO@NTO catalyst (**Figure 2C**). Higher magnification TEM images show the presence of the aggregated nanowires (**Figure S3**). HAADF-EDS elemental mapping characterisation of a

CuO particle from the freshly prepared CuO@NTO catalyst demonstrates a cubic Cu-O matrix but also shows the presence of the Ti phase on the periphery (**Figure 2D**). Following dispersion of the catalyst via ultrasonication, SEM characterisation suggested that the presence of NTO at the surface of the Cu-O matrices had increased (**Figure 2E**).

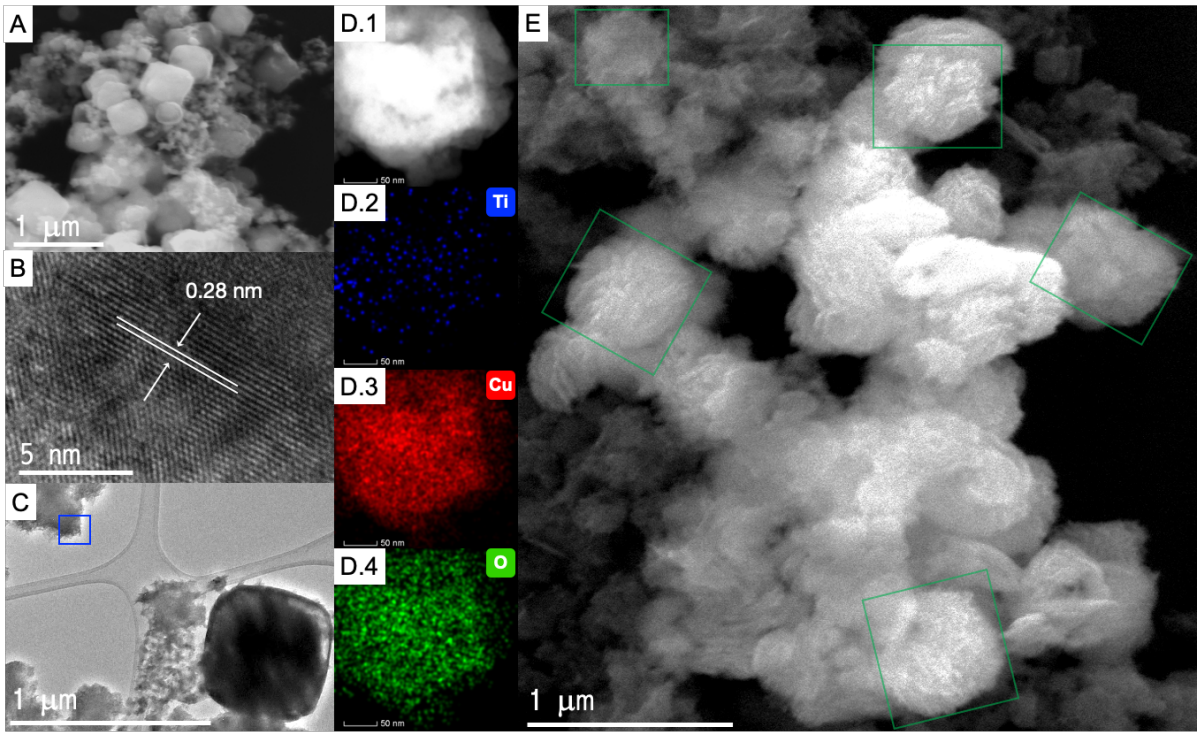

Figure 2. (A) Low magnification SEM image and (B) HRTEM image of cubic CuO particles. (C) Low magnification TEM image and (D) HAADF-STEM and corresponding EDS elemental mapping images of freshly prepared 10 wt.% CuO@NTO. (E) Low magnification SEM image of 10 wt.% CuO@NTO after catalyst was dispersed by ultra sonication in water for 30 min. Green squares highlight the presence cube-like structures. HRTEM image recorded at point indicated by blue square in (C) is presented in **Figure S3**.

Figure 3A presents the normalised XANES spectra of Cu foil, Cu(I) and Cu(II) standard oxide compounds in addition to the 'dry' nanostructured 9 wt.% Cu:NTO and 10 wt.% CuO@NTO electrodes (prior to flooding the cell with electrolyte).

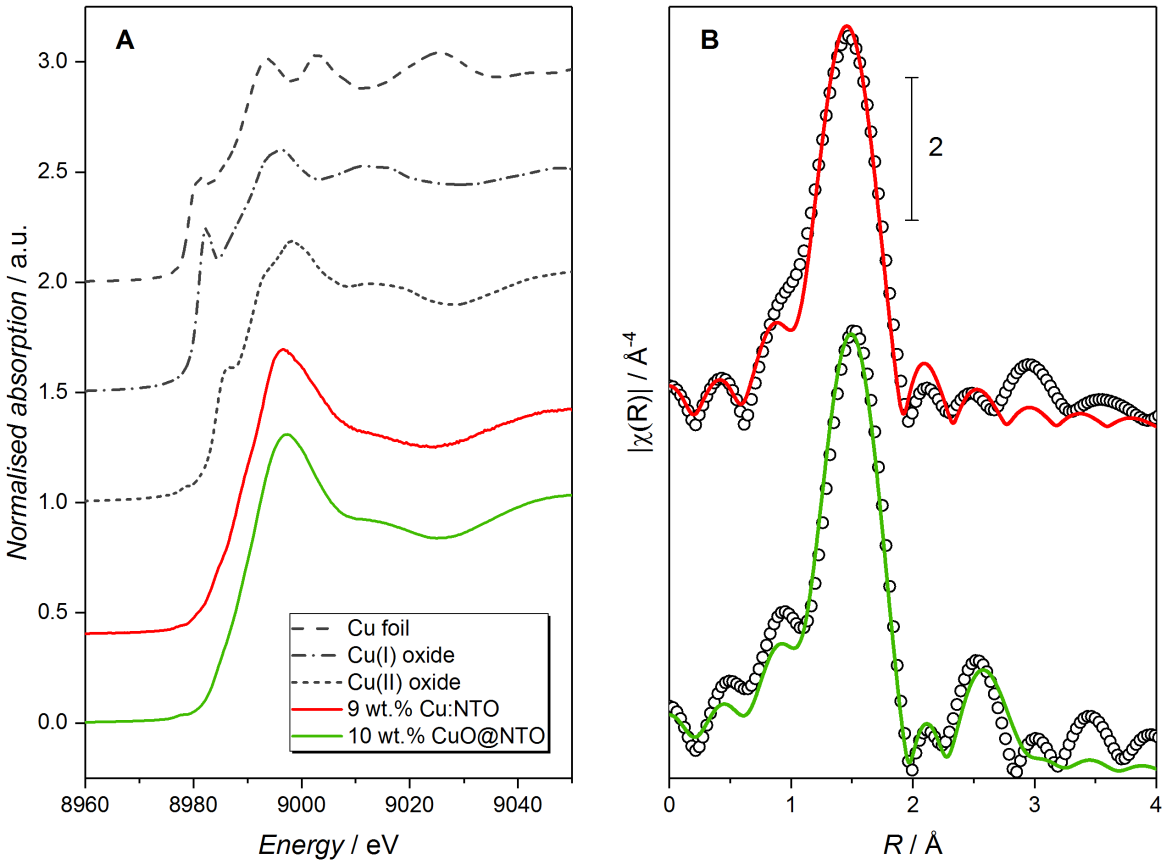

Figure 3. (A) Normalized Cu K-edge XANES spectra for the synthesised catalysts as well as reference materials. (B) FT signal of the k^3-weighted EXAFS data (empty circles) and fits (coloured lines) of 9 wt.% Cu:NTO (red) and 10 wt.% CuO@NTO (green).

Comparison against the Cu foil and standard oxide compound references suggested the Cu present in both 9 wt.% Cu:NTO and 10 wt.% CuO@NTO was in a +2 oxidation state. The intense white line peaks at 8996 and 8997 eV, respectively, for 9 wt.% Cu:NTO and 10 wt.% CuO@NTO, in combination with the significantly reduced intensity of the shoulder peak at 8986 eV are indicative of the presence of hydrated Cu^{2+} sites.[38]

Linear combination fit (LCF) analysis has been demonstrated as an effective means of elucidating the respective contributions of the various Cu species to measured XAS spectra.[39-41] Recently it was demonstrated that the LCF elucidation of Cu oxidation state of XANES

spectra is within 3-4% accuracy.[42] The results for the 'dry' electrodes of 9 wt.% Cu:NTO and 10 wt.% CuO@NTO indicate a +2 Cu oxidation state (**Table S1**), in agreement with the value obtained by the maximum of the derivative spectra.

Figure 3B shows the comparison between the Fourier transforms (FTs) of the experimental EXAFS spectra (empty circles) and the best-fit simulations (coloured lines) for 9 wt.% Cu:NTO and 10 wt.% CuO@NTO (k-space data is presented in **Figure S4**). The first coordination shell peak at around 1.4 Å (not phase corrected) is observed for both catalysts, corresponding to the Cu–O scattering pair. A significant second peak was only observed for 10 wt.% CuO@NTO at ≈2.5 Å (not phase corrected), corresponding to the Cu-Cu^{oxide} scattering pair. The best-fit parameters are summarised in **Table S2**.

7.3.2. Assessment of the electrochemical CO_2RR on the Cu:NTO and CuO@NTO catalysts

The cyclic voltammograms of undoped NTO were recorded in an Ar-saturated phosphate buffer (pH 8) (**Figure S5**) employing a rotating disk electrode (RDE) configuration to establish a constant rate of diffusion of solution species towards the catalyst and to promote the removal of surface-generated species during electrochemical investigation.

The blank voltammogram of 9 wt.% Cu:NTO is presented in **Figure 4A** . The onset potential was determined as -0.487 V *vs.* RHE (**Figure S6B**), 20 mV more cathodic than the undoped NTO catalyst (**Figure S6A**). Gas bubble formation was observed at the more negative applied potentials when the current density was highest, suggesting hydrogen formation via hydrogen evolution reaction (HER). Albeit the HER onset potential in the presence of intercalated Cu was kinetically less favourable, as observed by Bandi *et al.* following the addition of small amounts of Cu to RuO_2-TiO_2 electrodes,[43] the overall activity observed with incorporated Cu

ions was greater. However, the low magnitude of current density measured suggests that this catalyst would not be suitable for large-scale or industrial HER applications.

The blank voltammogram of 10 wt.% CuO@NTO is presented in **Figure 4B**. The HER onset potential was determined as -0.580 V *vs*. RHE (**Figure S6C**), significantly more cathodic than undoped NTO or 9 wt.% Cu:NTO, ascribed to the increased Cu concentration. The presence of CuO particles significantly hindered the HER activity.

Although the shape of the CVs for the two Cu-containing titanate samples was similar there were noticeable differences observed that suggest that the exact nature and coordination environment of the Cu sites had significant impact on the catalytic activity towards HER. There was a 93 mV difference in onset potential between the two catalysts, with better HER performance observed at less reducing potentials for the intercalated Cu catalyst and the magnitude of measured current density for 9 wt.% Cu:NTO being twice that of 10 wt.% CuO@NTO at -0.9 V vs RHE (**Figure 4A & B**). In the case of the Cu-intercalated catalyst, the Cu^{2+} ions are incorporated into the TiO_6^{2-} interlayer spacing of a material resulting in a surface mainly composed of Ti sites with low crystallinity, whereas Cu surface sites are more accessible in the mixed phase CuO@NTO catalyst. This difference in the surface structure of the two catalysts was anticipated to result in significant differences in their respective electrocatalytic CO_2RR activity given that Ti surfaces have high HER selectivity under CO_2RR conditions.[44] The blank CV results indicate that the HER activity is significantly hindered by the interface of the NTO phase with CuO. In contrast, the presence of doped Cu^{2+} ions between titanate layers enhanced the HER activity of NTO.

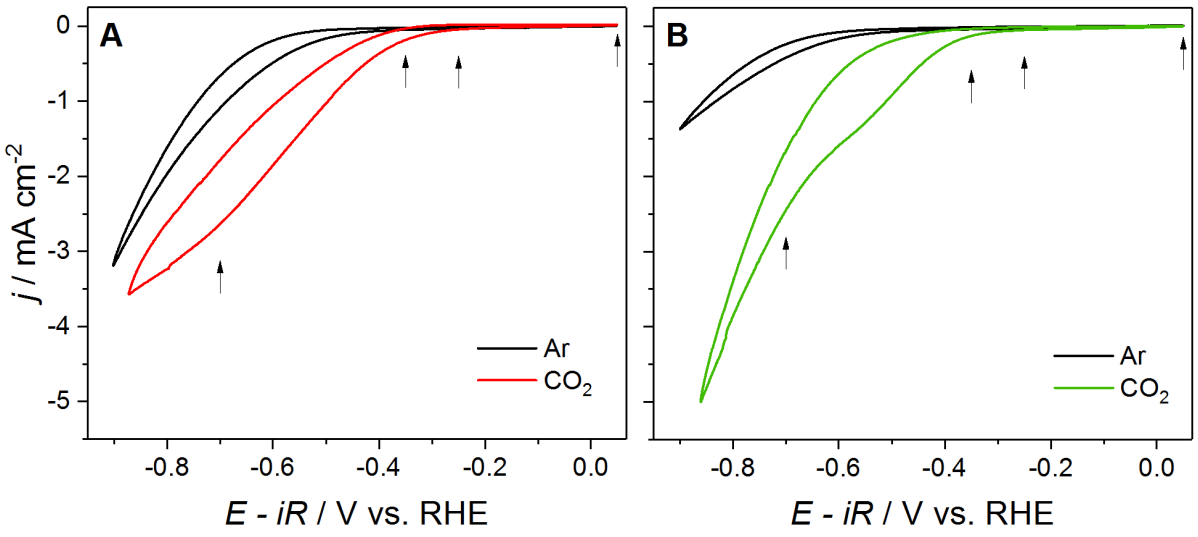

Figure 4. Stable cyclic voltammograms of (A) 9 wt.% Cu:NTO and (B) 10 wt.% CuO@NTO in Ar-saturated 0.1 M K_2HPO_4 / KH_2PO_4 buffer solution (pH 8) and CO_2-saturated 0.1 M K_2HPO_4 / KH_2PO_4 buffer solution (pH 6.5); ν = 50 mV s^{-1} and rotation = 1200 rpm for all measurements. Arrows are indicators of the applied potentials utilised during *in situ* XAS measurements.

Prior to evaluating CO_2RR activity of the Cu-containing titanates, measurements were performed with pure NTO to understand the electrochemical behaviour of the titanate phase in the presence of CO_2. The phosphate buffer solution was first saturated with Ar to expel any reactive gases present and was subsequently saturated with CO_2. Upon saturation with CO_2 the pH of the buffer solution decreased from pH = 8 to pH = 6.5. **Figure S5B** presents the CVs of NTO in CO_2-saturated phosphate buffer (0.1 M K_2HPO_4 + KH_2PO_4). Comparison of the current density profiles measured in the presence and absence of CO_2 indicate that NTO possesses negligible CO_2RR activity, as there was negligible difference in the magnitude of current density recorded in either electrochemical environment. The first cycle recorded in the CO_2-rich electrolyte closely resembled that of the first 'blank' cycle (**Figure 4B**). The decrease in pH did not have an enhancing effect on the catalytic activity of the NTO towards HER, when the reaction should have been more facile. Rather, a -33 mV shift in onset potential was determined (**Figure S6D**). Notably, the presence of dissolved CO_2, and reduced pH, nullified the anodic peak observed in the Ar-saturated CVs. This was ascribed to greater affinity for and stronger binding of CO_2 to the Ti surface sites. It was reported previously that two

competing processes occur at nanoporous titanate semiconductor electrodes in aqueous electrolyte.[45] The anodic peak observed via CV following a cathodic sweep is caused by the accumulation of charge (electrons) in the absence of an electrochemical reaction, that subsequently discharges during the anodic scan. The anodic peak is not visible in the return sweep if an electrochemical reaction occurs due to the consumption of the electrons. Therefore, our results suggest that in Ar-saturated phosphate HER does not occur at the NTO catalyst in the potential range applied, rather the catalyst acts as a capacitor. In the presence of CO_2, electrons are consumed for the CO_2RR, albeit with low current density measured, suggesting that the undoped catalyst is not ideal for efficient product formation.

The stable CV profile of 9 wt.% Cu:NTO in CO_2-saturated phosphate buffer solution is presented in **Figure 4A**. In the presence of dissolved CO_2 there was an anodic shift in the reduction onset potential relative to the blank measurements of +156 mV to -0.331 V vs RHE (**Figure S6E**) and an increase in the overall current density measured in the applied potential range. Through subsequent cycles the activity of CO_2RR decreases, i.e. the peak current density decreased but the nature of the electrochemical process, as suggested by the shape of the current density profile, was unchanged (**Figure S7B**). This was ascribed to the catalytic decay due to the increasing unavailability of Cu sites poisoning the catalyst activity and the strong binding of evolved CO to Ti sites.

The stable CV profile of 10 wt.% CuO@NTO in CO_2-saturated phosphate buffer solution is presented in **Figure 4B**. In the presence of CO_2 there was notable cathodic current density measured in the initial scan between +0.05 V and -0.2 V vs RHE, prior to the broad cathodic surface reconstruction peak previously observed in the blank when the applied potential exceeded -0.2 V vs RHE. However, this feature was only observed during the first cycle and was therefore attributed to a difference in surface reconstruction and rearrangement of the double layer. Furthermore, it was concluded that the current density measured in the

presence of CO_2 was a direct reflection of the CO_2RR activity of the catalyst because of the low magnitude of current density measured in the blanks. It was noted that the different Cu coordination environment of the CuO-derived catalyst had a significant impact on CO_2RR activity given that the activity of the mixed phase 10 wt.% CuO@NTO catalyst increased through subsequent cycles. Notably, for the first 6 cycles the peak current density increased gradually, followed by a significant boost to the catalytic activity observed during the seventh cycle that resulted in a near 2-fold increase in peak current density measured at -0.9 V vs RHE (**Figure S7A**), in stark contrast to 9 wt.% Cu:NTO. No noticeable change in the onset potential was determined for the mixed phase catalyst for the duration of the 10 cycles, indicating that it was not a change in the reaction kinetics that was responsible for the enhanced activity observed but rather a structural surface activation process that increased in the intrinsic activity of the Cu sites. This is in agreement with existing literature on the enhanced activity of oxide-derived Cu catalysts towards CO_2RR due to the increase in surface roughness route by the electrochemical reduction of the Cu oxide catalysts, generating metallic Cu NPs.[46-48] Furthermore, it was demonstrated that the reduction of Cu oxide electrodes generates surface defects that contain a greater number of under-coordinated sites which would also contribute to the boost in CO_2RR activity observed.[49]

To investigate the impact of the change in pH induced by the dissolution of CO_2 in the electrolyte, blank CVs were recorded in the 0.1 M K_2HPO_4 / KH_2PO_4 buffer solution with H_3PO_4 added to increase the acidity (**Figure S8**). The blank current density profile of 9 wt.% Cu:NTO obtained at pH = 6 did not vary significantly from that obtained at pH = 8 in the applied potential range employed in this study. These results confirmed that the relative shift in the onset potential observed was not wrought simply by the change in pH, but rather, it was a direct result of the presence of dissolved CO_2, thus, the onset potential observed was due to CO_2RR on this catalyst.

To summarise, we have demonstrated that the electrocatalytic activity observed for the Cu-containing titanate nanostructures towards CO_2RR in near-neutral phosphate buffer solution is not simply a function of the chemical composition of the catalysts. The physical and structural properties contribute significantly to the observed activity. Consequently, it is the specific chemical and structural nature of each catalyst generated during CO_2RR electrolysis that produces the greatest impact on the activity and product selectivity.

CO_2RR electrolyses were performed via chronoamperometry. Gaseous products were characterised by OLEMS. **Figure 5** shows the gas products of CO_2RR at 9 wt.% Cu:NTO and 10 wt.% CuO@NTO during 1-hour electrolysis at -0.8 V *vs.* RHE. In the case of 9 wt.% Cu:NTO (Figure 5A), the formation of H_2 (m/z = 2) accounts for the majority of gas product evolved at the beginning of the electrolysis and maintained a % gas product distribution between 50% and 65%, increasing over the 1-hour duration. The formation of CO (m/z = 28) and CH_4 (m/z = 16) was also detected during the 1-hour electrolysis. An inverse relationship was observed between the % gas products of CO and CH_4, in that the decrease in CO (a $2e^-$ product) was accompanied by a near-equivalent increase in the concentration of CH_4 (a $8e^-$ product). Similarly, the measured decrease in CH_4 after ≈2700 s gives rise to a small increase in % gas product of CO detected. These results provide evidence that CO is the dominant CO_2RR product for 9 wt.% Cu:NTO and that the catalyst is able to reduce evolved CO to CH_4. Our results are in agreement with Reske et al. who demonstrated that the dominant CO_2RR products were H_2 > CO > CH_4 for Cu nanocatalysts with sizes up to ≈20 nm.[14] Further, the change in % gas product distribution suggests that the Cu nanocatalyst size increases during CO_2RR electrolysis.

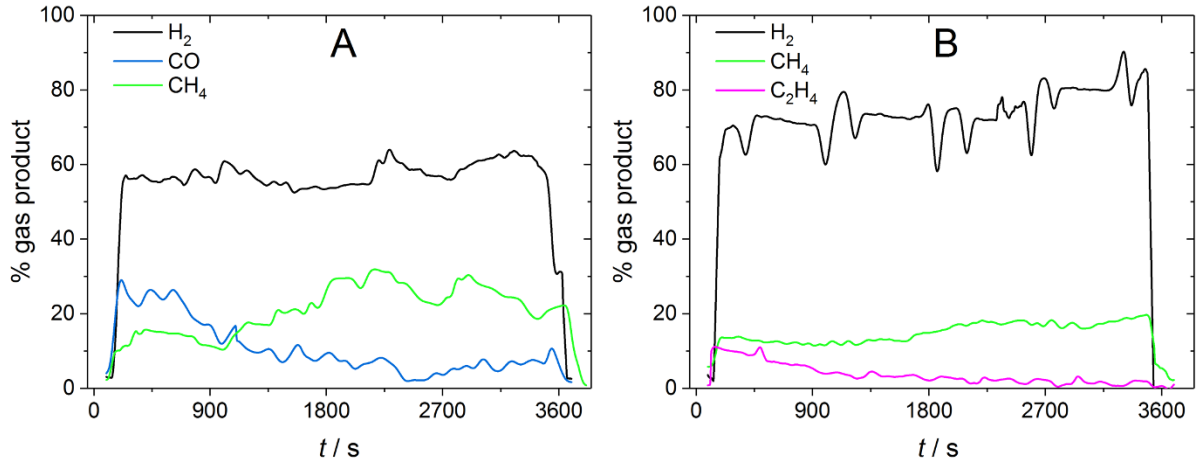

Figure 5. Product characterisation of gases produced during the CO_2RR at -0.8 V *vs*. RHE on (A) 9 wt.% Cu:NTO and (B) 10 wt.% CuO@NTO in CO_2-saturated 0.1 M K_2HPO_4 / KH_2PO_4 buffer solution (pH 6.5).

On the other hand, the % distribution of H_2 from CO_2RR electrolysis on the 10 wt.% CuO@NTO was higher than the Cu:NTO (**Figure 5B**) and gradually increased to > 80% after 1 hour. The distribution of CH_4 also demonstrated a gradual increase with a final % distribution similar to that observed for 9 wt.% Cu:NTO. Two significant differences were observed with the mixed phase catalyst. A C_2 product, C_2H_4 (m/z = 26) was initially detected in low abundance and subsequently decreased with increasing CH_4, suggestive of a change to the active sites and decrease in particle size. It has been reported that oxide-derived Cu CO_2RR catalysts generated from the reduction of nanocubes, which possess a high ratio of Cu(100) sites, form little to no CH_4 with increased efficiency towards C_2H_4 formation.[50-52] Therefore, our results suggest that the presence of NTO promotes the decrease in CuO particle size and restructuring of the oxide surface, altering the selectivity of the CO_2RR electrolysis.

Liquid products were probed by ^{1}H NMR, however, no appreciable liquid products were indicated by the spectra recorded after 1 hour CO_2RR electrolysis for both catalysts. This is in agreement with Hori et al. who demonstrated that gas products are produced via electrolysis in phosphate under more strongly reducing conditions.[53]

7.3.3. Blank in situ X-ray Absorption Spectroscopy (XAS) characterisation

To better understand the structural and chemical changes undergone by Cu in both 9 wt.% Cu:NTO and 10 wt.% CuO@NTO during CO_2RR, *in situ* XAS measurements were recorded under chronoamperometric conditions. First, and to be used as a comparison, data was collected in Ar-saturated 0.1 M phosphate buffer, at +0.05 V, -0.25 V, -0.35 V and -0.75 V (as indicated in **Figure 4**). The XANES spectra and results of LCF analysis are presented in **Figure S9A-D** and **Table S3-S4**, respectively.

Figure 6 presents the Cu species composition determined by LCF analysis of 9 wt.% Cu:NTO and 10 wt.% CuO@NTO in Ar-saturated electrolyte. A noticeable difference in the Cu(II) reducibility for the two catalysts was observed *in situ*. After 25 min under an applied potential of +0.05 V the contributions of Cu(II), Cu(I) and Cu(0) in 9 wt.% Cu:NTO were 10.3%, 89.7% and 0%, respectively. The Cu(II) contribution disappeared completely at -0.25 V, resulting in 47.1% Cu(I) species and 52.9% Cu(0) remaining after a total electrolysis time of 50 mins (**Figure 6A** and **B**, respectively). Interestingly, the Cu species distributions appeared to stabilise under an applied potential of -0.35 V. After 25 min at -0.75 V, a total electrolysis time of > 2 hours, no further significant changes in Cu species distribution was observed; Cu(I) and Cu(0) contributions were 35.9% and 64.9%, respectively, only marginally more reduced than Cu species contributions determined at -0.35 V. With 10 wt.% CuO@NTO the decrease in Cu(II) contribution was lesser after 25 mins at +0.05 V (**Figure 6E**). Following 25 mins under an applied potential of -0.25 V the Cu species contributions of Cu(II), Cu(I) and Cu(0) determined by LCF analysis were 10.5%, 57.3% and 32.1%, respectively. As was seen with 9 wt.% Cu:NTO, the LCF analysis suggested that the rate of change in Cu species was slower at -0.35 V, particularly in the case of Cu(I) (**Table S4**). At -0.75 V the rate of Cu(II) reduction increased and the resultant Cu compositions of Cu(II), Cu(I) and Cu(0) were 0%, 41.2% and 58.8%, respectively.

Following the cathodic measurements, the initial potential (+0.05 V) was applied to probe the reversibility of the oxidised Cu species reduction process. For 9 wt.% Cu:NTO, a relative ≈2% shift in both Cu(I) and Cu(0) was observed, increase in the former and decrease in the latter, suggesting that the Cu metallicity of generated under reducing conditions could be reversible. On the other hand, there was negligible change in the Cu species distribution at +0.05 V following the cathodic series for 10% CuO@NTO. Therefore, further spectra were recorded at more anodic (for 9 wt.% Cu:NTO) and cathodic (for 10% CuO@NTO) potentials in succession and results are presented in **Figures S10** and **S11**. The application of more anodic potentials to 9 wt.% Cu:NTO produced a decrease in Cu metallicity and subsequent increases in the Cu(I) contribution determined by LCF, confirming that the electrochemical reduced catalyst is susceptible to some re-oxidation in the phosphate buffer. Further cathodic electrolyses at 10 wt.% CuO@NTO demonstrate that Cu catalysts derived from 500 nm CuO cubes are not fully reduced to metallic Cu during 3 hours under reducing conditions in the absence of CO_2.

Overall, we have demonstrated that the different Cu^{2+} sites in 9 wt.% Cu:NTO and 10 wt.% CuO@NTO are reduced at different rates in Ar-saturated phosphate buffer solution. LCF analyses suggest that the CuO-containing catalyst is chemically more robust, experiencing relatively more gradual Cu^{2+} reduction and a higher overall approximate Cu oxidation state following cathodic treatment.

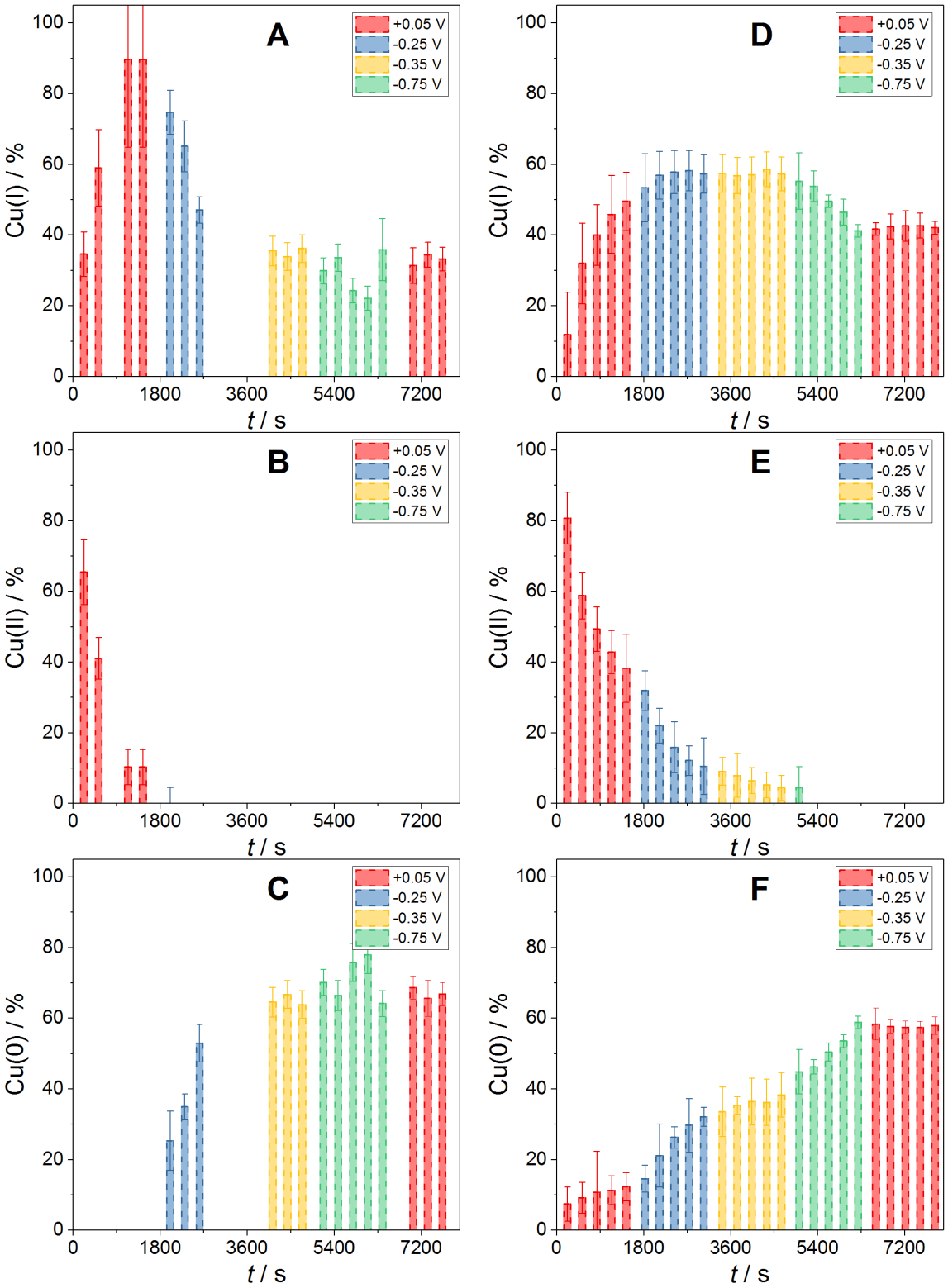

Figure 6. LCF determination of Cu species composition from *in situ* XANES spectra of (A-C) 9 wt.% Cu:NTO and (D-F) 10 wt.% CuO@NTO in Ar-saturated 0.1 M K_2HPO_4 / KH_2PO_4 solution (pH 8) at +0.05 V (red), -0.25 V (blue), -0.35 V (yellow) and -0.75V (green). Each bar represents 5 min under applied potential.

The k^3-weighted EXAFS signals and Fourier Transforms (FTs) for 9 wt.% Cu:NTO and 10 wt.% CuO@NTO are shown in **Figure S12**, with best fit parameters are presented in **Table S5** and **Table S6,** respectively. Generally, the EXAFS FTs for the two catalysts were very similar. At +0.05 V the Cu-O first coordination shell peak at ~1.4 Å (not phase corrected) can be observed for both catalysts (**Figure S12B,D**). The Cu-Cu coordination shell peak at ~2.5 Å (not phase corrected) is more prominent in 10 wt.% CuO@NTO than 9 wt.% Cu:NTO during the initial measurements, as expected given that the as-prepared CuO@NTO catalyst contained 500 nm CuO nanocubes whereas the Cu:NTO catalyst had been determined as existing as single atom complexes within the titanate layers. For 9 wt.% Cu:NTO, there was a more noticeable decrease in relative intensity of the Cu-O scattering peak at +0.05 V that corresponded to the more rapid reduction of Cu(II) indicated by XANES LCF analysis. The increase in intensity of the second shell coordination peak at ~2.2 Å (not phase corrected) under an applied potential of -0.35 V, corresponding to the Cu-Cu^{metal} scattering pair, was again similar for both catalysts, in agreement with XANES analyses that determined the initial reduction of Cu(II) to Cu(0) was dominant at less cathodic potentials in Ar-saturated phosphate.

7.3.4. In situ XAS characterization of the Cu titanates under relevant CO_2RR conditions

Figure 7 visualises the Cu species contribution determined by LCF analysis for 9 wt.% Cu:NTO and 10 wt.% CuO@NTO recorded in CO_2-saturated phosphate (XANES spectra are presented in **Figure S13**). Results of LCF analysis, including the estimated Cu oxidation states, are tabulated in **Table S7** and **Table S8**, respectively. After 5 mins at +0.05 V in CO_2-saturated phosphate LCF analysis indicates that there was noticeable reduction of Cu(II) species on either catalyst, contrasting the slight reduction that had been determined in the same time period in the absence of CO_2. At -0.25 V the reduction of Cu(II) was greatest for the 9 wt.% Cu:NTO catalyst such that the Cu species contribution were determined as 9.1%,

72.1% and 18.8%, respectively, for Cu(II), Cu(I) and Cu(0). In the same time period, the Cu species contribution for 10 wt.% CuO@NTO were determined as 18.4%, 55.9% and 25.8%, respectively. However, unlike the Ar-saturated measurements, there were significant changes in Cu species distribution observed at -0.35 V for both catalysts. In both cases the Cu(II) contribution reduced to zero under this applied potential, with the reduction occurring fastest for 9 wt.% Cu:NTO, reflected in the significant change in subsequent XANES spectra (**Figure S13C**). The difference in reducibility of the two catalysts was highlighted at this applied potential, where the major Cu species was Cu(0) for 9 wt.% Cu:NTO and Cu(I) for 10 wt.% CuO@NTO, respectively. At the end of the cathodic series ($E_{applied}$ = -0.75 V) it was determined that the oxide-derived catalyst was composed of 0% Cu(II), 42.4% Cu(I) and 57.6% Cu(0), with an estimated Cu oxidation state of 0.42 ± 0.06. Likewise, 9 wt.% Cu:NTO consisted of 0% Cu(II), 31.7% Cu(I) and 68.3% Cu(0), with an estimated oxidation state of 0.32 ± 0.02.

That similar Cu species compositions and corresponding estimated Cu oxidation states for each catalyst were obtained from blank (Ar-saturated) and CO_2-saturated measurements, regardless of the duration of the measurements, demonstrates that the applied potential imposes the greatest effect in the reduction of oxidised Cu species in 0.1 M K_2HPO_4 / KH_2PO_4. An analogous observation was recently reported using 100 mM $KHCO_3$.[49]

Our results agree with recent *in situ* and *operando* XAS studies that have also determined the presence of oxidised Cu species during and following CO_2RR at nanostructured oxide-derived Cu catalysts.[11, 42] However, our work reports a higher *in situ* Cu(II) composition than has been reported previously. The *in situ* XANES spectra measured in this work were obtained using a successive applied potential regime, increasing the magnitude of cathodic potential in stages to monitor the change in Cu oxidation state with time. Thus, although the total measurement time is comparable the overall cathodic potential applied to the catalysts

differs, and we have demonstrated that the magnitude of the applied cathodic potential has a significant impact on the nature of the Cu catalyst.

However, XAS techniques probe the bulk of the catalysts and given the difference in particle size between the Cu:NTO and CuO@NTO catalysts, the LCF analyses for Cu:NTO are more reflective of the nature of the catalyst surface generated under reducing conditions in the phosphate electrolyte, whilst the core of the CuO nanocubes in CuO@NTO add greater weighting to the LCF results than the catalyst surface. It must also be noted that the decrease in pH upon saturating the electrolyte with CO_2 accelerates the reduction of Cu species such that similar reduced Cu oxidation states can be obtained in significantly shorter timescales.

Fourier transforms of the data collected on a CO_2-saturated electrolyte are presented in **Figure S14**. As only XANES data was collected under these conditions, fit of the data was not possible, although we still carried out qualitative comparison of the data. The change in FTs observed in the presence of CO_2 was similar to the Ar measurements. The rate of Cu(II) reduction, evidenced by the disappearance of the Cu-O scattering peak and emergence of Cu-Cu scattering, was more pronounced for 9 wt.% Cu:NTO, in agreement with our XANES analyses. At -0.75 V the Cu-O peak of 10 wt.% CuO@NTO can still be distinguished, albeit at a greater bond length, indicative of Cu(I)-O.

Relating the *in situ* CO_2-saturated XANES and EXAFS results with the OLEMS results provides insight into the roles of Cu species in the formation of the observed gaseous products. Under CO_2RR conditions 10 wt.% CuO@NTO maintains a higher overall oxidation state with notable contribution of Cu(II) species during initial electrolysis and apparent sub-surface Cu-O. However, that blank EXAFS fit analysis indicates the presence of metallic Cu nanoclusters at more reducing potentials and that the applied potential has greatest impact on the Cu species generated *in situ*, suggests that the increased activity of this catalyst observed during CV cycling was generated by the under-coordinated metallic Cu sites.

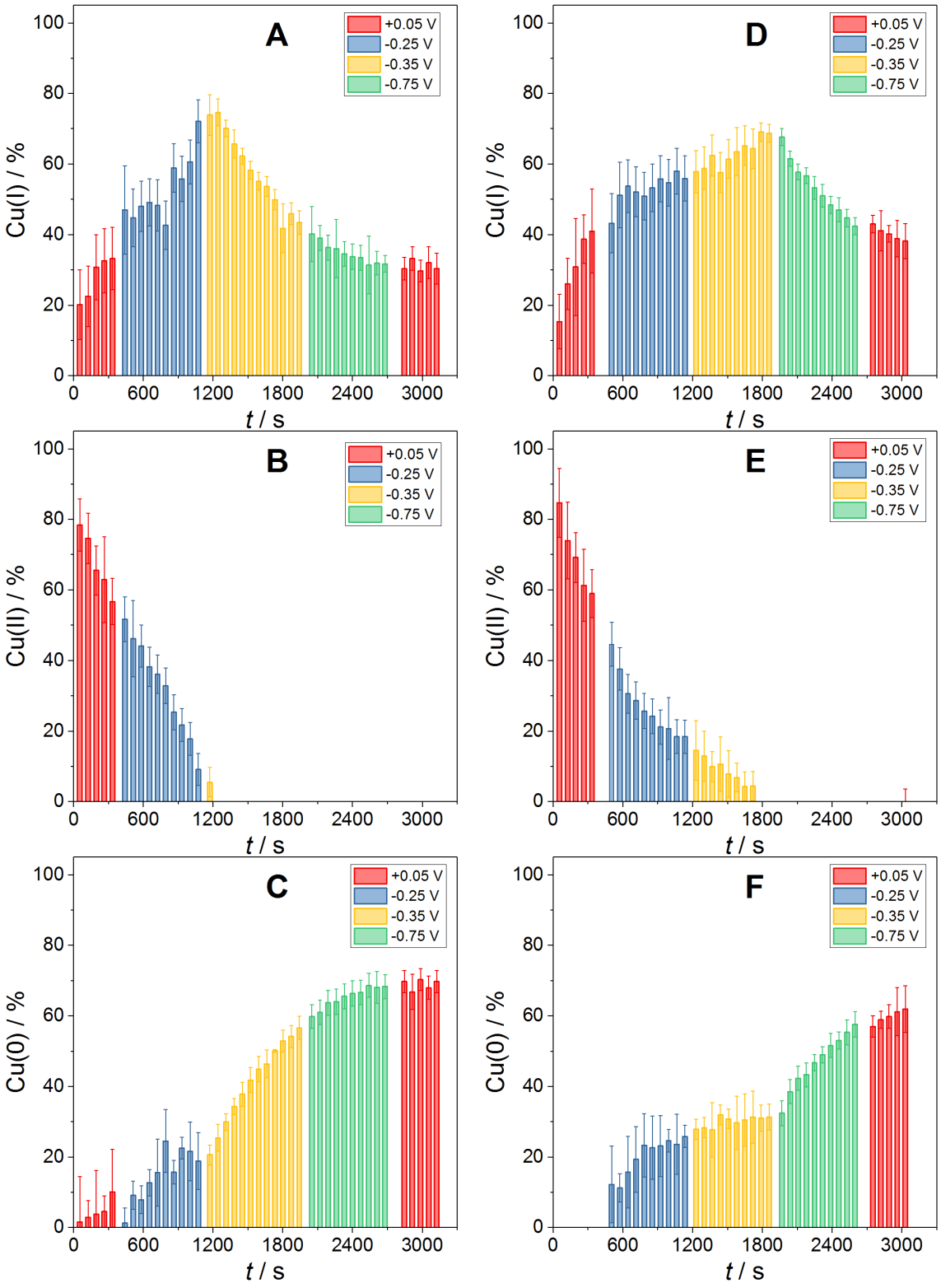

Figure 7. LCF determination of Cu species composition from *in situ* XANES spectra of (A-C) 9 wt.% Cu:NTO and (D-F) 10 wt.% CuO@NTO in CO_2-saturated 0.1 M K_2HPO_4 / KH_2PO_4 solution (pH 6.5) at +0.05 V (red), -0.25 V (blue), -0.35 V (orange) and -0.75V (green). Each bar represents 1 min under applied potential.

7.4. Conclusions

We have demonstrated the versatility of the cathodic corrosion method in the preparation of nanostructured metal oxide electrocatalysts by the effective preparation of Cu(II) NTO catalysts with intrinsically different Cu coordination environments. Namely, we investigated the differences between single atom Cu complexes in 9 wt.% Cu:NTO and a 'bulk' CuO lattice in 10 wt.% CuO@NTO.

XRD characterisation indicated the presence of CuO in the mixed phase catalyst. Electron microscopy demonstrated that interaction between the CuO and NTO forms a core-shell type structure in which CuO cubes are encompassed by the NTO nanowires. The absence of any diffraction pattern features corresponding to either metallic or oxidised Cu for 9 wt.% Cu:NTO, combined with the homogeneous Cu distribution observed via HAADF-EDS was indicative that the intercalated Cu did not form metallic or oxidic Cu clusters. This was confirmed via XANES analysis, where square planar Cu complexes were identified.

Blank electrochemical characterisation measurements demonstrated that the presence of intercalated Cu affords enhanced current density relative to undoped NTO, an enhancement not afforded by the mixed phase CuO@NTO catalyst.

CO_2RR activity was probed by CV and electrolysis, with gaseous products from the electrolysis characterised by OLEMS. We demonstrated that the NTO phase alone does not contribute to any observable CO_2RR activity but rather that the NTO surface is poisoned, as evidenced by the progressive decrease in double layer capacitance through subsequent CV cycles in the presence of CO_2, ascribed here to the presence of adsorbed CO. The observed CO_2RR activity on 9 wt.% Cu:NTO was therefore ascribed to the presence of Cu within the titanate layers. OLEMS characterisation identified that the gaseous products generated by CO_2RR at -0.8 V *vs*. RHE on 9 wt.% Cu:NTO over 1 hour were H_2, CO and CH_4. For 10 wt.% CuO@NTO the gaseous products identified were H_2, CH_4 and C_2H_4. A decrease in detected

C_2H_4 and subsequent increase in CH_4 concentration was shown to correlate to the increase in Cu(0) species and Cu-Cu^{metal} bonding determined through *in situ* XANES and EXAFS analyses. Generally, the reduction of the Cu^{2+} species was more gradual for the CuO-derived catalyst under CO_2RR conditions, particularly noticeable when comparing the *in situ* XANES spectra measured at -0.35 V. As XAS techniques probe the bulk of the material, it was anticipated that the inner core of the CuO phase, which does not directly participate in surface catalysis, would experience slower reduction kinetics, promoting the enhanced stability of oxidised Cu species observed. The observed decrease in C_2H_4 / CH_4 ratio with the CuO-derived catalyst was ascribed to the formation of the small nanoclusters over time. Likewise, the CO/CH_4 ratio for 9 wt.% Cu:NTO was ascribed to increase in Cu cluster size based on agreement with previous reports.

Further *in situ* investigation on the role of NTO during CO_2RR electrolysis with the catalysts is required to enable elucidation mechanistic pathways for the respective electrocatalysts.

Acknowledgements

We acknowledge the Diamond Light Source for provision of beamtime (SP21533). MJL acknowledges the University of Birmingham for financial support through Ph.D. scholarships at the School of Chemistry. PR acknowledges the University of Birmingham for financial support through the Birmingham fellowship program.

References

1. Olah, G. A.; Prakash, G. K.; Goeppert, A. *J. Am. Chem. Soc.* **2011,** 133, (33), 12881-98.

2. Alper, E.; Yuksel Orhan, O. *Petroleum* **2017,** 3, (1), 109-126.

3. Nielsen, D. U.; Hu, X.-M.; Daasbjerg, K.; Skrydstrup, T. *Nature Catalysis* **2018,** 1, (4), 244-254.

4. Schreier, M.; Héroguel, F.; Steier, L.; Ahmad, S.; Luterbacher, J. S.; Mayer, M. T.; Luo, J.; Grätzel, M. *Nature Energy* **2017,** 2, (7), 17087.

5. Seh, Z. W.; Kibsgaard, J.; Dickens, C. F.; Chorkendorff, I.; Norskov, J. K.; Jaramillo, T. F. *Science* **2017,** 355, (6321).

6. Montoya, J. H.; Seitz, L. C.; Chakthranont, P.; Vojvodic, A.; Jaramillo, T. F.; Norskov, J. K. *Nature Materials* **2016,** 16, (1), 70-81.

7. Whipple, D. T.; Kenis, P. J. A. *The Journal of Physical Chemistry Letters* **2010,** 1, (24), 3451-3458.

8. Kuhl, K. P.; Cave, E. R.; Abram, D. N.; Jaramillo, T. F. *Energy Environ. Sci.* **2012,** 5, (5).

9. Hori, Y.; Takahashi, I.; Koga, O.; Hoshi, N. *J. Phys. Chem. B* **2002,** 106, (1), 15-17.

10. Takahashi, I.; Koga, O.; Hoshi, N.; Hori, Y. *Journal of Electroanalytical Chemistry* **2002,** 533, (1-2), 135-143.

11. Mistry, H.; Varela, A. S.; Bonifacio, C. S.; Zegkinoglou, I.; Sinev, I.; Choi, Y. W.; Kisslinger, K.; Stach, E. A.; Yang, J. C.; Strasser, P.; Cuenya, B. R. *Nat. Commun.* **2016,** 7, 12123.

12. Arán-Ais, R. M.; Scholten, F.; Kunze, S.; Rizo, R.; Roldan Cuenya, B. *Nat. Energy* **2020,** 5, (4), 317-325.

13. Grosse, P.; Gao, D.; Scholten, F.; Sinev, I.; Mistry, H.; Roldan Cuenya, B. *Angew. Chem., Int. Ed.* **2018,** 57, (21), 6192-6197.

14. Reske, R.; Mistry, H.; Behafarid, F.; Roldan Cuenya, B.; Strasser, P. *J. Am. Chem. Soc.* **2014,** 136, (19), 6978-86.

15. Kas, R.; Kortlever, R.; Milbrat, A.; Koper, M. T. M.; Mul, G.; Baltrusaitis, J. *Phys. Chem. Chem. Phys.* **2014,** 16, (24), 12194-12201.

16. De Luna, P.; Quintero-Bermudez, R.; Dinh, C.-T.; Ross, M. B.; Bushuyev, O. S.; Todorović, P.; Regier, T.; Kelley, S. O.; Yang, P.; Sargent, E. H. *Nature Catalysis* **2018,** 1, (2), 103-110.

17. Gao, D.; Sinev, I.; Scholten, F.; Aran-Ais, R. M.; Divins, N. J.; Kvashnina, K.; Timoshenko, J.; Roldan Cuenya, B. *Angew. Chem., Int. Ed.* **2019,** 58, (47), 17047-17053.

18. Varela, A. S.; Kroschel, M.; Reier, T.; Strasser, P. *Catal. Today* **2016,** 260, 8-13.

19. Colic, V.; Pohl, M. D.; Scieszka, D.; Bandarenka, A. S. *Catal. Today* **2016,** 262, 24-35.

20. Favaro, M.; Xiao, H.; Cheng, T.; Goddard, W. A., 3rd; Yano, J.; Crumlin, E. J. *Proc. Natl. Acad. Sci. USA* **2017,** 114, (26), 6706-6711.

21. Eilert, A.; Cavalca, F.; Roberts, F. S.; Osterwalder, J.; Liu, C.; Favaro, M.; Crumlin, E. J.; Ogasawara, H.; Friebel, D.; Pettersson, L. G.; Nilsson, A. *J. Phys. Chem. Lett.* **2017,** 8, (1), 285-290.

22. Le Duff, C. S.; Lawrence, M. J.; Rodriguez, P. *Angew. Chem., Int. Ed.* **2017,** 56, (42), 12919-12924.

23. Garza, A. J.; Bell, A. T.; Head-Gordon, M. *J. Phys. Chem. Lett.* **2018,** 9, (3), 601-606.

24. Scott, S. B.; Hogg, T. V.; Landers, A. T.; Maagaard, T.; Bertheussen, E.; Lin, J. C.; Davis, R. C.; Beeman, J. W.; Higgins, D.; Drisdell, W. S.; Hahn, C.; Mehta, A.; Seger, B.; Jaramillo, T. F.; Chorkendorff, I. *ACS Energy Lett.* **2019,** 4, (3), 803-804.

25. Cueto, L. F.; Hirata, G. A.; Sánchez, E. M. *J. Sol-Gel Sci. Technol.* **2006,** 37, (2), 105-109.

26. Lawrence, M. J.; Celorrio, V.; Shi, X. B.; Wang, Q.; Yanson, A.; Adkins, N. J. E.; Gu, M.; Rodriguez-Lopez, J.; Rodriguez, P. *ACS Appl. Energ. Mater.* **2018,** 1, (10), 5233-5244.

27. Kromer, M. L.; Monzo, J.; Lawrence, M. J.; Kolodziej, A.; Gossage, Z. T.; Simpson, B. H.; Morandi, S.; Yanson, A.; Rodriguez-Lopez, J.; Rodriguez, P. *Langmuir* **2017,** 33, (46), 13295-13302.

28. Lawrence, M. J.; Kolodziej, A.; Rodriguez, P. *Curr. Opin. Electrochem.* **2018,** 10, 7-15.

29. Yanson, A. I.; Rodriguez, P.; Garcia-Araez, N.; Mom, R. V.; Tichelaar, F. D.; Koper, M. T. *Angew. Chem., Int. Ed.* **2011,** 50, (28), 6346-50.

30. Rodriguez, P.; Tichelaar, F. D.; Koper, M. T.; Yanson, A. I. *J. Am. Chem. Soc.* **2011,** 133, (44), 17626-9.

31. Garcia-Canadas, J.; Adkins, N. J.; McCain, S.; Hauptstein, B.; Brew, A.; Jarvis, D. J.; Min, G. *ACS Comb. Sci.* **2016,** 18, (6), 314-319.

32. Li, S.; Adkins, N. J. E.; McCain, S.; Attallah, M. M. *J. Alloys Compd.* **2018,** 768, 392-398.

33. Binninger, T.; Pribyl, B.; Patru, A.; Ruettimann, P.; Bjelic, S.; Schmidt, T. J. *Journal of Mass Spectrometry* **2018,** 53, (12), 1214-1221.

34. Dent, A. J.; Cibin, G.; Ramos, S.; Smith, A. D.; Scott, S. M.; Varandas, L.; Pearson, M. R.; Krumpa, N. A.; Jones, C. P.; Robbins, P. E. *J. Phys.: Conf. Ser.* **2009,** 190.

35. Sardar, K.; Petrucco, E.; Hiley, C. I.; Sharman, J. D.; Wells, P. P.; Russell, A. E.; Kashtiban, R. J.; Sloan, J.; Walton, R. I. *Angew. Chem., Int. Ed.* **2014,** 53, (41), 10960-4.

36. Newville, M. *J. Synchrotron Radiat.* **2001,** 8, (2), 96-100.

37. Ota, M.; Hirota, Y.; Uchida, Y.; Sakamoto, Y.; Nishiyama, N. *Langmuir* **2018,** 34, (23), 6814-6819.

38. Imbao, J.; van Bokhoven, J. A.; Clark, A.; Nachtegaal, M. *Nat. Commun.* **2020,** 11, (1), 1118.

39. Gaur, A.; Shrivastava, B. D.; Joshi, S. K. *J. Phys.: Conf. Ser.* **2009,** 190.

40. Pelliccione, C. J.; Li, Y. R.; Marschilok, A. C.; Takeuchi, K. J.; Takeuchi, E. S. *Phys. Chem. Chem. Phys.* **2016,** 18, (4), 2959-67.

41. Li, J.; Che, F.; Pang, Y.; Zou, C.; Howe, J. Y.; Burdyny, T.; Edwards, J. P.; Wang, Y.; Li, F.; Wang, Z.; De Luna, P.; Dinh, C. T.; Zhuang, T. T.; Saidaminov, M. I.; Cheng, S.; Wu, T.; Finfrock, Y. Z.; Ma, L.; Hsieh, S. H.; Liu, Y. S.; Botton, G. A.; Pong, W. F.; Du, X.; Guo, J.; Sham, T. K.; Sargent, E. H.; Sinton, D. *Nat. Commun.* **2018,** 9, (1), 4614.

42. Lee, S. H.; Sullivan, I.; Larson, D. M.; Liu, G.; Toma, F. M.; Xiang, C.; Drisdell, W. S. *ACS Catal.* **2020,** 10, (14), 8000-8011.

43. Bandi, A.; Kühne, H. M. *J. Electrochem. Soc.* **1992,** 139, (6), 1605-1610.

44. Hori, Y.; Wakebe, H.; Tsukamoto, T.; Koga, O. *Electrochimica Acta* **1994,** 39, (11–12), 1833-1839.

45. Fabregat-Santiago, F.; Mora-Seró, I.; Garcia-Belmonte, G.; Bisquert, J. *J. Phys. Chem. B* **2003,** 107, (3), 758-768.

46. Gao, D.; Arán-Ais, R. M.; Jeon, H. S.; Roldan Cuenya, B. *Nature Catalysis* **2019,** 2, (3), 198-210.

47. Li, C. W.; Ciston, J.; Kanan, M. W. *Nature* **2014,** 508, (7497), 504-7.

48. Li, C. W.; Kanan, M. W. *J. Am. Chem. Soc.* **2012,** 134, (17), 7231-7234.

49. Velasco-Velez, J.-J.; Mom, R. V.; Sandoval-Diaz, L.-E.; Falling, L. J.; Chuang, C.-H.; Gao, D.; Jones, T. E.; Zhu, Q.; Arrigo, R.; Roldan Cuenya, B.; Knop-Gericke, A.; Lunkenbein, T.; Schlögl, R. *ACS Energy Lett.* **2020,** 5, (6), 2106-2111.

50. Chen, C. S.; Handoko, A. D.; Wan, J. H.; Ma, L.; Ren, D.; Yeo, B. S. *Catal. Sci. Technol.* **2015,** 5, (1), 161-168.

51. Roberts, F. S.; Kuhl, K. P.; Nilsson, A. *Angew. Chem., Int. Ed.* **2015,** 54, (17), 5179-82.

52. Loiudice, A.; Lobaccaro, P.; Kamali, E. A.; Thao, T.; Huang, B. H.; Ager, J. W.; Buonsanti, R. *Angew. Chem., Int. Ed.* **2016,** 55, (19), 5789-92.

53. Hori, Y.; Murata, A.; Takahashi, R.; Suzuki, S. *J. Am. Chem. Soc.* **1987,** 109, (16), 5022-5023.

7.5. Supporting Information

Insight into the Activity and Selectivity of Nanostructured Copper Titanates during Electrochemical Conversion of CO_2 at neutral pH via in situ X-ray Absorption Spectroscopy

Matthew J. Lawrence,[a] Veronica Celorrio,[*b] Elizabeth Sargeant,[a] Haoliang Huang,[c] Nicholas J. E. Adkins,[d] Daisy Mutsau,[a] Yuanmin Zhu,[e,f] Meng Gu,[f] Andrea E. Russell[c] and Paramaconi Rodriguez[*a]

[a]*School of Chemistry, University of Birmingham, Edgbaston, Birmingham B15 2TT, United Kingdom*

[b]*Diamond Light Source Ltd, Harwell Campus, Didcot OX11 0DE, United Kingdom*

[c]*School of Chemistry, University of Southampton, Highfield, Southampton SO17 1BJ, United Kingdom*

[d]*School of Metallurgy and Materials, University of Edgbaston, Birmingham B15 2TT, United Kingdom*

[e]*SUSTech Academy for Advanced Interdisciplinary Studies, Southern University of Science and Technology, Shenzhen, 518055, China*

[f]*Department of Materials Science and Engineering, Southern University of Science and Technology, Shenzhen, 518055, China*

corresponding author: veronica.celorrio@diamond.ac.uk; p.b.rpdriguez@bham.ac.uk

Alloy preparation

The homogeneous $Cu_{19}Ti_{81}$ alloy was produced via suspended droplet alloying (SDA), a laser-assisted combinatorial metallurgical process for the rapid production of bulk alloys from pure metal wires.[1, 2] Pure Ti and Cu wires were fed into the focal point of a high energy laser beam within an Ar-filled chamber, generating metal droplets at the tips of the wires. As more wire was fed into the focal point the masses of the metal droplets continue to increase until they merge to form alloy droplets. The wire feed rates were controlled to accurately control the composition of the alloy droplets. The process continues until the mass of the alloy droplet is sufficiently large to detach from the ends of the wires onto the sample holder positioned below the focal point. Alloy droplets contine to form and detach from the wire tips, stacking on top of the previous ones, until the desired amount of alloy is produced. At which point the laser is switched off and the alloy is allowed to cool in the Ar-filled chamber.

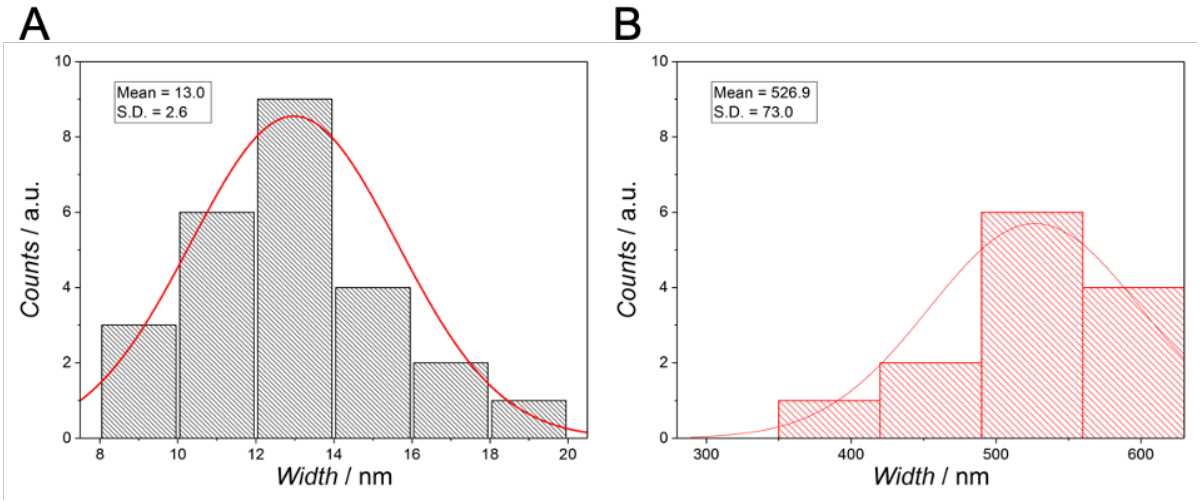

Figure S1. Size distribution histograms of (A) 9 wt.% Cu:NTO nanowire diameter and (B) 10 wt.% CuO@NTO CuO cube diameter, determined by HRTEM analysis.

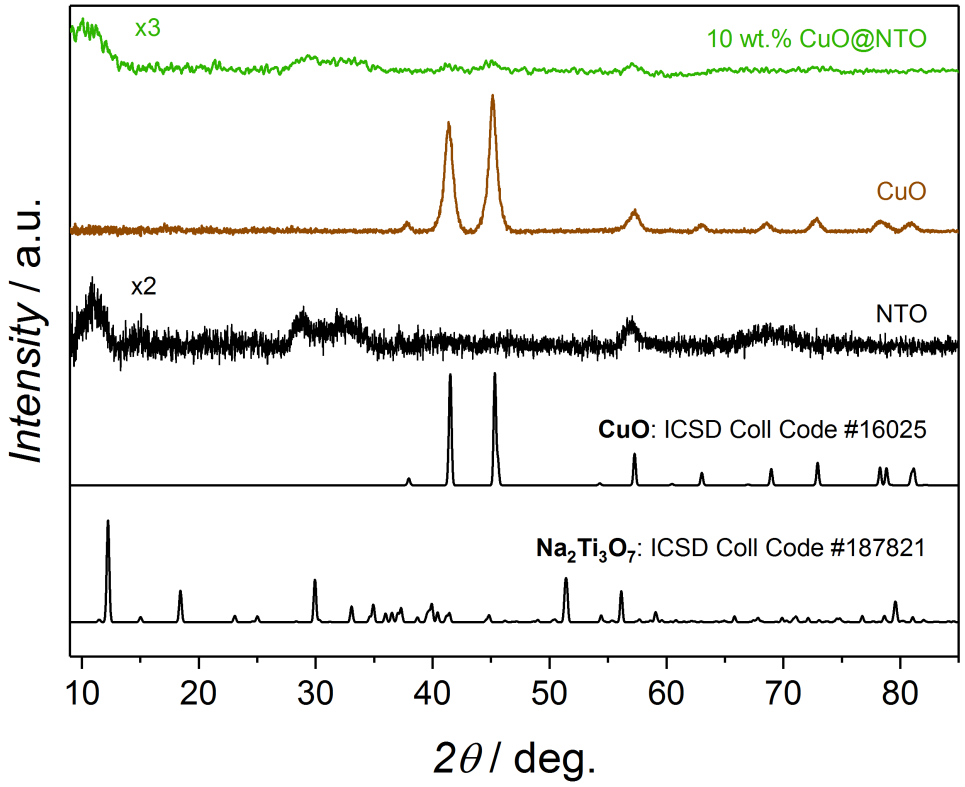

Figure S2. XRD pattern of NTO, CuO and 10 wt.% CuO@NTO catalysts as-prepared by cathodic corrosion. ICSD database patterns for $Na_2Ti_3O_7$ [Coll Code 187821] and CuO [Coll Code 16025] are shown for comparison.

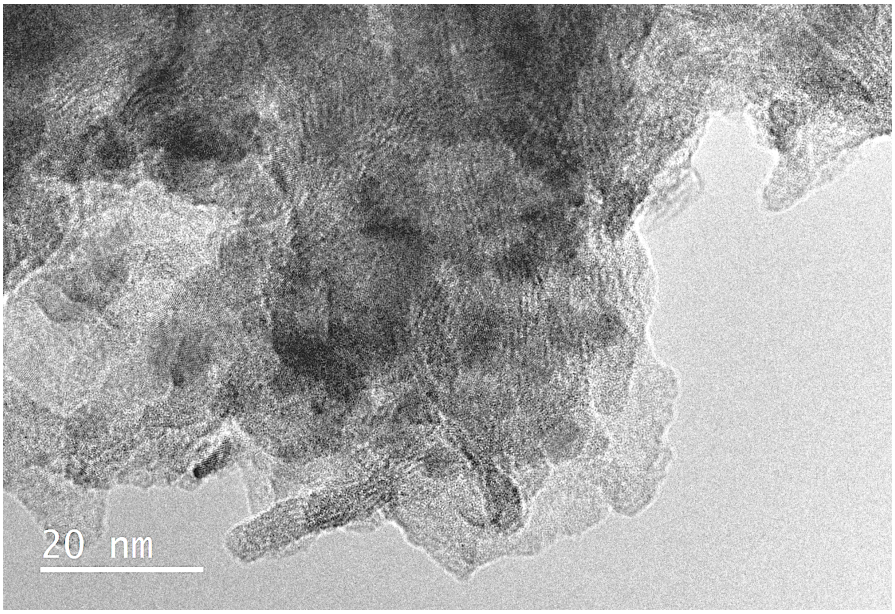

Figure S3. HRTEM image of 10 wt.% CuO@NTO, captured at point highlighted by blue square in **Figure 2C**, showing the presence of the aggregated NTO nanowires.

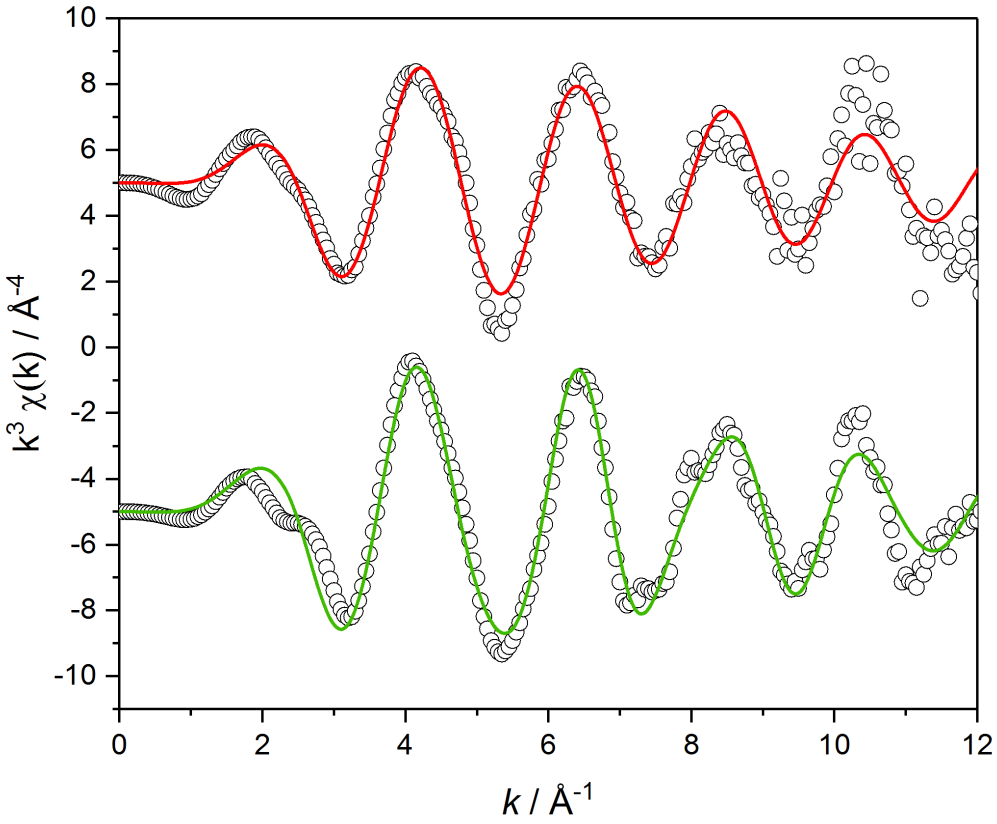

Figure S4. k^3-weighted χ data (empty circles) and fits (coloured lines) of the Cu-containing NTO catalysts electrodes in ex-situ conditions.

First derivative XAS spectra provide insight into the electronic structure of metal centres. A first derivative energy maximum at 8993 eV measured at the Cu K-edge is produced by a 1s → 4p transition at 4-coordinate square planar Cu(II) sites, which creates a 1s core-hole generating increased effective nuclear charge on the Cu valence d-orbitals, shifting these to higher energy values.[3, 4]

Table S1. Linear combination fit analysis results for *in situ* XANES spectra of Cu-containing NTO recorded at the Cu K-edge absent of electrolyte and any applied potential.

	Cu species composition / %			***Oxidation state***	***R_{factor}***
	Cu (0)	**Cu(I)**	**Cu(II)**		
9 wt.% Cu:NTO	0	20.4 ± 6.7	79.6 ± 6.7	1.80 ± 0.20	0.023
10 wt.% CuO@NTO	2.4 ± 3.7	0	97.6 ± 4.5	1.95 ± 0.13	0.029

Table S2. EXAFS distances and fitting parameters for the Cu-containing NTO catalysts electrodes ex-situ. Fitting parameters: $S_0^2 = 0.72$ calculated using a Cu foil standard; k and R fit ranges are tabulated.

	k range / $Å^{-1}$	**R range / Å**	**Scattering**	**CN**	**R / Å**	**Σ^2 X 10^3 / $Å^2$**	**ΔE_0 / EV**	**R_{factor}**
9 wt.% Cu:NTO	2.5 < k < 10.0	1 < R < 2.1	Cu-O	3.5 ± 0.5	1.93 ± 0.02	5.1 ± 2.4	-1.2 ± 1.6	0.007
10 wt.% CuO@NTO	3.5 < k < 10.8	1.0 < R < 3.2	Cu-O Cu-Cu^{oxide}	4.5 ± 0.6 2.2 ± 2.5	1.93 ± 0.02 2.91 ± 0.05	5.6 ± 1.6 15.5 ± 11.9	-1.6 ± 1.7	0.011

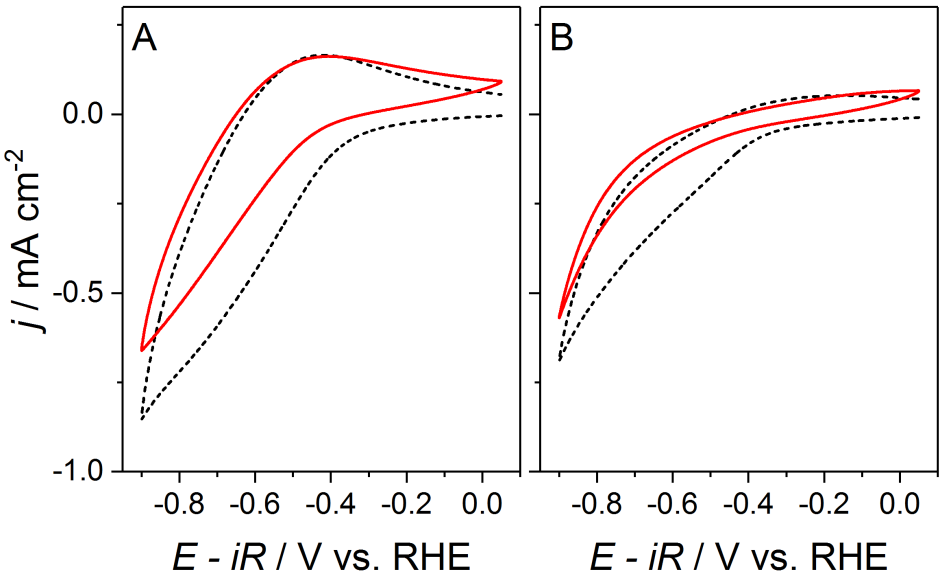

Figure S5. Selected cyclic voltammograms of NTO catalyst. First (dashed line) and tenth (red line) cycles in (A) Ar-saturated (pH 8) and (B) CO_2-saturated (pH 6.5) 0.1 M K_2HPO_4 / KH_2PO_4 buffer solution; ν = 50 mV s^{-1}, rotation rate = 1200 rpm.

As the applied potential became increasingly negative there was an increase in the magnitude of current density measured with a significant change in current density observed after -0.4 V vs RHE. The HER onset potential, here defined as the potential after which a significant change to the CV slope is observed due to increased reduction current density, was determined as -0.463 V vs RHE (**Figure S6A**), a significant HER overpotential. This indicated that the NTO catalyst would not be suitable for large scale HER applications. A broad peak at -0.5 V vs RHE appeared during the anodic sweep which decreased in magnitude with subsequent cycles due to peak broadening, resulting in an overall increase in anodic current density measured at more positive applied potentials. This peak was observable only for the undoped NTO catalyst. The peak broadening was also accompanied by a more noticeable decrease in the HER peak current density measured during the cathodic sweep. This would suggest that the anodic process was also poisoning the catalyst surface and hindering the HER. The current density profile of the NTO blank CVs stabilised after the ninth cycle, therefore, in the subsequent electrochemical investigations 10 cycles were recorded for each sample to have a controlled titanate phase for comparison.

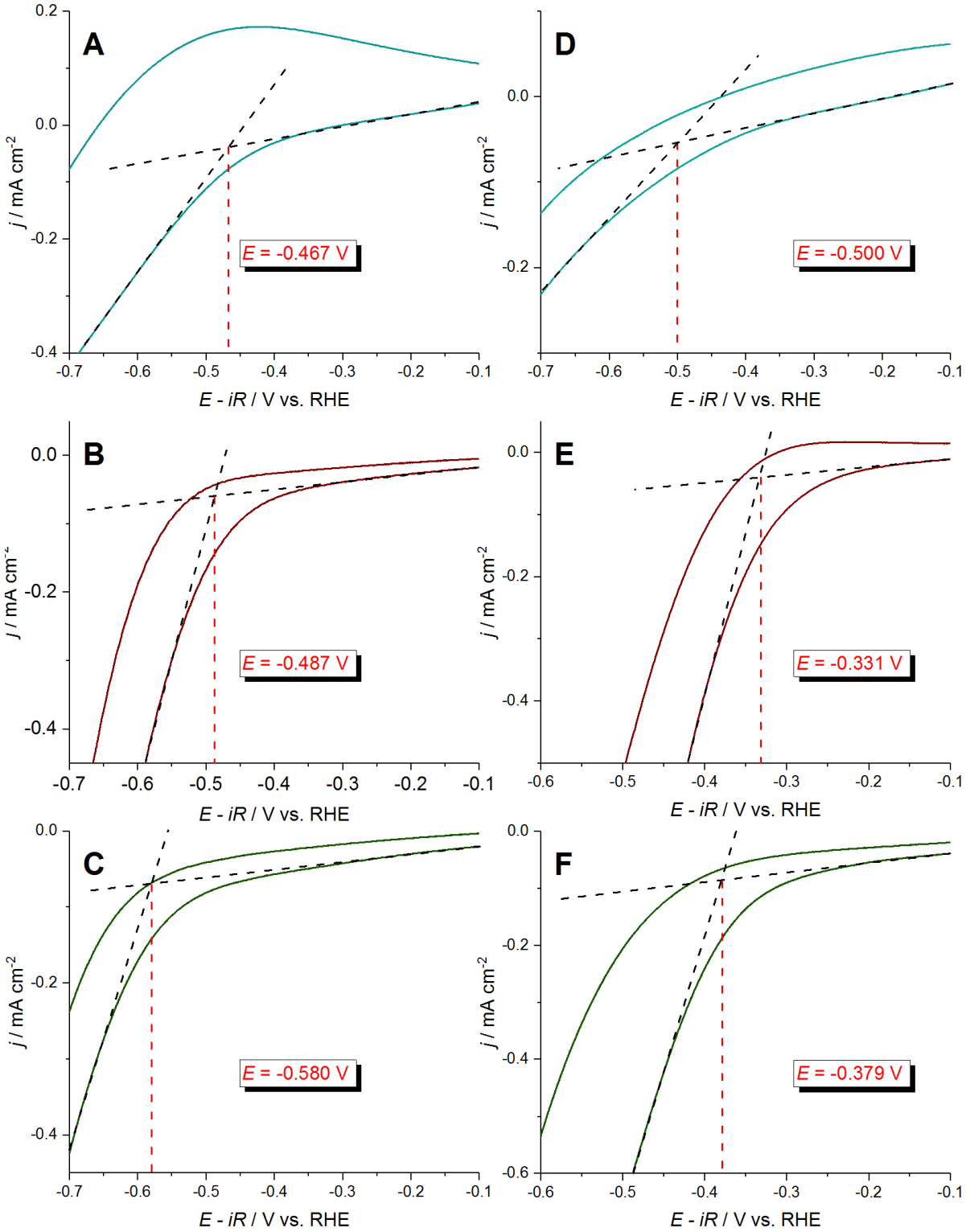

Figure S6. Determination of catalyst onset potentials for (A,D) NTO, (B,E) 9 wt.% Cu:NTO and (C,F) 10 wt.% CuO@NTO in (A-C) Ar-saturated 0.1 M K_2HPO_4 / KH_2PO_4 buffer (pH = 8) and (D-F) CO_2-saturated 0.1 M K_2HPO_4 / KH_2PO_4 buffer (pH = 6.5 after saturating with CO_2).

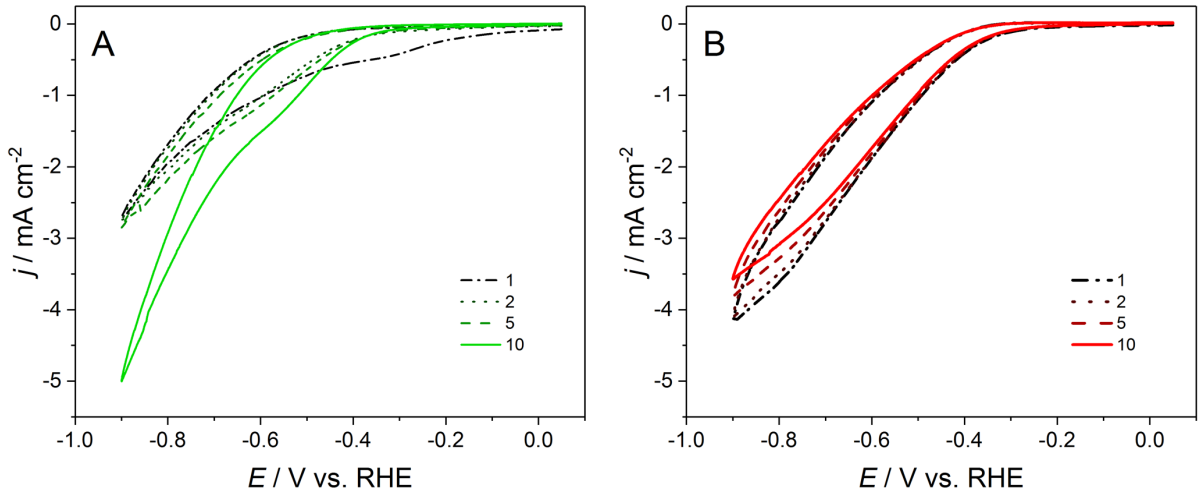

Figure S7. Selected successive cyclic voltammograms of (A) 10 wt.% CuO@NTO and (B) 9 wt.% Cu:NTO in CO_2-saturated 0.1 M K_2HPO_4 / KH_2PO_4 buffer (pH = 6.5 after saturation with CO_2). Scan rate ν = 50 mV s^{-1}; rotation rate ω= 1200 rpm.

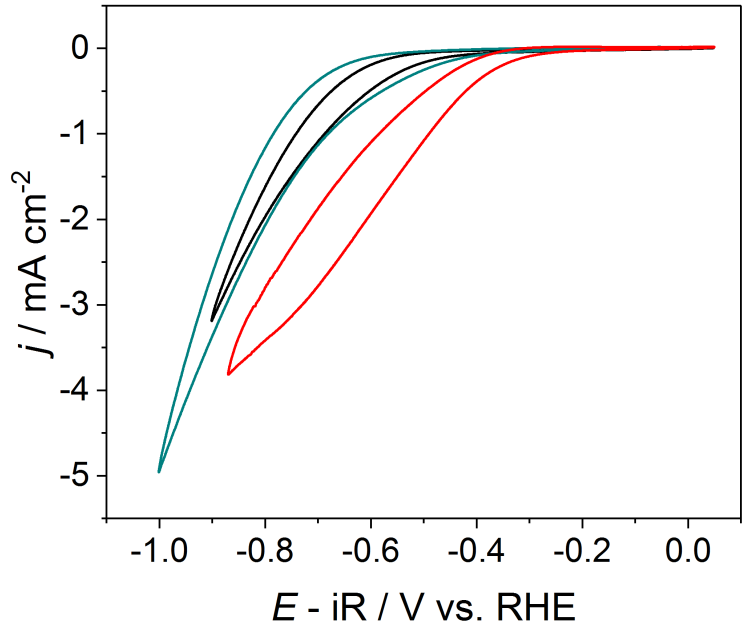

Figure S8. Cyclic voltammograms of 9 wt.% Cu:NTO in 0.1 M K_2HPO_4 / KH_2PO_4 buffer (pH 8) recorded in absence (black line @pH=8) (blue line @pH=6) and presence of CO_2 (red line @pH=6). In order to simulate the pH change induced in the phosphate buffer by dissolution of CO_2 pure H_3PO_4 solution was added to the electrolyte to compensate the change of pH associated to the CO_2/bicarbonate/carbonate equilibrium. Scan rate ν = 50 mV s^{-1}; rotation rate ω= 1200 rpm.

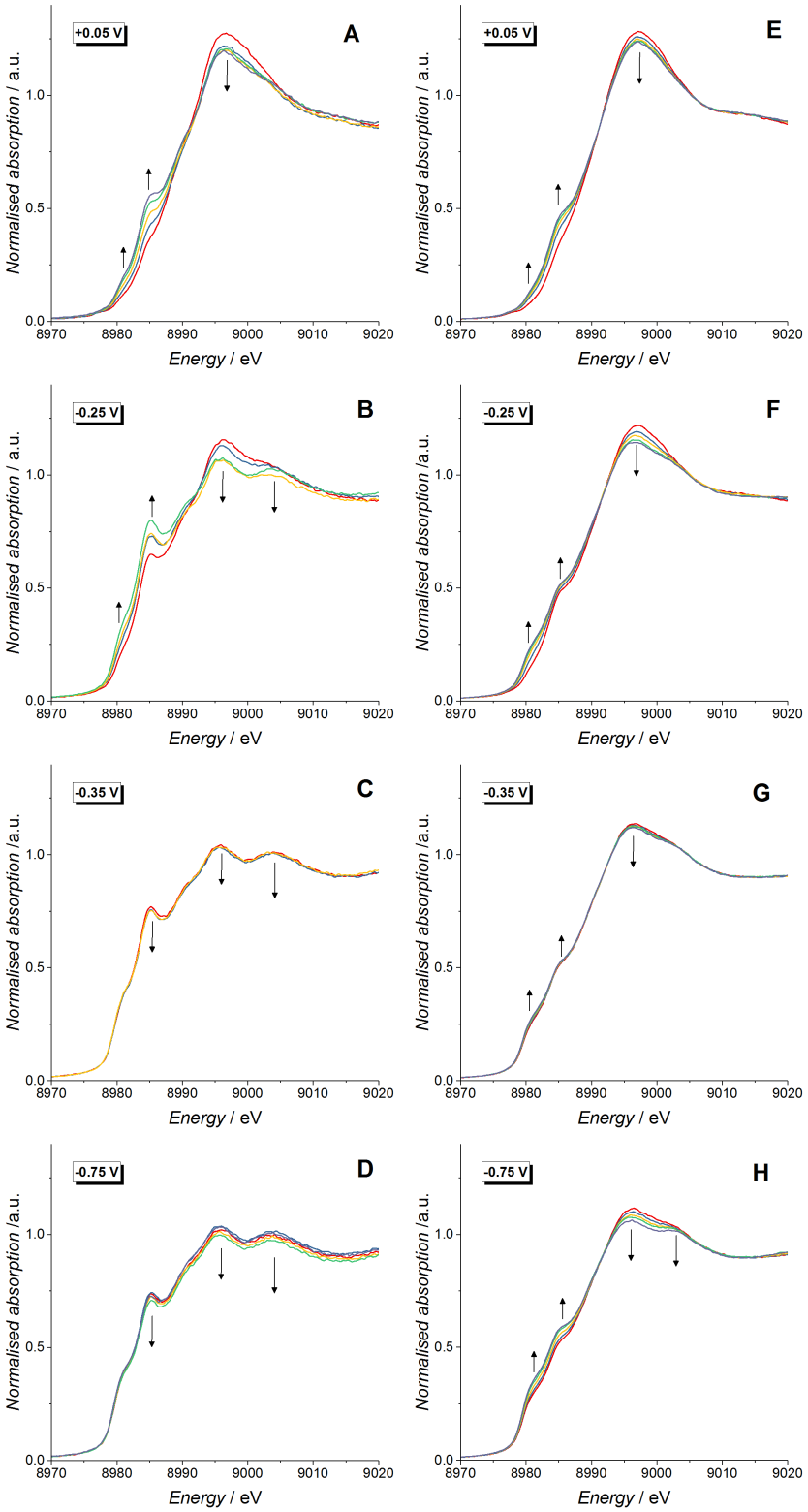

Figure S9. *In-situ* Cu K-edge XANES spectra of (A-D) 9 wt.% Cu:NTO and (E-F) 10 wt.% CuO@NTO in Ar-saturated 0.1 M K_2HPO_4 / KH_2PO_4 buffer solution (pH 8). Spectra were recorded consecutively, each with a 5 min duration each.

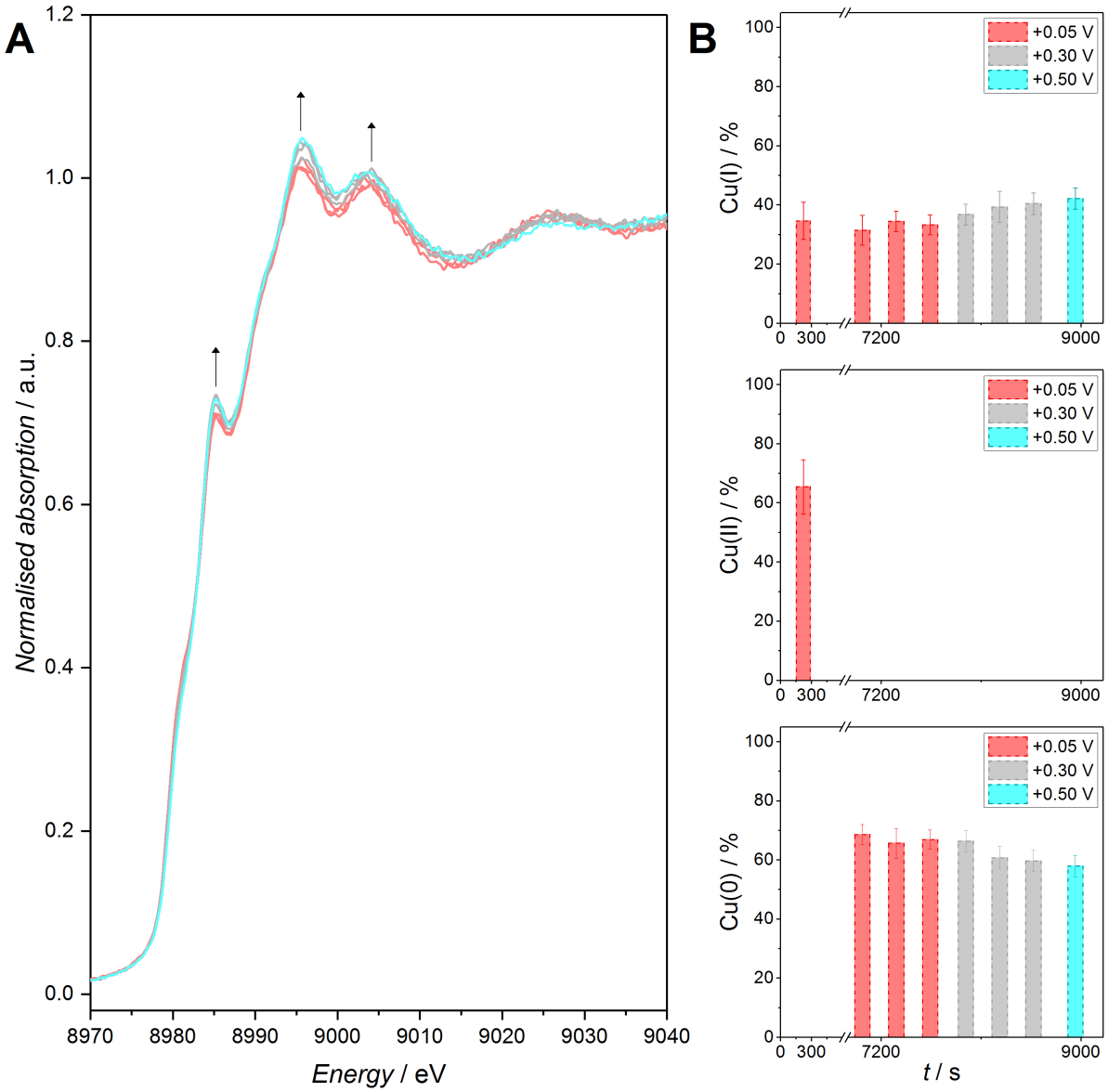

Figure S10. (A) *In situ* Cu K-edge XANES spectra and (B) corresponding LCF Cu species contribution of 9 wt.% Cu:NTO recorded at +0.05 V (red), +0.30 V (grey) and +0.50 V (turquoise) in Ar-saturated 0.1 M K_2HPO_4 / KH_2PO_4, after initial cathodic measurements. Each bar represents 5 min under applied potential.

Table S3. Linear combination fit analysis results for *in situ* XANES spectra of 9 wt.% Cu:NTO recorded at the Cu K-edge in Ar-saturated 0.1 M K_2HPO_4 / KH_2PO_4 solution (pH 8) at various applied potentials.

		Cu species composition / %				
E / V vs. RHE	***time / s***	**Cu (0)**	**Cu(I)**	**Cu(II)**	***Oxidation state***	R_{factor}
+0.05	305 (4.7min)	0	34.6 ± 6.3	65.4 ± 9.2	1.65 ± 0.23	0.020
	610(9.4min)	0	59.0 ± 10.8	41.0 ± 5.9	1.41 ± 0.23	0.019
	1220(18.8min)	0	89.7 ± 24.9	10.3 ± 5.0	1.10 ± 0.35	0.013
	1525(23.5min)	0	89.7 ± 24.9	10.3 ± 5.0	1.10 ± 0.35	0.003
-0.25	2061(4.7min)	25.3 ± 8.4	74.7 ± 6.2	0.0 ± 4.5	0.75 ± 0.24	0.011
	2366(9.4min)	34.9 ± 3.6	65.1 ± 7.2	0	0.65 ± 0.11	0.016
	2671(14.1min)	52.9 ± 5.3	47.1 ± 3.7	0	0.47 ± 0.10	0.020
-0.35	4153(4.7min)	64.5 ± 4.2	35.5 ± 4.2	0	0.36 ± 0.08	0.024
	4458(9.4min)	66.7 ± 3.9	33.9 ± 3.9	0	0.34 ± 0.08	0.021
	4763(14.1min)	63.8 ± 3.9	36.2 ± 3.9	0	0.36 ± 0.08	0.023
-0.75	5177(4.7min)	70.1 ± 3.7	29.9 ± 3.7	0	0.30 ±0.07	0.019
	5482(9.4min)	66.4 ± 4.3	33.6 ± 3.8	0	0.34 ± 0.08	0.019
	5787(14.1min)	75.7 ± 5.4	24.3 ± 3.5	0	0.24 ± 0.09	0.018
	6092(18.8min)	77.9 ± 5.3	22.1 ± 3.4	0	0.22 ± 0.09	0.023
	6397(23.5min)	64.1 ± 3.7	35.9 ± 8.8	0	0.36 ± 0.13	0.025
+0.05_return	7003(4.7min)	68.6 ± 3.3	31.4 ± 5.0	0	0.31 ± 0.08	0.022
	7308(9.4min)	65.6 ± 5.1	34.4 ± 3.5	0	0.34 ± 0.09	0.023
	7613(14.1min)	66.8 ± 3.3	33.2 ± 3.3	0	0.33 ± 0.07	0.022
+0.30_return	7907(4.7min)	63.3 ± 3.5	36.7 ± 3.5	0	0.37 ± 0.07	0.024
	8212(9.4min)	60.7 ± 3.7	39.3 ± 5.2	0	0.39 ± 0.09	0.025
	8517(14.1min)	59.6 ± 3.7	40.4 ± 3.7	0	0.40 ± 0.07	0.025
+0.50_return	8867(4.7min)	57.9 ± 3.6	42.1 ± 3.6	0	0.42 ± 0.07	0.024

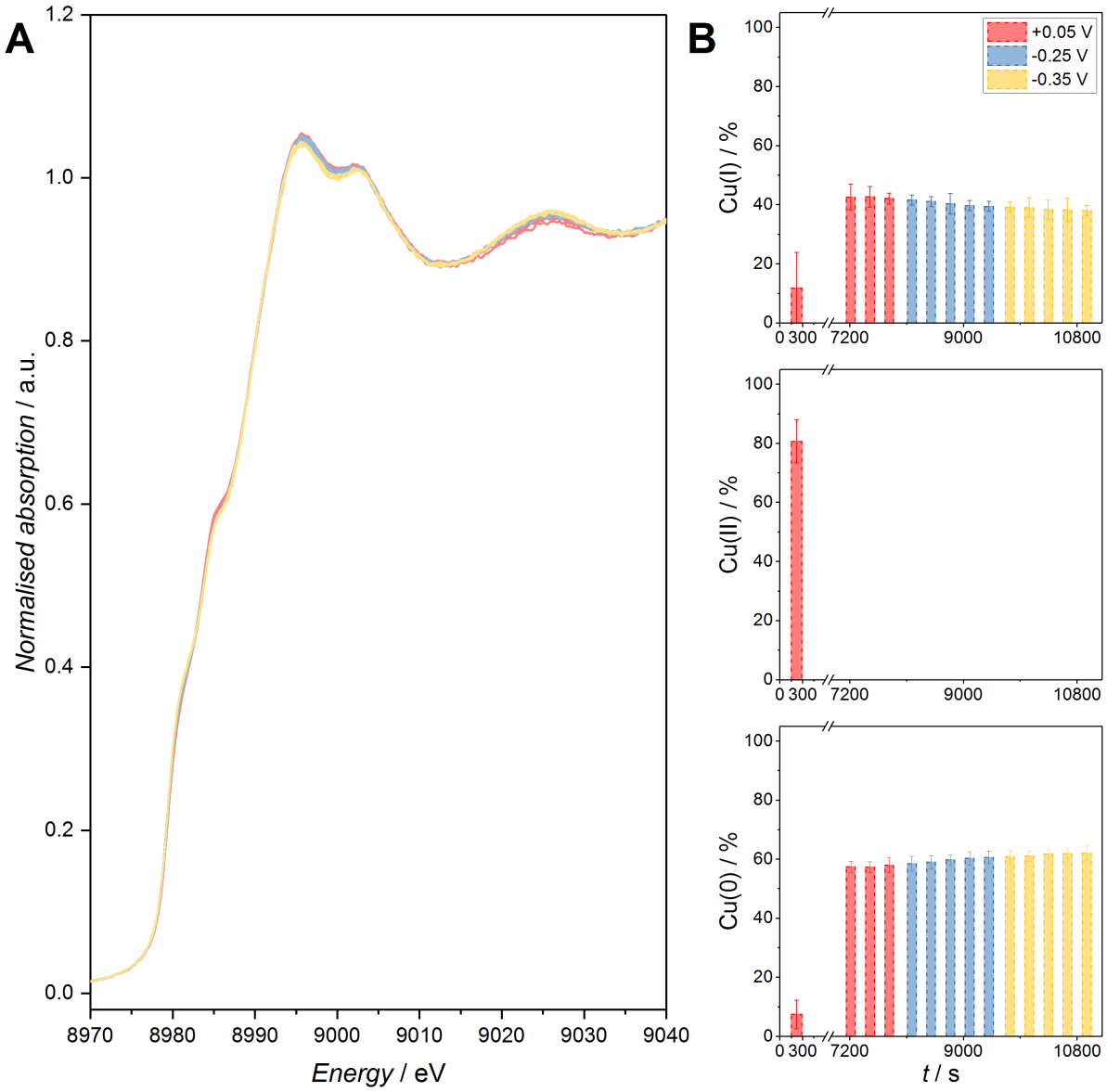

Figure S11. (A) *In situ* Cu K-edge XANES spectra and (B) corresponding LCF Cu species contribution of 10 wt.% CuO@NTO recorded at +0.05 V (red), -0.25 V (blue) and -0.35 V (yellow) in Ar-saturated 0.1 M K_2HPO_4 / KH_2PO_4, after initial cathodic measurements. Each bar represents 5 min under applied potential.

Table S4. Linear combination fit analysis results for *in situ* XANES spectra of 10 wt.% CuO@NTO recorded at the Cu K-edge in Ar-saturated 0.1 M K_2HPO_4 / KH_2PO_4 solution (pH 8) at various applied potentials.

		Cu species composition / %				
E / V vs. RHE	***time / s***	**Cu (0)**	**Cu(I)**	**Cu(II)**	***Oxidation state***	R_{factor}
	305(4.7min)	7.4 ± 4.9	11.8 ± 12.0	80.7 ± 7.3	1.73 ± 0.32	0.027
	610(9.4min)	9.2 ± 4.4	32.0 ± 11.4	58.8 ± 6.6	1.50 ± 0.29	0.023
+0.05	915(14.1min)	10.7 ± 11.6	40.0 ± 8.6	49.3 ± 6.3	1.39 ± 0.33	0.021
	1220(18.8min)	11.3 ± 4.1	45.8 ± 11.0	42.8 ± 6.1	1.31 ± 0.27	0.020
	1525(23.5min)	12.3 ± 4.0	49.5 ± 8.2	38.2 ± 9.6	1.26 ± 0.31	0.019
	1881(4.7min)	14.6 ± 3.8	53.4 ± 9.6	31.9 ± 5.6	1.17 ± 0.25	0.017
	2186(9.4min)	21.1 ± 8.9	56.9 ± 6.8	22.0 ± 4.9	1.01 ± 0.26	0.014
-0.25	2491(14.1min)	26.3 ± 3.0	57.8 ± 6.1	15.9 ± 7.2	0.90 ± 0.24	0.012
	2796(18.8min)	29.7 ± 7.6	58.2 ± 5.7	12.1 ± 4.2	0.82 ± 0.22	0.010
	3101(23.5min)	32.1 ± 2.7	57.3 ± 5.5	10.5 ± 8.0	0.78 ± 0.24	0.009
	3458(4.7min)	33.5 ± 7.0	57.4 ± 5.3	9.1 ± 3.9	0.76 ± 0.20	0.009
	3763(9.4min)	35.3 ± 2.5	56.8 ± 5.1	7.9 ± 6.2	0.73 ± 0.20	0.009
-0.35	4068(14.1min)	36.4 ± 6.6	57.1 ± 5.0	6.5 ± 3.7	0.70 ± 0.19	0.008
	4373(18.8min)	36.2 ± 6.5	58.6 ± 4.9	5.2 ± 3.6	0.69 ± 0.19	0.008
	4678(23.5min)	38.3 ± 6.3	57.3 ± 4.8	4.4 ± 3.5	0.66 ± 0.18	0.007
	5016(4.7min)	44.8 ± 6.3	55.2 ± 8.0	4.5 ± 5.9	0.64 ± 0.26	0.006
	5321(9.4min)	46.2 ± 2.0	53.8 ± 4.3	0	0.54 ± 0.04	0.005
-0.75	5626(14.1min)	50.4 ± 2.6	49.6 ± 1.8	0	0.50 ± 0.05	0.004
	5931(18.8min)	53.5 ± 1.8	46.5 ± 3.6	0	0.47 ± 0.05	0.004
	6236(23.5min)	58.8 ± 1.8	41.2 ± 1.8	0	0.41 ± 0.04	0.004
	6576(4.7min)	58.3 ± 4.5	41.7 ± 1.8	0	0.42 ± 0.06	0.006
	6881(9.4min)	57.6 ± 1.8	42.4 ± 3.5	0	0.42 ± 0.05	0.006
+0.05_return	7186(14.1min)	57.4 ± 1.8	42.6 ± 4.3	0	0.43 ± 0.06	0.006
	7491(18.8min)	57.3 ± 1.8	42.7 ± 3.5	0	0.43 ± 0.05	0.005
	7796(23.5min)	57.9 ± 2.5	42.1 ± 1.8	0	0.42 ± 0.04	0.005
	8128(4.7min)	58.4 ± 2.5	41.6 ± 1.7	0	0.42 ± 0.04	0.005
	8433(9.4min)	58.9 ± 2.3	41.1 ± 1.7	0	0.41 ± 0.04	0.005
-0.25_return	8738(14.1min)	59.7 ± 1.7	40.3 ± 3.5	0	0.40 ± 0.05	0.005
	9043(18.8min)	60.3 ± 2.2	39.7 ± 1.7	0	0.40 ± 0.04	0.005
	9348(23.5min)	60.6 ± 2.2	39.4 ± 1.7	0	0.39 ± 0.04	0.005
	9653(4.7min)	60.8 ± 2.2	39.2 ± 1.7	0	0.39 ± 0.04	0.005
	9958(9.4min)	61.0 ± 1.7	39.0 ± 3.3	0	0.39 ± 0.05	0.005
-0.35_return	10263(14.1min)	61.7 ± 1.6	38.3 ± 3.3	0	0.38 ± 0.05	0.005
	10568(18.8min)	61.8 ± 1.7	38.2 ± 4.0	0	0.38 ± 0.06	0.005
	10873(23.5min)	62.0 ± 2.4	38.0 ± 1.7	0	0.38 ± 0.04	0.005

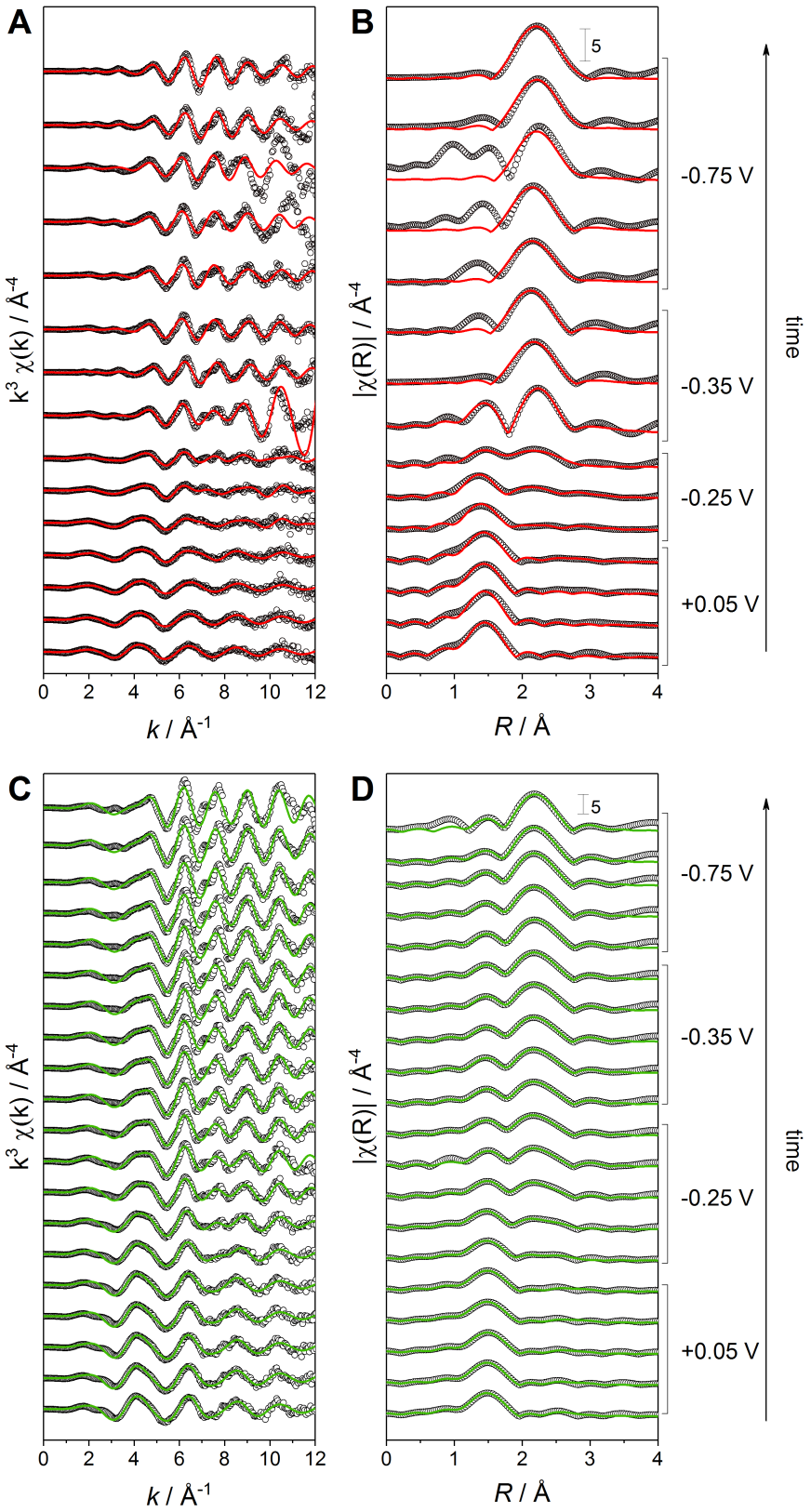

Figure S12. (A,C) k^3-weighted EXAFS data, (B,D) k^3-weighted FT EXAFS data (empty circles) and fits (coloured lines) for 9 wt.% Cu:NTO (red) and 10 wt.% CuO@NTO (green) catalysts at different potentials on an Ar-saturated electrolyte.

Table S5. EXAFS distances and fitting parameters for the 9 wt.% Cu:NTO catalyst collected in Ar-saturated electrolyte under different applied potentials. Fitting parameters: $S_0^2 = 0.72$ calculated using a Cu foil standard; fit range $1.0 < R < 3.2$, $3.5 < k < 10.8$.

E / V vs. RHE	time / s	R fit range / Å	Scattering	CN	R / Å	σ^2 X 10^3/Å^2	ΔE_0 / EV	R_{factor}
+0.05	305	1 < R < 2.1	Cu-O	3.4 ± 0.4	1.92 ± 0.01	5.2 ± 1.9	-2.0 (fixed)	0.008
	610	1 < R < 2.1	Cu-O	3.0 ± 0.5	1.91 ± 0.01	4.3 ± 2.7	-2.0 (fixed)	0.021
	1220	1 < R < 2.1	Cu-O	2.8 ± 0.3	1.90 ± 0.01	5.1 ± 1.9	-2.0 (fixed)	0.008
	1525	1 < R < 3.2	Cu-O Cu-$Cu^{Cu0xido}$	2.7 ± 0.3 2.9 ± 4.5	1.90 ± 0.01 3.10 ± 0.07	4.7 ± 2.2 12.2 ± 4.8	-2.0 (fixed)	0.021
-0.25	2061	1 < R < 3.2	Cu-O Cu-Cu^{Metal} Cu-Cu^{Oxide}	2.3 ± 0.4 0.8 ± 0.4 0.7 ± 0.5	1.88 ± 0.03 2.53 ± 0.05 3.10 ± 0.07	4.5 ± 2.9 9 (fixed) 6 (fixed)	-4.1 ± 2.2	0.025
	2366	1 < R < 3.2	Cu-O Cu-Cu^{Metal} Cu-Cu^{Oxide}	1.8 ± 0.3 1.5 ± 0.3 1.2 ± 0.4	1.86 ± 0.02 2.52 ± 0.03 3.07 ± 0.04	3.1 ± 2.5 9 (fixed) 6 (fixed)	-5.7 ± 2.2	0.016
	2671	1 < R < 3.2	Cu-O Cu-Cu^{Metal} Cu-Cu^{Oxide}	1.4 ± 0.5 2.5 ± 0.5 0.9 ± 0.7	1.90 ± 0.05 2.56 ± 0.04 3.13 ± 0.10	6.4 ± 4.4 9 (fixed) 6 (fixed)	-0.5 ± 3.9	0.038
-0.35	4153	1 < R < 3.2	Cu-O Cu-Cu^{Metal} Cu-Cu^{Oxide}	0.3 ± 0.2 5.0 ± 0.8 0.9 ± 0.9	1.89 ± 0.03 2.53 ± 0.03 3.11 ± 0.16	14.3 ± 5.4 9 (fixed) 6 (fixed)	-3.0 ± 4.9	0.026
	4458	1.6 < R < 3.2	Cu-Cu^{Metal} Cu-Cu^{Oxide}	4.9 ± 0.6 0.9 ± 0.7	2.52 ± 0.03 3.07 ± 0.11	9 (fixed) 6 (fixed)	-0.5 ± 3.4	0.031
	4763	1.7 < R < 3.2	Cu-Cu^{Metal} Cu-Cu^{Oxide}	5.2 ± 0.5 1.2 ± 0.6	2.53 ± 0.03 3.08 ± 0.08	9 (fixed) 6 (fixed)	-6.1 ± 3.1	0.018
-0.75	5177	1.7 < R < 3.2	Cu-Cu^{Metal} Cu-Cu^{Oxide}	4.9 ± 0.6 1.3 ± 0.7	2.52 ± 0.04 3.02 ± 0.09	9 (fixed) 6 (fixed)	-6.7 ± 3.8	0.017
	5482	1.7 < R < 3.2	Cu-Cu^{Metal} Cu-Cu^{Oxide}	5.4 ± 0.7 0.8 ± 0.9	2.54 ± 0.04 3.09 ± 0.15	9 (fixed) 6 (fixed)	-4.9 ± 4.2	0.036
	5787	1.7 < R < 3.2	Cu-Cu^{Metal} Cu-Cu^{Oxide}	5.2 ± 0.5 1.2 ± 0.6	2.53 ± 0.03 3.08 ± 0.08	9 (fixed) 6 (fixed)	-6.1 ± 3.1	0.018
	6092	1.6 < R < 3.2	Cu-Cu^{Metal} Cu-Cu^{Oxide}	5.7 ± 0.7 0.5 ± 1.0	2.54 ± 0.03 2.99 ± 0.16	9 (fixed) 6 (fixed)	0.5 ± 3.5	0.023
	6397	1.6 < R < 3.2	Cu-Cu^{Metal} Cu-Cu^{Oxide}	6.1 ± 0.6 1.3 ± 0.8	2.53 ± 0.03 3.01 ± 0.07	9 (fixed) 6 (fixed)	-0.9 ± 2.8	0.011
+0.05_return	7003	1.6 < R < 3.2	Cu-$Cu^{CuMetal}$ Cu-$Cu^{Cu0xido}$	6.0 ± 0.5 0.9 ± 0.6	2.53 ± 0.02 3.07 ± 0.09	9 (fixed) 6 (fixed)	-0.6 ± 2.3	0.013
	7308	1.6 < R < 3.2	Cu-$Cu^{CuMetal}$ Cu-$Cu^{Cu0xido}$	5.4 ± 0.5 0.9 ± 0.6	2.52 ± 0.02 3.03 ± 0.08	9 (fixed) 6 (fixed)	-1.4 ± 2.4	0.010
	7613	1.6 < R < 3.2	Cu-$Cu^{CuMetal}$ Cu-$Cu^{Cu0xido}$	5.7 ± 0.5 1.1 ± 0.6	2.52 ± 0.02 3.06 ± 0.08	9 (fixed) 6 (fixed)	-0.8 ± 2.3	0.013
+0.30	7907	1.6 < R < 3.2	Cu-$Cu^{CuMetal}$ Cu-$Cu^{Cu0xido}$	5.2 ± 0.5 1.2 ± 0.7	2.53 ± 0.03 3.05 ± 0.08	9 (fixed) 6 (fixed)	-0.8 ± 3.0	0.019

	8212	1.6 < R < 3.2	$Cu\text{-}Cu^{CuMetal}$ $Cu\text{-}Cu^{Cu0xido}$	4.8 ± 0.5 1.1 ± 0.6	2.53 ± 0.03 3.04 ± 0.09	9 (fixed) 6 (fixed)	-0.9 ± 3.1	0.019
	8517	1.6 < R < 3.2	$Cu\text{-}Cu^{CuMetal}$ $Cu\text{-}Cu^{Cu0xido}$	4.6 ± 0.5 1.1 ± 0.6	2.53 ± 0.03 3.05 ± 0.08	9 (fixed) 6 (fixed)	-0.4 ± 2.9	0.021
+0.50	**8867**	1.6 < R < 3.2	$Cu\text{-}Cu^{CuMetal}$ $Cu\text{-}Cu^{Cu0xido}$	4.2 ± 0.4 1.0 ± 0.5	2.53 ± 0.03 3.05 ± 0.07	9 (fixed) 6 (fixed)	-0.6 ± 2.7	0.017

Table S6. EXAFS distances and fitting parameters for the 10 wt.% CuO@NTO catalyst from collected in Ar-saturated electrolyte under different applied potentials. Fitting parameters: $S_0^2 = 0.72$ calculated using a Cu foil standard; fit range $3.5 < k < 10.8$; R fit ranges are tabulated.

E / V vs. RHE	time / s	R fit range / Å	Scattering	CN	R / Å	σ^2 X 10^3/Å^2	ΔE_0 / EV	R_{factor}
+0.05	305	1.0 < R < 3.2	Cu-O Cu-Cu^{Oxide}	4.4 ± 0.4 3.3 ± 3.3	1.92 ± 0.01 2.93 ± 0.04	5.7 ± 1.3 20.9 ± 12.1	-2.7 ± 1.4	0.007
	610	1.0 < R < 3.2	Cu-O Cu-Cu^{Oxide}	4.1 ± 0.4 5.2 ± 5.2	1.92 ± 0.01 2.96 ± 0.04	5.5 ± 1.2 26.8 ± 13.2	-2.5 ± 1.3	0.067
	915	1.0 < R < 3.2	Cu-O Cu-Cu^{Oxide}	4.0 ± 0.5 4.6 ± 4.8	1.92 ± 0.02 2.97 ± 0.05	6.0 ± 1.5 24.1 ± 12.9	-1.3 ± 1.5	0.009
	1220	1.0 < R < 3.2	Cu-O Cu-Cu^{Oxide}	4.2 ± 0.5 3.6 ± 6.8	1.90 ± 0.02 2.98 ± 0.05	6.4 ± 1.6 27.7 ± 14.4	-1.9 ± 1.6	0.009
	1525	1.0 < R < 3.2	Cu-O Cu-Cu^{Oxide}	3.9 ± 0.4 5.4 ± 5.3	1.92 ± 0.01 2.98 ± 0.04	5.8 ± 1.5 25.5 ± 12.6	-1.5 ± 1.5	0.009
-0.25	1881	1.0 < R < 3.2	Cu-O Cu-Cu^{Metal} Cu-Cu^{Oxide}	3.7 ± 0.6 0.5 ± 0.2 0.9 ± 0.5	1.91 ± 0.02 2.52 ± 0.05 2.94 ± 0.06	6.2 ± 2.1 6 (fixed) 9 (fixed)	-2.5 ± 2.2	0.01
	2186	1.0 < R < 3.2	Cu-O Cu-Cu^{Metal} Cu-Cu^{Oxide}	3.5 ± 0.6 1.1 ± 0.2 0.7 ± 0.5	1.91 ± 0.03 2.50 ± 0.07 2.96 ± 0.07	6.8 ± 2.3 6 (fixed) 9 (fixed)	-2.2 ± 2.5	0.009
	2491	1.0 < R < 3.2	Cu-O Cu-Cu^{Metal} Cu-Cu^{Oxide}	3.3 ± 0.5 1.8 ± 0.2 0.7 ± 0.5	1.93 ± 0.03 2.55 ± 0.02 3.05 ± 0.09	7.4 ± 2.5 6 (fixed) 9 (fixed)	0.1 ± 2.5	0.007
	2796	1.15 < R < 3.2	Cu-O Cu-Cu^{Metal} Cu-Cu^{Oxide}	3.1 ± 0.4 2.3 ± 0.2 1.2 ± 0.4	1.94 ± 0.02 2.56 ± 0.02 3.09 ± 0.05	8.0 ± 2.2 6 (fixed) 9 (fixed)	2.1 ± 2.0	0.003
	3101	1.15 < R < 3.2	Cu-O Cu-Cu^{Metal} Cu-Cu^{Oxide}	3.3 ± 0.7 2.5 ± 0.2 1.2 ± 0.4	1.93 ± 0.03 2.55 ± 0.02 3.06 ± 0.07	9.0 ± 3.2 6 (fixed) 9 (fixed)	0.2 ± 2.8	0.004
-0.35	3458	1.15 < R < 3.2	Cu-O Cu-Cu^{Metal} Cu-Cu^{Oxide}	3.3 ± 0.6 2.8 ± 0.2 1.2 ± 0.5	1.94 ± 0.03 2.55 ± 0.02 3.09 ± 0.06	9.3 ± 2.9 6 (fixed) 9 (fixed)	1.1 ± 2.2	0.003
	3763	1.15 < R < 3.2	Cu-O Cu-Cu^{Metal} Cu-Cu^{Oxide}	3.1 ± 0.7 2.9 ± 0.2 1.3 ± 0.5	1.93 ± 0.03 2.55 ± 0.02 3.06 ± 0.07	8.8 ± 3.6 6 (fixed) 9 (fixed)	-0.06 ± 2.8	0.004
	4068	1.15 < R < 3.2	Cu-O Cu-Cu^{Metal} Cu-Cu^{Oxide}	3.3 ± 0.6 3.0 ± 0.2 1.6 ± 0.4	1.93 ± 0.02 2.55 ± 0.02 3.08 ± 0.04	10.1 ± 2.9 6 (fixed) 9 (fixed)	0.9 ± 1.9	0.002
	4373	1.15 < R < 3.2	Cu-O Cu-Cu^{Metal} Cu-Cu^{Oxide}	3.4 ± 0.7 3.3 ± 0.2 1.4 ± 0.5	1.94 ± 0.03 2.56 ± 0.02 3.09 ± 0.05	11.2 ± 3.8 6 (fixed) 9 (fixed)	1.6 ± 2.2	0.003
	4678	1.15 < R < 3.2	Cu-O Cu-Cu^{Metal} Cu-Cu^{Oxide}	3.2 ± 0.7 3.4 ± 0.2 1.5 ± 0.5	1.93 ± 0.03 2.55 ± 0.02 3.08 ± 0.05	10.1 ± 3.6 6 (fixed) 9 (fixed)	1.1 ± 2.2	0.003

-0.75	**5016**	1.15 < R < 3.2	Cu-O Cu-Cu^{Metal} Cu-Cu^{Oxide}	3.1 ± 0.6 3.5 ± 0.2 1.4 ± 0.5	1.94 ± 0.03 2.56 ± 0.02 3.10 ± 0.05	10.0 ± 3.5 6 (fixed) 9 (fixed)	1.8 ± 1.9	0.002
	5321	1.15 < R < 3.2	Cu-O Cu-Cu^{Metal} Cu-Cu^{Oxide}	3.2 ± 0.8 3.7 ± 0.2 1.3 ± 0.5	1.93 ± 0.03 2.55 ± 0.02 3.08 ± 0.05	11.1 ± 4.0 6 (fixed) 9 (fixed)	0.7 ± 2.0	0.002
	5626	1.15 < R < 3.2	Cu-O Cu-Cu^{Metal} Cu-Cu^{Oxide}	3.0 ± 0.8 4.0 ± 0.2 1.7 ± 0.5	1.93 ± 0.03 2.55 ± 0.02 3.08 ± 0.05	11.5 ± 4.6 6 (fixed) 9 (fixed)	0.6 ± 1.9	0.002
	5931	1.15 < R < 3.2	Cu-O Cu-Cu^{Metal} Cu-Cu^{Oxide}	3.6 ± 1.8 4.3 ± 0.3 1.7 ± 0.7	1.93 ± 0.04 2.55 ± 0.02 3.08 ± 0.07	16.2 ± 9.3 6 (fixed) 9 (fixed)	0.4 ± 2.6	0.004
	6236	1.15 < R < 3.2	Cu-O Cu-Cu^{Metal} Cu-Cu^{Oxide}	2.9 ± 1.4 4.6 ± 0.3 1.9 ± 0.8	1.94 ± 0.04 2.56 ± 0.02 3.10 ± 0.06	12.9 ± 8.2 6 (fixed) 9 (fixed)	1.4 ± 2.4	0.004
+0.05_return	**6576**	1.15 < R < 3.2	Cu-O Cu-Cu^{Metal} Cu-Cu^{Oxide}	3.3 ± 1.7 4.7 ± 0.2 2.0 ± 0.7	1.93 ± 0.04 2.55 ± 0.02 3.08 ± 0.05	15.6 ± 8.8 6 (fixed) 9 (fixed)	-0.2 ± 2.1	0.003
	6881	1.15 < R < 3.2	Cu-O Cu-Cu^{Metal} Cu-Cu^{Oxide}	3.6 ± 2.3 4.7 ± 0.3 2.1 ± 0.7	1.93 ± 0.04 2.55 ± 0.02 3.07 ± 0.06	17.2 ± 11.4 6 (fixed) 9 (fixed)	-0.7 ± 2.5	0.004
	7186	1.15 < R < 3.2	Cu-O Cu-Cu^{Metal} Cu-Cu^{Oxide}	3.5 ± 2.0 4.9 ± 0.3 2.0 ± 0.8	1.93 ± 0.04 2.55 ± 0.02 3.08 ± 0.06	16.8 ± 10.3 6 (fixed) 9 (fixed)	-0.3 ± 2.3	0.004
	7491	1.15 < R < 3.2	Cu-O Cu-Cu^{Metal} Cu-Cu^{Oxide}	3.7 ± 2.4 4.8 ± 0.3 2.1 ± 0.7	1.93 ± 0.04 2.55 ± 0.02 3.08 ± 0.06	17.9 ± 11.7 6 (fixed) 9 (fixed)	-0.5 ± 2.5	0.004
	7796	1.15 < R < 3.2	Cu-O Cu-Cu^{Metal} Cu-Cu^{Oxide}	3.7 ± 2.1 4.8 ± 0.3 2.1 ± 0.7	1.93 ± 0.04 2.55 ± 0.02 3.08 ± 0.06	17.4 ± 10.7 6 (fixed) 9 (fixed)	0.02 ± 2.3	0.003
-0.25_return	**8128**	1.15 < R < 3.2	Cu-O Cu-Cu^{Metal} Cu-Cu^{Oxide}	3.4 ± 2.2 5.0 ± 0.3 2.0 ± 0.8	1.93 ± 0.04 2.55 ± 0.02 3.08 ± 0.06	16.8 ± 11.7 6 (fixed) 9 (fixed)	-0.3 ± 2.5	0.004
	8433	1.15 < R < 3.2	Cu-O Cu-Cu^{Metal} Cu-Cu^{Oxide}	3.5 ± 2.4 5.1 ± 0.3 2.1 ± 0.8	1.93 ± 0.05 2.55 ± 0.02 3.08 ± 0.06	17.2 ± 12.3 6 (fixed) 9 (fixed)	-0.4 ± 2.5	0.004
	8738	1.15 < R < 3.2	Cu-O Cu-Cu^{Metal} Cu-Cu^{Oxide}	3.6 ± 2.4 5.1 ± 0.3 2.2 ± 0.8	1.93 ± 0.04 2.55 ± 0.02 3.08 ± 0.06	17.6 ± 12.1 6 (fixed) 9 (fixed)	-0.4 ± 2.4	0.004
	9043	1.15 < R < 3.2	Cu-O Cu-Cu^{Metal} Cu-Cu^{Oxide}	3.6 ± 2.6 5.2 ± 0.3 2.2 ± 0.9	1.93 ± 0.05 2.55 ± 0.02 3.08 ± 0.06	17.6 ± 13.4 6 (fixed) 9 (fixed)	-0.3 ± 2.6	0.004
	9348	1.15 < R < 3.2	Cu-O Cu-Cu^{Metal} Cu-Cu^{Oxide}	3.6 ± 2.6 5.3 ± 0.3 2.2 ± 0.8	1.93 ± 0.05 2.55 ± 0.02 3.07 ± 0.06	17.7 ± 12.9 6 (fixed) 9 (fixed)	-1.0 ± 2.4	0.004

-0.35_return	**9653**	1.15 < R < 3.2	Cu-O Cu-Cu^{Metal} Cu-Cu^{Oxide}	3.7 ± 2.4 5.4 ± 0.3 2.0 ± 0.8	1.93 ± 0.04 2.55 ± 0.02 3.08 ± 0.06	18.3 ± 12.4 6 (fixed) 9 (fixed)	-0.1 ± 2.2	0.003
	9958	1.15 < R < 3.2	Cu-O Cu-Cu^{Metal} Cu-Cu^{Oxide}	3.7 ± 2.7 5.4 ± 0.3 2.1 ± 0.8	1.93 ± 0.04 2.55 ± 0.02 3.08 ± 0.06	18.9 ± 13.5 6 (fixed) 9 (fixed)	-0.5 ± 2.2	0.003
	10263	1.15 < R < 3.2	Cu-O Cu-Cu^{Metal} Cu-Cu^{Oxide}	3.8 ± 3.1 5.3 ± 0.3 2.2 ± 0.9	1.93 ± 0.05 2.55 ± 0.02 3.07 ± 0.06	19.5 ± 15.2 6 (fixed) 9 (fixed)	-0.9 ± 2.6	0.004
	10568	1.15 < R < 3.2	Cu-O Cu-Cu^{Metal} Cu-Cu^{Oxide}	3.7 ± 2.9 5.5 ± 0.4 2.2 ± 0.9	1.93 ± 0.05 2.55 ± 0.02 3.08 ± 0.06	18.5 ± 14.8 6 (fixed) 9 (fixed)	-0.3 ± 2.5	0.005
	10873	1.15 < R < 3.2	Cu-O Cu-Cu^{Metal} Cu-Cu^{Oxide}	3.6 ± 3.0 5.4 ± 0.3 2.3 ± 0.8	1.92 ± 0.05 2.54 ± 0.02 3.06 ± 0.06	18.6 ± 15.0 6 (fixed) 9 (fixed)	-1.2 ± 2.5	0.004

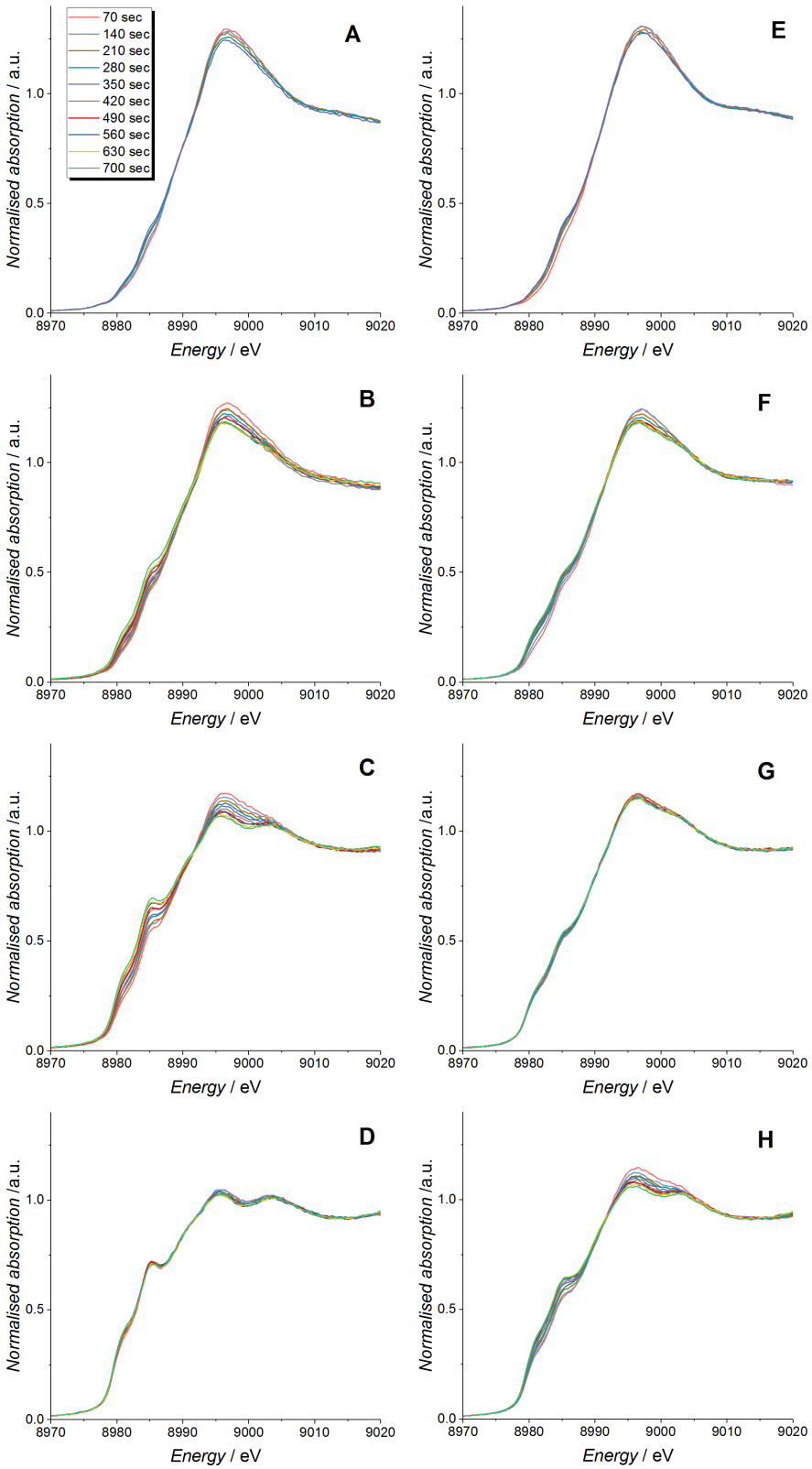

Figure S13. *In-situ* Cu K-edge XANES spectra of (A-D) 9 wt.% Cu:NTO and (E-F) 10 wt.% CuO@NTO in CO_2-saturated 0.1 M K_2HPO_4 / KH_2PO_4 buffer solution (pH 6.5) at (A,E) +0.05 V, (B,F) -0.25 V, (C,G) -0.35 V and (D,H) -0.75 V.

Table S7. Linear combination fit analysis results for *in situ* XANES spectra of 9 wt.% Cu:NTO recorded at the Cu K-edge in CO_2-saturated 0.1 M K_2HPO_4 / KH_2PO_4 solution (pH 6.5) at various applied potentials.

		Cu species composition / %				
E / V vs. RHE	***time / s***	**Cu (0)**	**Cu(I)**	**Cu(II)**	***Oxidation state***	R_{factor}
	70	0	22.2 ± 7.0	77.8 ± 7.0	1.78 ± 0.21	0.032
	140	0	26.7 ± 12.0	73.3 ± 6.8	1.73 ± 0.26	0.030
+0.05	210	0	36.3 ± 11.7	67.3 ± 6.5	1.71 ± 0.25	0.030
	280	0	39.1 ± 6.4	60.9 ± 9.4	1.61 ± 0.25	0.029
	350	0	47.9 ± 6.3	52.1 ± 9.3	1.52 ± 0.25	0.029
	450	0	48.9 ± 10.7	51.1 ± 6.1	1.51 ± 0.23	0.026
	520	9.1 ± 4.0	44.7 ± 8.2	46.2 ± 10.8	1.37 ± 0.30	0.025
	590	7.9 ± 3.9	48.0 ± 7.1	44.1 ± 6.0	1.36 ± 0.19	0.024
	660	12.7 ± 3.7	49.1 ± 6.7	38.2 ± 5.6	1.26 ± 0.18	0.021
	730	15.6 ± 9.5	48.3 ± 7.3	36.1 ± 5.4	1.21 ± 0.18	0.020
-0.25	800	24.5 ± 8.9	42.6 ± 6.9	32.8 ± 5.0	1.08 ± 0.17	0.012
	870	15.7 ± 3.3	58.9 ± 6.9	25.3 ± 5.0	1.10 ± 0.17	0.019
	940	22.5 ± 3.1	55.8 ± 6.4	21.7 ± 4.7	0.99 ± 0.16	0.011
	1010	21.6 ± 8.3	60.6 ± 6.2	17.8 ± 4.6	0.96 ± 0.15	0.010
	1080	18.8 ± 8.1	72.1 ± 6.1	9.1 ± 4.5	0.90 ± 0.15	0.010
	1172	20.6 ± 2.8	73.9 ± 5.8	5.5 ± 4.2	0.85 ± 0.14	0.009
	1242	25.4 ± 3.8	74.6 ± 3.8	0	0.75 ± 0.04	0.008
	1312	29.9 ± 2.4	70.1 ± 2.4	0	0.70 ± 0.02	0.007
	1382	34.3 ± 2.3	65.7 ± 4.0	0	0.66 ± 0.04	0.007
	1452	37.8 ± 3.4	62.2 ± 2.3	0	0.62 ± 0.02	0.007
-0.35	1522	41.8 ± 3.5	58.2 ± 2.5	0	0.58 ± 0.03	0.008
	1592	44.9 ± 3.6	55.1 ± 2.5	0	0.55 ± 0.03	0.008
	1662	46.4 ± 3.9	53.6 ± 2.8	0	0.54 ± 0.03	0.011
	1732	50.1 ± 0.4	49.9 ± 2.9	0	0.50 ± 0.03	0.011
	1802	52.9 ± 3.1	41.8 ± 7.0	0	0.42 ± 0.07	0.013
	2042	59.8 ± 3.3	40.2 ± 7.8	0	0.40 ± 0.08	0.014
	2112	61.0 ± 3.5	39.0 ± 3.5	0	0.39 ± 0.04	0.016
	2182	63.7 ± 3.5	36.3 ± 3.5	0	0.36 ± 0.04	0.015
	2252	64.0 ± 3.6	36.0 ± 8.3	0	0.36 ± 0.08	0.016
	2322	65.5 ± 3.5	34.5 ± 3.5	0	0.35 ± 0.04	0.016
-0.75	2392	66.3 ± 3.6	33.7 ± 3.6	0	0.34 ± 0.04	0.016
	2462	66.6 ± 3.5	33.4 ± 3.5	0	0.33 ± 0.04	0.016
	2532	68.6 ± 3.4	31.4 ± 8.2	0	0.31 ± 0.08	0.015
	2602	68.1 ± 4.5	31.9 ± 3.3	0	0.32 ± 0.03	0.015
	2672	68.3 ± 3.4	31.7 ± 2.4	0	0.32 ± 0.02	0.015
	2829	69.7 ± 3.2	30.3 ± 3.2	0	0.30 ± 0.03	0.135
	2899	66.8 ± 5.0	33.2 ± 3.4	0	0.33 ± 0.03	0.015
+0.05	2969	70.3 ± 3.1	29.7 ± 3.1	0	0.30 ± 0.03	0.013
	3039	68.0 ± 3.3	32.0 ± 4.5	0	0.32 ± 0.05	0.014
	3109	69.7 ± 3.1	30.3 ± 4.4	0	0.30 ± 0.04	0.013

Table S8. Linear combination fit analysis results for *in situ* XANES spectra of 10 wt.% CuO@NTO recorded at the Cu K-edge in CO_2-saturated 0.1 M K_2HPO_4 / KH_2PO_4 solution (pH 6.5) at various applied potentials.

		Cu species composition / %				
E / V vs. RHE	***time / s***	**Cu (0)**	**Cu(I)**	**Cu(II)**	***Oxidation state***	R_{factor}
+0.05	70	0	15.3 ± 7.7	84.7 ± 9.7	1.85 ± 0.27	0.034
	140	0	26.0 ± 7.3	74.0 ± 10.9	1.74 ± 0.29	0.032
	210	0	30.8 ± 13.7	69.2 ± 7.1	1.69 ± 0.28	0.032
	280	0	38.7 ± 6.9	61.3 ± 10.2	1.61 ± 0.27	0.030
	350	0	41.0 ± 11.9	59.0 ± 6.8	1.59 ± 0.26	0.030
-0.25	511	12.2 ± 10.9	43.2 ± 8.4	44.6 ± 6.2	1.32 ± 0.32	0.023
	581	11.2 ± 4.0	51.2 ± 9.3	37.6 ± 6.0	1.26 ± 0.25	0.022
	651	15.7 ± 10.1	53.7 ± 7.5	30.6 ± 5.5	1.15 ± 0.29	0.019
	721	19.3 ± 9.3	52.1 ± 7.1	28.6 ± 5.3	1.09 ± 0.27	0.019
	791	23.3 ± 9.0	50.9 ± 6.8	25.7 ± 5.0	1.02 ± 0.26	0.014
	861	22.6 ± 9.0	53.2 ± 6.7	24.2 ± 4.9	1.02 ± 0.26	0.015
	931	23.1 ± 8.7	55.8 ± 6.6	21.1 ± 4.9	0.98 ± 0.25	0.014
	1001	24.6 ± 3.2	54.7 ± 6.6	20.7 ± 8.8	0.96 ± 0.27	0.013
	1071	23.6 ± 8.5	58.0 ± 6.5	18.4 ± 4.8	0.95 ± 0.25	0.014
	1141	25.8 ± 3.1	55.9 ± 6.4	18.4 ± 4.7	0.93 ± 0.19	0.013
-0.35	1229	27.8 ± 2.9	57.8 ± 6.0	14.5 ± 8.5	0.87 ± 0.26	0.012
	1299	28.3 ± 2.9	58.8 ± 6.0	12.9 ± 7.1	0.85 ± 0.23	0.012
	1369	27.7 ± 7.7	62.4 ± 5.8	9.9 ± 4.3	0.82 ± 0.22	0.014
	1439	31.9 ± 2.8	57.6 ± 5.7	10.6 ± 7.7	0.79 ± 0.24	0.011
	1509	30.8 ± 2.7	61.4 ± 5.5	7.8 ± 6.6	0.77 ± 0.21	0.013
	1579	29.7 ± 7.5	63.5 ± 6.8	6.8 ± 4.1	0.77 ± 0.23	0.010
	1649	30.5 ± 7.4	65.2 ± 5.6	4.3 ± 4.1	0.74 ± 0.21	0.008
	1719	31.3 ± 7.4	64.3 ± 5.6	4.4 ± 4.1	0.73 ± 0.21	0.008
	1789	31.0 ± 3.7	69.0 ± 2.6	0	0.69 ± 0.06	0.008
	1859	31.3 ± 3.7	68.7 ± 2.5	0	0.69 ± 0.06	0.007
-0.75	1960	32.4 ± 3.6	67.6 ± 2.4	0	0.68 ± 0.06	0.007
	2030	38.5 ± 3.4	61.5 ± 2.2	0	0.62 ± 0.06	0.006
	2100	42.3 ± 3.4	57.7 ± 2.2	0	0.58 ± 0.06	0.006
	2170	43.3 ± 3.4	56.7 ± 2.2	0	0.57 ± 0.06	0.006
	2240	46.7 ± 2.3	53.3 ± 3.2	0	0.53 ± 0.06	0.006
	2310	49.0 ± 2.3	51.0 ± 3.2	0	0.51 ± 0.06	0.006
	2380	51.6 ± 3.4	48.4 ± 2.4	0	0.48 ± 0.06	0.007
	2450	53.0 ± 2.4	47.0 ± 3.4	0	0.47 ± 0.06	0.007
	2520	55.3 ± 3.6	44.7 ± 2.5	0	0.45 ± 0.06	0.008
	2590	57.6 ± 3.6	42.4 ± 2.4	0	0.42 ± 0.06	0.007
+0.05_return	2734	57.0 ± 3.0	43.0 ± 2.5	0	0.43 ± 0.06	0.008
	2804	58.9 ± 2.4	41.1 ± 5.7	0	0.41 ± 0.08	0.007
	2874	59.8 ± 3.4	40.2 ± 2.4	0	0.40 ± 0.06	0.007
	2944	61.2 ± 6.8	38.8 ± 5.2	0	0.39 ± 0.12	0.007
	3014	61.9 ± 6.6	38.1 ± 5.0	0	0.38 ± 0.12	0.007

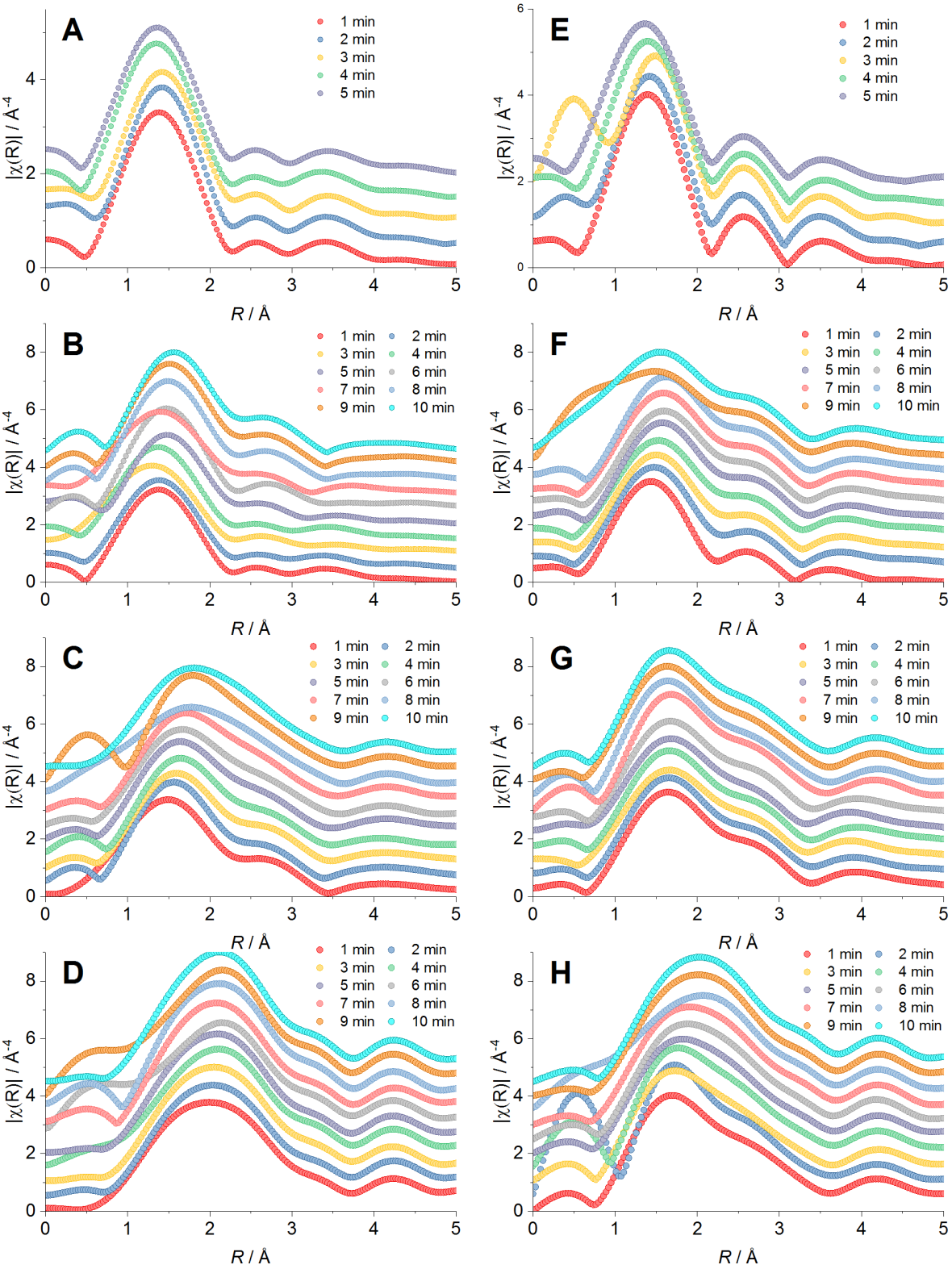

Figure S14. k^3-weighted Fourier Transforms of *in situ* Cu K-edge XAS spectra of (A-D) 9 wt.% Cu:NTO) and (E-F) 10 wt.% CuO@NTO in CO_2-saturated 0.1 M K_2HPO_4 / KH_2PO_4 (pH 6.5) at (A,E) +0.05 V, (B,F) -0.25 V, (C,G) -0.35 V and (D,H) -0.75 V.

References

1. Garcia-Canadas, J.; Adkins, N. J.; McCain, S.; Hauptstein, B.; Brew, A.; Jarvis, D. J.; Min, G. *ACS Comb. Sci.* **2016,** 18, (6), 314-319.

2. Li, S.; Adkins, N. J. E.; McCain, S.; Attallah, M. M. *J. Alloys Compd.* **2018,** 768, 392-398.

3. van Bokhoven, J. A.; Lamberti, C., *X-Ray Absorption and X-Ray Emission Spectroscopy : Theory and Applications*. John Wiley & Sons, Incorporated: New York, UNITED KINGDOM, 2016.

4. Zhang, R.; McEwen, J. S. *J. Phys. Chem. Lett.* **2018,** 9, (11), 3035-3042.

8. CONCLUSIONS AND FUTURE OUTLOOK

This thesis has explored the utilisation of cathodic corrosion electrochemical syntheses to prepare a range of useful metal oxide (photo)electrocatalysts for green energy applications, namely water oxidation and the electrochemical reduction of CO_2. Thorough characterisation has been undertaken to better understand the physical, chemical and optical properties of the prepared nanostructured materials and comparisons to existing synthetic methods have been presented.

The work presented has demonstrated, for the first time, that cathodic corrosion is a useful synthetic tool for the rapid and controlled preparation of key, crystalline nanoscale photoelectrocatalysts for the PEC water splitting reaction, namely H_2WO_4 and $BiVO_4$, with homogeneous particle size and elemental composition. The ease of tuning particle size of H_2WO_4 via cathodic corrosion parameters was demonstrated by varying the frequency of the applied square waveform. Furthermore, the successful preparation of $BiVO_4$ afforded exciting possibilities for the method to produce multi-metallic oxides and the incorporation of dopants using simple solution precursors. Both crystalline materials displayed PEC activity under illumination, albeit that $BiVO_4$ only demonstrated PEC activity in the presence of a hole scavenger, suggesting that the star-shaped structures suffered from bulk charge carrier recombination.

For the first time the single-pot, single-step synthesis of mixed metal oxide nanostructures via cathodic corrosion was achieved. Metal-doped titanate nanowires were produced by cathodically etching a series of Ti alloys produced via suspended droplet alloying, providing a rapid, electrochemical route for the production, screening and discovery of high surface

area nanomaterials with controlled composition. The as-prepared materials were thoroughly characterised by physical, optical and electrochemical methods, allowing elucidation of the structure of the nanowires: $Na_2Ti_3O_7$ (NTO) and M:NTO, where M (= Fe, Cu or Sn) was incorporated into the interlayer spacing of the TiO_6 octahedra. A low Cu^{2+} dopant concentration was observed to increase the UV-visible absorption capability of NTO, resulting in enhanced PEC water oxidation activity. The retention of the relative composition of the alloys was best achieved in the FeTi system, which was essentially identical to the parent alloy. Poorer compositional retention was achieved for M = Cu and Sn, due to the tendency of Cu ions to form soluble aqueous complexes in the presence of ^{-}OH and a maximum concentration of Cu intercalation in the oxide matrix, and the high dopant concentration and multiple crystalline phases of the SnTi alloy. These results serve to highlight that although experimentally the formation of metal oxides via cathodic corrosion is simple, the mechanistic complexity is non-trivial and requires further investigation.

Confined atoms/ions have been reported to possess enhanced intrinsic catalytic properties. Thus, following the successful preparation of Cu-doped NTO, possessing confined Cu^{2+} ions, the CO_2RR activity and selectivity of the catalyst was investigated in comparison to a CuO@NTO mixed phases catalyst. The Cu species composition and oxidation state were monitored via *in situ* XAS under CO_2RR conditions.

OLEMS characterisation identified that the gaseous products generated by CO_2RR at -0.8 V *vs*. RHE on 9 wt.% Cu:NTO over 1 hour were H_2, CO and CH_4. For 10 wt.% CuO@NTO the gaseous products identified were H_2, CH_4 and C_2H_4. A decrease in detected C_2H_4 and subsequent increase in CH_4 concentration was shown to correlate to the increase in Cu(0) species and Cu-Cu^{metal} bonding determined through *in situ* XANES and EXAFS analyses. Generally, the reduction of the Cu^{2+} species was more gradual for the CuO-derived catalyst under CO_2RR conditions, particularly noticeable when comparing the *in situ* XANES spectra

measured at -0.35 V. As XAS techniques probe the bulk of the material, it was anticipated that the inner core of the CuO phase, which does not directly participate in surface catalysis, would experience slower reduction kinetics, promoting the enhanced stability of oxidised Cu species observed. The observed decrease in C_2H_4/CH_4 ratio with the CuO-derived catalyst was ascribed to the formation of the small nanoclusters over time. Likewise, the CO/CH_4 ratio for 9 wt.% Cu:NTO was ascribed to increase in Cu cluster size based on agreement with previous reports.

There is still work to be done in better understanding the mechanism of oxide formation via cathodic corrosion that could provide greater insight in to the conditions needed to produce target catalysts with specific size, shape, morphology and elemental composition and the effect that various parameters such as etching time or solution composition have on the resulting particles. Despite this, cathodic corrosion was shown here to be a facile alternative method for producing metal oxide nanoparticles for green energy applications.

Cathodic corrosion is performed under conditions that are significantly far from equilibrium. As such, it is not currently possible to accurately predict the nature of nanostructured metal oxides based on existing knowledge that has been captured in Pourbaix diagrams, for example, without sufficient trial and error approaches modifying the synthetic conditions employed. Therefore, to advance the synthetic methodology presented in this thesis, it would be greatly advantageous to first compile a series of cathodic corrosion standards, similar to Pourbaix/phase diagrams based on the metal of choice, where the products obtained by varying electrolyte, concentration, applied potential range, frequency and duty cycle are combined. Although the syntheses themselves would be relatively trivial, the time and resource required to fully characterise each product would be relatively demanding, but greatly rewarding. Perceivably, during the course of such experiments greater understanding of the exact oxide formation mechanism(s) would come to light, allowing greater accuracy in

targeting specific mixed metal oxide catalysts via cathodic corrosion of ternary and even quaternary alloys in future.

Another parameter of cathodic corrosion that has yet to be fully explored is the effect of temperature on the metal oxide products formed. All the syntheses presented in this thesis were performed at ambient room temperature, but it would be interesting to investigate how a more controlled temperature environment would affect the speed and oxide product structure and morphology of cathodic corrosion syntheses, at both elevated and reduced temperatures.

The cathodic corrosion experimental setup allows the reaction to be tracked electrochemically but also visually which was particularly useful in understanding the formation of H_2WO_4 through multiple oxide phases by the colour changes observed. The use of other visualisation techniques, such as magnetic resonance imaging (MRI) could have a role to play in further understanding and visualising the oxide formation process. This could provide insight into the specific reactions within the vessel that lead to chemical oxidation, whether purely reaction with oxygen evolved at the CE or water in the electrolyte, or a combination of both with a defined ratio.